Distributing quantum information with holes in germanium

van Riggelen, F.

DOI
10.4233/uuid:890ceb06-cd33-4b0a-85f4-d664850e86c4

Publication date
2024

Document Version
Final published version

Citation (APA)
van Riggelen, F. (2024). *Distributing quantum information with holes in germanium*. [Dissertation (TU Delft), Delft University of Technology]. https://doi.org/10.4233/uuid:890ceb06-cd33-4b0a-85f4-d664850e86c4

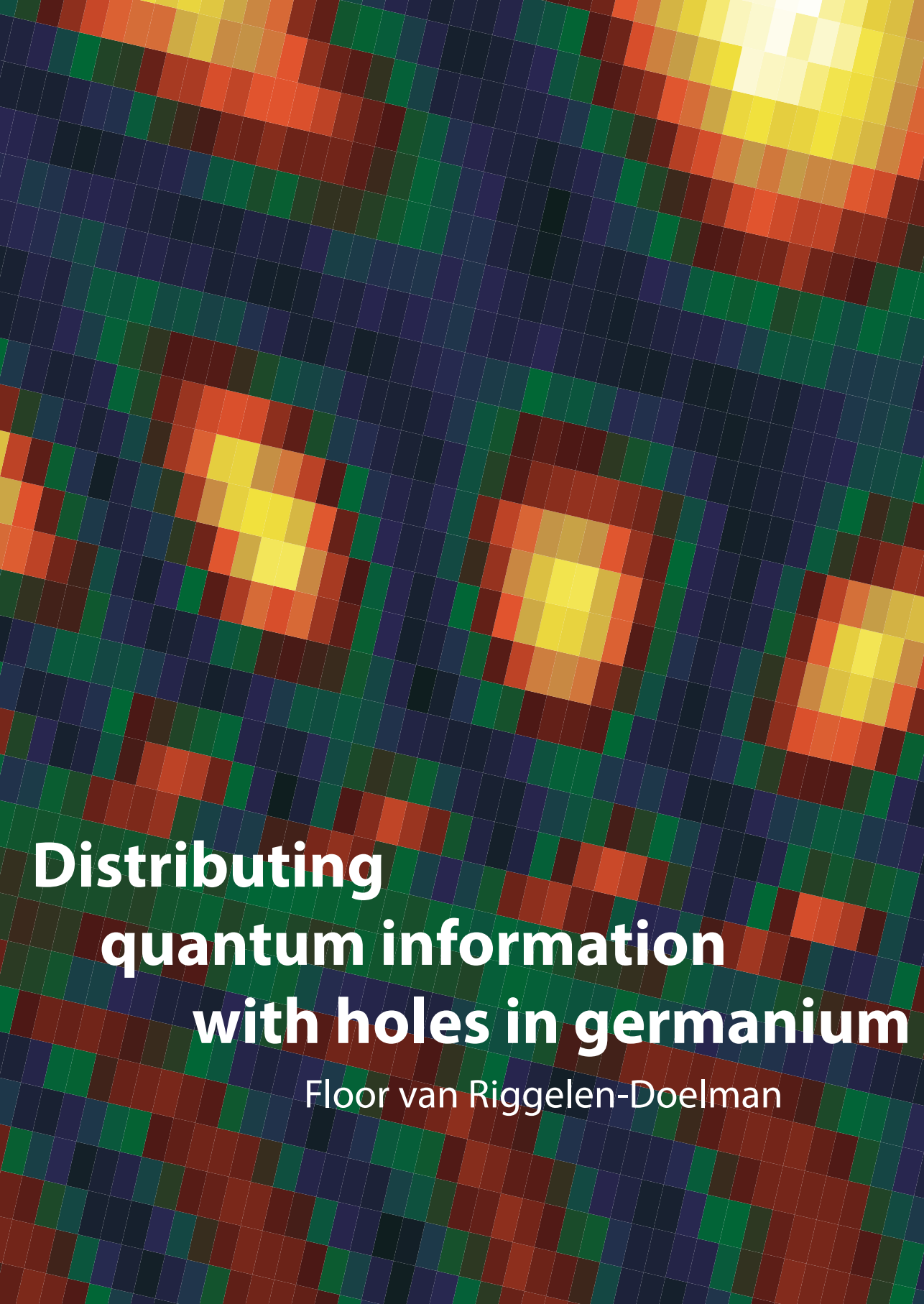

Distributing quantum information with holes in germanium

Floor van Riggelen-Doelman

DISTRIBUTING QUANTUM INFORMATION WITH HOLES IN GERMANIUM

DISTRIBUTING QUANTUM INFORMATION WITH HOLES IN GERMANIUM

Proefschrift

ter verkrijging van de graad van doctor
aan de Technische Universiteit Delft,
op gezag van de Rector Magnificus prof. dr. ir. T.H.J.J. van der Hagen,
voorzitter van het College voor Promoties,
in het openbaar te verdedigen op woensdag 26 juni 2024 om 10:00 uur

door

Floor VAN RIGGELEN-DOELMAN

Master of Science in Physics,
Universiteit van Amsterdam, Nederland
geboren te Amersfoort, Nederland.

Dit proefschrift is goedgekeurd door de

promotor: dr. ir. M. Veldhorst
copromotor: prof. dr. ir. L.M.K. Vandersypen

Samenstelling promotiecommissie:

Rector Magnificus,	voorzitter
Dr. ir. M. Veldhorst	Technische Universiteit Delft
Prof. dr. ir. L.M.K. Vandersypen	Technische Universiteit Delft

Onafhankelijke leden:

Prof. dr. B.M. Terhal	Technische Universiteit Delft
Prof. dr. A.F. Otte	Technische Universiteit Delft
Prof. dr. G. Platero	Materials Science Institute of Madrid, Spain
Dr. A. Chatterjee	Technische Universiteit Delft
Dr. N. Ares	New College, University of Oxford, United Kingdom

Paranymphs:

Dr. ir. A.M.J. Zwerver
Ir. M. van Riggelen

Trefwoorden: Quantum computing, hole spin qubits, quantum dots, germanium, phase flip code, shuttling
Geprint door: Gildeprint
Omslag: Bewerkt meetresultaat van een shuttling experiment met een electron-gat door drie quantum dots.

ISBN 978-94-6366-879-8

An electronic version of this dissertation is available at
http://repository.tudelft.nl/.

"Never be so kind, you forget to be clever.
Never be so clever, you forget to be kind." [1]

For my grandmothers:
Johanna Braakman-Holsappel
Ans van Riggelen-Clemens

1

INTRODUCTION

"The single story creates stereotypes, and the problem with stereotypes is not that they are untrue, but that they are incomplete. They make one story become the only story." [2]

1

1.1. ONE HUNDRED YEARS OF QUANTUM MECHANICS

A hundred years ago, in 1924, the term 'quantum mechanics' was introduced by physicists at the university of Göttingen [3]. Quantum mechanics, the theory that helps us to understand the physics of the microscopic world, has become one of the most extensively tested physical theories. At the same time, this theory confronts physicist with the most fundamental questions about nature and reality. Remarkably, although scientist still do not have conclusive answers to all of those elemental questions, the technological applications of quantum mechanics have changed the world.

Among the initial papers using the term quantum mechanics were two publications [9, 10] that introduced matrix mechanics[11] as a mathematical framework to formalize the ideas about quantum physics that were developed in the years before. One of the first demonstrations of the predictive power of quantum mechanics, applied to the properties of a real physical system, was performed by Lucy Mensing. She used the abstract mathematical framework of matrix mechanics to calculate the rotational vibration spectrum of diatomic molecules, such as O_2, N_2 and CO. The results of her calculations matched the experimental band spectrum (measured at the beginning of the twentieth century) exactly and were published in the Zeitschrift für Physik in 1926 [4]. As an additional result of these calculations, she was the first person to find the permissible values of the quantum number l for orbital angular momentum [7, 12].

Figure 1.1: **Dr. Lucy Mensing (1901-1995)**, later Lucy Schütz, was a German physicist. She received her doctorate in theoretical physics in 1925 under Wilhelm Lenz. Thereafter, she worked in Göttingen together with Pascual Jordan on applying matrix mechanics to diatomic molecules [4]. Later in her career she collaborated with Wolfgang Pauli, calculating the electrical polarizability of gases from diatomic molecules [5]. Alfred Landé offered her a position in Tübingen, where she worked on the scattering of slow electrons on atoms [6]. Her scientific career ended in 1930. For more information see Ref. [7], source image Ref [8].

Where the calculations of Mensing explained experimental results that could not be understood with classical physics, applying quantum mechanics to physical systems also resulted in predictions that could not be tested experimentally until years later. An example is the work by Maria Göppert in 1931. In her doctoral thesis, at the university of Göttingen, she proposed the possibility of, and developed the theory on, two-photon absorption in atoms [13]. In this process, two photons are absorbed (with either different or the same frequency) to excite a molecule from the ground state to a higher energy level. The experimental verification of the results in her thesis [14] was only possible with the invention of the laser thirty years later.

When the principles of quantum mechanics were established, they were used to provide new explanations and new predictions of physical phenomena. Not long after, quantum mechanics was applied to reevaluate existing theories, already (partly) based on quantum mechanics, leading to their refinement or replacement based on new experimental findings and evolving understanding. For instance, in 1930 the liquid-drop

model [15] was proposed. This theory treats the nucleus of an atom as a drop of high density, incompressible fluid, where the protons and neutrons are bound by the nuclear force. A quantitative representation of the liquid-drop model is given by the semi-empirical mass formula [16]. As the name suggests, it combines theory and empirical measurements and could give a good approximation of the atomic mass of a nucleus.

This model was used to provide an explanation for the effect of nuclear fission, as proposed by Lise Meitner, together with a colleague, in 1939 [27]. She calculated that the nuclear charge of a uranium nucleus was large enough to compensate almost entirely for its 'surface tension', so that the uranium nucleus would resemble an unstable drop of liquid. Furthermore, she realized that the sum of the masses of the two nuclei formed by the nuclear fission process would be smaller than the mass of the original uranium nucleus. Using the semi-empirical mass formula and $E = mc^2$, Meitner demonstrated that this difference in mass could provide the energy required for the two resulting nuclei to gain velocity as they are pushed apart by their mutual electric repulsion [28].

Figure 1.2: **Dr. Maria Göppert (1906-1972)**, later Maria Goeppert-Mayer, was a German-American physicist. She wrote her doctoral thesis on the theory of two-photon transitions [13], under supervision of Max Born. In 1930 she moved to the USA, where she worked on topics ranging from physical chemistry [17] to nuclear physics [18–22]. During the Second World War, she contributed to the Manhattan Project. In 1963 she received the Nobel prize, shared with Hans Jensen, "for their discoveries concerning nuclear shell structure" [23]. She was appointed full professor in 1960 at the University of California, where she continued to teach and do research after receiving the Nobel prize. For more information see Ref. [24, 25], source image Ref. [26].

However, there were questions that the liquid-drop model left unanswered. While studying the properties of nuclear fission products, Göppert encountered one of those phenomena. In 1948 she published an overview of experimental data which showed evidence of the existence of 'magical numbers' [19], certain numbers of proton and neutrons in the nucleus of an atom for which the nucleus is most stable. The liquid-drop model could not give a satisfying explanation and Göppert proposed an alternative theory: the nuclear shell model. This model is similar to the atomic shell model and proposes a structure of the atomic nucleus in terms of energy levels, taking into account the exclusion principle for particles with odd-half-integer spin [29] and spin-orbit interaction. With the nuclear shell model, Göppert was able to reproduce the magical numbers [20, 21] and it came to replace the liquid-drop model in describing nuclei. Among the later work of Meitner is the application of the nuclear shell model to nuclear fission [30].

Although quantum mechanics can be used to correctly predict the characteristics of microscopical systems, it has many aspects which are not intuitive. A typical example is superposition: a quantum mechanical system can be in multiple states at the same time, but the result of a measurement will be one of those states. For example, the spin of an

electron can be in a superposition of spin-up and spin-down, but when measured, the measurement outcome is either spin-up or spin-down. The wavefunction describing a quantum state in a superposition can only give a statistical prediction of the measurement, such as a 50% probability of observing spin-up and a 50% probability of observing spin-down.

It becomes even more curious when applying superposition to a two- (or multiple-) quantum particle system with a conserved quantity. Taking the example of electron spin once more: if two spins are made to interact, their quantum state can no longer be described as two separate systems. The spin state of one electron becomes strongly correlated with the spin state of the other electron. For instance, in the case of anti-parallel correlation, if one spin is measured to be spin-down (which cannot be known before the measurement, because the system is in superposition), the other will instantaneously become spin-up, and vice versa. This correlation holds, even if the distance between the spins becomes very large. This phenomenon is called entanglement. It was considered so extraordinary, that physicists questioned whether quantum mechanics actually provides a complete description of physical reality or if certain information is missing, leading to the idea of 'hidden variables' [39].

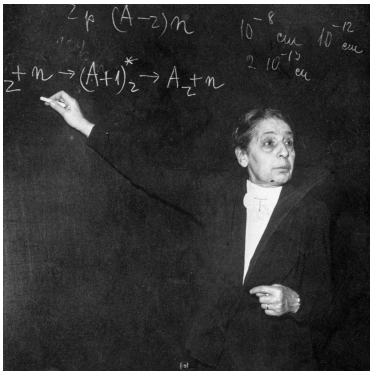

Figure 1.3: **Dr. Lise Meitner (1878-1968)** was an Austrian-Swedish physicist. She completed her doctoral dissertation in 1906, at the University of Vienna. After her PhD, she went to work in Berlin, where she started a long and successful collaboration with chemist Otto Hahn. They discovered the element protactinium in 1918 [31] and studied nuclear isomerism [32]. In 1922 she discovered the Meitner-Auger effect [33, 34]. In 1938 Meitner (who was from Jewish descend) fled from Germany to Sweden with help from her colleague physicists [35]. Together with Otto Frisch, she correctly interpreted the results of an experiment by Otto Hahn as the splitting of a uranium nucleus [27]. She refused to contribute to the Manhattan Project. Later in her career, she contributed to the design of Sweden's first nuclear reactor. For more information see Ref. [36, 37], source image Ref. [38].

At the beginning of the development of quantum mechanics, many physicists were involved in heated debates about the fundamental meaning of quantum mechanics. Among them, bringing in a sturdy philosophical background, was Grete Hermann. She wrote a manuscript in 1933 on how to reevaluate the concept of causality given to the recent progress in quantum mechanics [46]. She communicated this paper to leading scientists in the field and she was invited to stay in Leipzig to discuss her ideas. These discussions resulted in a paper in 1935 titled 'Die naturphilosophischen Grundlagen der Quantummechanik' [40]. There are several points that make this paper noteworthy [47]. Firstly, Hermann explains what problem is posed by the uncertainty principle (which states that it is, for example, impossible to know the position and momentum of a particle precisely and simultaneously). As a way of thinking about this problem, she points to the concept that we would now call contextuality: the information that can be acquired about a physical system depends on the context of the measurement device. More generally, she give a thorough explanation of 'complemen-

tarity' [48, 49], this is the idea that combining two contrasting theories makes it possible to explain a set of phenomena. According to her, complementarity applies to quantum mechanics in three different but related ways: a) the description as wave and particle, (b) the relationship between characteristic properties such as position and momentum, and (c) the complementarity of the intuitively classical description and the quantum mechanical formalism. Since the only way to obtain knowledge about the microscopic world is by using classical measurement devices, there will be a 'cut' between the two complimentary descriptions, meaning the observer can always only learn part of the reality of a physical system. Secondly, she gives one of the first clear descriptions in literature of entanglement between two particles. This phenomenon only got its name later that year [50]. Thirdly, she presents a fatal flaw in a 'proof' [51] published in 1932 that claimed to show that hidden variables are impossible. It was not until the 1960's that this became again the subject of scientific interest [52].

During the Second World War, the approach to science in general and physics specifically became more pragmatic. Due to the circumstances, scientists started to collaborate in large interdisciplinary projects aiming to develop certain technology, projects which were heavily government-funded [53]. The Manhattan project is a very well known example, but this was not the only project in its kind. 'Rad Lab', short for the MIT Radiation Laboratory, played a key role in the development of radar technology [54]. The Second World War, reinforced by the Cold War that followed, would have a lasting influence on the organisation and funding of science, and on the kind of research topics scientists would pursue [53], particularly in the United States. For quantum physics, this 'shut-up-and-calculate' mentality [55] resulted in many scientists focusing on nuclear and solid state physics. Although this approach proved very productive in these areas, it also resulted in the fact that thinking about the more fundamental and philosophical questions of quantum mechanics was regarded as a luxury, or even as pseudo-science, and became marginalized [53, 56].

Figure 1.4: **Dr. Grete Hermann (1901-1984)**, later Grete Henry-Hermann, was a German mathematician and philosopher. She was a doctoral student of Emmy Noether and received her PhD in 1926 in Göttingen. After that, she worked for two years as an assistant of the philosopher Leonard Nelson. Her stay in Leipzig resulted in her main contribution to the interpretation of quantum mechanics [40]. Next to her work, she was a political activist and socialist, and opposed the Nazi party. As a result, she had to leave Germany in 1936. After the Second World War, the focus of her work shifted towards ethics and political responsibility [41]. Besides that, she was heavily involved in the rebuilding of the educational system in Germany. For more information see Ref. [42–44], source image Ref. [45].

It was in this historical context, that the first experimental demonstration of entanglement was performed by Chien-Shiung Wu [61, 64, 65]. In 1949 she, together with her graduate student, performed an experiment to proof the pair theory [66, 67]. When an electron and a positron annihilate each other, this will result in two photons which travel in opposite direction with equal momen-

tum. According to pair theory, the polarization of these photons is correlated: if one of the photons is polarized in-plane, the other photon is linearly polarized out-of-plane, perpendicular to the first photon [66]. They were not the first ones to try this experiment, but they were the first to gather sufficient data to show a quantitative match to the theory [64]. Indeed, they found that the pairs of photons stayed consistently orthogonally polarized, even when the photons moved further away from each other. The results were published in 1950 [68]. These results were only much later in time explicitly described as demonstrating entanglement, both by others [64, 69, 70] and by Wu herself [71]. This experiment was not designed to proof or disprove the existence of hidden variables, but it did inspire experiments with this purpose [72, 73].

Figure 1.5: **Dr. Chien-Shiung Wu (1912-1997)**, was a Chinese-American experimental physicist. In 1936 she moved from China to the USA to pursue her PhD, which she obtained in 1940 at the University of California at Berkeley, under supervision of Ernest Lawrence. During her PhD, she performed her first experiments on beta-decay, on which topic she would become an expert [57, 58]. She joined the Manhattan Project at Columbia University, where she stayed to work on nuclear physics after the war. She is best known for the experimental proof of the violation of parity conservation for weak nuclear interactions [59]. For this work she received the Wolf Prize in Physics. In 1975 she became president of the American Physical Society. She retired as a professor in 1981. For further information, see Ref. [60–62], source image Ref. [63].

The 'shut-up-and-calculate' attitude proved to be fruitful. In the two decades after the Second World War, the pragmatic approach to quantum mechanics led to some incredible applications, such as transistors and lasers [74, 75]. These inventions combined form the cornerstone of technologies like classical computers and the internet, which shape our every day world. It is therefore also called the first quantum revolution [76]. It was in the 1970's that the interpretation of quantum mechanics slowly gained interest again [56]. Scientist started to examine, both experimentally and theoretically, concepts like entanglement [72], resulting for instance in the 'no cloning theorem' (which states that making a perfect copy of a pure, arbitrary quantum state is impossible) [56, 77, 78]. Around the same time, ideas were developed on how quantum mechanics relates to information processing and in the 1980's it was proposed to use quantum mechanics for computation purposes [79–81]. The advantage that quantum computing offers with respect to classical computing, has everything to do with the concepts of superposition and entanglement which make quantum mechanics so mind boggling. The proof that an arbitrary quantum system can be simulated by a digital quantum computer [82], combined with the establishment of the theoretical framework for quantum error correction [83, 84], provided the motivation for serious research effort to develop a quantum computer in the 1990's [85].

The first quantum revolution used the improved understanding of nature to build

devices of which the characteristics depend on the collective behavior of ensembles of particles. It is suggested that quantum computing could be part of a second quantum revolution, in which the quantum mechanical properties of nature are not only understood, but also manipulated and engineered at the level of individual particles [76]. Even understanding for which problems a quantum computer could give advantages over a classical computer is still an active field of research, but among predicted applications are the design of new materials [86], understanding complex chemical reactions [87], prime number factorization [88] and searching of databases [89]. Given these developments, quantum mechanics will probably change our daily life just as much in the coming hundred years as it did in the hundred years past.

1.2. THESIS OUTLINE

In this thesis, research is presented that explores the characteristics and possibilities of hole spin qubits defined in quantum dots in a germanium/silicon germanium heterostructure. The results of the most important experiments are concerned with distributing quantum information: either by entangling three qubits as the basis for the phase flip code or by shuttling quantum information encoded in a spin qubit. **Chapter 2** gives a brief description of the experimental and theoretical background needed to understand the experiments presented in this thesis. The focus lies on the theory that is specific for hole spin qubits in germanium/silicon germanium, in contrast to electron spin qubits in other semiconductor platforms. In **chapter 3**, the properties of a two-by-two quantum dot device that could facilitate hole spin qubits are discussed, including shell filling and control over the tunnel coupling between the quantum dots. **Chapter 4** provides a detailed discussion of the features of a two-by-two qubit system, showing high-fidelity single qubit gates and the implementation of two-, three-, and four-qubit gates. This two-by-two qubit system is used to implement the Phase flip code, of which the results are shown in **chapter 5**. To facilitate this, the SWAP, CS^{-1} and the Toffoli-like gate are demonstrated. **Chapter 6** explores the possibilities of diabatically shuttling a hole spin qubit through multiple quantum dots. The effects of spin-orbit interaction and the shuttling performances are described. Chapters 3 - 6 describe work which is published, either in a scientific journal (chapters 3, 4 and 5) or on open-access repository arXiv (chapter 6). The raw data supporting the conclusions in those publications are made available in open repositories and a link to the raw data can be found with the publication. Finally, **Chapter 7** discusses the results presented in this thesis and provides an outlook. Hopefully, this work can play a very modest role in the story about the development of quantum computers.

2

THEORETICAL BACKGROUND AND EXPERIMENTAL METHODS

2.1. PHYSICAL REALIZATION OF SPIN QUBITS

A qubit, short for quantum bit, is defined as a quantum mechanical two level system. It is a conceptually simple system, however a series of coupled qubits can simulate all the peculiar properties of quantum mechanics. There are many physical systems that can be used to encode a qubit: atoms [90, 91], ions [92, 93], photons [94–96], electrons [97, 98] and superconducting circuits [99, 100], just to name a few. One of the most conceptually straightforward examples is a spin-1/2 system.

All physical implementations of a qubit have their pro's and con's and it is not trivial to see if they would make a good building block for a quantum computer. Or to cite David DiVincenzo, if they are 'components that work the way they need to, in such a way that they could potentially be stuck together to form a system' [101]. He came up with the following criteria to this end [102]:

1. A scalable physical system with well characterized qubits
2. The ability to initialize the state of the qubits to a simple fiducial state
3. Long relevant decoherence times, much longer than the gate operation time
4. A 'universal' set of quantum gates
5. A qubit-specific measurement capability

On top of these criteria, he define two more, in case these qubits are to be used not only for quantum computing, but also for quantum communication:

6. The ability to interconvert stationary and flying qubits
7. The ability to faithfully transmit flying qubits between specified locations

The experiments presented in this thesis are performed with spin qubits defined on charge carriers which are isolated in quantum dots in a semiconductor material. Since the purpose for these qubits is primarily 'just' quantum computing, the first five criteria have priority. The idea to use the spin state of a single charge as the physical system to encode the qubit, was proposed by Loss and DiVincenzo in 1998 [98]. Their proposal also included capturing this single charge in a quantum dot. A quantum dot is a semiconductor box that traps an integer number of charge carriers. In gate-defined quantum dots, electric fields are used to confine individual charges, mimicking a small semiconductor island. A quantum dot is sometimes called an artificial atom, because the energy levels inside are discrete. Furthermore, approximating the potential landscape with a harmonic oscillator results in a separation of energy levels similar to shell filling of atoms. The size of quantum dots is typically tens of nanometers. Detailed reviews have been written describing the charge dynamics of quantum dots [103–105]. Details on how quantum dots are formed for the research in this thesis is detailed in section 2.2 and chapter 3.

The characterization of spin qubits (going back to the first criterion) depends heavily on the semiconductor material, the method of confinement and the charge carriers that are chosen to define the spin qubit. Pioneering work on semiconductor quantum dots was performed using electrons confined in quantum dots in a gallium arcinide (GaAs) heterostructure. In this platform it was possible to make fast progress in building quantum dot systems due to the high quality of the material and the small effective mass of the charge carriers. Single [106, 107], double [108–110] and larger quan-

tum dot arrays [111–113] were realized. However, group III-V semiconductors contain an abundance of isotopes with a net nonzero nuclear spin, which cause an effective time-dependent magnetic field. Due to interaction with the nuclear spins, the so-called hyperfine interaction, spin qubits in GaAs dephase very quickly. The challenges in overcoming the hyperfine interaction, motivated the study of materials with zero-nuclear spin isotopes and the focus of the research shifted towards silicon platforms. In this group IV material, only a few percent of the nuclei have net nonzero spin, moreover this material can be isotopically purified to decrease this fraction even further. This made it possible to increase the dephasing time to about a hundred microseconds [114] and enabled high fidelity single [115, 116] and two-qubit gates [117–120], making headway on meeting the DiVincenzo criteria. The state of the art at the moment of writing is a Si device with six well controlled spin qubits [121], which moreover shows a very good attempt to meet multiple criteria in one device.

Now a few years ago, the first papers [122–124] were published on yet another promising platform for spin qubits in quantum dots. Germanium (Ge) is also a group IV material, and similar to silicon, it has mostly isotopes with zero nuclear spin. In contrast to previous platforms, the charge carrier that is used to encode the qubit is not an electron, but a hole (an unoccupied state in the valence band). Similar to GaAs, the low effective mass of holes in Ge allows for slightly larger quantum dots, which makes it easier to fabricate working devices. Holes in Ge are subject to strong spin-orbit interaction, which is a double edged sword. It provides a way to drive the spin fast, using electric fields to do so, without the need for additional components on the chip, such as micromagnets or striplines. On the other hand, spin-orbit interaction can couple charge noise to the spin, which may cause decoherence. Because (and despite) these characteristics, spin qubit in Ge have been able to catch up with the developments of Si [125–127]. Initial attempts to make spin qubits in germanium were performed using various ways of confining holes, such as quantum dots in nanowires [128] and hutwires [123]. The spin qubits used for the experiments in this thesis are defined in high-quality Ge/SiGe heterostructures, which are discussed in more detail in sections 2.2 and 2.4. This chapter will highlight the theoretical background and the experimental methods used to make hole spin qubits in Ge a solid building block for a quantum computer.

2.2. QUANTUM DOTS ON GE/SIGE HETEROSTRUCTURES

The work that is presented in this thesis is obtained using two quantum dot devices defined on a germanium/silicon-germanium (Ge/SiGe) heterostructure. There are a lot of similarities and some differences between those two devices. The first device, which we will call device A from now on, was used for the experiments of which the results are shown in chapter 3 and the second device, the device B (falsely colored SEM image shown in Fig. 2.1), was used in all the other chapters: chapters 4, 5 and 6. In this section, we describe the devices and the processes used to fabricate them.

Fig. 2.1a shows a schematic of the Ge/SiGe heterostructure with the gate stack on top. The heterostructure is grown on a natural silicon wafer in a reduced-pressure chemical vapor deposition reactor (RP-CVD), as detailed in references [124, 129]. On top of the silicon, a 1.6 μm relaxed Ge layer is grown, followed by a 'virtual substrate' which is comprised of a layer of Si_xGe_{1-x} where gradually the ratio of Si is increased to $Si_{0.2}Ge_{0.8}$. By

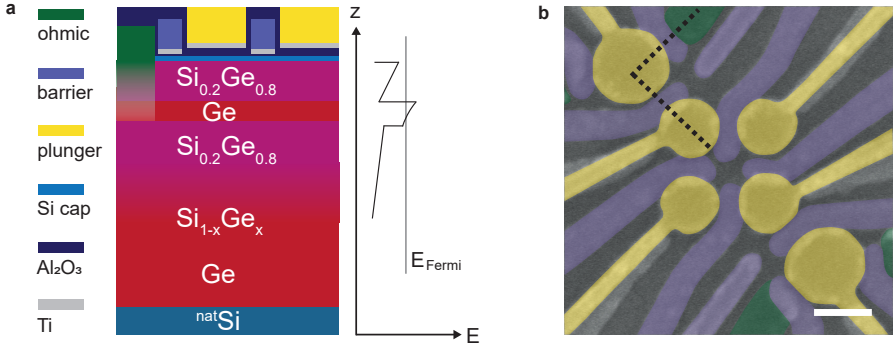

Figure 2.1: **Heterostructure and gate stack. a** Schematic of the Ge/SiGe heterostructure, indicating the different material layers, with the gate stack on top. Next to the diagram the band-structure of the Ge/SiGe heterostructure is sketched [124], in the case where a negative voltage (relative to the drain contact) is applied to an electrostatic gate on top of the heterostructure. Holes are accumulated in the Ge quantum well. **b** Falsely colored SEM image of a device identical to device B, which is used in the experiments detailed in chapters 4, 5 and 6. The colors correspond to the colors in **a**, the plunger gates are yellow, the barrier gates purple and the ohmics green. The black dotted line indicates of which part a cross section is shown in **a**. The white scale bar corresponds to 100 nm.

starting with a Ge layer and linearly increasing the Si concentration, most of the dislocations resulting from the lattice mismatch are buried in the virtual substrate, without making the virtual substrate too thick. Grown on top is a 650 nm relaxed $Si_{0.2}Ge_{0.8}$ layer, followed by the 16 nm thick Ge quantum well. Due to the lattice mismatch between $Si_{0.2}Ge_{0.8}$ and Ge, the quantum well has an in-plane compressive strain. On the quantum well, a $Si_{0.2}Ge_{0.8}$ barrier is grown, with a thickness of 22 nm (device A) or 55 nm (device B) and a thin Si cap (<2 nm).

One of the main differences between sample A and sample B is the thickness of the barrier between the Ge quantum well and the Si cap [129]. A good metric for the quality of a material hosting quantum dots is the percolation density. The percolation density is defined as the critical charge carrier density for establishing metallic conduction in the quantum well. It characterizes the disorder at low carrier densities, which is the typical regime in which quantum dots are operated. For samples where the quantum well was buried 22 nm below the surface (such as sample A), a percolation density of $p_p = 1.2 \times 10^{11}\text{cm}^{-2}$ was measured [124]. By making the barrier 55 nm thick (sample B), the percolation density can be reduced to $p_p = 2.14 \pm 0.03 \times 10^{10}\text{cm}^{-2}$ [129]. Additionally, the charge noise was measured for devices fabricated on both types of heterostructures. For devices with a quantum well buried 55 nm deep, an average detuning noise at 1 Hz of $\sqrt{S_E} = 0.6\mu\text{eV}/\sqrt{\text{Hz}}$ was found [129], where for a device with a 22 nm deep quantum well this was measured to be $\sqrt{S_E} = 1.4\mu\text{eV}/\sqrt{\text{Hz}}$ [122]. These results make sense: the quantum well was moved further away from the impurities at the semiconductor/dielectric interface and provides a more quiet electrostatic environment for spin qubits.

The ratio of Si and Ge in the different layers of the Ge/SiGe heterostructure give rise to a type-I band alignment [124], meaning that in principle either holes or electrons could be confined in the quantum well. The heterostructure is undoped and in order to ac-

cumulate holes, an negative external electric field is applied to an isolated top gate. A sketch of the band-structure is shown in Fig.2.1. In this way, the wavefunction of the hole is confined to the quantum well and 2D hole gas is created. This means that the holes are confined in the z-direction, but act as free charge carriers in the plane. In order to go from a 2D hole gas to quantum dots, the holes also need to be confined in the x- and y-direction. For this purpose the device structure is fabricated on top of the heterostructure. This process is described in detail in reference [130].

A SEM image of the gate layout similar to device B is shown in Fig 2.1b. First of all, note the white scale bar, which indicates 100 nm. The size of the quantum dots is set by the electrostatic gates. To define a qubit on the spin states of a hole inside a quantum dot, the splitting between the energy levels of a hole in the quantum dot needs to be sufficiently large. There are two terms that contribute to this energy splitting: the charging energy and the quantum confinement energy. The charging energy is the energy cost for adding another hole to the quantum dot due to the Coulomb repulsion between the holes. The quantum confinement energy is the result of the confinement in all three directions. Assuming a harmonic potential and a strong confinement in the z-direction, the quantum confinement energy is given by $\Delta E = \pi\hbar^2/m^*A$, where m^* is the effective hole mass and A is the quantum dot area. For the Ge/SiGe heterostructure used in this work, the effective hole mass can be as low as (0.048 ± 0.006) electron mass at zero charge carrier density [131], which is low compared to the effective mass of electrons in Si. This low effective mass allows for a relatively small quantum dot area, while keeping the quantum confinement energy large. This relaxes the lithographic fabrication requirements for the gate stack of the devices and provides well defined quantum dots with controllable tunnel couplings (as shown in Chapter 3).

The quantum well is contacted by ohmic contacts, as shown in green in both Fig. 2.1a and b. For many metals, when brought into contact with Ge, the Fermi energy aligns with the valence band of Ge, resulting in a direct ohmic contact [132]. In this way, a reservoir of holes is created, allowing to occupy the available valence band states in the quantum well and ultimately the quantum dots. This property of Ge simplifies the fabrication process for the ohmics on the Ge/SiGe devices. Electron beam lithography is used to define the ohmic contacts, after which the oxidized Si cap is locally etched and 30 nm of Al is deposited [122]. Next an Al_2O_3 layer is grown using atomic layer deposition (ALD). This fabrication step doubles as an annealing step for the ohmics, in order for the Al to diffuse into the $Si_{0.2}Ge_{0.8}$ layer towards the quantum well, as schematically shown in Fig. 2.1.

The dotted black line in Fig 2.1b corresponds to the schematic cross section shown in Fig. 2.1a. The quantum dots are formed by applying voltages to electrostatic gates which come in two sorts: plunger gates (shown in yellow) and barrier gates (shown in purple). The plunger gates are used to accumulate charge carriers, thereby forming a quantum dot in the quantum well under the plunger. Moreover, with the plunger gates, the energy levels in the quantum dots can be tuned. The barrier gates are used to control the tunnel coupling between the quantum dots. The design of both devices A and B, includes a two-by-two array of (smaller) quantum dot plungers. These plungers define the quantum dots in which the qubits are defined. Both devices also have two (larger) sensor plungers to the side of the two-by-two array, under which multi-hole quantum dots are formed, which function as charge sensors. The gates are fabricated in two overlapping

layers (with thicknesses of 20 nm and 40 nm), using titanium-palladium (gray-yellow in Fig 2.1a) as material for the gates. The gates are isolated from each other, the ohmics and the substrate with a 7-nm-thick Al_2O_3 layer (dark blue). In this way it is possible to apply different voltages to different gates, without leakage to other gates or the quantum well. The barrier gates are fabricated in the first layer, closest to the heterostructure, followed by the fabrication of the plunger gates. This order is chosen such that the barrier gates have a stronger capacitive coupling to the quantum well, i.e. that they have a larger lever arm. This optimizes the control over the tunnel coupling between the quantum dots.

For an intuitive picture on how the electrostatic gates shape the potential landscape and control the quantum dots, see Chapter 3, especially Fig. 3.1b. Fig. 3.1a shows an SEM image of a device which is identical to device A. Comparing this to Fig. 2.1b, the second important difference between the two devices becomes clear: the charge sensors in device A are in line with the two-by-two quantum dot array, whereas in device B they are positioned diagonally. This change in the gate layout was made because in device A it turned out to be challenging to tune the tunnel coupling between the two quantum dots closest to the sensors, independently from the tunneling of the charge sensor to the neighbouring quantum dot. Independent control over these couplings, however, is crucial for tuning Pauli Spin Blockade (PSB) readout (for an explanation of the spin readout technique, see section 2.7), resulting in the gate layout design of device B.

Being able to readout the spin state of a hole is a key asset for defining spin qubits, as is having a quiet electrostatic environment with low charge noise. These differences between device A and B, both in the depth of the quantum well and the design of the gate layout, determine whether a system is a functional quantum dot device or a system that can advance quantum computation with quantum dots.

2.2.1. DEVICE SELECTION

Once the devices are fabricated, a working device needs to be selected. The fabrication of quantum devices is research in progress. As a consequence, yield is often far from 100 %. An important mitigation strategy (as well as an important feed-back method for further development) is therefore a good screening plan. A flow chart of the selection procedure, as applied to device B, is shown in Fig. 2.2a. The devices that pass the visual test are cooled down to 4.2 K and transport measurements are performed, of which the results are shown in Fig. 2.2b. When performing transport measurements, a voltage difference is applied via the ohmics to the quantum well. By applying negative voltages to the gates, it is tested if a conducting channel can be turned on between the ohmics. Moreover, it also becomes clear if the gates have the effect on the conducting channel which can be expected from the device gate layout. During these measurements it will also become clear if leakage of the current occurs between the gates or from the gates to the quantum well.

2.3. EXPERIMENTAL SET-UP

When a device passes the selection procedure it is loaded into the experimental set-up for qubit experiments. A schematic of this set-up as used for the experiments in chapters 4, 5 and 6 is shown in Fig. 2.3. It consists of a dilution refrigerator, several type of elec-

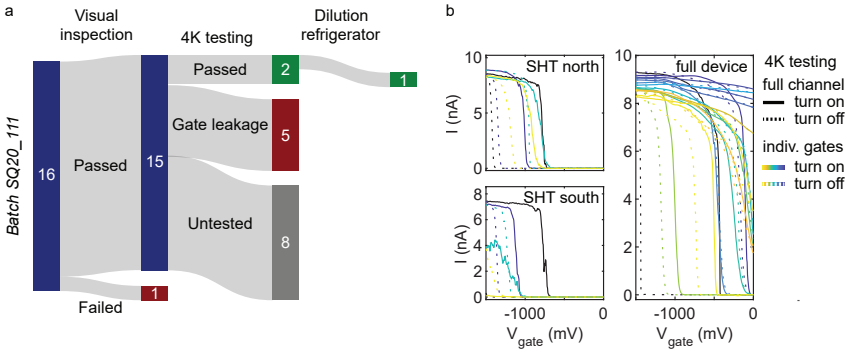

Figure 2.2: **Screening of qubit devices. a**, The qubit devices undergo a visual screening as well as a transport screening at a temperature of $T = 4.2$ K. Out of the full batch of 16 nominally identical devices, 15 passed visual inspection. Seven of these devices were tested at $T = 4.2$ K and two devices were found to pass all testing, of which one (device B) was mounted in a dilution refrigerator. **b**, 4.2 Kelvin transport data of device B. Three different channels are turned on by sweeping all gates down to $V_{gate} = -1500$ mV (black), thereby accumulating charge in the undoped strained Ge quantum well. Then the effect of the individual gates is tested by sweeping them up and down to $V_{gate} = 0$ V (coloured lines). All channels turn on and the gates affect the transport current as expected from the device layout.

tronic equipment and a computer. A detailed technical description of this experimental set-up can be found in reference [133].

The temperature in the dilution refrigerator goes down in stages, the different temperatures are indicated with dotted lines in Fig. 2.3. The device (device B, lower left of Fig. 2.3) is bonded to a printed circuit board (PCB) and mounted on the cold finger which is connected to the mK plate of a Bluefors LD-400 dilution refrigerator. In this way the sample can be cooled down to a base temperature of 20 mK. The cold finger fits into a superconducting magnet, which is used to apply an external magnetic field, varied in the experiments in this thesis between 0.25 and 1.1 Tesla.

2.3.1. ELECTRONIC EQUIPMENT

The electronic equipment in the set-up has four different functionalities: defining the electrostatic potential landscape (direct-current (DC) signals), fast control of the quantum dots (alternating-current (AC) signals), charge readout (radio-frequency (RF) signals) and spin qubit control (microwave (MW) signals). To mitigate noise at the sample, both from the environment of the fridge and the electronics itself, all lines connecting the electronics to the sample are filtered or attenuated at different temperatures, as indicated in Fig. 2.3.

Firstly, the potential landscape, i.e. the quantum dots, are defined by DC voltages applied to the plunger and barrier gates. Usually, these voltages are set to define the default mode for the device: to have four quantum dots with a charge occupation of one hole each (the (1,1,1,1) occupation) and to set the charge sensors in the multi-hole regime. The DC voltages are applied using digital-to-analogue converters (DACs). These voltage sources are battery powered and galvanically isolated from the other electrical equip-

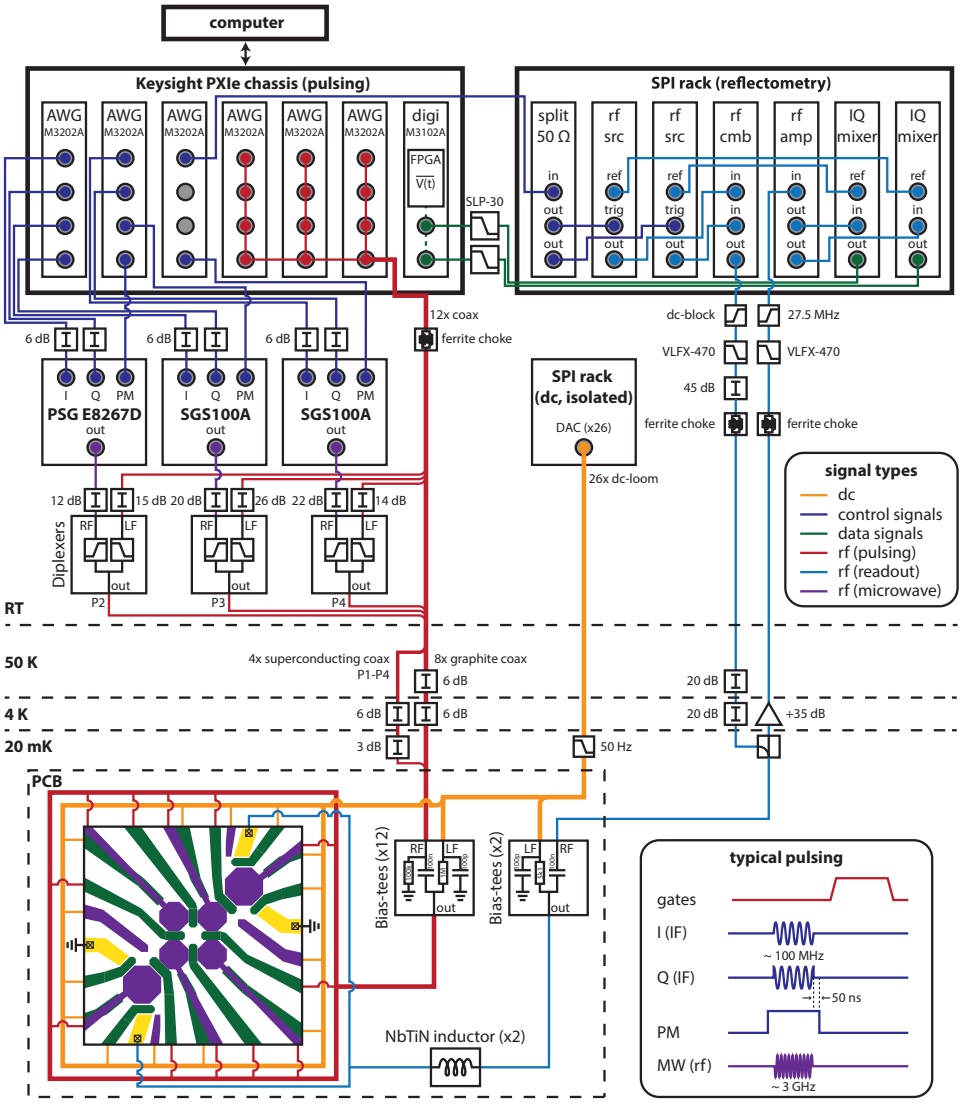

Figure 2.3: **Schematic drawing of the measurement set-up used for the qubit experiments.** The different type of signals are indicated with different colors and the different temperature stages of the dilution refrigerator are separated with dotted lines. The typical pulses used for qubit experiments are shown in the lower right corner.

ment to prevent interference. The DACs are part of a serial peripheral interface (SPI) measurement rack, which is build in house. In Fig. 2.3 the DC wiring looms connecting the DACs with the sample are colored yellow.

Secondly, to have fast control (in the order of 1 ns) over the tunnel coupling between the quantum dots, for fine tuning of the potential landscape and the initialization and readout of spin states (see section 2.7), most of the gates of the sample are connected to a Keysight M3202A arbitrary waveform generator (AWG). The connection is made using coaxial cables (indicated with red and called 'rf (pulsing)' in Fig. 2.3), which pass through a ferrite common mode choke, are attenuated as indicated in Fig. 2.3 and are combined with the DC signals with Bias-tees. The typical pulses that are applied with the AWG are also depicted in red and called 'gates' in Fig. 2.3.

Thirdly, to sense changes in the potential landscape, such as a hole tunneling from one quantum dot to another, rf-readout is used. Large quantum dots, which are the charge sensors, are located close to the quantum dots in the two-by-two configuration. The resistance of the sensor is strongly dependent on the charge state in the spin qubit quantum dots. The principle behind rf-readout is that a signal with a fixed frequency is applied to one of the ohmics of the sensing dot and the reflected signal is measured. The reflected signal is zero when there is impedance matching between the load of the readout circuit and the rf-source. In other words, when the load impedance of the complete circuit (including, among other things, the resistance of the sensor) is equal to the output resistance of the rf-source. Given the resistance of the sensor, impedance matching can be achieved by adding a matching circuit, which consists of an inductor and a capacitor. The impedance of this LCR circuit is frequency dependent and will only result in impedance matching for a certain resonance frequency. This is the frequency of the rf-signal send by the rf-module in the set-up. Now, when the resistance of the sensor changes, there is no impedance matching anymore and the reflected signal changes. In this way, changes in the potential landscape can be detected with a bandwidth of several MHz.

The implementation of rf-readout in the set-up is shown in Fig. 2.3 in light blue. A schematic of the RF-circuit is also shown in Fig. 3.1 in chapter 3. Two rf-tones are generated (rf src) in the in-house build reflectrometry set-up and are combined to one signal (rf cmb) and send towards the PCB, via filtering, attenuation and a directional coupler. The AWG is used to provide a trigger to make sure that the rf-tones are muted during the qubit operations. Since there are two sensing quantum dots on the sample, there are two rf-tones, each matching one LCR circuit connected to one sensor. The tank circuit consists of a niobium-titanium-nitride kinetic inductor on a separate chip in combination with the parasitic capacitance of the device. The reflected signal is amplified and demodulated (compared with a reference signal) at both the resonance frequencies separately (IQ mixer). Subsequently, the readout signal is filtered and send to the digitizer (green lines in Fig. 2.3). In the digitizer, the signal can be averaged over time by the field-programmable gate array (FPGA).

Finally, for the experiments presented in this thesis, high frequency (order of GHz) signals are used to manipulate the qubits, indicated in dark blue in Fig. 2.3. These signals are generated using three separate microwave (MW) vector sources (two Rohde&Schwarz SFS100A sources and a Keysight PSG E8267D source). The amplitude, frequency, phase

and duration of the MW pulses can be controlled by applying quadrature modulation, using signals generated by the AWG. A sine wave with a phase difference of $\pi/2$ is applied to the in-phase (I) and quadrature (Q) input of the vector sources. In this way, the frequency outputted can be varied around the base band frequency of the MW source. The MW source signals are send to the plunger gates via the same coaxial lines as the AWG signals used for the control of the potential landscape. To make this possible, high bandwidth superconducting coaxial lines are used and the signals are combined using room temperature diplexers. To suppress the microwave pulses when not driving the qubits, a pulse modulation (PM) envelope is applied around the microwave pulses.

2.3.2. SOFTWARE

Advanced qubit operations require a good software framework. To this end, we have taken many steps to write new software to facilitate and improve the qubit measurements. The task can be summarized by the following: in order to control the qubits, all the electronics described above need to be controlled in a synchronized way to optimize the performance.

Software which is used in all the experiments presented in this thesis, is code to define virtual gates. Although the plunger gates are designed to control the energy levels in the quantum dots and the barrier gate to control the potential barrier between them, this is not how it works in practise. A voltage on an electrostatic gate influences the potential landscape in a more general way. It is therefore needed to, for example, compensate the influence of a plunger gate on the barrier between two quantum dots. We label this combination of several physical gates as a virtual gate. In practice, we find that a linear combination gives a reasonable approximation in a stability diagram covering a few charge transitions. The virtual gate matrices used in the experiments in this thesis are in the supplementary information of chapters 3 and 4.

Many software packages have been developed in the last few years to control the AWG and MW pulses, which are needed to control and drive the qubits. Important packages include PulseLib and QConstruct. PulseLib is described in detail in reference [134] and can be found on Github [135]. An example of the code that could be used for a shuttling experiment using QConstruct is shown in Fig.2.4. QConstruct integrates the functionalities of packages such as PulseLib and makes it possible to directly implement single and two qubit gates, without detailing all the individual pulses. The qubit gates are build-in and make use of calibrations stored for this purpose. More information on QConstruct is also available on Github [136]. The measurement software is always a work in progress and different versions have been used for the experiments in this thesis.

2.4. DEFINING A HOLE SPIN QUBIT IN GE/SIGE

A qubit is a quantum mechanical two level system in which the orthogonal computational basis states $|0\rangle$ and $|1\rangle$ can be encoded. A spin 1/2-system, such as an electron, is very suitable for this. The spin of a particle is its intrinsic angular momentum and has a specific and unchangeable value for every type of fundamental particle [137]. The computational states can be encoded in the two eigenstates: 'spin down' $|\downarrow\rangle$ and 'spin up' $|\uparrow\rangle$. A superposition state takes the form $\alpha|\downarrow\rangle + \beta|\uparrow\rangle$. The two spin states are degenerate.

```
c = Circuit('Shuttling q2 - q3')
c += Init([1,2])

c += Kick_out_Q3Q4_sequence([1,2])
c += ConfigureBarriersSequence([1,2])

c += SetV([1,2], '_1100', wait_after = 10)

c += X90(2)

c += SetV([1,2], '_1100', wait_after = 10)
c += SetV([1,2], '_1010', wait_after = 0.95)
c += SetV([1,2], '_1100', wait_after = 10)

c += Phase(2, angle = phi)
c += X90(2)

c += ConfigureBarriersReverseSequence([1,2])
c += Reload_Q3Q4_sequence([1,2])
c += MeasureParity(1,2, 'm1')
```

Figure 2.4: **Example QConstruct code.** The code shown in this example would implement a simple shuttling experiment. Different charge configurations (such as '_1100' and '_1010'), pulse sequences (such as Init, Kick_out_Q3Q4_sequence and ConfigureBarriersSequence) and single qubit gates (such as 'X90' and 'Phase') are predefined and calibrated before the experiment. This simplifies the implementation of the experiment enormously.

However, since the magnetic dipole moment of a particle is proportional to its spin angular momentum, applying a magnetic field will lift this degeneracy. The resulting energy splitting is called the Zeeman energy and is given by:

$$E_Z = hf_L = g\mu_B B \tag{2.1}$$

Were E_Z is the Zeeman splitting, h is Planck's constant, f_L is the Larmor frequency, g is the Landé g-factor, μ_B is the Bohr magneton and B is the applied magnetic field.

This is a simple and elegant description of a spin qubit. However, for the spin qubits used for the experiments presented in this thesis, the physics is more complicated. Nonetheless, this simple description is still useful. All the complexity can be absorbed into equation 2.1 by turning the g-factor into a g-tensor and taking the direction of the applied magnetic field into account:

$$h\mathbf{f}_L = \overleftrightarrow{g}\mu_B\mathbf{B} \tag{2.2}$$

Where $h\mathbf{f}_L$ sets the direction of the quantization axis of the qubit, $|\mathbf{f}_L|$ is the Larmor frequency and the Zeeman energy is given by $E_Z = h|\mathbf{f}_L|$. The g-tensor can be described as a rotated diagonal matrix [127]:

$$\overleftrightarrow{g} = R^{-1}(\zeta,\theta,\phi)\mathrm{diag}(g_{x'}, g_{y'}, g_{z'})R(\zeta,\theta,\phi) \tag{2.3}$$

where the intrinsic rotations around the zyz axes are described by the Euler angles ζ,θ,ϕ and $g_{x'}$, $g_{y'}$ and $g_{z'}$ are the effective g-factors defined along the principle axes x'y'z'

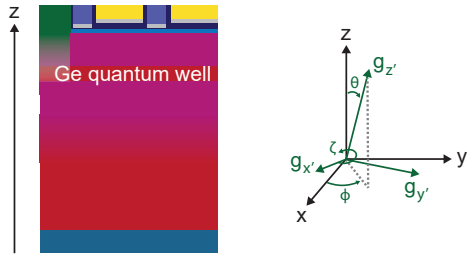

Figure 2.5: **Diagram indicating the g-tensor in the coordinate system of the device.** The z-direction of the device equals the growth direction of the heterostructure, the x- and y-direction are in-plane of the quantum well. This corresponds to the coordinate system drawn in black. In green are indicated the Euler-rotation angles of the g-tensor axes x', y' and z'. Drawn are the effective g-factors $g_{x'}$, $g_{y'}$ and $g_{z'}$ along the principle axes x'y'z'. Note that the x'y'z' axes of the g-tensor do not necessarily align with the axes of the heterostructure.

of the g-tensor. Now, there are two relevant questions to explore. Firstly, what might be the source of this complexity? And secondly, what implications arise from having a g-tensor instead of a g-vector?

The complexity originates from the fact that we define our spin qubit on a hole in a quantum dot in a Ge/SiGe heterostructure as described in section 2.2. In bulk Ge, the two highest energy levels are the heavy hole (HH) and the light hole (LH) band. Due to the confinement in the 2D plane and the compressive strain in the quantum well, the HH and LH bands have become separated from each other. As a result, in the quantum well of a Ge/SiGe heterostructures, the HH band is the topmost valence band and will be populated when a negative voltage is applied to the electrostatic gate on top of the heterostructure. Details can be found in references [124, 125, 133, 138].

The spin-orbit interaction (SOI) plays a very important role in complicating the g-tensor for a qubit defined on a hole in Ge quantum well. SOI is a relativistic effect which couples angular momentum and the spin degree of freedom of a particle. The type of spin-orbit interaction in this heterostructure is Rashba SOI. There are two conditions that need to be met to have Rashba SOI in a quantum well: an intrinsic SOI and a broken structural symmetry. The intrinsic SOI emerges from the relativistic version of the Schrödinger equation, the Dirac equation, which has a term linking the spin operator **S** to the angular momentum operator **L**. This is relevant for holes in Ge because they have a p-type wavefunction, i.e. $l = 1$, where l is the quantum number associated with the angular momentum. Due to this intrinsic SOI, the spin and angular momentum cannot be described separately anymore, instead we use the quantum number j for the effective spin. The eigenstates for the effective spin for the HH hole band are $j = \pm 3/2$ and for the LH band $j = \pm 1/2$. The structural symmetry in a Ge/SiGe heterostructure is broken by applying a negative voltage on the electrostatic gate on top of the heterostructure. As shown in Fig. 2.1, the resulting confining potential in the quantum well has a triangular shape, the hole wavefunction is drawn to the top of the quantum well by the electric field.

The g-tensor for HH states is predicted to be very anisotropic, its out-of-plane component can be a factor hundred larger than its component in plane of the quantum well.

On the other hand, the g-tensor for the LH states is much more isotropic. Since the eigenstates of holes confined in the quantum dots can be described quite well as HH, we expect the g-tensor to be highly anisotropic. However, the SOI will lead to a correction of the HH g-tensor, making it less anisotropic. This process is related to the mixing of HH and LH states.

To understand what the consequences are for defining the qubit, it is important to realize that the SOI strongly depends on the electric field, i.e. the confinement of the hole. This effect is captured in the g-tensor. The fact that the qubit is described by a tensor and not a vector implies that the direction of the quantization axis is not necessarily aligned with the applied magnetic field **B**. This effect is amplified by the strong anisotropy of the HH g-tensor: a small difference between the direction of the applied **B**-field and the x'y' plane of the g-tensor will cause a strong rotation of the quantization axis of the qubit into the z'-direction. Since the SOI, and therefore the g-tensor, depends on the details of the electric field which confine the quantum dots, both the direction and magnitude of the quantization axis can very significantly per quantum dot. For all the experiments presented in this thesis, the external magnetic field is applied approximately in-plane of the quantum well, and therefore approximately in the x'y'-plane of the g-tensor, and indeed, we see large differences in the Zeeman energy between the quantum dots in chapters 4, 5 and 6. Furthermore, in chapter 6 we see differences between the direction of the quantization axis of different quantum dots. The g-tensor not only is different for different quantum dots, it can also be tuned with the voltages on the gates defining the quantum dots, as shown in chapter 4. This has its advantages, since it can be used to provide individual addressability of the spin qubits, but even more important, it can be used to drive the spin, as described in the next section, section 2.5. The disadvantage is that it makes the spin qubit more susceptible to charge noise, as described in detail in section 2.9.

2.5. IMPLEMENTATION OF SINGLE QUBIT GATES

In order to run any arbitrary quantum algorithm on a quantum processor, it should be possible to perform operations on its qubits which bring them from any possible quantum state to any possible quantum state. In other words, there should be a universal set of quantum gates. A set of gates is universal when it is a minimal set of gates of which all other qubit operations can be created. It is possible to compose a universal gate set out of single- and two qubit gates. This section is dedicated to single qubit gates, how they can be visualized in an abstract way for spin qubits in general and how they are implemented for hole spin qubits in Ge specifically.

The states of a single qubit can be visualized with a Bloch sphere, as shown in Fig.2.6a. The basis states $|0\rangle$ and $|1\rangle$ are at top and the bottom of the sphere. A superposition $|\Psi\rangle = \alpha|0\rangle + \beta|1\rangle$ is represented by a point on the Bloch sphere ($|\alpha|^2 + |\beta|^2 = 0$) and can also be written as $|\Psi\rangle = \cos(\theta/2)|0\rangle + e^{i\phi}\sin(\theta/2)|1\rangle$, where θ is the amplitude and ϕ the phase. A single qubit gate can bring a qubit in a certain state on the Bloch sphere to another state on the Bloch sphere, for example a $X_{\pi/2}$-gate (where X refers to the rotation axis, and $\pi/2$ to the rotation angle) will bring a state in the $|0\rangle$ state to the equator of the Bloch sphere, see Fig.2.6b.

As explained in the previous section, the basis states for a spin qubit are 'spin down' $|\downarrow\rangle$ and 'spin up' $|\uparrow\rangle$, which are separated by the Zeeman energy. Since the spin is placed

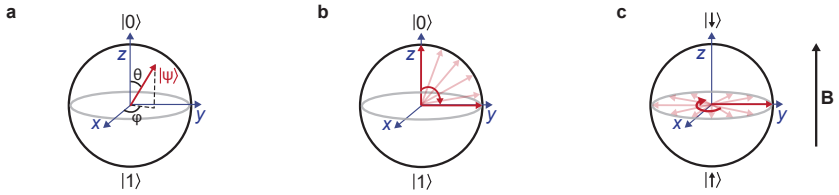

Figure 2.6: **Single qubit gates depicted on the Bloch sphere. a** A drawing of the Bloch sphere, indicating the basis states at the top and bottom. Any coherent superposition state $|\Psi\rangle$ is a point on the Bloch sphere and can be described by its angle θ and phase ϕ. **b** Depicted here the rotation induced by a $X_{\pi/2}$-gate, which in this case brings the qubit from the $|0\rangle$ state to the $(|0\rangle + i\,|1\rangle)/\sqrt{2}$ superposition state. **c** In the lab frame, a spin in superposition will precess about its quantization axis with the Larmor frequency. Viewed in the rotating frame, the spin in the same superpostion state, will just be a point on the equator of the Bloch sphere.

in an external magnetic field, the spin will rotate with the Larmor frequency around its quantization axis, which is set by the g-tensor and the direction of the external magnetic field. For example, Fig. 2.6c shows the simple case where the quantization axis of the spin qubit is oriented along the external magnetic field and the spin is in a superposition. What happens in that case, is that the spin is presessing along the equator of the Bloch sphere. This reference frame is called the 'lab frame' and is relevant for the interpretation of the results presented in chapter 6 of this thesis.

However, when we are considering just the single qubit and how to implement single qubit gates, it is more convenient to adopt the 'rotating frame' [139]. In this reference frame, the observer follows the Larmor precession of the spin, i.e. since the frame is rotating at the same frequency as the spin, it is like the state is 'standing still' in the Bloch sphere. In the rotating frame, a superposition state as depicted in Fig. 2.6c is just a point on the equator. The spin can be coherently rotated, i.e. single qubit gates can be implemented, when an effective oscillating magnetic field is applied of which the frequency is resonant with the Larmor frequency and the direction is perpendicular to the quantization axis. In the rotating frame, this oscillating magnetic field will be static with respect to the Larmor frequency and the spin will rotate about an axis perpendicular to the z-axis of the Bloch sphere, describing a circular trajectory. This rotation is called Rabi oscillation, its frequency depends on the strength and the rotation axis on the phase of the oscillating magnetic field. In the rotating frame, an $X_{\pi/2}$-gate can indeed be visualized in the Bloch sphere as shown in Fig. 2.6b, instead of some complicated trajectory which is a combination of the Larmor precession and the rotation around the X-axis.

For hole spin qubits in Ge, the effective oscillating magnetic field that drives the spin, can be applied with an oscillating electric field mediated by the SOI. This method is called Electric Dipole Spin Resonance or EDSR for short. Driving speeds that can be achieved with hole spin qubits in Ge are quite high, ranging from tens to a hundred MHz [126, 140, 141]. The physics behind this fast driving is still a field of active research.

One way how the oscillating electric field can couple to the spin is via the g-tensor, since due to the SOI the g-tensor is susceptible to the electric field. A modulation in the g-tensor $\delta\overleftrightarrow{g}$ relates directly to a change in the Larmor vector $\mathbf{f}_L$: $h\mathbf{f}_L = \mu_B \delta\overleftrightarrow{g}$. Changes

parallel to the quantization axis of the spin (changes in the diagonal terms of the g-tensor) will lead to a change in the Larmor frequency, which will lead to dephasing of the spin qubit. Changes perpendicular to the quantization axis (changes in the off-diagonal terms of the g-tensor) however, will lead to a change in the direction of the spin. This way of driving is called g-tensor modulation resonance (g-TMR) [127, 142, 143]. By applying an oscillating electric field, the confining potential of the spin changes shape. According to recent theoretical work, non-separability of the confinement potential (the confinement potential can not be described separately in-plane and out-of-plane), which leads to coupling between the in-plane and out-of plane motion of the spin, plays a role [144]. Moreover, inhomogeneity of the electric driving field could also contribute [144], as well local differences in strain in the quantum well, induced by the difference in thermal expansion coefficients of the metal of the electrostatic gates and the materials of the heterostructure, which become relevant when the device is cooled down to mK temperatures [145].

In practice, driving the spin qubit using g-TMR means that we apply a microwave pulse (resonant with the Zeeman energy) to a close-by gate, which can result in Rabi oscillations. The phase and the duration of the microwave pulse give control over the phase and the amplitude of the single qubit rotation, respectively. Since the g-tensor is very sensitive to the electric fields and therefore unpredictable, tuning a hole spin qubit is not trivial. Finding the resonant frequency requires scanning a large frequency range. Moreover, finding the direction from which the qubit can be driven most efficiently is a process of try-and-error by applying the microwave signal to different electrostatic gates close to the quantum dot. These calibration efforts result, however, in hole spin qubits which can be driven at high Rabi frequencies. More importantly, using g-TMR it is possible to implement high-fidelity single qubit gates (see chapter 4). Moreover, the fact that the spin can be manipulated with electric fields, without extra components on the chip (such as a micro magnet) is an advantage when scaling to larger qubit arrays.

2.6. A TWO-SPIN QUBIT SYSTEM

To understand the spin initialization, readout and of course the two-qubit gates that we use in the experiments in this thesis, it makes sense to study a two-spin qubit system. In a two-spin system, it becomes relevant that holes (like electrons) are fermions. Since fermionic states are antisymmetric under interchange, it follows that two identical fermions cannot be in the same quantum state. This we see in our experiments in two forms: the first is the famous Pauli exclusion principle, which is used for spin qubit readout. The second is the exchange interaction, which is used to implement the two-qubit gates in our system.

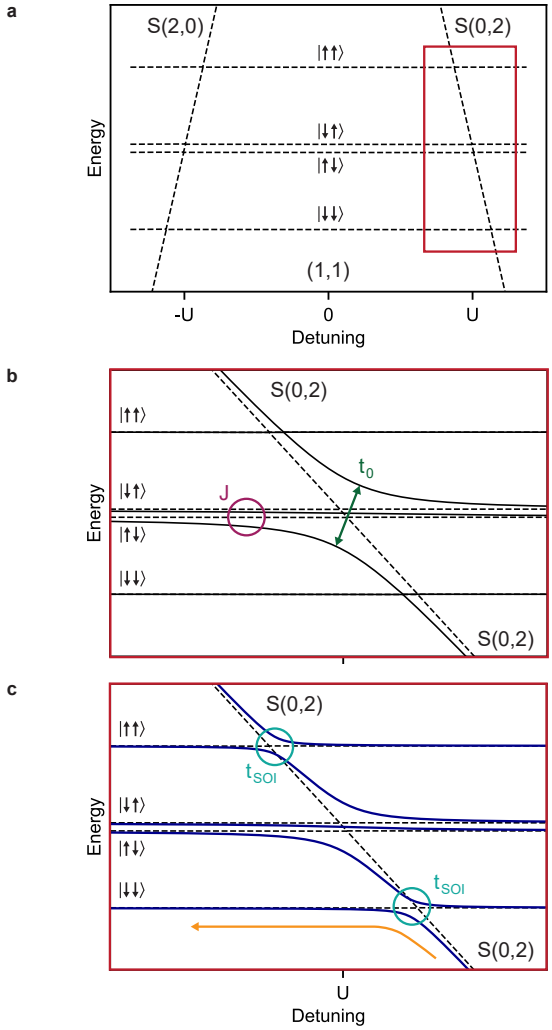

Figure 2.7: **Energy spectrum of spins qubits confined in a double quantum dot a** Plotted are the eigenenergies of two spin qubits confined in a double quantum dot. Note, shown is the 'electron picture': the ground state is plotted as the lowest level on the energy scale. The dotted lines indicate the energy levels in case where there is no interaction between the two particles at all, i.e. the tunnel coupling terms (both spin conserving and spin flip terms) between the quantum dots are zero. The charge anticrossing between the two quantum dots is at the points where the detuning is equal to U or -U, where U is the energy needed to move both holes in the same quantum dot. **b** Depicted here is a zoom in of the spectrum shown in (a), now with a finite amount of spin-conserving tunnel coupling between the quantum dots. Indicated with a green arrow is the resulting anticrossing between the anti-parallel spin states and the S(0,2) state. When there is finite tunnel coupling between the quantum dots, there is finite exchange J. In the regime where the difference in Zeeman energy between the spin qubits is large compared to the coupling, this will effectively result in a shift of the anti-parallel spin states compared to the parallel spin state (highlighted with the circle). **c** Energy spectrum including both spin-conserving and spin-nonconserving tunnel coupling. The latter is due to the spin-orbit interaction and couples also the parallel spin states to the S(0,2) state (highlighted with the circles). The yellow arrow indicates how to initialize in the $|\downarrow\downarrow\rangle$ state.

We operate our spin qubit system in the single hole regime, therefore to study a two qubit system, we have to take into account a double quantum dot. The confinement potential is used to control the interaction between the two qubits, i.e. the overlap of the wavefunction of the two particles. There are two tuning knobs: the detuning energy ϵ between the quantum dots (relative alignment of the potential of the two quantum dots) or the tunnel coupling t_0 between the quantum dots.

Plotted in Fig. 2.7a are the six lowest energy eigenstates of two spin qubits as a function of detuning, using realistic values: external magnetic field of 1.1 Tesla, effective g-vectors of 0.18 and 0.22 and in the regime where the tunnel coupling is completely turned off. The basis chosen is $|\downarrow\downarrow\rangle, |\uparrow\downarrow\rangle, |\uparrow\downarrow\rangle, |\uparrow\uparrow\rangle$ S(0,2) and S(2,0), where the arrows indicate the state of the spin in both quantum dots and S(0,2) and S(2,0) are the singlet states of the different charge occupations. The triplet state for two holes in the same quantum dots is much higher in energy and not shown in Fig. 2.7.

This basis is suitable when the difference in Zeeman energy between the two quantum dots is relatively large compared to the coupling between the quantum dots [146]. For the experiments presented in this thesis, this is indeed the configuration that we are working in. The difference in Zeeman energy is set by the difference in effective g-factor between the quantum dots. In this picture we do not take into account that the g-tensor depends on the confinement potential and can therefore be changed by the detuning.

Figure 2.7b shows a zoom-in of the energy diagram around the interdot charge transition (detuning = U), in the regime where the spin-conserved tunneling is turned to a finite value. Close to the point where the detuning is zero (the two holes are well separated in their own quantum dots), the eigenstates are mostly unaffected and their energies are still determined by the magnetic field and effective g-vectors. Moving closer to the charge transition, the energy levels of parallel spin states do not change as a function of detuning, since they are not coupled to the S(0,2) (or the S(2,0)) state. The anti-parallel spin state however move down in energy, since they contain a S(1,1) component which couples to the S(0,2) (and the S(2,0)) state. The width of the anticrossing, indicated in Fig. 2.7b by a green arrow, increases with increasing tunnel coupling.

So far we have ignored the spin-orbit interaction (SOI) which plays an important role for hole spin qubits in germanium. Since the SOI couples the spin of the particle to its momentum, the SOI enables a tunneling process between the (1,1) and (0,2) charge state for which the spin state is not preserved. In the basis used here, the SOI translates into a coupling between the S(0,2) and S(2,0) singlet states and the parallel spin states [133, 146, 147]. These avoided crossing are highlighted in Fig. 2.7c with light blue circles. For plotting the energy levels shown in Fig. 2.7c we choose the simplified case where the tunnel coupling terms due to the SOI terms are all equal [133].

2.7. PAULI SPIN BLOCKADE READOUT AND INITIALIZATION

For spin qubits, the quantum information is encoded in the spin state of a single charge carrier. The magnetic moment of a spin is very small and it is very challenging to measure it directly. Therefore, to readout the state of the spin, we make use of spin-to-charge conversion. The different spin states are mapped onto different charge states. The charge state in turn is measured using a single-hole transistor, also called a sensing dot, located close to the quantum dots confining the spin qubits. When tuned to a Coulomb peak, the

capacitance of the single-hole transistor is very sensitive to the surrounding electrostatic field. Moving a single charge will cause a small change in the capacitance, which can be measured with an rf-circuit, as described in section 2.3.

An elegant way of performing spin-to-charge readout is by Pauli Spin Blockade (PSB) readout. In this protocol we used the principle that two fermions cannot be in the same quantum state, for example: two holes cannot occupy the same energy level in the same quantum dot if they have the same spin state. As shown in the energy diagram depicted in Fig. 2.7b, if there is a finite tunnel coupling between the two quantum dots, only if the two spins are in the $|\uparrow\downarrow\rangle$ state, they can tunnel into the same quantum dot and form the S(0,2) state. In an experiment it would work as follows: when two qubits are confined in a quantum dot each, one of them is initialized in the $|\downarrow\rangle$ state, the other one can be in any state. By pulsing the detuning past the charge anticrossing into the (0,2) charge state, a distinction can be made between the $|\uparrow\downarrow\rangle$ state, which will tunnel, and the other spin states, for which the tunneling is blocked. Whether or not the charge carrier can tunnel to the neighbouring quantum dot, can be measured with the sensing dot and thereby realizing spin-to-charge conversion. PSB readout works within certain boundaries. Firstly, the measurement window in terms of the detuning is set by the orbital energy, if a higher energy level is available (not shown in Fig. 2.7), the blockade is lifted. Secondly, the integration time for the charge signal is limited by the time it takes for the blocked states to decay to the S(0,2) state.

As discussed in the previous section, and shown in Fig. 2.7, SOI can introduce non-spin conserving tunneling terms, resulting in anticrossings between the parallel spin states and the S(0,2) state. The energy diagram shown in Fig. 2.7c is just an example, the actual size of the anticrossings, both spin conserving and non-spin conserving, depend on the tunnel coupling, the magnitude and direction of the external magnetic field, relative angle of the quantization axes and the effective g-factors. Realizing spin-to-charge conversion using PSB in this system requires careful tuning of the tunnel coupling between the quantum dots and of all the ramp rates between the different detuning points of the readout sequence.

How to initialize a spin qubit in this system depends on the size of the SOI anticrossing between the $|\downarrow\downarrow\rangle$ state and the S(0,2) state. When the SOI anticrossing is large, it is possible to initialize in the $|\downarrow\downarrow\rangle$ state, by ramping adiabatically from the S(0,2) state to the (1,1) charge state. This is indicated in Fig. 2.7c by the yellow arrow. When the SOI anticrossing is small, ramping adiabatically will initialize the two spins in the $|\uparrow\downarrow\rangle$ state. For the experiments presented in this thesis, initialization in the $|\downarrow\downarrow\rangle$ state was used.

An additional effect of the SOI is an increased decay rate from the different spin states to the S(0,2) ground state, when close to the charge anticrossing in detuning [147, 148]. To increase the readout visibility, we make used of latched PSB readout [149, 150]. In this readout protocol, the tunnel rates of the two quantum dots to their respective reservoirs are tuned asymmetrically. Pulsing from the (1,1) charge state, to the (0,2) charge state and then over the extended (1,1)-(0,1) charge transition line makes it possible for the states blocked from tunneling into the (0,2) charge state to tunnel to the (0,1) instead. The different spin states are now converted to either the (0,2) or the (0,1) charge state, where the decay from the (0,1) to the (0,2) state is set by the tunnel rate to the reservoir. This allows for a sufficiently long readout integration time to achieve spin readout with

reasonable visibility. The downside of the latched PSB readout protocol is that a reservoir close to the quantum dots is needed, which making this approach less suitable for large qubit arrays. Since the rapid decay of the blocked states to the S(0,2) state depends on the external magnetic field, it could be an option to work at lower magnetic field where readout using the Pauli spin blockade is possible without resorting to the latched protocol [151].

2.8. TWO QUBIT GATES

The other crucial ingredient to obtain a universal gate set, besides single qubit gates, is a two-qubit gate. For a two-qubit gate to complete the universal set, it needs to create entanglement between qubits. An example is a controlled NOT (CNOT) gate, which implements a spin flip on the target qubit if and only if the control qubit is in the $|\uparrow\rangle$ state. In general, what a two qubit gate needs to do is implement an operation on a qubit which is conditional on the state of another qubit.

For spin qubits confined in quantum dots, two-qubit gates are usually implemented using the exchange interaction J [98]. When there is a finite amount of tunnel coupling between the quantum dots, the wavefunctions of the two charge carriers have some overlap. Due to the fact that fermions are antisymmetric under interchange, the S(1,1) state and the T_0 state are decreased in energy. In the regime where the difference in Zeeman energy is larger than the exchange, $\Delta Z_E > J$, which is the regime of the experiments presented in this thesis, this is well approximated by lowering the anti parallel spin states compared to the parallel spin states [146]. This is illustrated in the energy diagram plotted in Fig. 2.7b, there is a clear difference between the energy levels when the coupling between the quantum dots is zero (striped lines) and when the coupling is finite (solid line), whereas the parallel spin states are unaffected. The antiparallel spin states are shifted by $J/2$ where $J = (4Ut_0^2)/(U^2-\epsilon^2)$. It is clear from Fig. 2.7b that J can be tuned by the tunnel coupling and the detuning.

There are three types of two-qubit gates that can be implemented using exchange: a controlled rotation (CROT), a controlled phase (CPhase) and the SWAP gate. The implementation of the CROT relies on the fact that when the energy levels of the antiparallel spin states are shifted down, the Larmor frequency of the individual qubits become dependent on the spin state of the other qubit, i.e. the energy difference between $|\downarrow\downarrow\rangle$-$|\uparrow\downarrow\rangle$ is different from the energy difference between $|\downarrow\uparrow\rangle$-$|\uparrow\uparrow\rangle$. The CROT is implemented by driving resonant with one of these transitions. In chapter 4 the CROT gate is demonstrated.

The two-qubit gate which is most suitable for (hole) spin qubits, is the CPhase gate. To implement this gate, the value of the exchange is pulsed, from (practically) zero, to a finite value, and back to zero. When doing this, the energy states of the anti parallel spin states are lowered and than pulsed back to their original value. During this pulse, the anti parallel spin states acquire a spin dependent phase shift with respect to the parallel spin states. In other words, pulsing the exchange results in a phase gate on the target qubit, conditional on the state of the control qubit, due to the temporary change in the resonance frequency of the qubits. The amount of phase acquired depends to which value the exchange is pulsed and on the length of the pulse. When the total phase acquired by the two antiparallel states $\phi = \phi_{|\downarrow\uparrow\rangle} + \phi_{|\uparrow\downarrow\rangle} = (2n+1)\pi$, which n an integer, a CPhase gate

is obtained.

To realize a high fidelity CPhase gate, it is important that the exchange is pulsed adiabatically with respect to the difference in Zeeman energy between the two qubits. Otherwise, the exchange pulse will induce SWAP oscillations between the $|\downarrow\uparrow\rangle$ and the $|\uparrow\downarrow\rangle$ states. A full SWAP oscillation only occurs when the difference in Zeeman energy between the qubits is much smaller than the exchange. However, when the difference in the Zeeman energy is significant, partial SWAP oscillations can still be induced, introducing an error in the CPhase gate. This can be mitigated by ramping the exchange instead of tuning it on and off instantaneously. In the experiments presented in this thesis, the exchange is controlled by controlling the tunnel coupling between the quantum dots using the barrier gate. Optimizing the CPhase gate therefore relies on calibrating the depth, length and ramp time of the pulse on the barrier gate. Implementation of the CPhase gate is shown in chapters 4 and 5.

Although the regime where $\Delta Z_E > J$ is not suitable to implement a SWAP gate by simply pulsing the exchange, it is possible to realize a resonant SWAP gate [152]. By driving the exchange on resonant with the energy difference between the $|\downarrow\uparrow\rangle$ and $|\uparrow\downarrow\rangle$ state, Rabi rotations in the $|\downarrow\uparrow\rangle$, $|\uparrow\downarrow\rangle$ subspace are implemented. This can also be understood as stroboscopically applying an exchange pulse whenever the phase evolution due to the CPhase-like evolution is back at its initial state. In practise, we would implement the resonant SWAP gate by applying a drive to the barrier gate controlling the tunnel coupling $V_B(t)$, according to the formula: $V_B(t) = V_B^{DC} + V_B^{AC} cos(2\pi f_{\Delta E(|\downarrow\uparrow\rangle,|\uparrow\downarrow\rangle)} t + \phi)$, where V_B^{AC} is the amplitude of the drive, V_B^{DC} a DC off-set and $f_{\Delta E(|\downarrow\uparrow\rangle,|\uparrow\downarrow\rangle)}$ the frequency resonant with the energy difference between the anti parallel spin states. SWAP oscillations can be used to implement a $\sqrt{\text{SWAP}}$ gate, which is an entangling gate, or to interchange the spin state of to neighbouring qubits. The resonant SWAP gate is demonstrated in chapter 5 and used for the latter purpose. For a universal gate set, only one type of entangling two-qubit gate is needed, however, being able to implement more than one type will increase the flexibility when compiling algorithms.

So far we have, again, ignored the effects of the SOI. As shown in Fig. 2.7c, among these effects is the spin non-conserving tunneling, which couples the parallel spin states to the S(0,2) state, causing a slight shift in the parallel spin states as well. The relative shift between the parallel spin states and the anti parallel spin states depends therefore on the difference between the spin conserving tunnel coupling t_0 and the non-spin conserving tunnel coupling t_{SOI}. As long as these two coupling terms are not equal, a two-qubit gate based on the exchange interaction can be implemented. Moreover, recent work [153] shows that the SOI can also give rise to an exchange interaction between hole spin qubits which is anisotropic with respect to the external magnetic field. They relate this anisotropy of the exchange to the non-spin conserving tunnel coupling t_{SOI}. Although the SOI makes the interactions in the two-qubit system more complicated, their work suggests that the anisotropy in exchange can be used to optimize the two-qubit gate.

2.9. DECOHERENCE

In order to be able to implement any kind of (useful) quantum algorithm, the qubits should be able to store their quantum information long enough, much longer than the

time it takes to implement qubit gates. There is a fundamental problem however, if we want to be able to manipulate the qubit, we need a way to interact with the qubit, but this will also allow the environment to couple to the qubit. Interaction of the qubit with the environment will lead to loss of quantum information, i.e. decoherence of the qubit. A coherent qubit state is a point on the surface of the Bloch sphere and in this picture, decoherence can be understood as shrinking of the Bloch sphere. There are two types of decoherence: spin randomization and spin dephasing. Spin randomization can be understood as shrinking of the Bloch sphere along the z-axis. For this process to happen, an exchange of energy with the environment is necessary. The kind of error that this introduces is a spin flip error. Due to the low temperature at which we perform our experiments, in most cases the randomization of the spin will be relaxation: the spin decays to the ground state. Spin dephasing is the loss of phase coherence of a superposition state, i.e. the phase of a superposition state is no longer well defined. In this case the Bloch sphere becomes smaller along the equator. If the length of the quantization axis is varied over time, i.e. the Larmor frequency is not constant, this will cause random phase shifts over time. The kind of error that this process introduces is a phase flip error.

The spin randomization is characterized by the typical time T_1. Spin randomization can be caused by several mechanisms: hyperfine interaction, interaction with the hole reservoir and phonons which can couple to the hole spin qubit via the SOI. The hyperfine interaction will be discussed in detail later in this section, but is not limiting T_1 [154]. The interaction with the hole reservoir can easily be controlled by the tunnel coupling to the leads. Since in all the experiments presented in this thesis, we used charge sensing via a sensing dot, the qubits are always well isolated. Moreover, tight confinement in the quantum dot leads to large energy splittings to the excited states, which in turn leads to a long T_1, because the phonon-hole interaction connects the orbital ground state to excited state [154]. When the qubit is confined in a quantum dot, the randomization process that takes place is almost always relaxation to the $|\downarrow\rangle$ ground state. The T_1 in this regime is in the order of tens of milliseconds [155]. However, when the hole spin qubit is not confined in a quantum dot, for example because it is moved from one quantum dot to another (such as in chapter 6 of this thesis), it needs to pass the charge anticrossing. The T_1 at this point in detuning can be significantly smaller, because the hole is delocalized between the two quantum dots. Excitations to higher energy levels mediated by the SOI are more likely to happen [156], which can randomize the spin state. Since single qubit operations are performed with well isolated qubits, this process is not relevant for implementing quantum algorithms and T_1 is not the limiting time scale.

Similar to the spin randomization, the spin dephasing is characterized by a typical time T_2. In practise, the dephasing is measured using thousands of single shot measurements, effectively taking the average over the fluctuations of the Larmor frequency during the total measurement time. This is comparable to measuring the dephasing of an ensemble of spins and the typical time is indicated by T_2^*. Dephasing of hole spin qubits in germanium is caused by two mechanisms: hyperfine interaction and charge noise which can couple to the spin via the SOI. The hyperfine interaction is the coupling of the spin of the qubit to the nuclear spins in the heterostructure. Of the natural germanium in the quantum well, only 7.7% is ^{73}Ge, which is the only isotope with a non-zero nuclear spin. For electrons, the main contribution to the hyperfine interaction is the so called

direct hyperfine interaction: the overlap of the wavefunction of the spin qubit with the nuclei. The direct hyperfine interaction is isotropic. However, since the hole wavefunction is p-type, the overlap with the nuclear sides of the lattice is very small and the direct hyperfine interaction is suppressed. There are additional hyperfine interaction terms, arising from the dipole-dipole interaction between the hole spin and the nuclear spins and from the interaction between the orbital momentum of the hole and the nuclear spins. These terms are highly anisotropic, where the Ising term (i.e. out-of-plane of the quantum well) for the ^{73}Ge isotope is predicted to be about 50 times larger than the in-plane terms [157]. Therefore, if a sufficiently large external magnetic field is applied in-plane of the quantum well, the fluctuations due to these hyperfine interaction terms are perpendicular to the quantization axis of the qubit. As a result, their effect on the Larmor frequency of the qubit is limited and also these terms of the hyperfine interaction are suppressed. However, due to the sensitivity of the g-tensor of the hole spin qubits to the electric fields, the principle axis of the g-tensor might not align perfectly with the axis of the heterostructure. Moreover, a small misalignment between the in-plane axis of the g-tensor and the external magnetic field can lead to a significant tilt of the quantization axis. Therefore, the hyperfine interaction can still have a measurable effect on hole spin qubits in germanium, even when the external magnetic field is almost perfectly in-plane [127, 158]. If the hyperfine interaction is the dominant mechanism causing the dephasing of the spin qubits, we would expect the T_2^* to increase with the value of the external magnetic field.

Since the SOI for hole spin qubits in germanium is strong, it is expected that charge noise has a significant effect on the phase coherence. Charge noise comes from randomly fluctuating charge defects, which are present everywhere in the heterostructures, but mostly at the semiconductor-oxide interface. A model often used for charge noise is an ensemble of two-level fluctuators, which give rise to a $1/f$ noise frequency spectrum, as shown in chapter 4. Due to the SOI, the g-tensor $\overleftrightarrow{g}$ is sensitive to the electrostatic confinement and can therefore be modulated by charge noise. This variation in the g-tensor $\delta\overleftrightarrow{g}$ will lead to change in the Larmor vector: $h\delta\mathbf{f}_L = \mu_B\delta\overleftrightarrow{g}\mathbf{B}$. Again, if the fluctuation in the electric field are parallel to the quantization axis of the qubit, this will lead to a change in the Larmor frequency, which will lead to dephasing. From this equation it is clear that if charge noise, coupling to the qubit via modulation of the g-tensor, is the dominant noise source, we expect the noise to have a more severe effect when the external magnetic field increases. Another way the charge noise can couple to the spin qubits, is via the exchange interaction. The exchange depends on the detuning and the tunnel coupling, which both depend on the electrostatic confinement, and the exchange in turn can alter the Larmor frequency. The coherence of the single qubits can therefore be improved by turning the exchange off.

Comparing results of T_1 ($\approx$ 1- 10 ms) and T_2^* ($\approx$ 300 - 500 ns) measurements, it is clear that dephasing is the limiting decoherence process for hole spin qubits in germanium. Measurements of T_2^* as a function of external magnetic field show that dephasing increases with magnetic field, which give a strong indication that charge noise is the main noise source [127, 155]. This trend breaks at very low magnetic field, where the differences in frequencies of the nuclear spin in the substrate limit the phase coherence [127]. There are several measures that could be combined to increase the phase coherence,

for example, operating at low magnetic field (which will limit the effect of charge noise) and using isotopically purified germanium in the quantum well (which can eliminate the hyperfine interaction [159, 160]). Moreover, since changes in the g-tensor parallel to the quantization axis lead to dephasing, but modulation of the g-tensor perpendicular to the quantization axis is required for driving, there might exist an orientation for the quantization axis which minimizes decoherence and at the same time optimizes driving. Such a configuration in which the qubit is less sensitive to charge noise, but qubit driving is still efficient, is called a sweet spot. For a given g-tensor, the direction of the quantization axis is set by the direction of the external magnetic field. Therefore it might be possible to find a sweet spot by carefully optimizing the direction of the external magnetic field [127]. However, for this optimization to be useful, there are two conditions that need to be met. Firstly, to find a real sweet spot in the direction of the magnetic field, it is important to work with purified germanium, to not be directly limited by hyperfine noise when the magnetic field is not in-plane of the g-tensor. Secondly, when scaling to an array with multiple qubits, the g-tensors need to be sufficiently uniform such that there is a common sweet spot for all qubits. The first impression for hole spin qubits might be that the stronger the interaction, the faster the spin qubit drive, the faster the decoherence. However, it becomes clear from the mechanisms discussed above, that there are ways around this.

2.10. QUANTUM ERROR CORRECTION

As described above, we try our best to make our qubits as 'good' as possible, minimize the coherent errors: errors due to the operation of the single- and two-qubit gates, cross talk i.e. errors on qubits due to the driving of the neighbouring qubits and incoherent errors: errors due to charge noise and hyperfine interaction. Moreover, also errors in the initialization and the read-out of the qubits need to be minimized. Despite these efforts, optimizing the qubits and all the operations performed on them well enough to run long and complicated algorithms, is an (almost) impossible task. Therefore, ways need to be found to correct errors before they can accumulate and propagate throughout the qubit register.

In classical computing error correction is widely used. The actual implementation can be quite complicated but the basic idea behind it, is that the information is encoded [161]. For example, we can replace a bit with three copies of itself. If the bit was 0, the encoding becomes 000, if it was 1, it becomes 111. The bit strings 000 and 111 are called the logical 0 and the logical 1. Now, when an error occurs on one of the bits, there is redundancy in the system. For instance, if we start out with 000, and after some time we find that we have 001, we can decode the information and apply a majority vote. It becomes clear that the right value of our bit was 0. This method of error correction works only if maximally one error occurred, in other words this error correction protocol will only give an overall improvement if the probability of an error p is smaller than 0.5.

For quantum computing encoding information by introducing redundancy is much harder to implement, since quantum error correction comes with additional challenges. Firstly, it is not possible to perfectly clone a perfect unknown quantum state using an unitary operation. For the proof see reference [161]. It is therefore impossible to create redundancy in a quantum system by simply copying the state of the qubit. Secondly, a

direct measurement of the state of a qubit will collapse the wavefunction, i.e. destroy the quantum state. It will reduce the state with an amplitude and a phase to a single value. So even if it would be possible to make copies of the quantum state, comparing them by measuring the value, detecting where the error has occurred and correcting the quantum state is impossible, because it was destroyed by the measurement. The third complication is that where a classical bit is a binary system, a qubit is an analogue system. For a bit it is sufficient to determine if it is a 0 where it should have been a 1 (or the other way around) and correct this: a bit flip. A quantum error correction protocol needs to be able to correct an arbitrary error, there is an infinite amount of possible errors and it would take infinite precision to correct them.

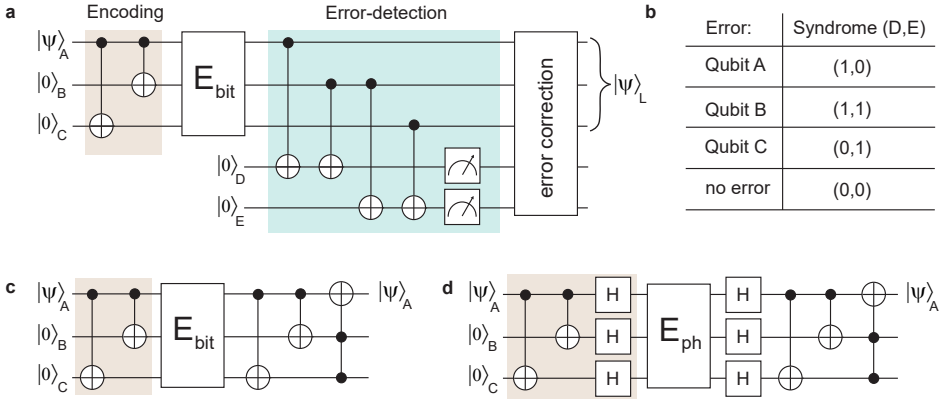

Figure 2.8: **Simple error correction codes a** Shown here is a textbook version of a circuit diagram of the bit flip code, using two helper qubits to perform syndrome measurements. **b** Truth table relating the error syndrome to a bit flip error occurring on the different physical qubits making up the logical qubit. **c** Circuit diagram of a different implementation of the bit flip code. Instead of performing syndrome measurements, a conditional three qubit gate, the Toffoli gate, is used to correct a possible bit flip error. **d** Circuit diagram of the phase flip code. This error correction code is very similar to the bit flip code, but due to the Hadamard gates in the encoding and decoding, this code can correct for a phase flip error.

Remarkably, none of these complications makes quantum error correction fundamentally impossible. By explaining the simplest quantum error correction code, the bit flip code, the solutions that were found to these challenges will become clear. Suppose we have the situation where our qubit will remain untouched with a probability of $(1-p)$ and that there is a probability of p that it will experience a π-rotation around the x-axis of the Bloch sphere, i.e. a bit flip error. The code to detect for these type of errors is shown in Fig. 2.8a. The first step in the error correction code is the encoding. The information of one physical qubit, $|\Psi\rangle = \alpha|0\rangle + \beta|1\rangle$ is encoded in three physical qubits, forming one logical qubit: $|\Psi\rangle = \alpha|000\rangle + \beta|111\rangle$. In the bit flip code, the encoding consists of two CNOT gates, entangling the first qubit with the other two. This is the way in which redundancy can be built into a quantum system: by entangling several physical qubits. Then comes the part where possible bit flip errors are introduced (box with E_{bit}), followed by the error-detection step (blue box in Fig. 2.8a). The error detection consists of two times

a CNOT gate, between two of the physical qubits in the logical qubit (labeled qubits A, B and C) and a helper qubit (qubits D and E). The measurement on the helper qubits gives the error syndrome (Fig.2.8b), which will tell if the quantum state on the physical qubits is different (measurement outcome 1) or the same (measurement outcome 0). In this way, an error can be detected, without directly measuring the qubits and therefore without collapsing the wavefunction. Note that the error syndrome does not contain any information on the quantum state of the qubits, just on the differences between them. Based on the error syndrome, the error can be corrected, since the quantum state on the logical qubit is still intact. The error correction step happens via classical feedback. Since it becomes clear from the error syndrome where/if a bit flip has occurred, this bit flip can be undone by applying an X-gate. The final result of this version of the bit flip code, is the encoded state, i.e. the logical qubit. The fact that this works, not only for full bit flips, but any X-error, has to do with the quantum nature of the qubits. When an error occurs on qubit A, B or C it is in a superposition of having a bit-flip error and of not having a bit flip error. By entanglement with the helper qubit, and the subsequent measurement of the helper qubit, the state of the qubit will be projected into having an error or not having an error. Depending on the syndrome, the feedback can consist of a X-gate, instead of an arbitrary correction.

A different version of the bit flip code, using only three qubits, is shown in Fig. 2.8c. The encoding of the logical qubit is the same, however, the error correction and detection are different. Instead of performing syndrome measurements using helper qubits, the encoding of the logical qubit is reversed after a possible error has occurred. Two CNOT gates are used to indicate on qubits B and C whether a bit flip error has occurred on qubit A. Subsequently, a Toffoli gate is used to correct a potential bit flip error on qubit A, based on the states of qubits B and C. A successful outcome of this version of the bit flip code is when qubit A has the same quantum state $|\Psi\rangle$ as before the encoding step. Since the three qubit bit flip code can correct for maximum one error, the chance of getting the state $|\Psi\rangle_A$ back is $1-3p^2+2p^3$. The bit flip code gives an improvement over not implementing an error correction code when $(1-3p^2+2p^3) > (1-p)$, which is true for $p = 0.5$.

Fig. 2.8d shows the circuit diagram of the phase flip code with three qubits. The phase flip code can correct the other fundamental error on a qubit: an error in the phase of the qubit, i.e. a Z-error. The difference between the bit flip and the phase flip code is the encoding for the logical qubit, which becomes $|\Psi\rangle = \alpha|+++\rangle + \beta|---\rangle$. As explained in section 2.9, the lifetime of spin qubits is limited by dephasing. Therefore, correcting phase errors is more of interest than correcting bit flip errors. An experimental implementation of the phase flip code is shown in chapter 5. The bit flip code and the phase flip code can be combined to a quantum error correction algorithm that can correct for both types of errors, the Shor code. The minimal implementation of this code requires nine qubits.

Quantum error correction codes such as the bit flip code, phase flip code and Shor code, are nice as a proof of principle, but in practise they are not very useful to mitigate errors. This is mainly because these codes assume perfect initialization, encoding and measurements. These schemes can only correct an error on the encoded qubit, but during the encoding, decoding or syndrome measurements and the correction, the physical

qubits are still vulnerable to errors. Looking at Fig. 2.8, an error can only be corrected when it happens in the box marked 'E' in the circuit diagram. We need an error correction protocol that prevents errors from propagating from one qubit to another and turning from an error on a physical qubit to an error on a logical qubit. When this is achieved, the error correction code will have a better success rate when the number of physical qubits used for the logical qubit is increased. Moreover, the ultimate application of quantum error correction would not be the protection of the information stored in logical qubits, but the protection of quantum information during the processes of computation with these logical qubits. It turns out that it is possible to achieve arbitrarily good computation, even using imperfect gates on logical qubits, as long as the chance of an error on a gate operation is below a certain threshold [84]. This holds the promise for fault-tolerant quantum computation. There are several error correction codes that could be made compatible with spin qubits [162]. One which holds most potential, is the surface code. It is favoured because it only requires nearest-neighbour coupling between the qubits and it has a relatively high threshold error rate. The development of spin qubits has now reached the point where the first proof of principle experiments with error correction codes can be done (see chapter 5 and similar work [163]). Hopefully, the development of error correction codes tailored to the properties of spin qubits, will meet the developments of spin qubits half way on the road to fault tolerant quantum computing.

3

A TWO-DIMENSIONAL ARRAY OF SINGLE-HOLE QUANTUM DOTS

Quantum dots fabricated using methods compatible with semiconductor manufacturing are promising for quantum information processing. In order to fully utilize the potential of this platform, scaling quantum dot arrays along two dimensions is a key step. Here we demonstrate a two-dimensional quantum dot array where each quantum dot is tuned to single-charge occupancy, verified by simultaneous measuring with two integrated radio frequency charge sensors. We achieve this by using planar germanium quantum dots with low disorder and small effective mass, allowing the incorporation of dedicated barrier gates to control the coupling of the quantum dots. We measure the hole charge filling spectrum and show that we can tune single-hole quantum dots from isolated quantum dots to strongly exchange coupled quantum dots. These results motivate the use of planar germanium quantum dots as building blocks for quantum simulation and computation.

This chapter has been adapted from F. van Riggelen, N.W. Hendrickx, W.I.L. Lawrie, M. Russ, A. Sammak, G. Scappucci, M. Veldhorst, Applied Physics Letters **118** (4) (2021) [164].

3.1. INTRODUCTION

Quantum information requires qubits that can be coherently controlled and coupled in a scalable manner [102], while quantum error correction and scalable interconnects strongly benefit from the ability to couple qubits along at least two dimensions [165, 166]. Across all the different qubit technologies, quantum dots [98] fabricated using techniques compatible with standard semiconductor manufacturing are particularly promising [167]. Furthermore, realizing two-dimensional quantum dot arrays may allow to construct highly scalable qubit tiles such as crossbar arrays [168] supporting quantum error correction [169] for fault-tolerant quantum computation.

A key challenge is therefore to develop two-dimensional arrays of quantum dots that exhibit a high level of uniformity, long quantum coherence, and that can be operated with excellent control. Initial research centered around low-disorder gallium arsenide (GaAs) heterostructures [108, 110], which advanced to exciting demonstrations such as coherent spin transfer across an array of quantum dots [170], and the operation of a two-dimensional quantum dot array [171]. Nonetheless, group III-V materials suffer from hyperfine interaction, resulting in fast spin dephasing and reduced operation fidelity. Instead, group IV materials can be isotopically enriched [159, 160] to virtually eliminate dephasing due to a nuclear spin bath. This has stimulated research on silicon and led to orders of magnitude improvement in coherence times [114, 172]. While advances in devices based on silicon heterostructures have led to the operation of linear arrays containing up to nine quantum dots [173], the relatively large effective mass of silicon electrons, the presence of valley energy states, and the finite disorder complicates progress [174]. Though fabrication is advancing to complementary metal–oxide–semiconductor (CMOS) foundry-manufactured devices [175, 176], demonstrations on two-dimensional quantum dot arrays have been limited to reaching single-electron occupancy in up to three dots within a 2x2 array [177–180]. Reaching simultaneously the single-charge regime with all quantum dots in a two-dimensional array fabricated using CMOS foundry compatible materials remains thereby an outstanding challenge.

Germanium is rapidly emerging as an alternative material to realize spin qubits [125], since holes in germanium have favorable properties such as a small effective mass [131], large excited-state energies due to the absence of valley degenerate states, and strong spin-orbit coupling for electrically driven single-qubit rotations without the need for external components [123, 181, 182]. High-quality Ge/Si core-shell nanowires enabled the construction of a triple quantum dot in a linear arrangement, albeit only in the multi-hole regime [128]. The realization of high-quality strained Ge/SiGe quantum wells [124] has led to the development of quantum dots [122, 130], demonstration of long hole spin relaxation times [155], the operation of a single-hole qubit [140], and enabled the execution of two-qubit logic in germanium [141]. Furthermore, quantum dots in planar germanium are realized using industry compatible techniques [176], promising large-scale implementations provided that germanium quantum dots can be engineered beyond linear arrangements.

Here, we realize a two-dimensional quantum dot array using materials compatible with existing CMOS technology and demonstrate a quadruple germanium quantum dot. We obtain excellent control over the charge occupancy and the interdot coupling. The

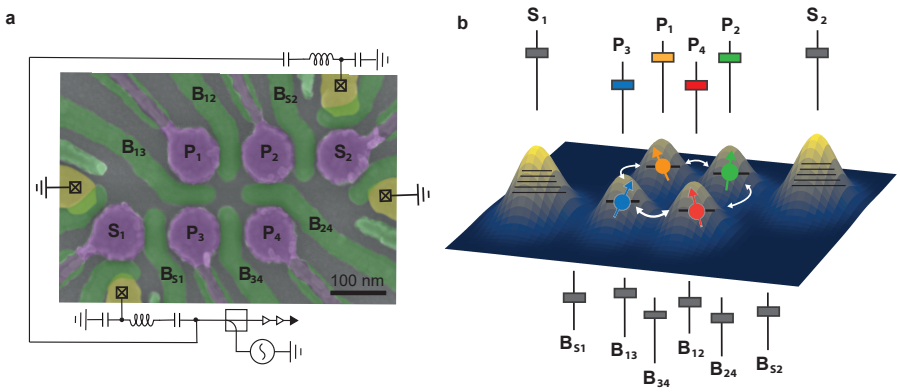

Figure 3.1: **A 2x2 germanium quantum dot grid with two integrated rf sensors** (a) False colored SEM image of a sample similar to the one on which the measurements are performed. The plunger gates of the quantum dots P are colored in purple, the barrier gates B are colored in green and the aluminum ohmics in yellow, which serve both as source and drain contacts for rf sensing, as well as charge reservoirs for the quantum dots. (b) Schematic representation of the potential landscape, illustrating how the plunger and barrier gates control the quantum dots. In the image, each quantum dot is occupied with a single hole (N=1), which is color coded per quantum dot (yellow for Q_1, green for Q_2, blue for Q_3, and red for Q_4). The charge occupation in a quantum dot is controlled by a plunger gate, symbolized by a slider above the image with the same color. The sensing dots are tuned into the multi-hole regime, illustrated by the many energy levels drawn in the quantum dot. The coupling between the quantum dots, indicated by the arrows, is controlled by a barrier gate, depicted by a slider below the image.

device consists of the quantum dot grid and an additional two quantum dots on the sides that are used for radio frequency (rf) charge sensing. We are able to tune each quantum dot to the single-hole occupancy and we find shell filling as is expected for a circular quantum dot and with spin degeneracy. This demonstrates a qubit state manifold with large separation energy, since excited states, such as valley energy states, are absent. We exploit the integrated barrier gates to gain independent control over the hole occupancy and the tunnel coupling between neighboring quantum dots. We use this to demonstrate the single-hole occupancy in the full quadruple quantum dot array as a stepping stone toward two-dimensional arrays of quantum dot qubits.

3.2. A 2X2 QUANTUM DOT ARRAY IN GERMANIUM

Figure 3.1(a) shows a scanning electron microscopy (SEM) image of a quantum dot grid and Figure 3.1(b) shows a schematic image of the potential landscape and the control gates of the quantum dot system. Fabrication is based on a multilayer gate design [155] and described in Supplementary Information section I. Holes in strained germanium benefit from a low effective mass, low disorder, and absence of valley states. These assets ease constraints in fabrication and relax the quantum dot design, which makes it possible to define a 2x2 quantum dot grid with only two overlapping gate electrodes. The quantum dots are defined using plunger gates P and are coupled through barrier gates B. We have fabricated the barrier gates as the first layer and the plunger gates as the second

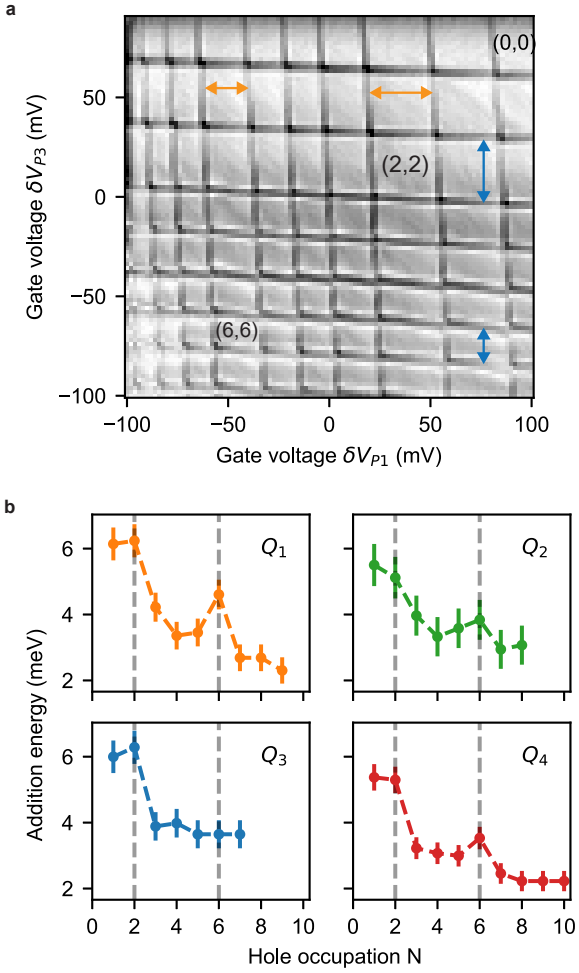

Figure 3.2: **Charge filling in the individual quantum dots** (a) Shown is a charge stability diagram of the double quantum dot Q_1 - Q_3 with negligible tunnel coupling (See Supplementary Information section II for the quantum dot pair Q_2-Q_4). Here, the results are shown as measured with sensor S_1, the sensor closest to the quantum dot pair. We can observe all transitions with both sensors, albeit with reduced sensitivity for the more remote quantum dots, as shown in Figure 3.4. The hole occupation (N_{Q1}, N_{Q3}) is indicated in the charge stability diagram. (b) Addition energy for the four quantum dots, extracted from the corresponding stability diagrams and converted using a lever arm $\alpha = 0.19$ eV/V. The dashed grey lines correspond to the hole fillings for which increased addition energy is expected due to shell filling when considering a circular potential landscape and spin degeneracy (also indicated by orange and blue arrows in (a) for Q_1 and Q_3 respectively).

layer, which results in a good addressability of both the tunnel couplings and quantum dot energy levels. The aluminum ohmics serve as hole reservoirs for the charge sensors. Controllable loading of the quantum dots is obtained through an additional barrier gate between the sensor and the quantum dots (B_{S1} and B_{S2}). The charge occupation in the dots is measured with the nearby sensing dots. We use rf reflectometry to achieve a high measurement bandwidth of the sensor impedance, which allows for measuring charge stability diagrams in real time.

3.3. HOLE FILLING OF QUANTUM DOTS

Figure 3.2(a) shows a charge stability diagram corresponding to quantum dot pair Q_1-Q_3. See Supplementary Information, Note 2 for the stability diagram corresponding to quantum dot pair Q_2-Q_4. In this measurement we preserve the sensitivity of the sensor, by offsetting the effect of a change in voltage on the plunger gate of the quantum dots with a small change in voltage on the plunger gate of the sensors. From the linear charge addition lines in Figure 3.2(a) we infer that the capacitive coupling between the plunger gate and the neighboring quantum dot is small and does not require compensation. In Figure 3.2(b), we show the addition energies for each of the four quantum dots in the few-hole regime. We define the addition energy as the energy required for adding an extra hole to the quantum dot. The addition energies are extracted from the charge stability diagrams, by analysing the spacing between the addition lines for all the dots. The change in gate voltage is converted into energy, using a lever arm α = 0.19 eV/V. Steps are observed for hole occupations N = 2 and N = 6 that are consistent with shell filling for a circular quantum dot and considering the spin degree of freedom [184, 185]. These experiments also highlight the absence of low-energy excited states such as valley states, which would give rise to a different shell filling pattern [186]. It is interesting to observe that quantum dot Q_1 and Q_4 show shell filling as expected of circular quantum dots, while for Q_2 and Q_3 the expected peaks in addition energy are less pronounced. Moreover, Q_2 and Q_3 show an increased addition energy for N = 4. We ascribe this difference to Q_2 and Q_3 being positioned closely to the sensors quantum dots, which are operated using relatively large negative potentials. The electric field from the sensors might distort the circular potential to a more elliptical shape, which would in turn modify the electronic structure and cause an increased addition energy at half-filling [187].

3.4. CONTROLLABLE TUNNEL COUPLING

Having shown control over the hole occupation of the individual quantum dots, we focus on the interdot tunnel coupling. Figures 3.3(a-c) show charge stability diagrams of a double quantum dot defined by plunger gates P_3 and P_4 for different barrier gate potentials, compensating the effect of the change in voltage on the sensor. We find that we can tune the quantum dots from being fully isolated, to a strongly coupled regime, and to merging quantum dots, indicating a high level of tunability. Importantly, we reach all regimes while freely choosing the hole occupancy.

To quantify the tunnel coupling between the quantum dots we analyze the charge polarization lines. Figure 3.3(d) shows the anticrossing corresponding to the (1,1)-(0,2) charge configurations. We measure charge sensor response along the detuning axis and

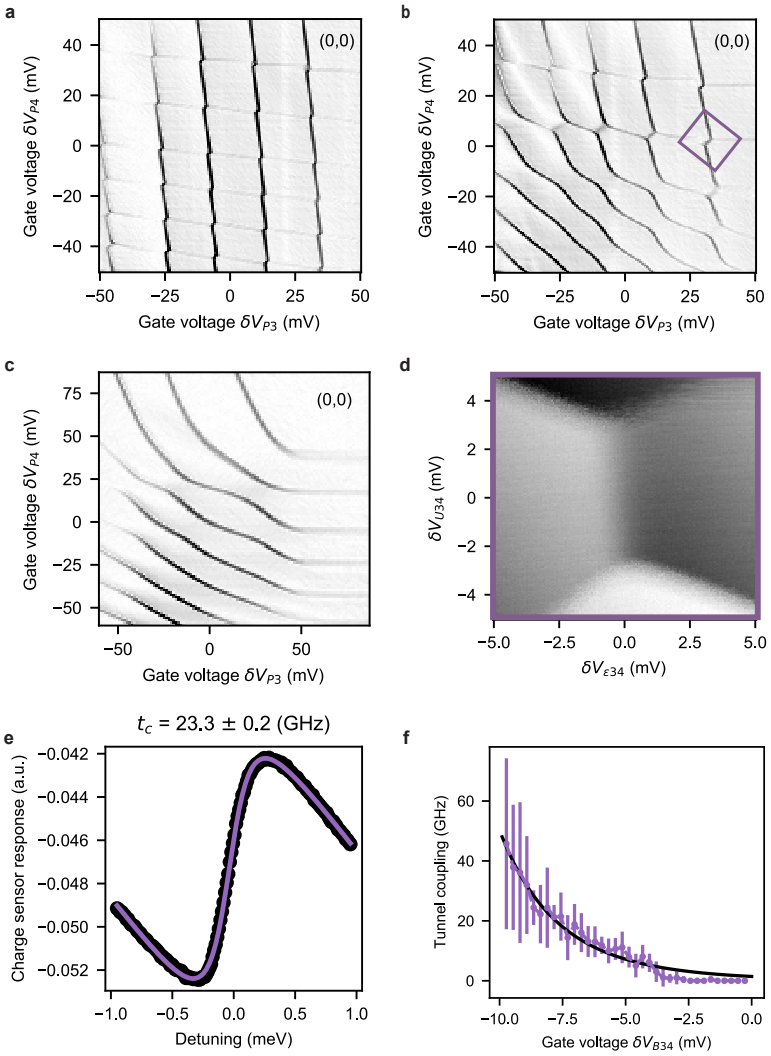

Figure 3.3: **Controllable interdot tunnel coupling.** (a,b,c) Charge stability diagram for quantum dot pair Q_3 - Q_4 with barrier gate voltage V_{B34} = -1010.6 mV (a), V_{B34} = -1055.1 mV (b), and V_{B34} = -1137.1 mV (c). By varying the barrier gate voltage we can freely tune the tunnel coupling over a large range. (d) Zoom-in on the relevant (1,1)-(0,2) charge configuration where we quantify the tunnel coupling. (e) By fitting the charge polarization line [183] we obtain the tunnel coupling, which is t_C = 23.3 ± 0.2 GHz. (f) By varying the gate voltage V_{B34} we can control the tunnel coupling up to 40 GHz. Reduced charge sensor sensitivity for higher tunnel coupling causes the uncertainty in the measurement to increase. The trend of the tunnel coupling corresponds well to a fit based on the WKB theory (see Supplementary Information section V for further details).

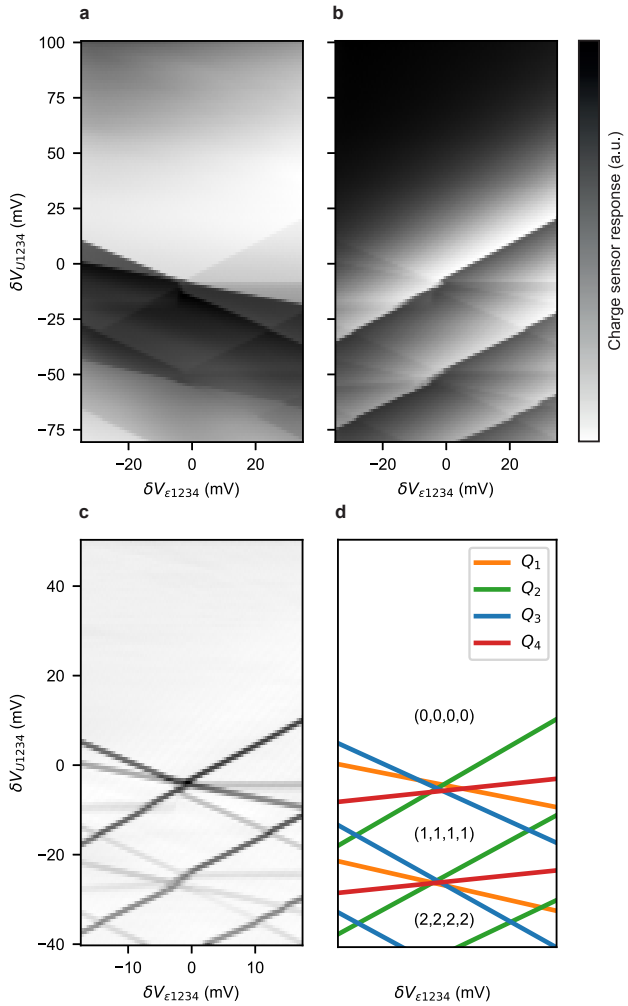

Figure 3.4: **Quadruple quantum dot in germanium** (a,b) Charge stability diagram of the four quantum dot system, obtained by simultaneous readout of S_1 and S_2. (a) Charge sensor response of sensor S_1. (b) Charge sensor response of S_2. While we can observe all transitions with each sensor, we observe a significant larger sensitivity to the quantum dots neighboring the sensor. (c) Derivative of the combined response signal, clearly revealing the charge addition lines for each of the quantum dots. (d) Schematic representation explaining the charge addition lines as measured in (c), confirming the absence of additional lines from spurious quantum dots or traps and demonstrating a single-hole quadruple quantum dot array. Hole occupation in the dots (N_{Q1}, N_{Q2}, N_{Q3}, N_{Q4}) is indicated for an empty system, single-hole occupation, and double hole occupation for all four dots.

determine the tunnel coupling by fitting the charge polarization lines [183], as shown in Figure 3.3(e). By changing the barrier gate voltage we can control the tunnel coupling and find that we can tune the interdot tunnel coupling over a range from completely off to beyond 40 GHz. Note that we can set larger tunnel couplings, see for example Figure 3.3(c). However, in this regime we are not able to make reliable fittings of the charge polarization line, due to the reduced charge sensitivity of the sensor, as a result of the merging of Q_3 and Q_4.

3.5. A QUADRUPLE QUANTUM DOT

After focusing on the interdot coupling, we now show that we can form a quadruple quantum dot in the 2x2 array, reaching single-hole occupation for all four quantum dots simultaneously. With both sensors we can detect charge transitions of each quantum dot within the array, although a significantly stronger sensitivity is obtained for the quantum dots neighboring the sensor. In order to conveniently tune and demonstrate the single-hole occupation for all quantum dots, another virtual gate set is defined (see Supplementary Information, Note 3), such that the addition lines of all four dots have a distinctive slope. In Figure 3.4(a) and (b) we show the charge stability diagram as measured by the individual charge sensors. Taking the derivative of the signal and summing them results in Figure 3.4(c). The observed charge addition lines are explained in Figure 3.4(d).

3.6. CONCLUSION

In conclusion, we have demonstrated shell filling, tunable interdot coupling, and the tuning of a quadruple quantum dot to the single-hole states. The shell filling experiments underscore the high-quality of planar germanium quantum dots as a platform for spin qubits. Moreover, this statement is supported by the demonstration that the tunnel coupling between single holes can be tuned over a large range, from isolated quantum dots to strongly coupled and merging quantum dots. This tunability is promising for quantum simulation with quantum dots such as simulating metal-insulator transitions [169]. Simultaneously, the ability to turn the exchange interaction on and off is highly advantageous for digital quantum computation and can be used to program two-qubit logic at their sweet spots. The demonstration of a quadruple quantum dot positioned in a two-dimensional array is an important stepping stone toward quantum information processing using standard semiconductor manufacturing.

3.7. SUPPLEMENTARY INFORMATION

NOTE 1: CHARGE STABILITY DIAGRAM Q_2-Q_4

NOTE 2: VIRTUAL GATES

The data shown in Figure 3d-f of the main text was taken in a virtual gate space of detuning and energy (ϵ_{34} and U_{34}). The matrix defining the voltages on gates ϵ_{34} and U_{34} as a linear combination of the voltages on gates P_3 and P_4 is the following:

$$\begin{pmatrix} V_{P3} \\ V_{P4} \end{pmatrix} = \begin{pmatrix} 0.5 & 0.5 \\ -0.5 & 0.5 \end{pmatrix} \begin{pmatrix} V_{\epsilon 34} \\ V_{U34} \end{pmatrix} \tag{3.1}$$

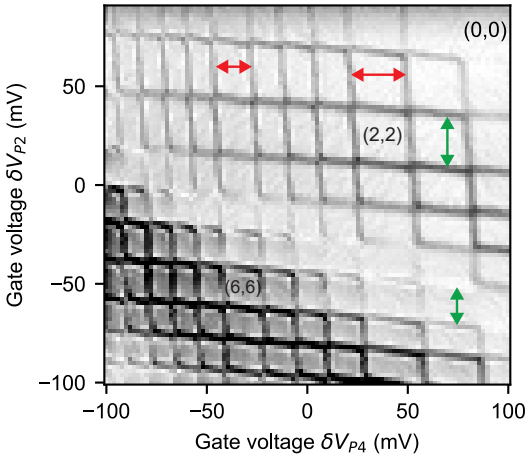

Figure 3.5: **Charge filling** Q_2 - Q_4 Shown is a charge stability diagram of the double quantum dot Q_2 - Q_4 with negligible tunnel coupling. Here the results are shown as measured with sensor S_2, the sensor closest to this quantum dot pair. The numbers added to the diagram (N_{Q2},N_{Q4}) indicate the hole occupancy in quantum dots Q_2 and Q_4 respectively. The colored arrows correspond to the hole filling for which one would expect a peak in the addition energy due to the shell filling of a quantum dot with a circular potential and spin degeneracy.

For the data shown in Figure 4 of the main text, a virtual gate sets was defined such that for all four quantum dots the filling of N=1 coincides and that the slope of the addition lines of all four dots can be distinguished from each other. The voltages on the two virtual gates e_{1234} and U_{1234} were constructed as a linear combination of the voltages on all the four plunger gates P_1 - P_4. The matrix defining the virtual gate space is the following:

$$\begin{pmatrix} V_{P1} \\ V_{P2} \\ V_{P3} \\ V_{P4} \end{pmatrix} = \begin{pmatrix} 0.65 & 1.92 \\ -0.38 & 0.38 \\ 0.66 & 0.77 \\ -0.14 & 0.42 \end{pmatrix} \begin{pmatrix} V_{e1234} \\ V_{U1234} \end{pmatrix} \tag{3.2}$$

During both of these measurements, the effect on the plunger gates of the sensors were also compensated.

NOTE 3: LEVER ARM

The lever arm, used to convert the applied gate voltage to the detuning energy (meV) in Figure 3e and 3f of the main text, is $\alpha = 0.19$ eV/V. This value was obtained by performing a photon assisted tunneling (PAT) measurement [188] at the (1,1)-(0,2) anticrossing in virtual gate space of detuning and energy (ϵ_{34}, U_{34}). For a PAT measurement a microwave field is used to induce the re-population of states. Resonance peaks are observed when the frequency of the microwave source is equal to the energy difference between two states, i.e. the resonance frequency is given by $hf = \sqrt{\epsilon^2 + 4t^2}$, where h is Planck's con-

stant, f is the frequency of the microwave source, t is the interdot tunneling and ϵ is the detuning which is given by $\alpha\delta\epsilon_{34}$. This measurement is taken in the regime where the tunnel coupling was turned off, making the extracting of the lever arm α straight forward.

To calculate the addition energies as plotted in Figure 1b from the main text, the same lever arm $\alpha = 0.19$ eV/V was used. Since the virtual gate matrix defining ϵ_{34} and U_{34} is symmetric for the gates P_3 and P_4 (see previous section) and the capacitance of the four plunger gates to the quantum dots underneath is similar (estimated from the lope of the addition lines from the charge stability diagrams shown in Figure 3.2 and 3.5 in the Supplementary Information), we conclude this as a reasonable assumption.

NOTE 4: TUNNEL COUPLING

For fitting the extracted values for the tunnel coupling we use a model based on tunneling through a rectangular barrier. In the limit of weak tunneling the tunnel probability can be approximated by the WKB approximation, which reads for a rectangular barrier (see Supplementary Materials in Ref. [189]):

$$|t|^2 = 16c\frac{|V_B - V_0|}{(V_B - V_1)^2}\exp\left(-2b\sqrt{\frac{2m\alpha}{\hbar^2}|V_B - V_0|}\right). \tag{3.3}$$

Here, V_0 is the voltage when the barrier height is equal to the energy of the hole, V_1 is the voltage when the barrier height is zero, α is the lever arm which translates the barrier voltage into energy units, b is the width of the barrier, m is the effective mass of the hole, and c is an overall scaling factor. By fitting the experimentally determined values we extract V_0 = -17.6 mV, V_1 =-25.2 mV, and $b\sqrt{2m\alpha/\hbar^2} = 2.41\frac{1}{\sqrt{\text{mV}}}$, and $c = 2.82\times10^9\,\frac{\text{GHz}^2}{\text{mV}}$.

4

A FOUR-QUBIT GERMANIUM QUANTUM PROCESSOR

The prospect of building quantum circuits [87, 165] using advanced semiconductor manufacturing makes quantum dots as an attractive platform for quantum information processing [98, 167]. Extensive studies on various materials have led to demonstrations of two-qubit logic in gallium arsenide [111], silicon [189, 191–196], and germanium [141]. However, interconnecting larger numbers of qubits in semiconductor devices has remained an outstanding challenge. In this chapter, we demonstrate a four-qubit quantum processor based on hole spins in germanium quantum dots. We find single-qubit gate fidelities as high as 99.99%. Furthermore, we define the quantum dots in a two-by-two array and obtain controllable coupling along both directions. Qubit logic is implemented all-electrically and the exchange interaction can be pulsed to freely program one-qubit, two-qubit, three-qubit, and four-qubit operations, resulting in a compact and highly connected circuit. We execute a quantum logic circuit that generates a four-qubit Greenberger-Horne-Zeilinger state and we obtain coherent evolution by incorporating dynamical decoupling. These results are an important step towards quantum error correction and quantum simulation with quantum dots.

This chapter has been adapted from N.W. Hendrickx, W.I.L. Lawrie, M. Russ, F. van Riggelen, S.L. de Snoo, R.N. Schouten A. Sammak, G. Scappucci, M. Veldhorst, Nature **591** (7851), 580-585 (2021) [126],
and W.I.L. Lawrie, M. Rimbach-Russ, F. van Riggelen, N.W. Hendrickx, , S.L. de Snoo, A. Sammak, G. Scappucci, J. Helsen, M. Veldhorst, Nature Communications **14** (1), 3617 (2023) [190].

4.1. INTRODUCTION

Fault-tolerant quantum computers utilizing quantum error correction [165] to solve relevant problems [87] will rely on the integration of millions of qubits. Solid-state implementations of physical qubits have intrinsic advantages and remarkable progress has been made using qubits based on superconducting circuits [99]. While the development of quantum dot qubits has been at a more fundamental stage, their resemblance to the transistors that constitute the building block of virtually all our electronic hardware promises excellent scalability to realize large-scale quantum circuits [98, 167]. Fundamental concepts for quantum information, such as the coherent rotation of individual spins [108] and the coherent coupling of spins residing in neighbouring quantum dots [110], were first implemented in gallium arsenide heterostructures. The low disorder in the quantum well allowed the construction of larger arrays of quantum dots and to realize two-qubit logic using two singlet-triplet qubits [111]. However, spin qubits in group III-V semiconductors suffer from hyperfine interactions with nuclear spins that severely limit their quantum coherence. Group IV materials naturally contain higher concentrations of isotopes with a net-zero nuclear spin and can furthermore be isotopically enriched [160] to contain only these isotopes. In silicon electron spin qubits, quantum coherence can therefore be sustained for a long time [114, 172] and single qubit logic can be implemented with fidelities exceeding 99.9 % [115, 116]. By exploiting the exchange interaction between two spin qubits in adjoining quantum dots or closely separated donor spins, two-qubit logic could be demonstrated [189, 191–196]. Silicon, however, suffers from a large effective mass and valley degeneracy [174], which has hampered progress beyond two-qubit demonstrations.

Holes in germanium are emerging as a promising alternative host material for spin qubits in quantum dots [125]. It combines favourable properties such as a host material with a natural abundance of zero nuclear spin isotopes that can furthermore be enriched for long quantum coherence [159, 181], low effective mass and the absence of low-energy valley states [131] (allowing device design requirements to be relaxed), low charge noise (providing a quiet qubit environment) [129], and low disorder (enabling reproducible and well controlled quantum dots) [122, 130]. In addition, strained germanium quantum wells defined on silicon substrates are compatible with semiconductor manufacturing [176]. Furthermore, hole states in general can exhibit strong spin-orbit coupling that allows for all-electric operation [123, 141, 175, 182] and that removes the need for microscopic components such as microwave striplines [108, 191, 193, 196] or nanomagnets [189, 192, 197, 198], which is particularly beneficial for the fabrication and operation of two-dimensional qubit arrays. The realization of strained germanium quantum wells in undoped heterostructures [124] has led to remarkable progress. In two years, germanium has progressed from the formation of stable quantum dots and quantum dot arrays [122, 130, 164], to demonstrations of single qubit logic [140], long spin lifetimes [155], and the realization of fast two-qubit logic in germanium double quantum dots [141].

4.2. A TWO-BY-TWO SPIN QUBIT DEVICE

Here we advance beyond beyond two-qubit logic in semiconductor quantum dots, executing a four-qubit quantum circuit using a two-dimensional array of quantum dots. We

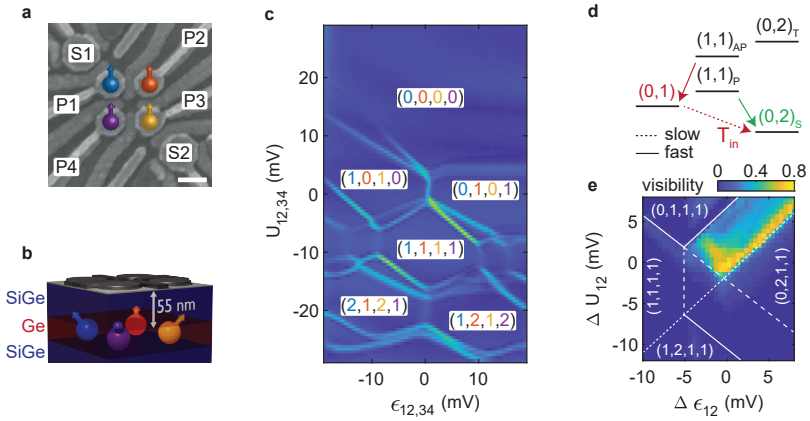

Figure 4.1: **Four germanium hole spin qubits. a**, Scanning electron microscope image of the four quantum dot device. We define qubits underneath the four plunger gates indicated by P1-P4. The qubits can be measured using the two charge sensors S1 and S2. The scale bar corresponds to 100 nm. **b**, Schematic drawing of the Ge/SiGe heterostructure. Starting from a silicon wafer, a germanium quantum well is grown in between two $Si_{0.2}Ge_{0.8}$ layers at a depth of 55 nm from the semiconductor/dielectric interface. **c**, Four quantum dot charge stability diagram as a function of two virtual gates. At the vertical and diagonal bright lines a hole can tunnel between two quantum dots or a quantum dot and its reservoir respectively. As a result of the virtual axes $\epsilon_{12,34}$ and U_{1234} (for the definition see Supplementary Information), the addition lines of the different quantum dots have different slopes, allowing for an easy distinction of the different charge occupations indicated in the white boxes as (N_1, N_2, N_3, N_4), with N_m the hole occupation in the mth quantum dot. **d**, Energy diagram illustrating the latched Pauli spin blockade readout. When pulsing from the (1,1) charge state to the (0,2) charge state, only the polarized (P) triplet states allow the holes to move into the same quantum dot, leaving an $(0,2)_S$ charge state (green). Interdot tunnelling is blocked for the two antiparallel (AP) spin states, since the $(0,2)_T$ state is energetically unavailable. As a result the hole on the first quantum dot will tunnel to the reservoir leaving an (0,1) charge state (red), thus locking the different spin states into different charge states. **e**, Readout visibility as defined by the difference in readout between either applying no rotation and a π-rotation to Q2. The readout point is moved around the (1,1)-(0,2) anticrossing of the Q1Q2 system and a clear readout window can be observed, bounded by the different (extended) reservoir transition lines, as indicated by the dotted lines.

achieve this by defining the four-qubit system on the spin states of holes in gate-defined germanium quantum dots. Fig. 4.1a shows a scanning-electron-microscopy (SEM) image of the germanium quantum processor. The quantum dots are defined in a strained germanium quantum well on a silicon substrate [129] (Fig. 4.1b) using a double layer of electrostatic gates and contacted by aluminium ohmic contacts. A negative potential on plunger gates P1-P4 accumulates a hole quantum dot underneath that hosts qubits Q1-Q4, which can be coupled to neighbouring quantum dots through dedicated barrier gates. In addition, two quantum dots are placed to the side of the two-by-two array, and the total whole system comprises six quantum dots. Via an external tank circuit, we configure these additional two quantum dots as radio-frequency charge sensors for rapid charge detection. Using the combined signal of both charge sensors [164], we measure the four quantum dot stability diagram as shown in Fig. 4.1c. Making use of two virtual gate axes $U_{12,34}$ and $\epsilon_{12,34}$, we arrange the reservoir addition lines of the four quantum dots to have different relative slopes of approximately -1 mV mV^{-1}, $+1$ mV mV^{-1}, -0.75 mV mV^{-1}, 0.75 mV mV^{-1} for Q1, Q2, Q3, and Q4 respectively. Well defined charge regions (indicated by (N_1, N_2, N_3, N_4) in the white boxes, with N_m the number of holes in the mth quantum dot) are observed, with vertical anticrossings marking the different interdot transitions.

For the qubit readout we make use of Pauli-spin blockade to convert the spin states into a charge signal that can be detected by the sensors. In germanium, however, the spin-orbit coupling can significantly lower the spin lifetime during the readout process, in particular when the spin-orbit field is perpendicular to the external magnetic field, reducing the readout fidelity [140, 147]. Here, we overcome this effect by making use of a latched readout process [149, 150]. During the readout process, shown in Fig. 4.1d and e, a hole can tunnel spin-selectively to the reservoir as a result of different tunnel rates of both quantum dots to the reservoir. After this process, the system is locked in this charge state for the (long) reservoir tunnel time T_{in}. The high level of control in germanium allows tuning T_{in} to arbitrarily long time scales by changing the potential applied to the corresponding reservoir barrier gate. We set $T_{\text{in, Q2}} = 200$ μs and $T_{\text{in, Q4}} = 2.4$ ms (see Supplementary Information, Fig. 4.10), both significantly longer than the signal integration time $T_{\text{int}} = 10$ μs. Furthermore, we project all qubit measurements on the Q1Q2 and Q3Q4 readout pairs, such that the spin-orbit field is oriented along the direction of the external magnetic field $B_0 = 1.05$ T to minimize spin relaxation. The latched PSB readout process is described in more detail in the Methods chapter of this thesis.

4.3. CHARACTERISING THE SINGLE QUBITS

Coherent rotations can be implemented by applying electric microwave signals to the plunger gates that define the qubits, exploiting the spin-orbit coupling for fast driving [123, 182]. We initialize the system in the $|\downarrow\downarrow\downarrow\downarrow\rangle$ state by sequentially pulsing both the Q1Q2 and Q3Q4 double quantum dot systems from their respective $(0,2)_{\text{S}}$ states adiabatically into their $(1,1)_{\text{T}-}$ states. We then perform the qubit manipulations, after which we perform the spin readout as described above. We observe qubit resonances at $f_{\text{Q1}} = 2.304$ GHz, $f_{\text{Q2}} = 3.529$ GHz, $f_{\text{Q3}} = 3.520$ GHz, and $f_{\text{Q4}} = 3.882$ GHz, corresponding to effective g-factors of $g_{\text{Q1}} = 0.16$, $g_{\text{Q2}} = 0.24$, $g_{\text{Q3}} = 0.24$, and $g_{\text{Q4}} = 0.26$. We note that these g-factors can be electrically modulated using nearby gates as a means of ensuring

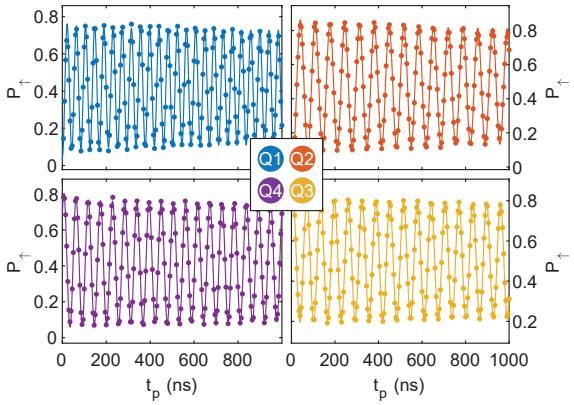

Figure 4.2: **Coherent Rabi rotations.** The qubits can be rotated by applying a microwave tone resonant with the Zeeman splitting of the qubit. Coherent Rabi rotations can be observed as a function of the microwave pulse length t_p for all qubits Q1-Q4. P_{up} indicates the single-shot spin-up probability.

individual qubit addressability [155], as can also be observed in Fig. 4.6. Fig. 4.2 shows the single-shot spin-up probability $P_\uparrow$ for each of the four qubits after applying an on-resonant microwave burst with increasing time duration t_p, resulting in coherent Rabi oscillations.

To quantify the quality of the single qubit gates, we perform benchmarking of the Clifford group [199] (Supplementary Information, Fig. 4.12) and find single qubit gate fidelities exceeding 99 % for all qubits. The fidelity of Q3 reaches to 99.9 %, which is comparable to benchmarks for quantum dot qubits in isotopically purified silicon [115, 116]. We find spin lifetimes between $T_1 = 1 - 16$ ms (Supplementary Information, Fig. 4.13a), comparable to values reported before for holes in planar germanium [155]. Furthermore, we observe T_2^* to be between 150-400 ns for the different qubits (Supplementary Information, Fig. 4.13b), but are able to extend phase coherence up to $T_2^{\mathrm{CPMG}} = 100$ μs by performing Carr-Purcell-Meiboom-Gill (CPMG) refocusing pulses (Supplementary Information, Fig. 4.14b), more than two orders of magnitude larger than previously reported for hole quantum dot qubits [123, 141, 175]. This indicates the qubit phase coherence is mostly limited by low-frequency noise, which is confirmed by the predominantly $1/f^\alpha$ noise spectrum we observe by Ramsey and dynamical decoupling noise spectroscopy (Supplementary Information, Fig. 4.15).

4.4. OPTIMIZING SINGLE QUBIT PERFORMANCE

In this section we take a small detour from the initial four qubit work and look into the characterization of the single qubits and the single qubit gates at two different values for the external magnetic field, $B_{\mathrm{ext}} = 1$ T and $B_{\mathrm{ext}} = 0.65$ T. We do this to provide a comparison between the different regimes of coherence, qubit response, and qubit resonance frequency spacing. Fig. 4.3 shows how the spin dephasing time of the qubits Q1-Q4

($T^*_{2,\mathrm{Q1}} - T^*_{2,\mathrm{Q4}}$) performs at different magnetic fields, via Ramsey decay experiments.

To estimate the quality of each qubit, we perform randomized benchmarking. This technique provides the average fidelity of a gate set applied to each qubit. Operations randomly selected from the Clifford group are applied to each single-qubit initialised in a known state. A final recovery Clifford C^{-1} is applied to bring the qubit back to its original state. Imperfections in the applied gates and gradual qubit decoherence result in a decay of the recovered state probability as the number of applied Clifford operators (N_C) is increased, allowing the extraction of a fidelity by fitting the decay [199]. Each element of the Clifford group can be constructed from a variety of generator gates. We construct a Clifford group from a minimal generator set $\mathrm{G}_i \in \{\mathrm{X}_{\pi/2}, \mathrm{Y}_{\pi/2}\}$ (see Supplementary Information). We find this set advantageous since it contains on average 3.217 qubit $\pi/2$ rotations (generators) per Clifford, that differ only by a software phase shift. This means the estimated Clifford fidelity is a direct indicator of the generator fidelity, by equally weighting the generators of the same length [200]. Working with generators of equal length has the additional advantage of simplifying the experimental implementation of benchmarking qubits simultaneously [201].

Fig. 4.4a,b show the randomized benchmarking sequences for Q1-Q2 and Q3-Q4 respectively. A red (green) measurement window indicates PSB readout on the Q1Q2 (Q3Q4) double quantum dot pair. Each qubit is initialised in the spin down state. For each sequence length N_C, 32 random permutations of N_C Cliffords are averaged to give the final trace, each of which comprises 1500 single shot measurements. An exponential decay is fit to the resulting trace (see Supplementary Information), yielding a circuit level fidelity F_{Q_i}, from which an average generator fidelity $F^{\pi/2}_{Q_i} = 1-(1-F_{Q_i})/(2\times 3.217)$ can be extracted for each qubit. Holes in germanium allow for very fast electrical driving, with Rabi frequencies exceeding hundreds of MHz [202, 203]. However, rapid qubit manipulation is not always optimal for coherent qubit control, with high powers leading to enhanced systematic errors in qubit operation arising from effects such as sample heating or pulse imperfections. Indeed we find a strong dependence of the single-qubit fidelities on the drive speed. Fig. 4.4c-f show the generator infidelities (1-$F^{\pi/2}_{Q_i}$) as a function of qubit drive speed. Despite being able to drive qubit rotations in as fast as 10 ns, we find that the associated single-qubit fidelity suffers as a result, visible by a sharp decrease in the fidelity for qubits Q1 and Q3. Fidelity in these cases could be limited by a number of mechanisms, such as quantum dot anharmonicities [143, 204] or systematic Pauli errors due to gate tuning. We also observe change in the resonance frequency of each qubit as a result of large applied microwave powers, where the single-qubit fidelity is observed to be lower. From the analysis we obtain that there is an optimum in the qubit driving speed (see Supplementary Information, Fig 4.16).

Fig. 4.4g-j show the randomized benchmarking data for the optimal t_π. We extract generator fidelities above 99 % for each qubit in the array, with qubit Q3 performing the best with $F^{\mathrm{Q3}}_{\pi/2}$ = 99.992(1) %, where the error on the last digit is given by the 95 % confidence interval of the fit uncertainty. For single-qubit randomized benchmarking, we expect a fully decohered state to exhibit a blocked state probability of about $P_{\mathrm{Blocked}} \approx 0.5$. However in the presence of finite exchange and classical cross-talk between the active qubit and the readout qubit in the spin blockade pair, state leakage can occur to all four states in the two-qubit subspace, resulting in a readout signal of about P_{Blocked} =

0.329. We find that for the case of qubit Q4, the plateau of the spin blocked probability approaches the expected value of the fully depolarized two-qubit subspace for all driving powers. This is likely due to the high power required to drive Q4 via plunger gate P_2 as a consequence of the larger distance between qubit and drive-gate, resulting in a large degree of cross-talk on qubit Q3. To account for state leakage, a second exponential decay is added for fitting randomized benchmarking traces for qubit Q4, yielding two characteristic decay constants (see Supplementary Information). From this analysis, we calculate a generator fidelity $F_{\mathrm{Q4}}^{\pi/2} = 99.7(2)\%$, containing a leakage rate of $L_{\mathrm{Q4}}^{\pi/2} = 0.07(2)\%$ per generator.

For further optimization of the single qubit gate fidelites, the operation amplitude and angle of the external magnetic field are important factors. In this work, we benchmark single-qubit gate fidelities at in-plane external magnetic fields of 0.65 T and 1 T. Spin dephasing times are higher at 0.65 T, however driving speeds and resonance frequency spacings are lower. We observe that trying to drive faster at lower field results in more frequency crowding due to the additional power required. This leads to larger cross-talk effects and will ultimately limit fidelities when driving all qubits simultaneously, but allows for the highest single-qubit fidelities when driven sparsely owing to the enhanced coherence.

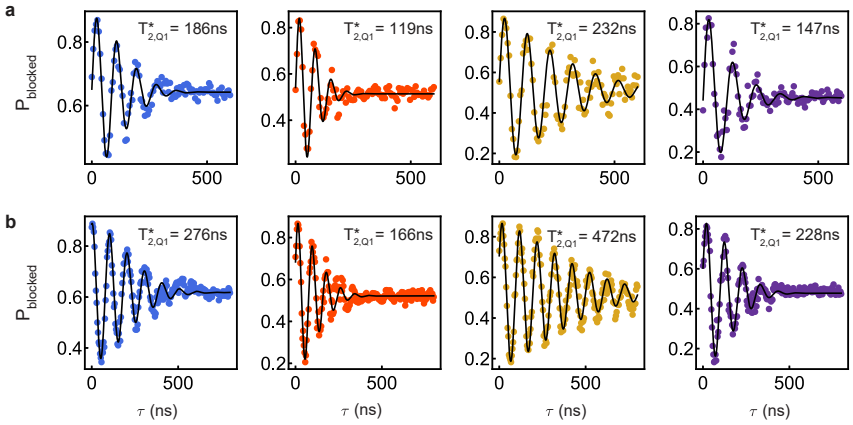

Figure 4.3: **Spin dephasing time at 1 T and 0.65 T. a** Ramsey sequences on qubits Q1-Q4 at magnetic field B_{ext} = 1 Tesla. Extracted spin dephasing times at 1 T for qubits Q1, Q2, Q3 and Q4 are $T_{2,Q1}^{*}$ = 186 ± 19 ns, $T_{2,Q2}^{*}$ = 119 ± 14 ns, $T_{2,Q3}^{*}$ = 323 ± 52 ns and $T_{2,Q4}^{*}$ = 147 ± 26 ns. **b** At 0.65 T the dephasing times increase to $T_{2,Q1}^{*}$ = 276 ± 22 ns, $T_{2,Q2}^{*}$ = 166 ± 14 ns, $T_{2,Q3}^{*}$ = 472 ± 31 ns and $T_{2,Q4}^{*}$ = 228 ± 15 ns.

4.5. CONDITIONAL ROTATIONS

Universal quantum logic can be accomplished by combining the single qubit rotations with a two-qubit entangling gate. We implement a conditional rotation (CROT) gate [189, 192, 193, 196], where the resonance frequency of the target qubit depends on the state

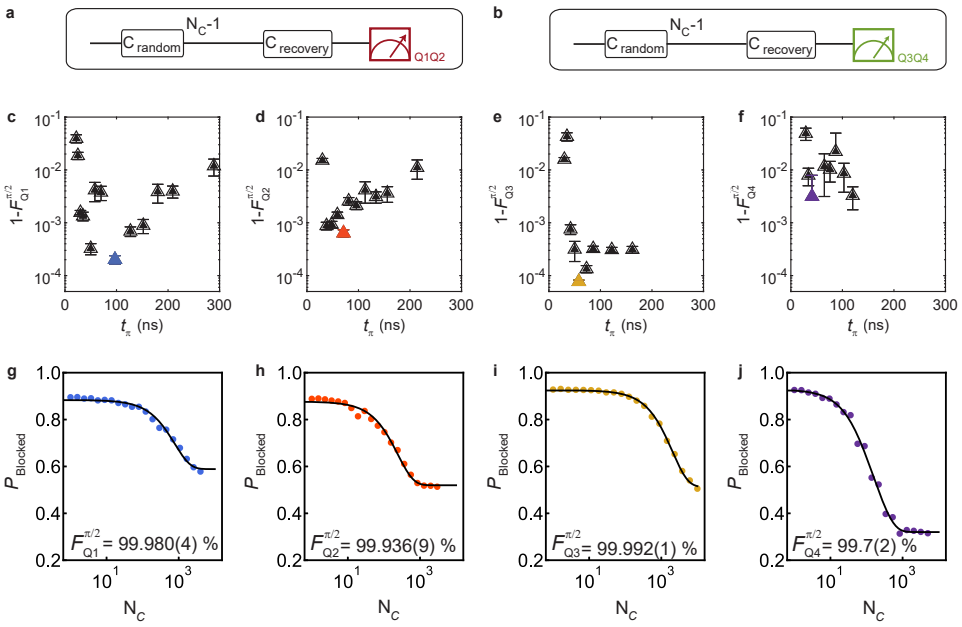

Figure 4.4: **Single-qubit randomised benchmarking at 0.65 Tesla. a,b** Random Clifford sequences applied to each qubit. Each qubit in the array is prepared in the spin down state. N_C-1 randomly selected Cliffords are applied to a single qubit, after which a recovery Clifford (C^{-1}) is applied bringing the system back to the $|\downarrow\downarrow>$ state. Each sequence is repeated 32 times with different random permutations of Cliffords. Readout occurs via PSB on one of the two readout pairs Q1Q2 (**a**, red) or Q3Q4 (**b**, green). **c-f** Dependence of qubit fidelity on t_π. An optimal t_π occurs due to a trade-off between decoherence (high t_π) and errors introduced at low t_π including gate calibration errors and driving non-linearities. Error bars reflect the fit uncertainty. **g-j** Best single-qubit benchmarks for each qubit. All native $\pi/2$ fidelities except $F^{\pi/2}_{\mathrm{Q4}}$ exceed 99.9 %, with $F^{\pi/2}_{\mathrm{Q3}}$ exceeding four nines. These traces correspond to the respective highlighted points in (**c-f**).

of the control qubit, mediated by the exchange interaction J between the two quantum dots. The exchange interaction between the quantum dots is controlled using a virtual barrier gate (details in the Supplementary Information), coupling the two quantum dots while keeping the detuning and on-site energy of the quantum dots constant and close to the charge-symmetry point. We demonstrate CROT gates between all four pairs of quantum dots in Fig. 4.5, proving that spin qubits can be coupled in two dimensions. Because the target qubit's resonance frequency depends on the control qubit state, the CROT is characterized by the fading in and out of the target qubit rotations as a function of the control qubit pulse length. For driving the two separate transitions, the pattern is shifted by a π rotation on the control qubit. When the control qubit is in a different readout pair from that of the target qubit (rows 3 and 4 in Fig. 4.5), we can independently observe the single qubit control and two-qubit target qubit rotations in the two readout systems. By setting the pulse length at $\phi_{\mathrm{Q}} = \pi$, a fast controlled-X (CX) gate can be obtained within approximately $t_{\mathrm{p}} = 100$ ns between all of the four qubit pairs.

The low effective mass and high uniformity in the material allow full control over the

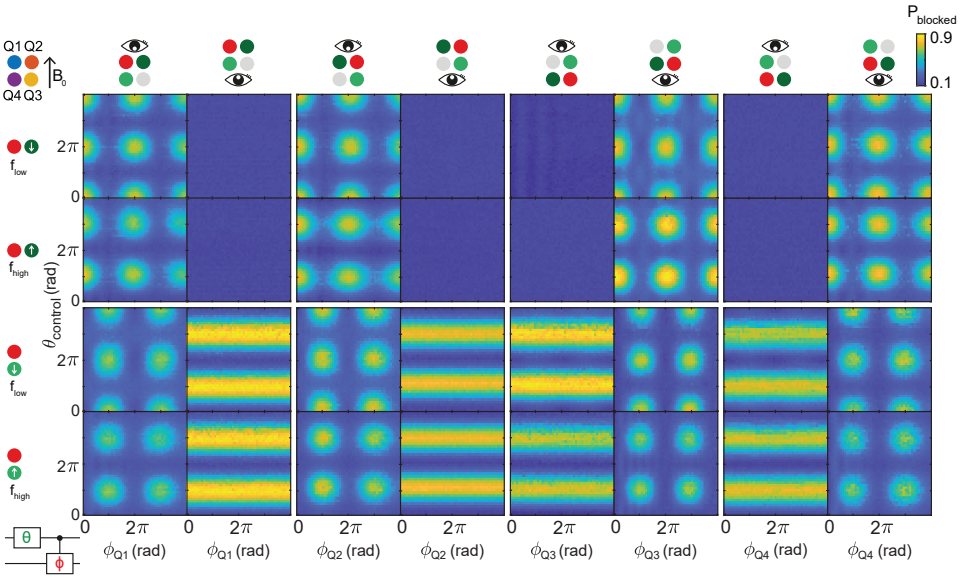

Figure 4.5: **Controlled rotations between all nearest-neighbour qubit pairs.** By selectively enabling the exchange interaction between each pair of qubits, we can implement two-qubit CROTs. The pulse sequence consists of a single preparation gate with length θ on the control qubit (labelled green), followed by a controlled rotation on one of the two resonance lines of the target qubit (labelled in red). Both qubit pairs Q1Q2 and Q3Q4 are read out in single-shot mode, and the position of the eye on top of each column indicates the respective readout pair. Each of the four main columns corresponds to CROTs on a different qubit, as indicated by the red dot. Rows one and two show the results for the horizontal interaction (dark green), while rows three and four show the two-qubit interaction for the vertical direction (light green) with respect to the external magnetic field, as indicated in the top left. Rows one and three correspond to driving the lower frequency f_{low} conditional resonance line, while rows two and four show driving of the other resonance line f_{high}.

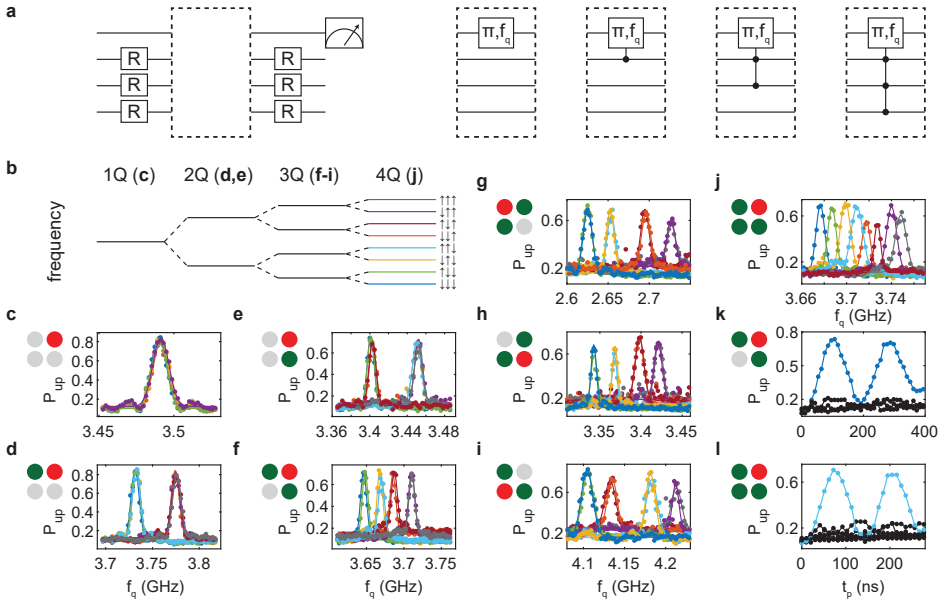

Figure 4.6: **Resonant one, two, three, and four-qubit gates. a**, Circuit diagram of the experiment performed in panels **c-l**. All eight permutations of the three control qubit eigenstates are prepared, with R being either no pulse or a π-pulse on the respective qubit. Next, the resonance frequency of the target qubit is probed using a π-rotation with varying frequency f_q. Finally, the prepared qubits are projected back and the target qubit state is measured. By changing the different interdot couplings J, we can switch between resonant single, two, three, and four-qubit gates as indicated in the dashed boxes. **b**, Turning on the exchange interaction between the different qubit pairs splits the resonance frequency in two, four, and eight for 1, 2 and 3 enabled pairs respectively. The colours of the line segments correspond to the colours in panels **c-l**. **c**, By turning all exchange interactions off, the qubit resonance frequency of Q2 is independent of the prepared state of the other three qubits, resulting in an effective single-qubit rotation. **d-e**, By turning on a single exchange interaction J_{12} (**d**) or J_{23} (**e**), the resonance line splits in two. The additional offset of the resonance frequencies is caused by electric modulation of the hole g-factor. **f-i**, Turning on both exchange interactions to the neighbouring quantum dots results in the resonance line splitting in four, for Q2 (**f**), Q1 (**g**), Q3 (**h**), Q4 (**i**) respectively. **j**, Turning on the exchange interactions between three pairs of quantum dots J_{12}, J_{23}, J_{41} splits the resonance line in eight. **k-l**, Resonant driving of the three-qubit gate (**k**) and the four-qubit gate (**l**) with Q2 being the target qubit, shows Rabi driving as a function of pulse length t_p, demonstrating the coherent evolution of the operation.

interdot coupling, using dedicated tunnel barrier gates. To demonstrate this, we measure the qubit resonance frequency as a function of the eight possible permutations of the different basis states of the other three qubits, as illustrated in Fig. 4.6a,b. Without any exchange present, the resonance frequency of the target qubit should be independent on the preparation of the other three qubits, as schematically depicted in Fig. 4.6c. When the exchange interaction with one of the neighbouring quantum dots is enabled, the resonance line splits in two (Fig. 4.6d,e), allowing for the operation of the CROT gate. When both barriers to the nearest-neighbours are pulsed open at the same time, we observe the expected fourfold splitting of the resonance line (Fig. 4.6f-i). This allows us to performing a resonant i-Toffoli three-qubit gate (Fig. 4.6k and Supplementary Information, Fig. 4.17), which has theoretically been proposed as an efficient manner to create the Toffoli, Deutsch, and Fredkin gates [205]. We observe a difference in the efficiency at which the different conditional rotations can be driven, as can also be seen from the width of the resonance peaks in Fig. 4.6f-i. This is expected to happen when the exchange energy is comparable to the difference in Zeeman splitting and is caused by the mixing of the basis states due to the exchange interaction between the holes [206] (see details in the Supplementary Information). Finally, we open three of the four virtual barriers and observe the resonance line splitting in eight, corresponding to all eight permutations of the control-qubit preparation states (Fig. 4.6j). This enables us to execute a resonant four-qubit gate and in Fig. 4.6l we show the coherent operation of a three-fold conditional rotation (see Supplementary Information, Fig. 4.17 for the coherent operation of the other resonance lines). The good control over the interdot coupling thus enables a demonstration of the localized nature of the exchange interaction [98], coupling the different spins by electric gate pulses.

4.6. CONTROLLED PHASE GATES

While the demonstration of these conditional rotations can be beneficial for the simulation of larger coupled spin systems, the ability to dynamically control the exchange interaction allows for faster two-qubit operations. We efficiently implement controlled phase (CPHASE) gates [191, 192, 196] between the different qubit pairs by adiabatically pulsing the exchange interaction with the respective virtual barrier gate. We control the length and size of the voltage pulse (Fig. 4.7) to acquire a controlled-Z (CZ) gate, in which the antiparallel spin states accumulate a phase of exactly $\theta = \pi$ with respect to the parallel spin states. We demonstrate this in Fig. 4.8a,b, where we employ a Ramsey sequence to measure the conditional phase. After the exchange pulse U_{CZ}, we apply a software Z gate to both the target and control qubits to correct the individual single qubit phases. The virtual barrier pulses enable fast CZ gates between all neighbouring qubit pairs, all executed well within 10 ns (details in Table 4.3).

To prepare our system for quantum algorithms, we implement decoupling pulses into the multi-qubit sequences to extend phase coherence [192], as is demonstrated in Fig. 4.8c,d. We perform a CPHASE gate of length t between qubits Q2 and Q3 (Fig. 4.8d, left, triangles) and compare the decay of the resulting exchange oscillations for the situations with (orange) and without (blue) a Y^2 echo pulse. We observe an increased decay time of $\tau = 220$ ns for the decoupled CPHASE gate, as compared to $\tau = 130$ ns for a standard CPHASE gate. Next, we entangle Q2 and Q3 by forming the $|\Psi^+\rangle$ Bell state and let

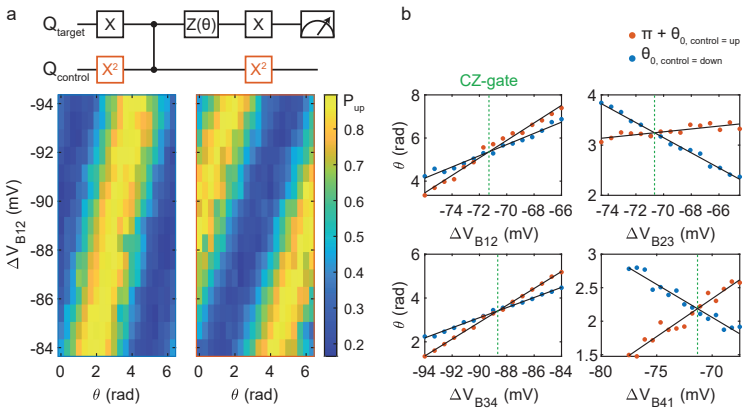

Figure 4.7: **Tuning of the CZ-gates. a,b**, The CZ-gates between all four qubit pairs are tuned using a Ramsey sequence, as shown in Fig. 4.8, where the spin-up probability is measured as a function of the phase θ of the final $\pi/2$ pulse as well as the depth of the exchange pulse $V_{\mathrm{B}mn}$, with m and n the relevant qubits (**a**). We choose to tune the height of the voltage pulse rather than its length, due to the limited temporal resolution of the exchange pulses (1 ns). The acquired phase θ_0 is obtained by fitting each line to $P = A\cos(\theta + \theta_0) + y_0$, with A the visibility and y_0 an offset. A CZ-gate is achieved when the difference in acquired phase is exactly $\Delta\theta = \pi$, for the situation where the control qubit is $|\downarrow\rangle$ (blue) compared to $|\uparrow\rangle$ (orange). The barrier gate voltage at which this occurs is obtained from the intersection of two locally linear fits to the extracted acquired phase (**b**).

the system evolve for time $2t$ (Fig. 4.8d, right, circles). We then disentangle the system and measure the spin-up probability of Q3 as a function of the evolution time. Without the decoupling pulse, we observe a loss of the two-qubit coherence after a characteristic time $\tau = 200$ ns. However, by applying an additional Y^2 pulse to both Q2 and Q3, we can extend this time scale beyond 2 μs, sufficient to perform a series of single and multi-qubit gates, owing to our short operation times.

4.7. A FOUR-QUBIT ENTANGLED STATE

We show this by coherently generating and disentangling a four-qubit Greenberger-Horne-Zeilinger (GHZ) state (see Fig. 4.9). Making use of the fast two-qubit CZ gates, as well as a decoupling pulse on all qubits, we can maintain phase coherence throughout the experiment. We perform parity readout on both the Q1Q2 (red) and Q3Q4 (green) qubit system at different stages of the algorithm (I-IX). Both qubit systems are sequentially readout after each experiment and the observed blocked state fraction is normalized to the readout visibility. We prepare a varying initial state by applying a microwave pulse of length t_{prep} to Q3, as can be seen at point I. After applying CZ gates between all four qubits, the system resides in an entangled GHZ type state at point IV/V, for a $\mathrm{X}(\pi/2)$ preparation pulse on Q3. The effective spin state oscillates between the antiparallel $|1010\rangle$ and $|0101\rangle$ states as a function of t_{prep}, resulting in a high readout signal for all t. The small oscillation that can still be observed for the Q1Q2 system, is caused by a small difference in readout visibility for the two distinct antiparallel spin states. Next,

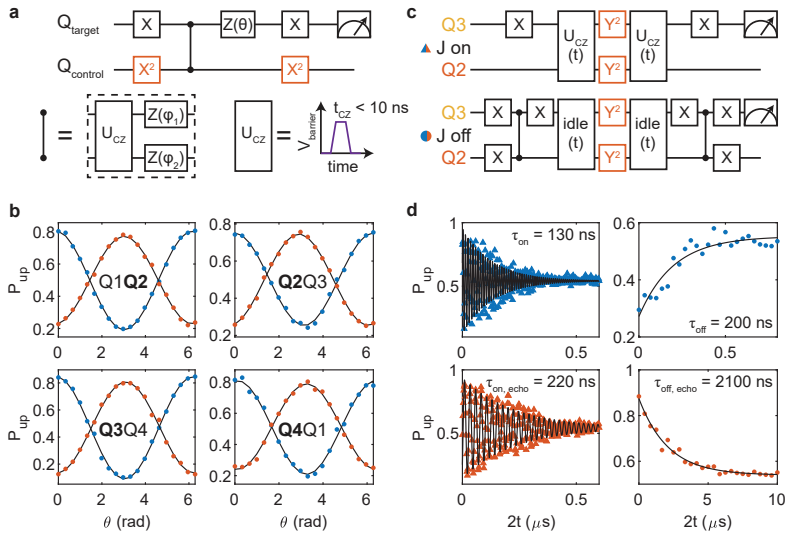

Figure 4.8: **CPHASE gate and dynamical decoupling. a**, Circuit diagram of the experiment performed in panel **b**. The CPHASE gate is probed by performing a Ramsey sequence on the target qubit for both basis states of the control qubit. The phase of the second X($\pi/2$) gate (indicated by X) is swept by performing an update of the microwave phase through quadrature modulation. Additionally, a phase update is performed on both the target and control qubit to compensate for any single qubit phases picked up as a result of the gate pulsing to achieve a CZ gate. **b**, The spin-up probability of the target qubit (in bold) as a function of the phase θ of the second X gate for the control qubit initialized in the $|\downarrow\rangle$ (blue) and $|\uparrow\rangle$ (red) state. Measurements for the inverted target and control qubits in Supplementary data Fig. 4.18c. By applying an exchange pulse and single qubit phase updates, we achieve a CZ gate at $\theta = 0$ rad. **c**, Circuit diagrams of the experiment performed in panel **d**. The phase coherence throughout the two-qubit experiment is probed using a Ramsey sequence, both for the case with J on (top) and off (bottom) and both with (orange) and without (blue) applying an echo pulse. **d**, Spin-up probability as a function of the experiment length, for the situation with exchange on (left, triangles) and off (right, circles). From the decay data we extract characteristic decay times τ of $\tau_{\text{on}} = 130$ ns, $\tau_{\text{on, echo}} = 220$ ns, $\tau_{\text{off}} = 200$ ns, and $\tau_{\text{off, echo}} = 2100$ ns (details in the Supplementary Information).

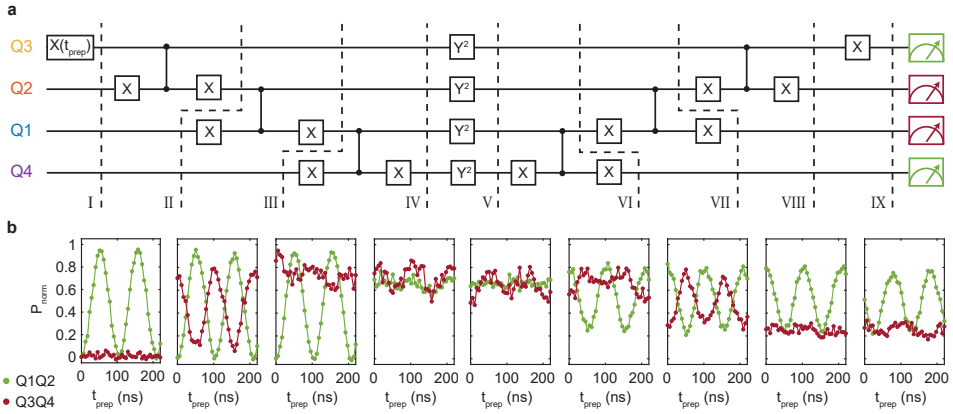

Figure 4.9: **Coherent generation of a four-qubit Greenberger-Horne-Zeilinger (GHZ) state. a-b**, A four-qubit GHZ state is created by applying three sequential two-qubit gates, each consisting of an X-CZ-X gate circuit. Next, a Y^2 decoupling pulse is applied, after which we disentangle the GHZ state again (circuit diagram in **a**). Pulses pictured in the same column are applied simultaneously. The initial state of Q3 is varied by applying a preparation rotation of length $t_t extprep$. For different stages throughout the algorithm (dashed lines), we measure the non-blocked state probability as a function of t for both the Q1Q2 and Q3Q4 readout system, normalized to their respective readout visibility. At the end of the algorithm the qubit states correspond to the initial single qubit rotation, and the clear oscillations confirm the coherent evolution of the algorithm from isolated qubit states to a four-qubit GHZ state. (**b**).

we deploy a Y^2 decoupling pulse to echo out all single qubit phase fluctuations during the experiment (Supplementary Information, Fig. 4.19). After disentangling the system again, we project the Q3 qubit state by applying a final $X(\pi/2)$ gate, and indeed recover the initial Rabi rotation as a demonstration of the coherent evolution of a multi-spin entangled state (see Supplementary Information, Fig. 4.20).

4.8. CONCLUSION

The demonstration of a two-by-two array of four qubits shows that quantum dot qubits can be coupled in two-dimensions and multi-qubit logic can be executed. The hole states used are subject to strong spin-orbit coupling, enabling all-electrical driving of the spin state, beneficial for scaling up to even larger systems. By optimizing the value of the external magnetic field, the duration of the driving pulse and driving power it is possible to reach generator fidelities up until $F_{\pi/2}$ = 99.992(1) %. In future experiments the performance of two-qubit gates can be further optimized, by making use of tailored pulses and quantifying their performance using benchmarking sequences. The ability to freely couple one, two, three and four spins using electric gate pulses has great prospects both for performing high-fidelity quantum gates as well as studying exotic spin systems using analog quantum simulations. Furthermore, we envision that the low-disorder in planar germanium and the potential to leverage advanced semiconductor manufacturing will be beneficial for the realization of scalable qubit tiles [168, 207, 208] for fault-tolerant quantum processors.

4.9. SUPPLEMENTARY INFORMATION

NOTE 1: VIRTUAL GATE MATRICES

In order to map out the transition lines of all four quantum dots in a single measurement, we define the following virtual gates [209] as linear combination of the physical gates P_1-P_4, as well as the sensor plunger gates P_{S1} and P_{S2}. We write:

$$\begin{pmatrix} P_1 \\ P_2 \\ P_3 \\ P_4 \\ P_{S1} \\ P_{S2} \end{pmatrix} = \begin{pmatrix} 1 & 1 \\ -1 & 1 \\ 0.75 & 1 \\ -0.75 & 1 \\ -0.1 & -0.4 \\ -0.05 & -0.51 \end{pmatrix} \begin{pmatrix} \Delta\epsilon_{12,34} \\ \Delta U_{1234} \end{pmatrix}$$

with $\Delta\epsilon_{12,34}$ and ΔU_{1234} the virtual gates used in Fig. 4.1c of the main text.

In addition, we define a virtual gate system to allow independent control of the different interdot couplings and quantum dot detuning and on-site energy and write

$$\begin{pmatrix} P_1 \\ P_2 \\ P_3 \\ P_4 \\ B_{12} \\ B_{34} \\ B_{23} \\ B_{41} \\ P_{S1} \\ P_{S2} \end{pmatrix} = \begin{pmatrix} 1.2600 & 0.7400 & 0.3100 & -0.1700 & -0.5500 & 0 & 0 & -0.4900 \\ -1.3900 & 0.6100 & -0.3600 & -0.3600 & -1.0300 & 0 & -0.6000 & 0 \\ 0.2800 & -0.2800 & 1.3900 & 0.6100 & 0 & -0.4700 & -0.6000 & 0 \\ -0.3000 & -0.3000 & -1.3900 & 0.6100 & 0 & -0.9100 & 0 & -0.9200 \\ 0 & 0 & 0 & 0 & 1.0000 & 0 & 0 & 0 \\ 0 & 0 & 0 & 0 & 0 & 1.0000 & 0 & 0 \\ 0 & 0 & 0 & 0 & 0 & 0 & 1.0000 & 0 \\ 0 & 0 & 0 & 0 & 0 & 0 & 0 & 1.0000 \\ -0.0900 & -0.1500 & 0.0100 & -0.0300 & 0 & 0 & 0 & 0 \\ 0 & 0 & -0.0900 & -0.1500 & 0 & 0 & 0 & 0 \end{pmatrix} \begin{pmatrix} \epsilon_{12} \\ U_{12} \\ \epsilon_{34} \\ U_{34} \\ vB_{12} \\ vB_{34} \\ vB_{23} \\ vB_{41} \end{pmatrix}$$

with ϵ_{mn} the detuning voltage and U_{mn} the voltage controlling the on-site energy of quantum dots m and n, vB_{mn} the virtual barrier gate controlling the coupling between quantum dots m and n, and P_n, B_{mn} and P_{S1-2} the various physical gates.

NOTE 2: LATCHED READOUT MECHANISM

To reduce readout infidelity as a result of spin relaxation, we make use of charge latching through the reservoir [149, 150]. We achieve this effect by pulsing into the area in the (0,2) charge region bounded by the extended (1,1)-(0,1) (fast) and the extended (1,1)-(1,2) (slow) transitions (dotted lines in Fig. 4.1e). When the interdot tunnelling into the (0,2) charge state is blocked, the hole in the first quantum dot will quickly tunnel into the reservoir. This locks the spin state in the metastable (0,1) charge state, with the decay to the (0,2) ground state governed by the slow tunnel rate T_{in} between the second quantum dot and the reservoir.

We operate in a parity readout mode where we observe both antiparallel spin states to be blocked (Extended Data Fig. 4.11a,c), opposite to conventional parity Pauli spin blockade readout [148]. This may be explained by the strong spin-orbit coupling mixing the parallel (1,1) states with the (0,2) state and causing strong relaxation of the upper parallel spin state. We note that both singlet-triplet readout for single state discrimination and parity readout are compatible with the execution of quantum algorithms [148]. However, by both increasing the interdot coupling and elongating the ramp between the manipulation and readout point, we can transition into a state selective readout where only the $|\downarrow\uparrow\rangle$ state results in spin blockade (Extended Data Fig. 4.11b,d), with a

slightly reduced readout visibility. Optimal parity readout is obtained for a ramp time of $t_{\text{ramp}} \approx 20$ ns, while single state readout is optimal at $t_{\text{ramp}} \approx 800$ ns.

Each charge sensor can detect transitions in both qubit pairs, but is most sensitive to their respective nearby quantum dots. We maximize the readout visibility as defined by the difference between the readout of a spin-up and spin-down state by scanning the readout level around the relevant anticrossing. This is illustrated for the Q1Q2 pair in Fig. 4.1e, where a clear readout window with maximum visibility can be observed bounded between the (extended) reservoir transitions of the two quantum dots.

NOTE 3: FITTING DECAY SINGLE QUBIT BANCHMARKING

Standard fitting of randomized benchmarking decays assumes a single exponential decay of the form $P_{\text{Blocked}} = A \times F^{N_c} + c$, where A represents the visibility of the system, F is the circuit level fidelity, N_c is the number of Clifford sequences, and c should be equal to the average signal of the $|\downarrow,\downarrow\rangle$ and $|\uparrow,\downarrow\rangle$ subspace (where the first index corresponds to the qubit being benchmarked). However, for qubit Q4, and for the high power regime of qubits Q1-3, we observe that the blocked signal plateaus to values corresponding to the fully decohered two-qubit subspace, indicating state leakage. In this case, we fit with two exponential decays $P_{\text{Blocked}} = A_1 \times (1-\epsilon)^{N_c} + A_2 \times (1-L)^{N_c} + c$, where c is set to the average signal of the four two-qubit states in the readout pair. Here, ϵ and L correspond to the leakage-free and leakage error rates respectively, from which a circuit level fidelity can be extracted $F = 1-\epsilon-L$ [210]. The estimate for leakage error rate is always taken to be the longer decay rate.

NOTE 4: GENERATION OF THE SINGLE-QUBIT CLIFFORD SET

We quantify the quality of the single-qubit gates on all qubits by performing randomized benchmarking using the Clifford group $\boldsymbol{C}_1 = \{C_n \in U_1 | C_n \boldsymbol{P} C_n^\dagger = \boldsymbol{P}\}$ with the single-qubit Pauli group $\boldsymbol{P} = \{\text{I}, \text{X}, \text{Y}, \text{Z}\}$. All 24 elements of the Clifford group are generated from a minimal set, $C_n = \prod_{g_i \in \mathcal{G}} g_i$ with $\mathcal{G} = \{\text{X}_{\pi/2}, \text{Y}_{\pi/2}\}$. The average number of elementary gates per Clifford is 3.217. All 24 Clifford gates are provided in Table 4.1.

NOTE 5: CONDITIONAL ROTATION GATES

To characterize the CROT gates, we perform a series of qubit pulses, consisting of a single qubit control pulse (green) and a target qubit two-qubit pulse (red), as indicated in the diagram in Fig. 4.5. The length of both the control pulse θ_{control} as well as the target qubit pulse $\phi_{\text{Q1-Q4}}$ are varied, with $t_{\text{p}}(\phi = \pi) = 50 - 110$ ns (details in Table 4.2). The conditional rotations are performed on all four target qubits (four double columns) for both the horizontally interacting qubits (rows 1 and 2), as well as the vertically interacting qubits (rows 3 and 4), by driving the $|\downarrow\downarrow\rangle$-$|\uparrow\downarrow\rangle$ transitions with f_{low} (rows 1 and 3), as well as the inverse $|\downarrow\uparrow\rangle$-$|\uparrow\uparrow\rangle$ transitions with f_{high} (rows 2 and 4), with $|\text{Q}_{\text{target}}\text{Q}_{\text{control}}\rangle$. We then perform a measurement on both readout pairs by sequentially pulsing the Q1Q2 (left sub-columns), and the Q3Q4 qubit pairs (right sub-columns) to their respective readout points. When driving the $|\downarrow\downarrow\rangle$-$|\uparrow\downarrow\rangle$ transition of the qubit pairs used for readout (row 1), we apply an additional single-qubit π-pulse to the preparation qubit to preserve symmetry with the other measurements, as the control qubit also serves as the readout ancillary qubit.

Clifford	Composition
C_1	I
C_2	$Y_{\pi/2}$
C_3	$X_{\pi/2}$
C_4	$Y_{\pi/2}X_{\pi/2}$
C_5	$X_{\pi/2}Y_{\pi/2}$
C_6	$Y_{\pi/2}Y_{\pi/2}$
C_7	$X_{\pi/2}X_{\pi/2}$
C_8	$Y_{\pi/2}X_{\pi/2}X_{\pi/2}$
C_9	$Y_{\pi/2}Y_{\pi/2}X_{\pi/2}$
C_{10}	$Y_{\pi/2}X_{\pi/2}Y_{\pi/2}$
C_{11}	$Y_{\pi/2}Y_{\pi/2}Y_{\pi/2}$
C_{12}	$X_{\pi/2}X_{\pi/2}X_{\pi/2}$
C_{13}	$X_{\pi/2}X_{\pi/2}Y_{\pi/2}$
C_{14}	$X_{\pi/2}Y_{\pi/2}Y_{\pi/2}$
C_{15}	$Y_{\pi/2}X_{\pi/2}Y_{\pi/2}Y_{\pi/2}$
C_{16}	$Y_{\pi/2}Y_{\pi/2}X_{\pi/2}Y_{\pi/2}$
C_{17}	$X_{\pi/2}X_{\pi/2}X_{\pi/2}Y_{\pi/2}$
C_{18}	$Y_{\pi/2}X_{\pi/2}X_{\pi/2}X_{\pi/2}$
C_{19}	$Y_{\pi/2}Y_{\pi/2}X_{\pi/2}X_{\pi/2}$
C_{20}	$X_{\pi/2}Y_{\pi/2}Y_{\pi/2}Y_{\pi/2}$
C_{21}	$Y_{\pi/2}Y_{\pi/2}Y_{\pi/2}X_{\pi/2}$
C_{22}	$Y_{\pi/2}Y_{\pi/2}Y_{\pi/2}X_{\pi/2}Y_{\pi/2}$
C_{23}	$Y_{\pi/2}X_{\pi/2}X_{\pi/2}X_{\pi/2}Y_{\pi/2}$
C_{24}	$Y_{\pi/2}X_{\pi/2}Y_{\pi/2}Y_{\pi/2}Y_{\pi/2}$

Table 4.1: **Single-qubit Clifford sequences and their composition via the minimal generator set.** We benchmark by selecting a random sequence of Cliffords from the table below excluding C_1, and calculate the recovery Clifford that projects the system back into its original state. We only use a gate set containing $\pi/2$ rotations around the Bloch Sphere, so the gates $X_{\pi/2}$ and $Y_{\pi/2}$ are explicitly referring to a rotation of $\pi/2$ around the x-axis and y-axis of the Bloch sphere of a single-qubit respectively. A $Y_{\pi/2}$ rotation is just an $X_{\pi/2}$ rotation with a $\pi/2$ software phase correction. There are on average 3.217 generators per Clifford composition. The extracted fidelity then corresponds exactly to the $\pi/2$ rotation fidelity.

The controlled phase gate is achieved by applying a voltage pulse to the virtual barrier gate. This pulse consists of a ramp up, a plateau, and a ramp back to ensure adiabaticity. The ramp and gate durations of the different controlled phase gates are indicated in Table 4.3).

NOTE 6: SHIFT IN RABI FREQUENCY DUE TO EXCHANGE

When exchange interaction is present in the quantum dot system, the energy levels of the qubit are modified and the qubit basis states hybridize. Conditional driving of the spin states is a direct consequence of the shift of the energy levels, which allows for controlled multi-qubit gates as previously employed to drive two-qubit gates [189, 191, 192,

211]. The hybridization of the qubit states on the other hand gives rise to conditional Rabi frequencies that also depend on the strength of the exchange interaction [211]. Furthermore, the exchange interaction can become anisotropic in the presence of spin-orbit coupling [206]. When only considering the exchange interaction between neighbouring quantum dots, a general Hamiltonian can be written for the four quantum dots in the (1,1,1,1) charge regime as:

$$H = \sum_{\langle i,j \rangle} \boldsymbol{S}_i \cdot \overline{\mathscr{J}}_{ij} \boldsymbol{S}_i + \sum_{i=1}^{4} \left(\mathscr{B} + \mathscr{B}_{\mathrm{ac}} \cos(2\pi f t + \phi) \right) \cdot \boldsymbol{S}_i, \tag{4.1}$$

where the first sum runs along every neighbouring quantum dot pair $\langle i, j \rangle$ with the corresponding tensorial exchange interaction $\overline{\mathscr{J}}_{ij}$. We note that the term $\mathscr{B}$ consists of both the Zeeman effect due to the external magnetic field, and the contribution due to the spin-orbit interaction. We also explicitly separate the static Zeeman interaction from the field induced by the electric driving.

We take $\mathscr{D}$ to be the unitary matrix which diagonalizes Hamiltonian (4.1) for $\mathscr{B}_{ac} = 0$, e.g., $\mathscr{D}^\dagger H(\mathscr{B}_{\mathrm{ac}} = 0)\mathscr{D} = \mathbf{1}$. Now, the effective Rabi amplitude between the eigenstates of the undriven Hamiltonian $|\xi\rangle$ and $|\zeta\rangle$ in the adiabatic limit of exchange is given by:

$$\Omega_{|\xi\rangle \to |\zeta\rangle} = \frac{1}{4} \langle \xi | \mathscr{D}^\dagger \mathscr{B}_{\mathrm{ac}} \mathscr{D} | \zeta \rangle, \tag{4.2}$$

where the prefactor 1/4 is coming from the spin and the rotating wave approximation. Therefore, the Rabi amplitude depends on the exact form of the exchange interaction, as well as which transition is driven.

NOTE 7: FITTING OF THE TWO-QUBIT DECAY DATA

In order to extract the decay time scale in Fig. 4.8d of the main text, we fit the exchange interaction data to the model function $P = A\cos(2\pi(f_0 + t\delta)\,t + \phi_0)\exp(-t/\tau) + y_0$, with amplitude A, frequency f_0, phase offset ϕ_0, and offset y_0. We note that we allow for a small linear shift of the precession frequency δ, typically of size $\delta = 10$ MHz/μs, as a result of pulse imperfections in these relatively large and extended exchange pulses. We observe a small creep towards the final pulse amplitude to be present, most likely caused by the skin effect in the coaxial lines, explaining the small observed frequency shift throughout the experiment. The data for the situation with no exchange present is fitted to the exponential decay $P = \exp(-t/\tau) + y_0$, from which we deduce the decay time scale τ.

NOTE 8: SPECIFICATION OF THE CROT AND CZ GATE TIMES

The different two-qubit gate times are listed below both for the CROT (Table 1) as well as the CZ (Table 2) gates.

target	transition	control	$t_{\pi,\text{control}}$ (ns)	$t_{\pi,\text{target}}$ (ns)
1	$\|\downarrow\downarrow\rangle$-$\|\downarrow\uparrow\rangle$	2	67	85
1	$\|\downarrow\uparrow\rangle$-$\|\uparrow\uparrow\rangle$	2	67	95
1	$\|\downarrow\downarrow\rangle$-$\|\downarrow\uparrow\rangle$	4	61	104
1	$\|\downarrow\uparrow\rangle$-$\|\uparrow\uparrow\rangle$	4	61	108
2	$\|\downarrow\downarrow\rangle$-$\|\downarrow\uparrow\rangle$	1	45	105
2	$\|\downarrow\uparrow\rangle$-$\|\uparrow\uparrow\rangle$	1	41	105
2	$\|\downarrow\downarrow\rangle$-$\|\downarrow\uparrow\rangle$	3	38	113
2	$\|\downarrow\uparrow\rangle$-$\|\uparrow\uparrow\rangle$	3	38	100
3	$\|\downarrow\downarrow\rangle$-$\|\downarrow\uparrow\rangle$	2	65	53
3	$\|\downarrow\uparrow\rangle$-$\|\uparrow\uparrow\rangle$	2	65	83
3	$\|\downarrow\downarrow\rangle$-$\|\downarrow\uparrow\rangle$	4	49	83
3	$\|\downarrow\uparrow\rangle$-$\|\uparrow\uparrow\rangle$	4	45	68
4	$\|\downarrow\downarrow\rangle$-$\|\downarrow\uparrow\rangle$	1	45	105
4	$\|\downarrow\uparrow\rangle$-$\|\uparrow\uparrow\rangle$	1	45	120
4	$\|\downarrow\downarrow\rangle$-$\|\downarrow\uparrow\rangle$	2	38	68
4	$\|\downarrow\uparrow\rangle$-$\|\uparrow\uparrow\rangle$	2	38	74

Table 4.2: CROT driving times used in Fig. 4.5 of the main text.

two-qubit system	t_{ramp} (ns)	t_{gate} (ns)
Q1Q2	3	6
Q2Q3	10	4
Q3Q4	10	5
Q4Q1	3	6

Table 4.3: CZ gate details.

SUPPLEMENTARY FIGURES

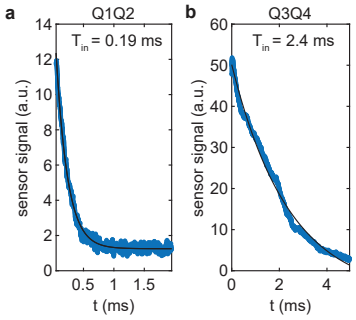

Figure 4.10: **Decay of the readout signal.** We measure the difference in charge sensor signal between the blocked and non-blocked states as a function of the measurement time at the readout point. An exponential decay can be observed related to the tunnel time T_{in} of Q2 (Q4) to the reservoir for the Q1Q2 (**a**) and Q3Q4 (**b**) readout system respectively.

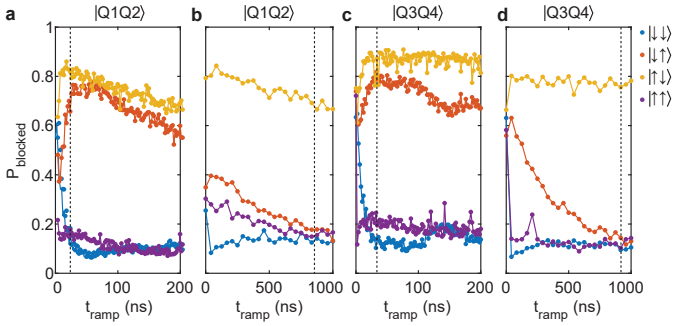

Figure 4.11: **Readout visibility of blocked and non-blocked states. a-d**, We vary the ramp time between the manipulation phase and the readout phase and measure the blocked state probability of the four different two qubit basis states by applying preparation π pulses to the relevant qubits, both for the Q1Q2 readout system (**a**,**b**) and the Q3Q4 readout system (**c**,**d**). By increasing the interdot coupling during the readout and elongating the ramp between the manipulation and readout point, we can switch between a parity readout (**a**,**c**) and a single state readout (**b**,**d**). The dashed line corresponds to the optimized readout ramp time used for the measurements in this work.

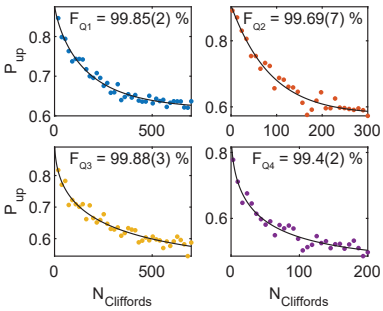

Figure 4.12: **Randomized benchmarking of the Clifford group of the different qubits at $B_{\mathbf{ext}}$ = 1.05T.** We quantify the quality of the single qubit gates by performing randomized benchmarking of the single-qubit Clifford group [199]. The decay curve of the qubit state is measured as a function of the number of Clifford gates applied. Each data point consists of 1000 single shots for 30 different randomly selected Clifford sequences of length $N_{\text{Cliffords}}$. The decay is fitted to $P_{\text{up}} = a\exp(-(N_{\text{Cliffords}}/m)) + y_0$, with a the initial spin-up probability, m the decay parameter, and y_0 an offset. $F = 1 - \frac{m}{2\cdot 1.875}$ is extracted based on the average single qubit gate length of 1/1.875 Clifford gates. Error margins correspond to 1σ.

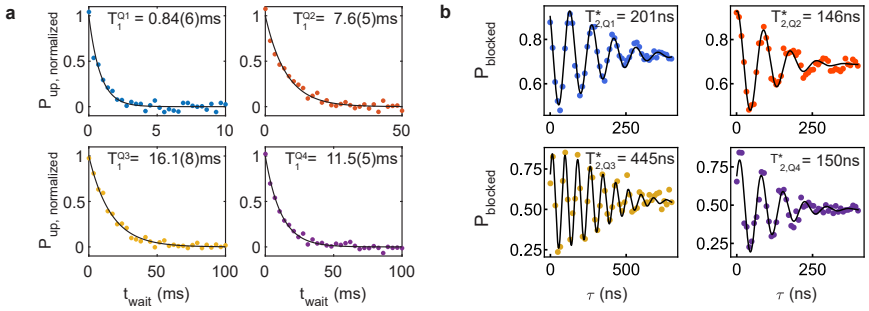

Figure 4.13: **Phase coherence times and spin relaxation times of the different qubits at $B_{\mathbf{ext}}$ = 1.05T. a** The spin relaxation time T_1 is measured at the manipulation point by applying a π_X-pulse separated by a waiting time t_{wait} from the readout phase. By fitting the normalized spin-up fraction to $P = \exp(-t_{\text{wait}}/T_1)$, we find spin relaxation times of $T_1^{\text{Q1}} = 0.84(6)$ ms, $T_1^{\text{Q2}} = 7.6(5)$ ms, $T_1^{\text{Q3}} = 16.1(8)$ ms, and $T_1^{\text{Q4}} = 11.5(5)$ ms. Error margins (in parentheses) correspond to 1σ. **b** The phase coherence time T_2^* is measured using a Ramsey sequence consisting of two X(π/2)-pulses separated by a waiting time τ. By fitting the data to $P = \cos(2\pi\Delta f\tau + \phi_0)\exp(-(\tau/T_2^*)^\alpha)$, with Δf the frequency detuning, ϕ_0 a phase offset and α the power of the decay, we find spin dephasing times of $T^*_{2,\text{Q1}} = 201$ ns, $T^*_{2,\text{Q2}} = 146$ ns, $T^*_{2,\text{Q3}} = 445$ ns, and $T^*_{2,\text{Q4}} = 150$ ns for Q1 to Q4, respectively.

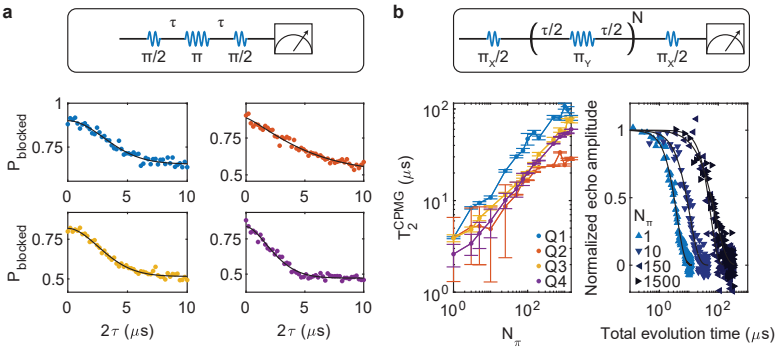

Figure 4.14: **Hahn echo and Carr-Purcell-Meiboom-Gill (CPMG) measurements on the different qubits. a**, Using a Ramsey sequence with an additional X(π)-pulse, low-frequency fluctuations of the qubit resonance frequency can be echoed out, allowing to probe the Hahn-echo decay time T_2^{Hahn}. Fitting the data to $P = \exp(-(\tau/T_2^{\text{Hahn}})^{\alpha})$, we find Hahn echo times of $T_{2,\text{Q1}}^{\text{Hahn}} = 4.3\mu$s, $T_{2,\text{Q2}}^{\text{Hahn}} = 5.5\mu$s, $T_{2,\text{Q3}}^{\text{Hahn}} = 3.8\mu$s, and $T_{2,\text{Q4}}^{\text{Hahn}} = 2.9\mu$s. **b**, Using a CPMG sequence of repeated Y(π) pulses, we can increase the echo bandwidth and extend the phase coherence to over $T_{2,\text{Q1}}^{\text{CPMG}} > 100\ \mu$s. The phase coherence can be observed to increase with the amount of refocusing pulses N_π (left), with exemplary decay traces for Q1 plotted in the right panel.

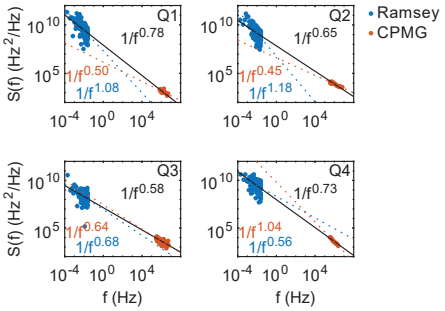

Figure 4.15: **Noise spectroscopy using Ramsey and CPMG measurements.** We measure the effective noise spectrum acting on the qubit, both tracing the resonance frequency using repeated Ramsey measurements [115] (in blue), as well as by using the filter function of a dynamical decoupling measurement [172, 212] (in red). Dashed blue and red lines are fits to the Ramsey and CPMG data respectively. The black line is a fit to the combined data set, where the weight of both sets is normalized for the amount of data points. The effective noise can be observed to increase towards low frequencies, consistent with the upwards trend of T_2^{CPMG} observed in Supplementary Information Fig. 4.14b. The effective charge noise measured in this heterostructure is $S_{\text{cn}}(f) = 6\ \mu\text{V}/\sqrt{\text{Hz}}$ at 1 Hz [129]. Combining this with a typical resonance frequency slope of $df/dV = 5$ MHz/mV [155], results in an effective resonance frequency noise power of $S(f) = 9 \cdot 10^8$ Hz^2/Hz, comparable to what is observed experimentally, suggesting coherence is limited by charge noise in our system. The effect of charge noise could be mitigated by careful optimization of the electric field environment [154] or moving to a multi-hole charge occupancy, screening the influence of charge impurities [213], potentially enabling even higher fidelity operations. Alternatively, noise could originate in the nuclear spin bath present in natural germanium, which could be overcome by isotopically enriching the material.

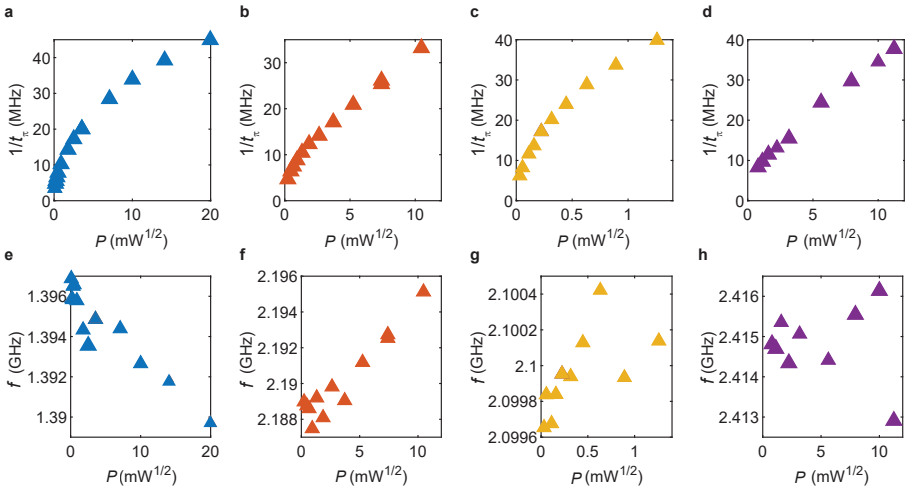

Figure 4.16: **Power dependence of resonance frequency shifts and $1/t_\pi$ for single qubit tuning.** Data in this figure are from Fig.4.4. Extracted frequencies $1/t_\pi$ at which an X_π rotation on qubits Q1-Q4 is performed, respectively. (e-h) Resonance frequency dependence on driving power. The deviation in resonance frequency is likely due to an average change in position of the quantum dot due to the electric field modulation during driving, which in combination with a strong Rashba spin orbit interaction, can alter the frequency eigenstates of the qubits.

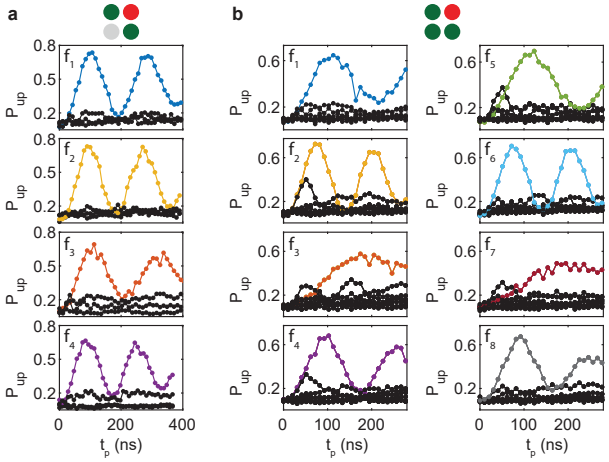

Figure 4.17: **Driving of all resonance lines of the coupled three- and four-qubit system. a**, Both the coupling between Q2 and Q1 as well as Q2 and Q3 are enabled, using the respective virtual barrier gates. This splits the resonance line in four, as shown in Fig. 4.6 of the main text. Driving each of the separate lines, results in the conditional rotation of Q2 depending on the states of Q1 and Q3. We measure the spin up probability P_{up} after driving each of the four resonance lines for time t_{p}, for all four permutations of the Q1 and Q3 basis states as initial state, following the colour scheme of Fig. 4.6. The driving power is adjusted for each of the transitions to synchronize the π-rotation times, with a_{f_1} = 330 mV, a_{f_2} = 500 mV, a_{f_3} = 280 mV, and a_{f_4} = 400 mV, for $f_1 - f_4$ from low to high. **b**, Similarly, by additionally opening up the coupling between Q3 and Q4 as well, the resonance line splits in four and we can drive all separate lines individually. The eight lines are driven using the same microwave power in this figure and a strong difference in rotation frequencies can be observed for the different transitions $f_1 - f_8$ from low to high. This also results in a small off-resonant driving effect for some of the lines.

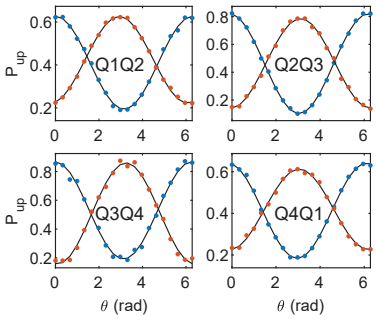

Figure 4.18: **CZ-gates: inverse target and control qubits.** The CZ-gates between all four qubit pairs probed by a Ramsey sequence using the inverse qubits as target and control as compared to the data in Fig. 4.8b. The target qubit is marked in boldface.

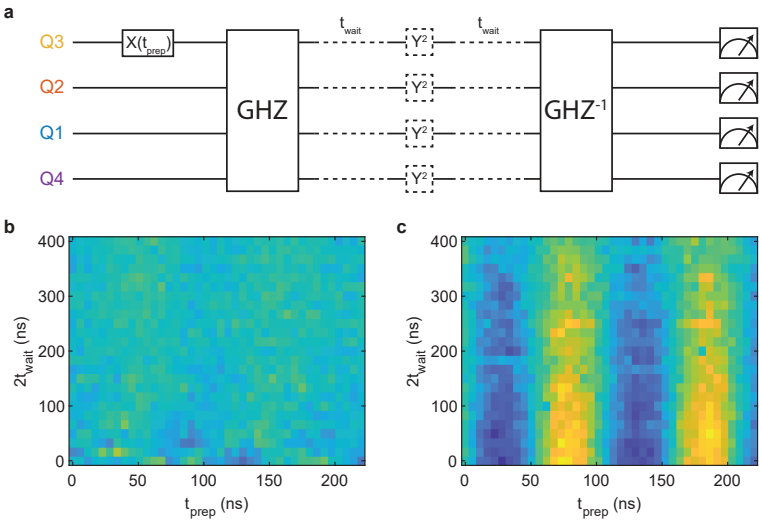

Figure 4.19: **Time evolution of the four-qubit GHZ state. a**, Circuit diagram of the experiments performed in panels **b,c**. We first apply a preparation pulse to Q3 and then generate a four qubit GHZ-state analogous to Fig. 4.9. Next we let the entangled system evolve for time t_{wait}, then apply an optional Y^2 decoupling pulse and finally disentangle the GHZ-state again. **b,c**, We vary both the waiting time and preparation time t_{prep} and plot the spin-up fraction of Q3 in the case without (**b**) and with (**c**) decoupling pulse. It can be clearly observed that without the echo pulse, the system has fully decohered at the end of the algorithm. However, by applying the decoupling pulse, the coherence of the entangled system can be maintained for a prolonged time scale, with a characteristic decay time of $\tau = 390$ ns.

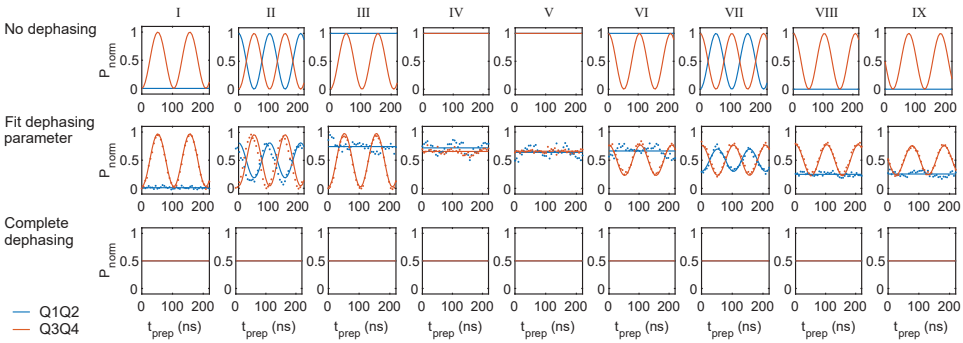

Figure 4.20: **Dephasing of the four-qubit GHZ state.** We model the quantum circuit performed in Fig. 4.9 and account for qubit decoherence by applying a depolarizing channel $\Lambda_\lambda(\rho) = \lambda\rho + [(1-\lambda/d)]\mathbb{1}$, with ρ the density matrix, λ the depolarization parameter, d the dimension of the Hilbert space and $\mathbb{1}$ the identity operator. We plot the expected measurement outcomes for qubit pairs Q1Q2 (blue) and Q3Q4 (orange). The top row corresponds to the case of perfect coherence in each panel. In the centre row, we fit the depolarization parameter to the measurement data. The finite rotations visible in panels IV and V in Fig. 4.9 can be reproduced by including gate or readout errors in the model. Finally, the bottom row corresponds to a full depolarization of the state. If the qubit system is completely dephased at any point in time, no recovery of the signal can be observed in panel IX.

5

PHASE FLIP CODE WITH SEMICONDUCTOR SPIN QUBITS

The fault-tolerant operation of logical qubits is an important requirement for realizing a universal quantum computer. Spin qubits based on quantum dots have great potential to be scaled to large numbers because of their compatibility with standard semiconductor manufacturing. Here, we show that a quantum error correction code can be implemented using a four-qubit array in germanium. We demonstrate a resonant SWAP *gate and by combining controlled-Z and controlled-S^{-1} gates we construct a Toffoli-like three-qubit gate. We execute a two-qubit phase flip code and find that we can preserve the state of the data qubit by applying a refocusing pulse to the ancilla qubit. In addition, we implement a phase flip code on three qubits, making use of a Toffoli-like gate for the final correction step. Both the quality and quantity of the qubits will require significant improvement to achieve fault-tolerance. However, the capability to implement quantum error correction codes enables co-design development of quantum hardware and software, where codes tailored to the properties of spin qubits and advances in fabrication and operation can now come together to advance semiconductor quantum technology.*

This chapter has been adapted from F. van Riggelen, W.I.L. Lawrie, M. Russ, N.W. Hendrickx, A. Sammak, M. Rispler, B.M. Terhal, G. Scappucci, M. Veldhorst, npj Quantum Information **8** (1), 124 (2022) [214].

5.1. INTRODUCTION

A universal quantum computer may be able to address a range of challenges [87–89], but will require many logical qubits for fault-tolerant operation [215]. While errors on individual qubits are unavoidable, logical qubits can be encoded in multiple physical qubits, facilitating error correction codes that preserve the quantum state [165]. There are several ways to encode logical qubits that allow for the correction of different errors using a variety of error-correction strategies. The simplest error correction codes, the bit flip code and the phase flip code [216–220], correct for the fundamental type of error after which they are named. One of the most promising error correction codes is the surface code [221], which can correct any error affecting a sufficiently low number of qubits. Using an error correction code, however, can only help to achieve low logical error rates when all error rates on the physical qubits (of initialization, control and readout) are below a threshold, dependent on the protocol.

The relevance of quantum error correction has spurred significant research in a multitude of platforms and exciting progress has been made in superconducting qubits [222–225], solid-state qubits using NV centers in diamond [226–228], and trapped-ion qubits [229, 230]. Semiconductor qubits based on spins in quantum dots have not yet advanced to match the larger qubit counts of competing technologies [231], but important progress has been made in achieving high-fidelity operations. Fast and high-fidelity readout [149, 232], single-qubit control [115, 116, 126, 190], two-qubit logic [117–119], and resonant three-qubit and four-qubit gates [126] have been demonstrated in separate experiments.

Quantum wells in planar germanium heterostructures (Ge/SiGe) can bring together advantages of several semiconductor quantum dots platforms [125]. Like silicon, natural germanium contains nuclear-spin-free isotopes and can be isotopically purified [159, 160]. Holes in Ge/SiGe have a low effective mass [131], relaxing the fabrication requirements of nanostructures. Moreover, the strong spin-orbit interaction allows for fast and all-electric qubit operation [123, 141, 175, 182]. The spin-orbit interaction also creates a channel through which charge noise can couple to the spin states, currently limiting the coherence time. A dephasing time $T_2^* = 800$ ns has been reported for single spin qubits [141] and $T_2^* = 1$ µs for singlet-triplet qubits operated at low magnetic fields [233]. Using dynamical decoupling sequences, coherence times could be extended up to $T_2 = 100$ µs [126]. On the other hand, hole spin qubits in Ge/SiGe do not suffer from valley degeneracy [131], which still presents a major challenge for electrons in silicon [174, 234]. Furthermore, advancements in heterostructure growth have yielded low disorder and charge noise [129]. These characteristics have facilitated the development of planar germanium quantum dots [122] and quantum dot arrays [130], spin relaxation times up to 32 ms [155], single-hole qubits [140], singlet-triplet qubits [233], two-qubit logic [141], and universal operation of a four-qubit germanium quantum processor [126]. The spin-orbit coupling in germanium avoids the need to implement components such as striplines and nanomagnets, promising scalability in two dimensions [126, 164], crucial for the implementation of error correction codes [165].

Here, we perform quantum error correction on a two-by-two array of spin qubits in germanium. Similar to other spin qubit platforms, hole spin qubits have long relaxation times [155], such that the dominant type of decoherence is dephasing. We therefore focus on the implementation of a rudimentary phase flip code. In order to realize this, we implement a controlled-Z (CZ) gate, a controlled-S^{-1} (CS^{-1}) gate and a native resonance SWAP gate [152]. Using the CZ and CS^{-1} gates, together with single qubit gates, we construct a Toffoli-like gate. Additionally, we show that we can coherently transfer phase information between the data and ancilla qubits and implement the majority vote for error correction of the phase flip code on three qubits.

5.2. PHASE FLIP CODE

The error correction code considered here is a three-qubit phase flip code [161], the steps of which are depicted in Figure 5.1a. At the start of the experiment, the data qubit could in principle hold any quantum state $|\Psi\rangle = \alpha|0\rangle + \beta|1\rangle$ and both ancilla qubits start in the basis state $|0\rangle$. In the encoding step, the state of the data qubit is mapped to the ancilla qubits and the system is brought into the state $\alpha|+++\rangle + \beta|---\rangle$. After the encoding, we intentionally induce errors either by deterministically implementing a rotation around the Z axis of the Bloch sphere with angle φ ($Z(\varphi)$), a full phase flip $Z(\varphi = \pi)$ with a probability p, or by leaving the qubits idle for some time. In the decoding step, we disentangle the logical qubit, where all single phase errors lead to a unique error syndrome. In the final step of the code, a phase error is corrected. The ancillas are not measured, but the data qubit is corrected using a three-qubit gate depending on the error syndrome of the ancilla qubits [235]. This correction protocol is capable of correcting any phase error $Z(\varphi)$ on a single qubit, but it cannot correct phase errors that occur on different physical qubits simultaneously, nor can it handle errors in the encoding, decoding and correction steps.

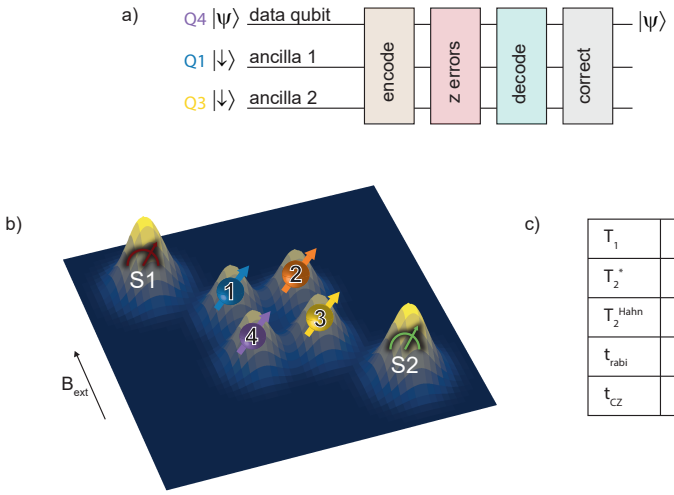

Figure 5.1: **Error correction circuit diagram and properties of the four spin qubit register.** (a) Quantum error correction circuit using one data qubit and two ancilla qubits. Qubits are encoded to a logical state (beige) in which they are resilient against single-qubit phase errors (soft red), since these errors result in distinct states of the ancilla qubits which, after the decoding (turquoise), can be used to correct the data qubit (grey). (b) Schematic drawing giving an impression of the electrostatic potential of the quantum device. Using electrostatic potentials on metallic gates, four quantum dots are defined, each containing a single hole spin qubit. The qubits are indicated with a color: qubit 1 (Q1) in blue, qubit 2 (Q2) in orange, qubit 3 (Q3) in yellow and qubit 4 (Q4) in purple. The spin states are read out by spin-to-charge-conversion using latched Pauli blockade using the two charge sensors, S1 and S2, indicated in red and green respectively. (c) Table showing the relevant time scales of the four qubits used in this work. The spin relaxation time is measured on the same device but at a higher magnetic field [126].

5.3. PROPERTIES OF THE FOUR QUBIT REGISTER

The implementation of the phase flip code strongly depends on the design and properties of the quantum device. The quantum dots are defined in a strained germanium quantum well, using two layers of metallic gates and low resistance Ohmic contacts are made by diffusing aluminium contacts directly into the quantum well [126, 130]. Figure 5.1b gives an impression of the potential landscape which is formed by applying negative voltages on four plunger gates, forming quantum dots underneath. Each quantum dot is occupied by a single hole spin. The coupling between the quantum dots is controlled by dedicated barrier gates. We construct virtual barrier and plunger gates at the software level, to independently control the detuning, on-site energy, and exchange [126]. Two additional quantum dots (S1 and S2) act as charge sensors and are operated using radio frequency reflectometry for rapid readout [126]. Spin state readout is achieved using spin-to-charge-conversion in the form of latched Pauli spin blockade (PSB) [126, 236] (see Supplementary Information, Note 1). We can read out the spin state of Q1 and Q2 using S1 (readout system Q1Q2, red) and the spin state of Q3 and Q4 using S2 (readout system Q3Q4, green).

An external magnetic field of 0.65 T is applied in plane of the quantum well, resulting in energy splittings of 1.393 GHz, 2.192 GHz, 2.101 GHz and 2.412 GHz for Q1, Q2, Q3 and Q4 respectively, between the spin down $|\downarrow\rangle$ (which we define to be $|0\rangle$) and spin up ($|1\rangle$). Here, we use the convention of an X (Y) gate as a $\pi/2$ rotation, X^2 (Y^2) as a π rotation and X^{-1} (Y^{-1}) as a $-\pi/2$ rotation around the $\hat{x}$ ($\hat{y}$) axis of the Bloch sphere [192]. Single qubit rotations are implemented by electric dipole spin resonance.

The choice of two-qubit gate is also dictated by the properties of the device. Fast controlled-Z (CZ) gates [191] are possible by controlling the exchange interaction using the barrier gates [126]. The CZ gate is calibrated using a Ramsey experiment [192], where we use a Tukey shaped pulse to turn exchange on and off. Details of this experiment can be found in the Supplementary Information, Note 2. We use CZ gates between Q1 and Q4 and between Q3 and Q4 for the entangling and disentangling in the phase flip code.

5.4. TWO-QUBIT PHASE FLIP CODE

As a stepping stone towards the three-qubit phase flip code, we first implement a two-qubit phase flip code. The two-qubit code consists of the same steps (encode, phase errors, decode, and correct) but differs from the three-qubit code in that a phase error can only be corrected on the data qubit. However, it does demonstrate that information can be coherently transferred between data and ancilla qubits.

The compiled gate set of the two-qubit phase flip code is depicted in Figure 5.2a. We use Q4 as data qubit and Q1 as ancilla qubit. The encoding (beige) is performed by a Hadamard-CZ-Hadamard sequence [161], where the Hadamards are replaced by Y^{-1} gates. The phase errors are induced by leaving the qubits idle for some time (soft red). Since this code should correct for a phase error on the data qubit, one would expect that the dephasing time of the ancilla qubit Q1 is the limiting factor. Ramsey experiments (Figure 5.2e) yield pure dephasing times (T_2^*) of 0.28 ± 0.1 µs and 0.23 ± 0.1 µs for Q1 and Q4 respectively. These are comparable to the decay time (τ) of 0.26 ± 0.01 µs corresponding to the two-qubit phase flip code, shown in Figure 5.2b. The fact that the phase errors on the ancilla qubit are limiting can be seen even more clearly when a refocusing pulse is applied to the ancilla qubit (blue box in Figure 5.2a). The result of this experiment is shown in Figure 5.2c and gives $\tau = 1.86 \pm 0.05$ µs. We have also run this experiment with the data qubit starting in the basis state $|\downarrow\rangle$ (see Supplementary Information, Note 4). The result is shown in Figure 5.2d and gives $\tau = 2.31 \pm 0.02$ µs. For comparison, the results of a Hahn echo experiment are shown for both Q1 and Q4 in Figure 5.2e. We extract $T_2^{\text{Hahn}} = 2.72 \pm 0.05$ µs and 3.26 ± 0.04 µs for Q1 and Q4 respectively. The two-qubit phase flip code is also performed with Q3 as ancilla

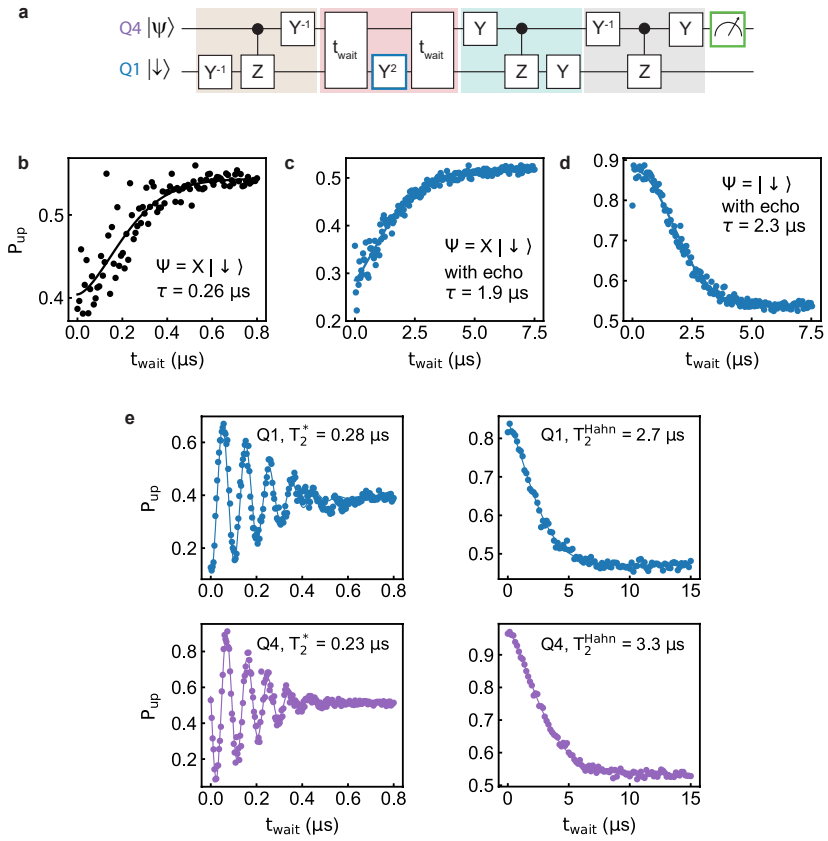

Figure 5.2: **Two-qubit phase flip code.** (a) Circuit diagram. The encoding, decoding and correction are implemented using a combination of Y, Y^{-1} and CZ gates. By adding a wait time (t_{wait}) after the encoding, phase errors will occur due to the dephasing of the qubits. Q4 is the data qubit and Q1 the ancilla qubit. (b-d) P_{up} as a function of t_{wait} when executing the two-qubit phase flip code, which gives a decay time τ. Results for the data qubit prepared in $|\Psi\rangle = X|\downarrow\rangle$ and through single qubit gates projected to a basis state for readout, without an echo pulse Y^2 (b), with an echo pulse Y^2 (c), and with an echo pulse with the data qubit prepared to $|\Psi\rangle = |\downarrow\rangle$ (d). (e) For comparison we show the individual qubit dephasing T_2^* and coherence T_2^{Hahn} times for Q1 (blue) and Q4 (purple).

qubit instead of Q1 (see Supplementary Information, Note 4), in which case we find $\tau = 3.16 \pm 0.03$ μs. Note that when a different ancilla qubit is used (Q3 instead of Q1), but the same data qubit (Q4), τ changes. The fact that τ is limited by the decoherence of the ancilla qubit, instead of the data qubit, shows that the quantum information is indeed transferred to the ancilla qubit and we implemented the two-qubit phase flip code successfully.

5.5. RESONANT SWAP, CS^{-1} AND TOFFOLI-LIKE GATE

Since we use PSB readout, we can only read out the state of an individual qubit when the state of the other qubit in the readout system is known. Therefore, when using Q4 as data qubit and Q3 as

one of the ancilla qubits, it is necessary to reinitialize Q3. We enable this by performing a SWAP gate on Q3 and Q2, with Q2 initialized to the state $|\downarrow\rangle$. Implementing a diabatic SWAP gate is difficult due to the relatively large Zeeman energy difference between Q2 and Q3 [146, 211]. While a SWAP can be compiled from a series of CZ gates and single-qubit operations, here we implement a resonant SWAP [152] by applying an electric pulse as depicted in Figure 5.3a to the barrier gate. This pulse is an oscillating exchange pulse, resonant with the difference in Zeeman energy of Q2 and Q3, superimposed on a Tukey shaped pulse (see the Supplementary Information, Note 3 for details on calibration). Figure 5.3a shows the circuit diagram to demonstrate resetting the state of Q3 using the SWAP. The result is shown in Figure 5.3b, reading out either system Q1Q2 (red) or system Q3Q4 (green). This measurement shows that the states of Q2 and Q3 are swapped, but imperfections in the readout and initialisation and in the calibration of the resonant exchange pulse result in a small residual amplitude on Q3.

Figure 5.3c shows the circuit diagram to demonstrate the controlled-S^{-1} (CS^{-1}) gate. The calibration of the CS^{-1} gate is similar to the CZ gate (see Supplementary Information, Note 2), however, for the CS^{-1} gate the exchange pulse is calibrated to give a phase difference of -$\pi/2$ between the experiments with and without a preparation pulse on the control qubit. This is demonstrated in Figure 5.3d, where the results of a Ramsey experiment are shown with (blue) and without (black) an X^2 pulse on the control qubit Q1.

The Toffoli gate is a three-qubit gate, also called Controlled-Controlled-NOT gate. In the three-qubit phase flip code, the combination of the decoding step and the Toffoli gate performs the majority vote. A resonant i-Toffoli was demonstrated in previous work [126], which would be the fastest implementation when working in a regime where the exchange is on [205]. However, the qubit states are also strongly sensitive to noise in this regime. Here, we implement a Toffoli-like gate composed of CZ and CS^{-1} gates (Figure 5.3e). This is equal to a Toffoli gate up to single and two-qubit rotations on the control qubits [237, 238], which are irrelevant in the protocol under study [220]. The matrix representing of this gate is shown in the Supplementary Information, Note 6. We test the Toffoli-like gate by applying it to different input states, as shown in Figure 5.3e. Here a Rabi pulse $X(\theta)$ is applied to control qubit Q1 and the state of the target qubit Q4 is measured using readout system Q3Q4. Figure 5.3f shows the result with (pink) and without (black) an additional preparation pulse on the second control qubit, Q3. If neither of the control qubits is in the $|\uparrow\rangle$ state (when $X(\theta = 0)$) or when only one control qubit is in the $|\uparrow\rangle$ state (when $X(\theta = \pi)$ on Q1), the target qubit remains in the $|\downarrow\rangle$ state. Only when both control qubits are in the $|\uparrow\rangle$ state, the target qubit flips. The result of a similar experiment, where a Rabi pulse $X(\theta)$ is applied to the other control qubit, Q3, is shown in the Supplementary Information, Note 6. By applying a Rabi pulse $X(\theta)$ on Q1 (Q3), it is shown that this implementation of the Toffoli-like gate works for all $X(\theta)|\downarrow\rangle$ of Q1 (Q3).

5.6. THREE-QUBIT PHASE FLIP CODE

We now turn to the three-qubit phase flip code, of which the circuit diagram is shown in Figure 5.4a. The four qubit system is initialized to the $|\downarrow\downarrow\downarrow\downarrow\rangle$ state, after which we prepare the data qubit, Q4, in a state $|\Psi\rangle$. After the encoding step (beige), refocusing pulses are applied to all three qubits. The errors are implemented by either sweeping the phase $Z(\varphi)$ or by applying a full phase flip $Z(\varphi = \pi)$ with probability p (soft red). Subsequently, the qubits are decoded (turquoise). The correction step (grey) is implemented with the Toffoli-like gate shown in Figure 5.3e. The data qubit state is projected through single qubit gates to $|\downarrow\rangle$, the states of Q3 and Q2 are swapped and finally the data qubit, Q4, is read out using readout system Q3Q4.

This quantum error correction code corrects for a full phase flip as well as an arbitrary $Z(\varphi)$ rotation on a single qubit. When a phase error $Z(\varphi)$ occurs on a qubit, it is in a superposition of

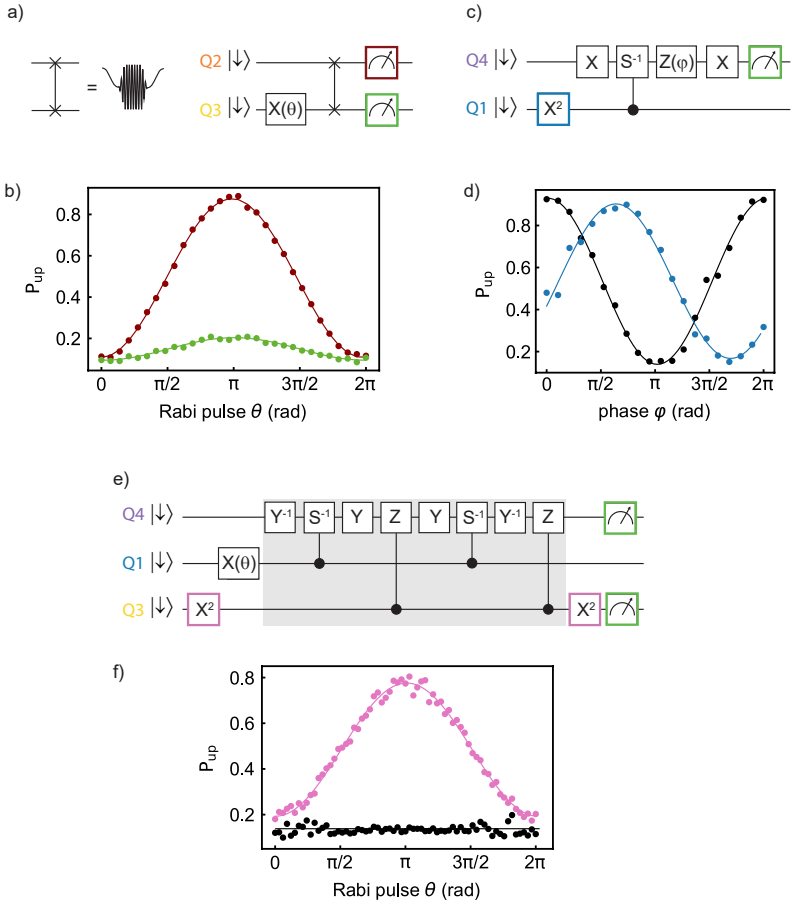

Figure 5.3: **SWAP, CS^{-1} and Toffoli-like gate.** (a) A resonant SWAP gate is implemented by applying a Tukey shaped pulse with an oscillation superimposed to the barrier gate between Q2 and Q3. It is tested using the depicted circuit diagram. (b) To demonstrate the SWAP gate, a Rabi pulse X(θ) is applied to Q3, followed by a SWAP gate between Q2 and Q3. Then, either Q2 is read out using readout system Q1Q2 (red) or Q3 is read out using readout system Q3Q4 (green). (c) Circuit diagram of the experiment demonstrating the CS^{-1} gate. (d) The CS^{-1} gate is obtained by calibrating the phase difference to be $-\pi/2$, for the experiments with (blue) and without (black) a X^2 gate on the control qubit Q1. (e) Circuit diagram of the Toffoli-like gate (gray) composed of CS^{-1} and CZ gates. (f) Demonstration of the Toffoli-like gate with target qubit Q4 and control qubits Q1 and Q3. An X(θ) pulse is applied to Q1 and the final state of Q4 is measured using readout system Q3Q4. Results of the experiment in (e) with (pink) and without (black) a preparation pulse X^2 on ancilla qubit Q3.

being in the correct state (with the ancillas indicating as such) and a state with a phase error (with one or both ancillas being flipped), and the Toffoli-like gate will be able to correct this superposition state. Figure 5.4b and c show the state probability (Γ) (i.e. the chance that the data qubit is successfully rotated back to the $|\downarrow\rangle$ state) for errors implemented by sweeping the phase Z(φ). This error is applied to one qubit at a time, the results are plotted in purple, blue and yellow for an error

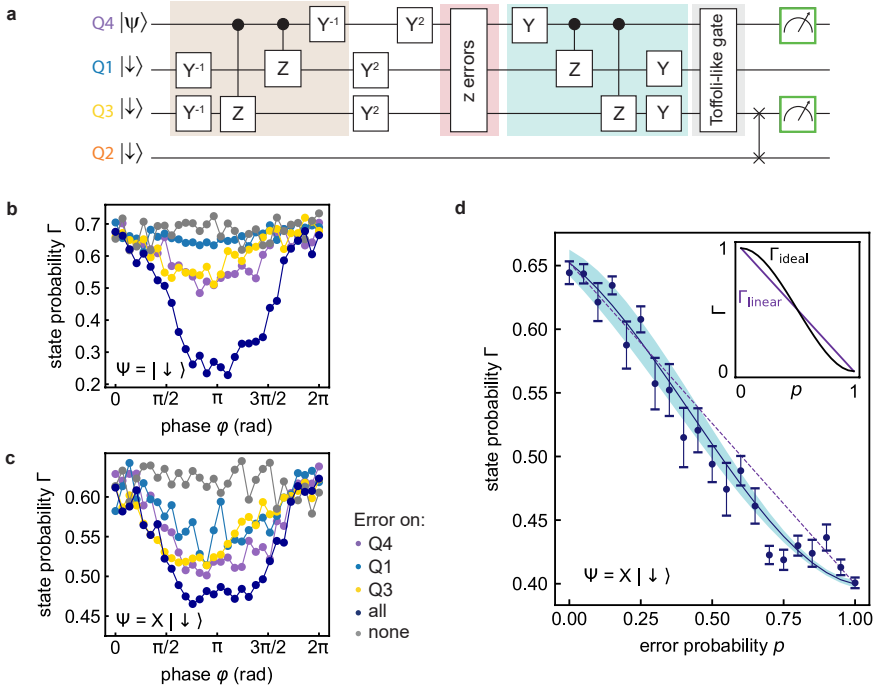

Figure 5.4: **Three-qubit phase flip code.** (a) Implementation of the three-qubit phase flip code. Q4 serves as data qubit, Q1 and Q3 as ancilla qubits, and Q2 as reset qubit for Q3. The correction step is implemented with the Toffoli-like gate as shown in Figure 5.3e. The data qubit is read out with readout system Q3Q4, which makes it necessary to reset Q3 using a resonant SWAP operation with Q2. (b,c) Results of the phase error correction while introducing a phase error Z(φ) on none of the qubits (gray), on Q4 (purple), Q1 (blue) or Q3 (yellow) or on all three qubits simultaneously (dark blue). The initial state of the data qubit is $|\downarrow\rangle$ in (b) and X$|\downarrow\rangle$ in (c). (d) Phase-error correction by introducing phase errors Z($\varphi = \pi$) with probability p. The data qubit is prepared to the state X$|\downarrow\rangle$ and through single qubit gates projected to the $|\downarrow\rangle$ state for readout. Plotted is the state probability (Γ), the error bars indicate the standard deviation. The results are fitted using a model which takes into account the readout and reset errors (see Supplementary Information, Note 9). The standard deviation of the fit is indicated by the light blue area. The inset shows the curve for ideal phase flip correction (Γ_{ideal}) and the linear line for no phase flip correction (Γ_{linear}).

implemented on Q4, Q1 and Q3 respectively. For comparison, the result is also shown when the phase flip code is performed while implementing the error Z(φ) on all three qubits simultaneously (dark blue) and without implementing an error at all (gray). These experiments are performed for two different input states of the data qubit, a basis state ($|\Psi\rangle = |\downarrow\rangle$) and a superposition state ($|\Psi\rangle$ = X$|\downarrow\rangle$), shown in Figure 5.3b and 5.3c respectively. Only when the data qubit is prepared in a superposition state, does the encoding step entangle the data qubit with the two ancilla qubits. One expects that when sweeping the phase Z(φ) on one of the qubits, the error is corrected and the result is a constant high Γ. For sweeping the phase on all three qubits simultaneously, it is expected that the error is not corrected and Γ varies from high to low and back. It is apparent from the results in Figure 5.4b and 5.4c that for both input states the single-qubit errors are not corrected

perfectly. This is due to unintentional errors, i.e. errors occurring in the encoding, decoding and correction steps of the algorithm. These errors are caused by decoherence of the qubits, and are coherent errors such as residual exchange between the qubits (see Supplementary Information, Note 5 for measurements of the residual exchange), cross talk [190, 239] and imperfect two-qubit gates. When comparing the results for the different input states of the data qubit, it becomes clear that for an input state $|\downarrow\rangle$ of the data qubit the visibility is higher and the correction of the single-qubit errors is more successful. We ascribe this improvement to the decreased time during which any unintentional errors can affect the data qubit when it starts in a basis state, and the fact that is less sensitive to imperfections in the two-qubit gates. To gain further insight into the results of this experiment, we performed a simulation (shown in the Supplementary Information, Note 7). We ran the simulation with only coherent errors and with coherent errors plus decoherence, in order to understand which of these unintentional errors are the main limiting factors for the implementation of the phase flip code. When including both coherent errors and decoherence, the simulation results are in qualitative agreement with the measurement results. Both the experimental and simulated data show that errors have a more profound impact when starting in a superposition state compared to starting in a basis state. We can therefore conclude from the simulations that a limiting factor for the implementation of the phase flip code is the decoherence of the qubits.

Furthermore, we study the three-qubit error phase flip code by inserting a full phase flip Z($\varphi = \pi$) with probability p. The data qubit starts in the state $|\Psi\rangle = X|\downarrow\rangle$ and before the data qubit is measured, we project the state to $|\downarrow\rangle$ by applying corresponding single qubit gates. In Figure 5.4d the state probability Γ is plotted against the probability of implementing a phase flip (p). Ideally, the data is described by $\Gamma_{\text{ideal}}(p) = 1 - 3p^2 + 2p^3$ [161]. The ideal function shows a modest improvement of the state probability for $p < 0.5$, compared to the linear line $\Gamma_{\text{linear}}(p) = 1 - p$ expected for no error correction (see inset Figure 5.4d). While the data in Figure 5.4d follows the overall trend, there are some interesting differences. We first note that since the data qubit starts in the $|\Psi\rangle = X|\downarrow\rangle$ state, the data qubit is very sensitive to unintentional errors, resulting in a reduced visibility. Second, the data in Figure 5.4d does not show a trend symmetric around $\Gamma(p = 0.5)$. This asymmetry can be caused by errors in the reset of Q3 combined with asymmetry in the readout scheme (illustrated in the Supplementary Information, Note 1). For example, when the reset of Q3 using the SWAP is imperfect, the error that is introduced is not random, but depends on the history of Q3. Due to the asymmetry of the readout, an imperfect reset of Q3 affects the measurement results of zero or a single intentional error differently than the measurement results for two or three intentional errors. This physical knowledge of the qubit system is taken into account as boundary conditions for the fit and gives the fit function: $\Gamma(p) = b + a(0.95 - 1.73\epsilon\, p - 2.79\, p^2 + 3.9\epsilon\, p^2 + 1.86p^3 - 2.17\epsilon\, p^3)$, where a is the visibility, b the offset and ϵ the error parameter modeling asymmetry (see the Supplementary Information, Note 9 for the derivation). We obtain the fit parameters $a = 0.272 \pm 0.007$, $b = 0.394 \pm 0.003$ and $\epsilon = 0.37 \pm 0.13$. As expected a and b reflect that the visibility is reduced and that the offset is significant. We note that if $\epsilon = 0$, the symmetric shape of Γ_{ideal} is recovered, meaning that Γ is improved for $p < 0.5$ when comparing to Γ_{linear} with similar visibility (dashed purple line in the main panel of 5.4d). For $\epsilon = 0.37$ as fitted here, the state probability still shows a small improvement for $p < 0.27$, compared to Γ_{linear}. When we insert the found fit parameters into the fit function, it simplifies to a polynomial with a linear term of -0.17 ± 0.06. This corresponds to a modest flattening of the curve for small error probability as is visible in Figure 5.4d.

When considering Figure 5.4d, it is important to realize that the experiment performed to obtain this data is significantly different compared to prior works [219, 220]. In these works, the effective probability of a phase error was calculated using $p_{\text{eff}} = sin^2(\varphi/2)$, where the error Z($\varphi$) is implemented on all three qubits simultaneously. We instead run the phase flip code numerous times and randomly implement a phase flip error with a certain probability on all three qubits.

Rather than changing φ, we actually changed the probability of the error. This procedure requires significantly more data and time, thus results in larger error bars, but it does capture the realistic scenario in which it is not known *a priori* if an error would occur and on which qubit. For completeness, we used the data shown in Figure 5.4b and c to also plot Γ as a function of p_{eff} (shown in the Supplementary Information, Note 8). This data is fitted using a polynomial and gives a linear term of -0.07 ± 0.05. The conclusion we can draw from this analysis is similar to the conclusion we draw from the data shown in Figure 5.4d: although not perfectly, the logical error rate has a suppressed first order contribution in p, meaning that single errors are suppressed.

5.7. CONCLUSION

In summary, we have shown a rudimentary quantum error correction circuit. We have executed a two-qubit phase flip code and confirmed that by applying an echo pulse to the ancilla qubit we can preserve the state of the data qubit. We have demonstrated a resonant SWAP gate and have implemented a Toffoli-like gate using CZ and CS^{-1} gates. Utilizing these gates has allowed us to implement a three-qubit phase flip code. Though scaling quantum dots in two dimensions and readout using Pauli spin blockade are central aspects in virtually all semiconductor qubit architectures [167], we have also observed that they affect the quantum gate compilation as well as the correction itself. Running quantum error correction codes such as the surface code [221] will require significant advances. Both the quantity and the quality of the qubits will need to increase. In particular, scaling the number of qubits in two dimensions will require the development of architectures. The qubit coherence is currently limited, but this may be improved by several means. First, by using purified germanium the hyperfine interaction can be avoided. Second, sweet spots with respect to charge noise have recently been proposed and observed for hole qubits [240]. Finally, tailored pulsed will need to be implemented to optimize the initialization, readout and qubit operation. While formidable improvements will have to be made to obtain fault-tolerant operation, we envision that the capability to test tailored quantum algorithms in real devices will serve as a crucial link in developing scalable quantum technology.

5.8. SUPPLEMENTARY INFORMATION

NOTE 1: LATCHED PSB READOUT PROTOCOL

The readout and initilization fidelities strongly affect the visibility. To optimise the initialization and readout, we make use of the same latched PSB protocol [148, 149] as used in previous works [126, 190]. The aim is to reduce the readout infidelity which results from spin relaxation due to spin-orbit interaction [140, 147]. The tunneling rates from the quantum dots to the reservoir are tuned to be asymmetrical, resulting in a high tunneling rate for the (1,1)-(0,1) charge transition and a low tunneling rate for the (1,1)-(1,2) charge transition, as depicted in Figure 5.5a. For the readout we pulse from (1,1) to a spot in the (0,2) charge regime that is bounded by the extension of the (1,1)-(0,1) and (1,1)-(1,2) charge transition lines. When the transition to the (0,2) state is blocked, the (0,1) state is accessible and one hole will tunnel to the reservoir. Since the decay to the (0,2) state from the (0,1) state is determined by the slow tunneling rate, the system is now locked in a metastable charge state, thereby enabling spin-to-charge conversion. We use this readout method on two pair of qubits, Q1 and Q2, using S1 as charge sensor (called readout system Q1Q2), and Q3 and Q4, using S2 as charge sensor (called readout system Q3Q4). Each sensor can measure both pairs of qubits, however it is more sensitive to the quantum dots that are closest. We operate in the regime where the $|\downarrow\downarrow\rangle$ state is blocked and the other spin states are (partially) non-blocked, as shown in Figure 5.5c,e. The difference between the readout systems is due to differences in spin-orbit interactions, as well as differences in the various tunnel rates [126].

This readout method can only be used to determine the spin state of one of the qubits in the readout pair when the state of the other qubit is $|\downarrow\rangle$. The Q3Q4 readout system is used in the final three-qubit phase flip experiment described in the main text. The fraction of tunneling that is blocked for the different spin states influences how well we can read out the final results of this experiment. If the desired output state is $|\downarrow\downarrow\downarrow\rangle$ (as for no errors or a single error), any error will give a different readout result. However, if the desired output state is $|\downarrow\uparrow\rangle$ (as for two or three errors), an error is very hard to detect. This is what we call asymmetry in the readout. The effect of the readout in combination with the SWAP gate is described in more detail in Supplementary Discussion, Note 9.

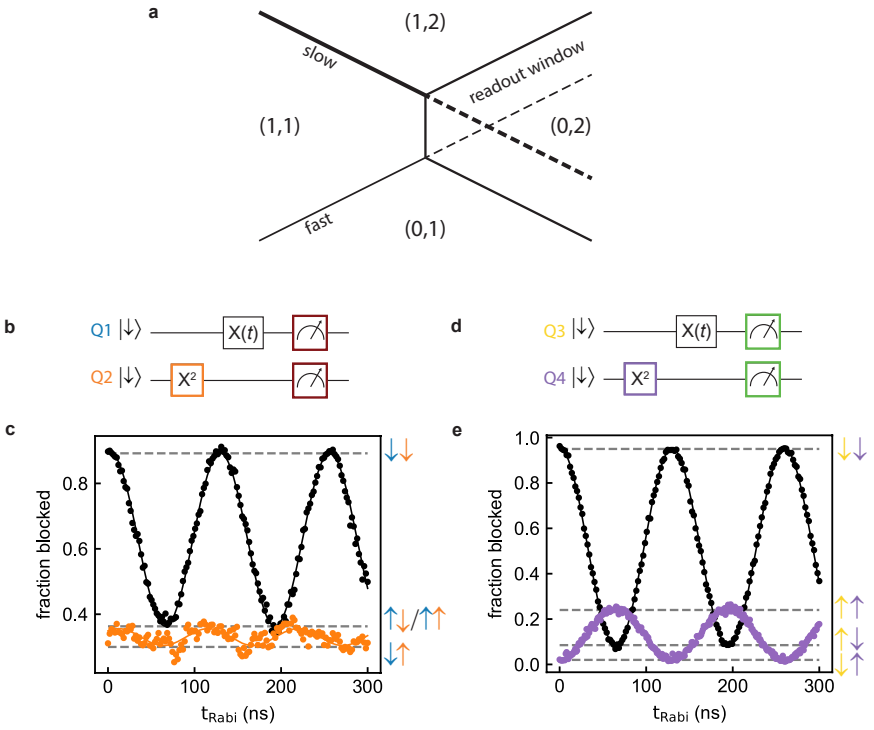

Figure 5.5: **Fraction of the tunneling that is blocked per spin state** (a) Schematic drawing of the charge stability diagram showing the (1,1)-(0,2) anticrossing and indicating the readout window. (b) Circuit diagram describing the experiment to map out the fraction of the tunneling that is blocked per spin state in the two-qubit subspace of the Q1Q2 readout system [130]. A Rabi experiment is performed on Q1 with Q2 either in the $|\downarrow\rangle$ (without the X^2 on Q2, indicated with the orange box) or $|\uparrow\rangle$ state (with the X^2 on Q2). (c) Results of the experiment described in (b). The black data points correspond to the Rabi experiment with Q2 in the $|\downarrow\rangle$ state and the orange data points to the experiment with Q2 in the $|\uparrow\rangle$ state. It shows that there is good contrast between the $|\downarrow\downarrow\downarrow\rangle$ state and the anti-parallel states, but the $|\uparrow\uparrow\rangle$ state can hardly be distinguished from the anti-parallel states. (d) Circuit diagram describing the same experiment as in (b), but for the Q3Q4 readout system. (e) Shown are the results of the experiment as described in (d). For the Rabi experiment performed on Q3 with Q4 in the $|\downarrow\rangle$ state, the data is plotted in black, with Q4 in the $|\uparrow\rangle$ state, the data is plotted in purple. It becomes apparent that also for this readout system there is a clear contrast between $|\downarrow\downarrow\downarrow\rangle$ and both anti-parallel spin states. The $|\uparrow\uparrow\rangle$ state however is partially blocked.

NOTE 2: CALIBRATION OF THE CZ AND CS^{-1} GATES

The CZ and CS^{-1} gates are calibrated using a Ramsey type experiment in which P_{up} is measured as a function of the phase $Z(\varphi)$ before the final X gate. Overall we follow the same strategy for the calibration as in previous work [126]. For the CS^{-1} gate the circuit diagram of this sequence is shown in Figure 3c of the main text. For the CZ between Q4 and Q3 the circuit is shown in Figure 5.6a, the same experiment was performed with Q1 as control qubit.

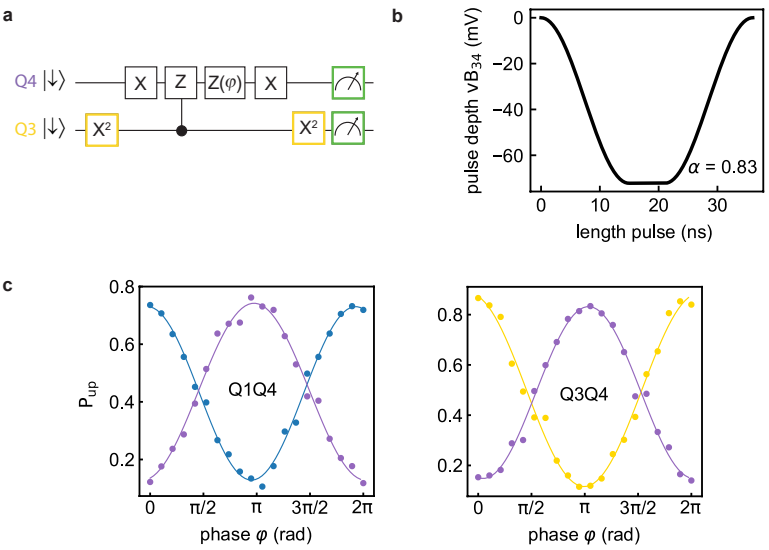

Figure 5.6: **Calibration and pulse shape CZ and CS^{-1} gates** (a) Circuit diagram of a Ramsey type experiment to measure the conditional phase. This experiment is performed with and without the preparation gate X^2 on the control qubit. The conditional-Phase gate is implemented with a pulse on the virtual barrier gate [126] between the two relevant qubits (either gate vB_{34} or vB_{41}). The length and depth of this pulse determines the acquired phase and makes a CZ or CS^{-1} gate. (b) Tukey shape with $\alpha = 0.83$ as is used for the implementation of the CZ and CS^{-1} gates. Here we show the pulse with length (36 ns) and depth (-77.2 mV) on the virtual barrier vB_{34} to implement the CZ gate between Q3 and Q4. The depth of the pulse on the virtual barrier is relative to the value it has in the 'exchange off' regime. To implement the CZ (CS^{-1}) between Q4 and Q1 a similar pulse is applied to vB_{41} with a length of 34 ns (14 ns) and a depth of -74.6 mV (-73.6 mV). (c) Implementation of a CPhase gate, using a Tukey shaped exchange pulse on the barrier gate. This experiment is performed with (blue and yellow for target qubit Q1 or Q3 respectively) and without (purple) an X^2 pulse on the control qubit. The difference in acquired phase is calibrated to be π, thus implementing a CZ gate [126].

To calibrate the phase difference between experiments with and without a preparation pulse on the control qubit, the depth and the length of the pulse on the virtual barrier are tuned. The shape of this pulse is a Tukey window, also called a cosine-tapered window [241]. It is a pulse of which the slopes are the shape of a cosine and in the middle it is flat like a rectangle, as shown in Figure 5.6b. A factor α determines the precise shape of the pulse: the cosine lobe has width $N \cdot \alpha/2$, which is combined with a rectangular window of width $N(1-\alpha/2)$, where N is the length of the pulse. For the CZ and CS^{-1} gates we used $\alpha = 0.83$. We use the Tukey shape to optimize the adiabaticity of the variation in exchange with respect to the difference in Zeeman energy between the qubits. A CZ gate is obtained when the phase difference is π, for the situation where the control qubit is in the $|\downarrow\rangle$ state compared to when it is in the $|\uparrow\rangle$ state. A CS^{-1} gate is obtained when the

difference in acquired phase is -π/2. For both the calibration of the CZ as for the CS^{-1}, after the exchange pulse, a software Z gate is applied to both of the qubits, to compensate for acquired single-qubit phases. For the CS^{-1} gate the result of this calibration is shown in Figure 3d of the main text. For the CZ gate it is shown in 5.6c.

NOTE 3: CALIBRATION OF THE RESONANT SWAP GATE

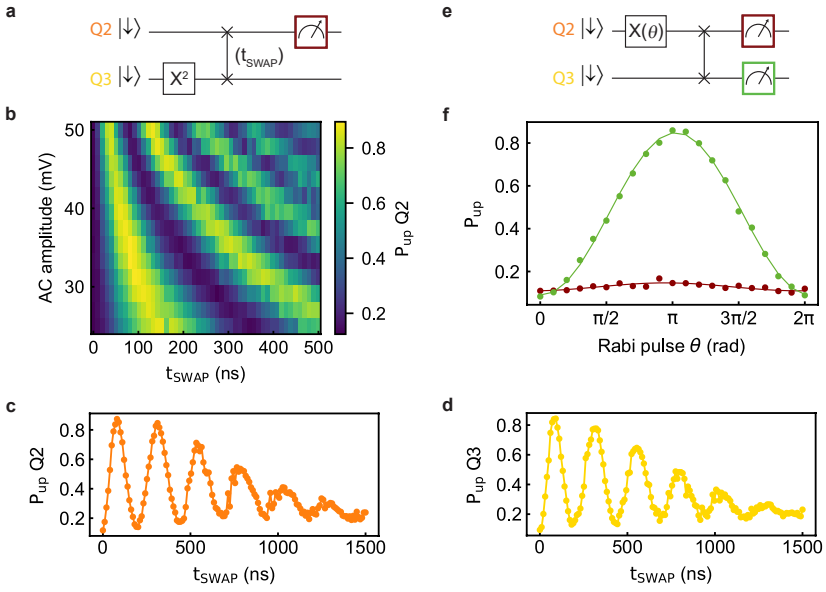

Figure 5.7: **SWAP gate** (a) Circuit diagram of the experiment used to calibrate the length and AC amplitude of the exchange pulse which implements the resonant SWAP gate. An X^2 gate is applied to Q3, after which the SWAP gate is applied and Q2 is read out using the Q1Q2 readout system. (b) Result of the experiment in (a), it shows SWAP oscillations which become faster when the AC amplitude of the exchange pulse is increased [152]. (c, d) Similar experiment as shown in (a), which a fixed value for the AC amplitude of 35 mV. (c) Result of the experiment with an X^2 gate on Q3 and using readout system Q1Q2, while (d) shows the result of the same experiment but with an X^2 gate on Q2 and using readout system Q3Q4. The decay of the SWAP oscillations is asymmetric, slightly more so for the oscillation shown in (d) than in (c). A possible explanation is that spin states in the qubit partially get swapped with down spins in Q1 and Q4, because the exchange between Q2 and Q1 and between Q3 and Q4 is finite, as shown in section VI. (e) Circuit diagram of an experiment where we put a Rabi oscillation on Q2, swap the states of Q2 and Q3 and read out either with readout system Q1Q2 (red) or Q3Q4 (green). (f) Result of the experiment in (e). It demonstrates that the resonant SWAP gate can also be used to reset Q2, similar to how the SWAP gate can be used to reset Q3, which is shown in Figure 3b of the main text.

To implement a resonant SWAP gate between Q2 and Q3, a Tukey shaped pulse with an oscillation superimposed is applied to the virtual barrier vB_{23}, as shown in Figure 3a of the main text. The Tukey shaped pulse is discussed in detail in section II, for the implementation of the SWAP we use $\alpha = 0.5$. To correctly implement the SWAP the length and depth of the Tukey pulse and the AC amplitude and frequency of the oscillation need to be calibrated. We start by choosing the depth of the pulse on vB_{23} as -30 mV compared to the 'exchange off' regime. With this pulse on the virtual barrier we first do a first rough measurement of the difference in resonance frequency between Q2

and Q3. This value we use as the frequency of the oscillation and we vary the length of the SWAP pulse (t_{SWAP}) and the AC amplitude (Figure 5.7a), resulting in the measurement shown in Figure 5.7b. Based on this measurement we choose a length (80 ns) and AC amplitude (35 mV) of the pulse. As a final step in the calibration, we fine tune the frequency of the oscillation. This we do using the measurement depicted in Figure 3a of the main text, for various values of the frequency and choosing the one where the amplitude measured on Q3 is smallest.

NOTE 4: ADDITIONAL DATA TWO-QUBIT PHASE FLIP CODE

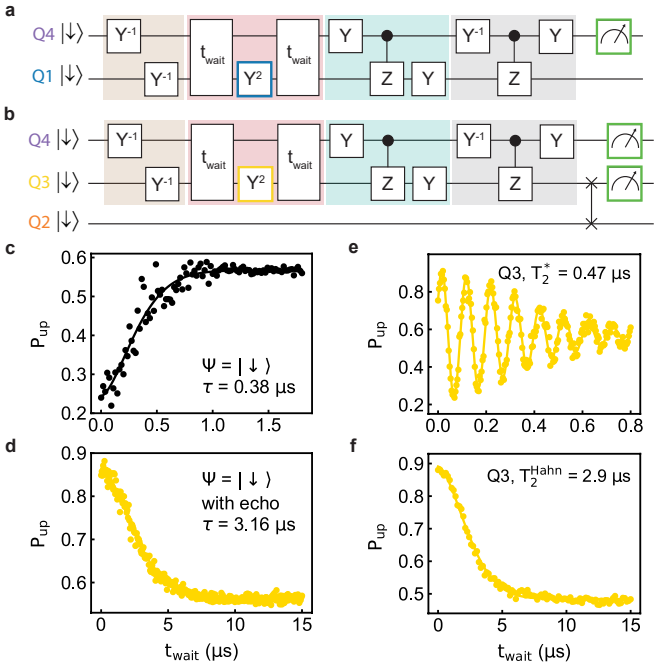

Figure 5.8: **Two-qubit phase flip code with input state** $|\Psi\rangle = |\downarrow\rangle$ (a) Circuit diagram describing the experiment for which the result is shown in Figure 2d of the main text. In this experiment both the data qubit, Q4, and the ancilla qubit, Q1, start in the $|\downarrow\rangle$ basis state. For this input state, the logical qubit after the encoding step is $|--\rangle$, which is not an entangled state. Therefore, the first CZ gate becomes obsolete and the algorithm can be simplified. An echo pulse is applied to the ancilla qubit (indicated by the blue box), resulting in an experiment that closely resembles a Hahn echo experiment, plus the decoding and correction step. (b) Circuit diagram similar to the one shown in (a), but with Q3 as ancilla qubit. Since the spin state of Q4 is read out with respect to the spin state of Q3, the state of Q3 is reset by applying a resonant SWAP gate between Q3 and Q2. The echo on the ancilla is indicated with a yellow box. (c,d) Plotted here are the spin-up probability as a function of t_{wait} when executing the circuit diagram in (b), without (c) and with an echo pulse Y^2 (d). Individual qubit T_2^* (e) and T_2^{Hahn} times (f) for Q3.

NOTE 5: RESIDUAL EXCHANGE

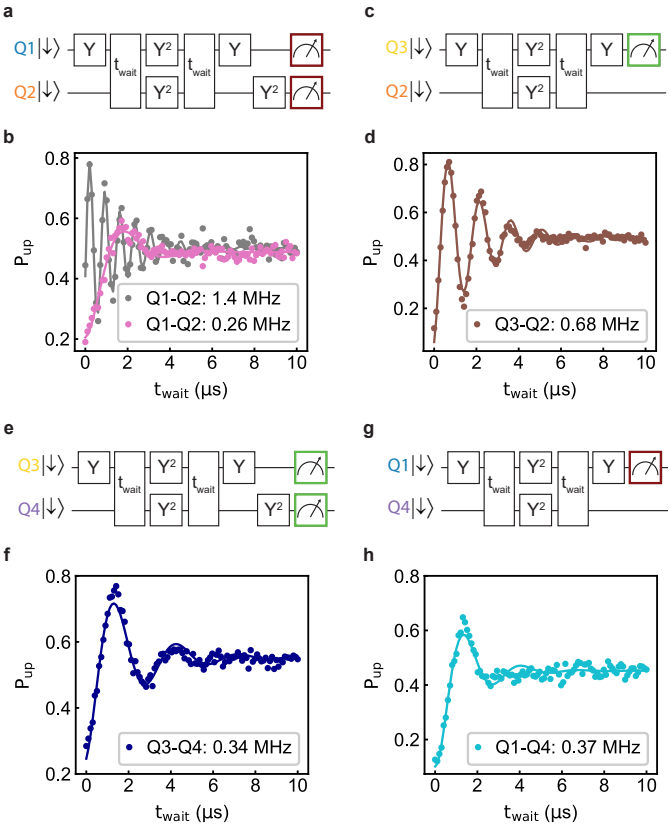

Figure 5.9: **Residual exchange (or ZZ crosstalk)** (a) Circuit diagram of the measurement of the residual exchange between Q1 and Q2, i.e. the exchange in the regime where the single qubit gates are performed. We execute a Hahn echo experiment on Q1 and apply a Y^2 gate on Q4 simultaneous with the echo pulse Y^2 on Q1. We measure an oscillation due to the ZZ interaction as a function of t_{wait}. (b) Measurement result of the residual exchange between Q1 and Q2. It was first measured to be 1.40 ± 0.01 MHz (gray). After decreasing the detuning and increasing the voltage on the virtual barrier gate, the exchange was measured again and found to be 0.26 ± 0.01 MHz (pink). For this qubit pair we chose to reduce the exchange because it was significantly larger than between the other pairs. (c-g) Circuit diagram and results of measurement of the residual exchange between Q3-Q2 (c,d), Q3-Q4 (e,f) and Q1-Q4 (g,h). Values found are 0.68 ± 0.1 MHz, 0.34 ± 0.01 MHz and 0.37 ± 0.01 MHz for Q3-Q2, Q3-Q4 and Q1-Q4 respectively.

NOTE 6: ADDITIONAL DATA ON THE TOFFOLI-LIKE GATE

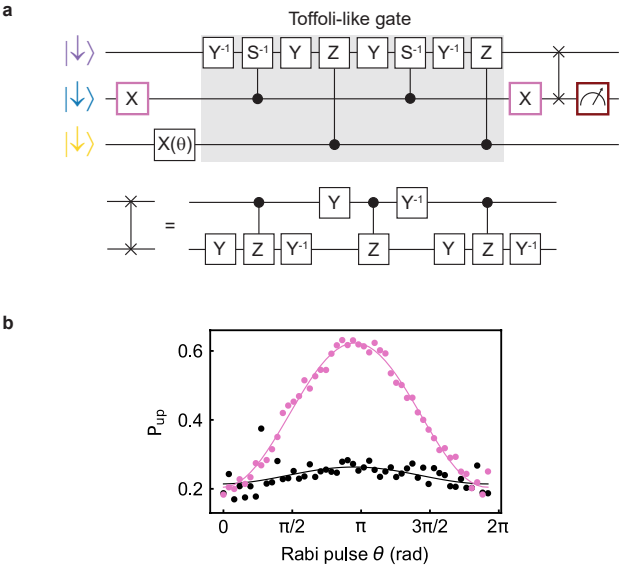

Figure 5.10: **Toffoli-like gate** (a) Circuit diagram of the Toffoli-like gate composed of CS^{-1} and CZ gates. Before the readout, a SWAP operation is performed between Q4 and Q1. The SWAP gate is composed of three CNOT gates, each one broken down into CZ and Y and Y^{-1} as shown below the circuit diagram. (b) Results of implementing the Toffoli-like gate with target qubit Q4 and control qubits Q1 and Q3. A Rabi oscillation X(θ) is applied to Q3 and the final state of Q4 is measured by swapping the state of Q4 with the state of Q1 and using readout system Q1Q2. If ancilla qubit Q1 stays in the $|\downarrow\rangle$ state, the target qubit Q4 also stays in the $|\downarrow\rangle$ state, as plotted in black. However, when Q1 is prepared in the state $|\uparrow\rangle$, Q4 starts to oscillate like Q3, as plotted in pink. With this experiment we demonstrate that the Toffoli-like gate also works for all possible input states of Q3. The overall visibility is smaller compared to the results shown in Figure 3f in the main text, which can be contributed to the SWAP operation, which is composed of multiple gates.

5

The matrix representation of the circuit diagram of the Toffoli-like gate (see Fig. 5.10 a) in the basis $\{|\downarrow\rangle_{Q4}, |\uparrow\rangle_{Q4}\} \otimes \{|\downarrow\rangle_{Q1}, |\uparrow\rangle_{Q1}\} \otimes \{|\downarrow\rangle_{Q3}, |\uparrow\rangle_{Q3}\}$ reads

$$\text{Toffoli-like gate} = \begin{pmatrix} 1 & 0 & 0 & 0 & 0 & 0 & 0 & 0 \\ 0 & 1 & 0 & 0 & 0 & 0 & 0 & 0 \\ 0 & 0 & -i & 0 & 0 & 0 & 0 & 0 \\ 0 & 0 & 0 & 0 & 0 & 0 & 0 & 1 \\ 0 & 0 & 0 & 0 & 1 & 0 & 0 & 0 \\ 0 & 0 & 0 & 0 & 0 & 1 & 0 & 0 \\ 0 & 0 & 0 & 0 & 0 & 0 & -i & 0 \\ 0 & 0 & 0 & 1 & 0 & 0 & 0 & 0 \end{pmatrix}. \tag{5.1}$$

Note, that this matrix corresponds to the real Toffoli-gate up to phases on the two control qubits (here Q1 and Q3) which is irrelevant due to the imminent measurement.

NOTE 7: SIMULATION OF THE PHASE FLIP CODE WITH ERROR Z(φ)

In order to improve our understanding of the result shown in Figure 4 of the main text, we ran simulations of the three qubit phase flip code. The results of this simulation are shown in Figure 5.11a, b, c and d. When comparing the simulation which only takes into account the coherent errors (Figure 5.11a and c) with the simulation results taking into account the decoherence of the qubits as well (Figure 5.11b and d), it is clear that for both input states the visibility is strongly reduced when including decoherence. We also observe that like in the measured data, the visibility is more reduced when the data qubits starts in the superposition state then when the data qubit starts in the basis state. Overall, when comparing the simulated data with the measured data, it is clear that they are in qualitative agreement. Especially note the resemblance between the simulated data (Figure 5.11d) and the measured data (Figure 5.11e) for which an error Z(φ) is implemented on all three qubits simultaneously when starting in the superposition state (dark blue data points).

There are at least two possible explanations for the differences between the simulations and the measurement results. Firstly, the coherent errors taken into account for the simulations shown in Figure 5.11a and c are the coherent errors as estimated from individual qubit calibrations. The joint operation of these gates in the phase flip code can cause additional errors, such that the coherent errors in the experiment are underestimated. Secondly, it is possible that the pulses applied to implement the gates in the phase flip code have a negative influence on the coherence of the qubits [121]. Overall we can conclude from these simulations that the limiting factor for implementing the phase flip code is the decoherence of the qubits.

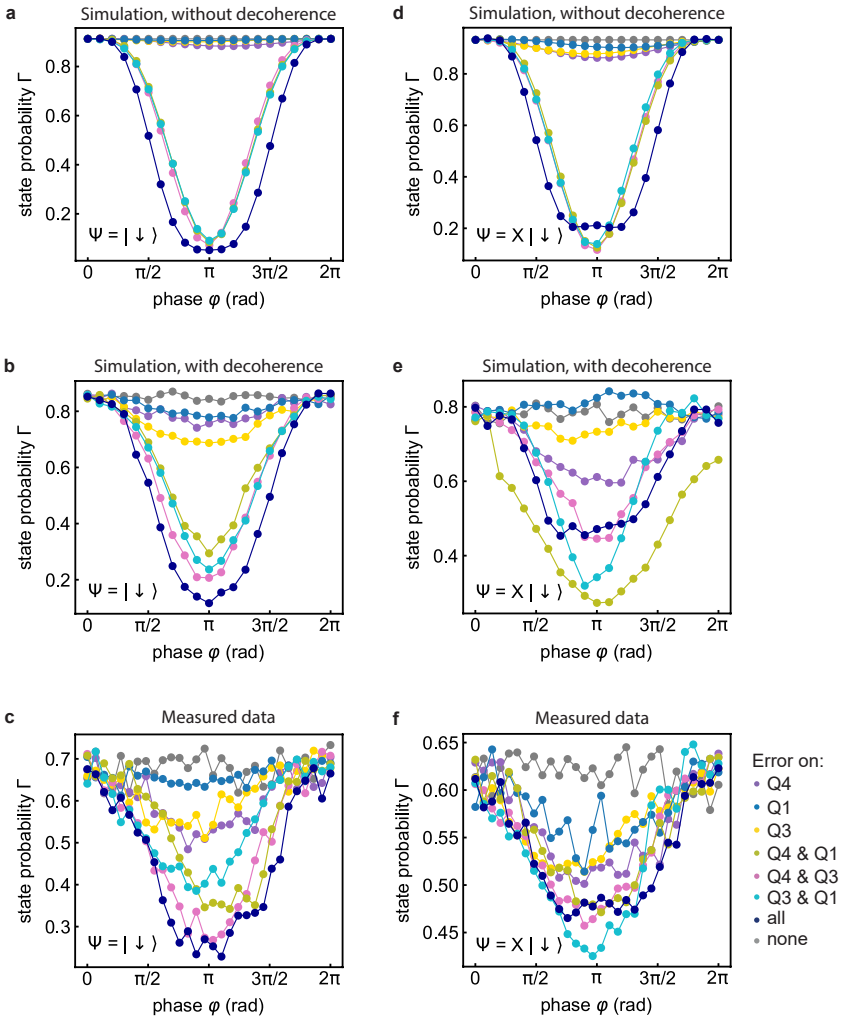

Figure 5.11: **Comparing numerical simulation and experiment of the phase flip code while sweeping the error Z(φ)** (a) Result of simulating the phase flip code of which the implementation is shown in Figure 4a of the main text, starting in the basis state $|\downarrow\rangle$ and projecting back to $|\downarrow\rangle$ at the end. An error Z(φ) is implemented on the individual qubits and on combinations of qubits simultaneously as indicated in the legend of the figure. For this simulation, the following coherent errors are taking into account: residual exchange, cross-talk, imperfections of the single and two qubit gates through realistic modeling of the pulse signals and filters and imperfections in readout and initialization. (b) Similar to (a), but now also taking into account errors due to decoherence of the qubits. Noise is modeled as quasi-static fluctuations of the resonance frequencies of each qubit befitting the corresponding measured T_2^*. Each data point is averaged on 250 initializations of the noise. The low number of runs is due to limitations in computational power and causes some uncertainties in the simulations. (c) Same measured data as shown in Figure 4b of the main text, plus the results of implementing the error Z(φ) at two qubits simultaneously. (c, d, e) Similar to (a, b, c) respectively, however starting with the data qubit in the superposition $|\Psi\rangle = X|\downarrow\rangle$.

NOTE 8: EFFECTIVE PROBABILITY

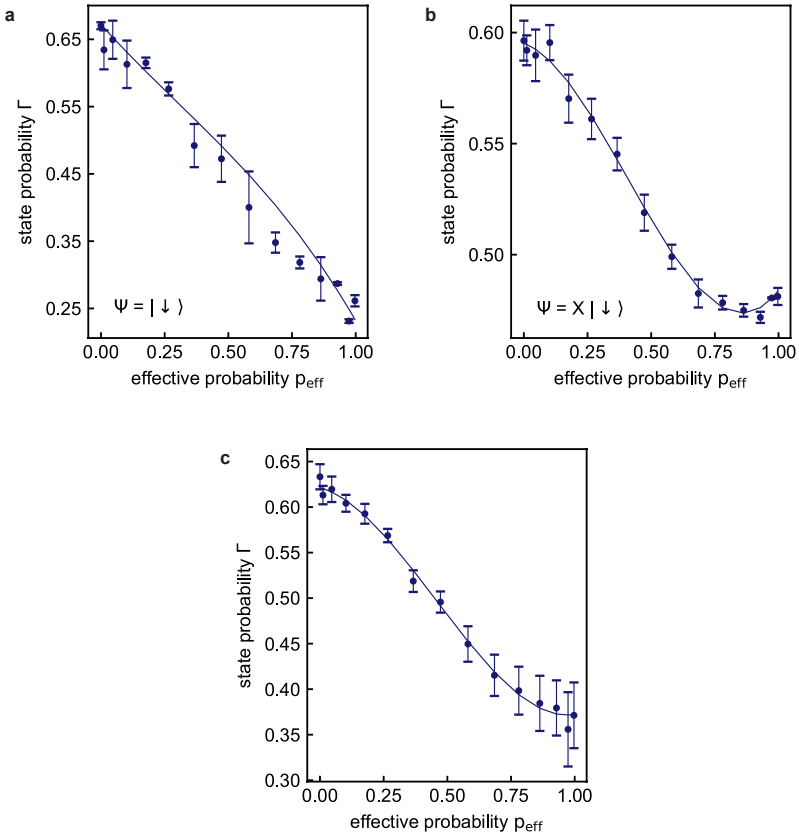

Figure 5.12: **State probability versus effective probability** (a) Plotted is the state probability versus the effective probability of implementing a phase error while starting with the data qubit Q4 in the basis state $|\Psi\rangle = |\downarrow\rangle$. The data shown here is the same as in Figure 4b of the main text and Figure 5.11c where we show Γ versus $Z(\varphi)$. However, here we use $p_{eff} = sin^2(\varphi/2)$ and the error bar is an indication for the difference between the value $\Gamma(Z(\varphi))$ between 0 and π and $\Gamma(Z(\varphi))$ between π and 2π. We fit using a polynomial function giving $\Gamma(p_{eff}) = (0.67 \pm 0.02) - (0.4 \pm 0.2)p_{eff} + (0.2 \pm 0.5)p_{eff}^2 - (0.2 \pm 0.3)p_{eff}^3$. (b) Similar to (a), but with the data qubit starting in the superposition state $|\Psi\rangle = X|\downarrow\rangle$. The data shown is the same as in Figure 4c of the main text and Figure 5.11c, plus two additional data sets. Fitted is $\Gamma(p_{eff}) = (0.595 \pm 0.004) - (0.04 \pm 0.04)p_{eff} - (0.41 \pm 0.08)p_{eff}^2 + (0.33 \pm 0.05)p_{eff}^3$. (c) Average of the data shown in (a) and (b). Fitted is $\Gamma(p_{eff}) = (0.621 \pm 0.004) - (0.07 \pm 0.05)p_{eff} - (0.64 \pm 0.14)p_{eff}^2 + (0.47 \pm 0.11)p_{eff}^3$.

In previous works [219, 220], instead of implementing a phase error on the qubits with a certain probability, an error $Z(\varphi)$ on all three qubits is simultaneously implemented and an effective probability of error per qubit $p_{eff} = sin^2(\varphi/2)$ is used. To compare with these experiments, we used the data presented in Figure 5.4b and c of the main text and calculated p_{eff} using this method. The results are shown in Figure 5.12, which are fitted with a polynomial function.

Figure 5.12a shows the result for running the three qubit phase flip code, while starting in

the basis state $|\Psi\rangle = |\downarrow\rangle$. Figure 5.12b shows the results when the data qubit is prepared in the superposition state $|\Psi\rangle = X|\downarrow\rangle$. This data can be reasonably fit using a polynomial function and we find a linear term of 0.04 ± 0.04. In Figure 5.12c we show the combined results for starting in a basis and superposition state. We can fit the data using $\Gamma(p_{\text{eff}}) = (0.621 \pm 0.004) - (0.07 \pm 0.05)p_{\text{eff}} - (0.64 \pm 0.14)p_{\text{eff}}^2 + (0.47 \pm 0.11)p_{\text{eff}}^3$. From this analysis we conclude that the linear term, although not completely zero, is largely reduced. This is consistent with the expectation of suppression of single qubit phase errors. The conclusion of a reduced linear term is also in agreement with the result of the experiment presented in the main text, where we obtain Γ by implementing a full phase error $Z(\varphi = \pi)$ with a certain probability.

NOTE 9: DERIVATION OF THE FIT FUNCTION OF THE THREE-QUBIT PHASE FLIP CODE

In this section we derive a model for the three-qubit phase flip code experimentally implemented in the main text and the logical error probability fit function $\Gamma(p)$. For simplicity the implemented gates are assumed to be perfect and are described by their corresponding unitary matrix except for the final SWAP gate. To follow the notation in the main text, we define an X (Y) gate as a $\pi/2$ rotation, X^2 (Y^2) as a π rotation and X^{-1} (Y^{-1}) as a $-\pi/2$ rotation around the $\hat{x}$ ($\hat{y}$) axis. Thus, the unitaries of the single qubit gates read

$$Q = \exp(-i\frac{\pi}{4}\sigma_q) \tag{5.2}$$

with $Q = X, Y, Z$, $q = x, y, z$, the Pauli matrices σ_q, and $Q^{-1} = Q^\dagger$ being it's inverse. The unitary of the CZ gate reads

$$\text{CZ} = \text{diag}(1, 1, 1, -1). \tag{5.3}$$

Here, we additionally make use of indices to label the affected qubit(s), i.e., X_{Q1} corresponds to a X-gate on Q1 and CZ_{12} corresponds on a CZ-gate between Q1 and Q2.

Moreover, we define the unitary of the two-qubit CS gate as

$$\text{CS} = \text{diag}(1, 1, 1, i) \tag{5.4}$$

and we model an imperfect SWAP gate by the following unitary

$$\text{SWAP}(\epsilon) = \begin{pmatrix} 1 & 0 & 0 & 0 \\ 0 & -i\sqrt{\epsilon}\, e^{\frac{i\pi}{2}\sqrt{1-\epsilon}} & -i\sqrt{1-\epsilon}\, e^{\frac{i\pi}{2}\sqrt{1-\epsilon}} & 0 \\ 0 & -i\sqrt{1-\epsilon}\, e^{\frac{i\pi}{2}\sqrt{1-\epsilon}} & i\sqrt{\epsilon}\, e^{\frac{i\pi}{2}\sqrt{1-\epsilon}} & 0 \\ 0 & 0 & 0 & 1 \end{pmatrix} \tag{5.5}$$

with an error probability $\epsilon = [0, 1]$. This mimics the time-evolution of a strongly driven resonant-SWAP gate [152]. Note, that strong driving can yield errors similar to off-resonant driving due to non-linear exchange $J \propto \exp\left[2\alpha(v_0 + v_D\cos(2\pi f_D t))\right] \approx \exp(2\alpha v_0)(1 + 2\alpha v_D\cos(2\pi f_D t) + \alpha^2 v_D^2[1 + \cos(4\pi f_D t)])$ causing a shift in the resonance condition. Here, v_0 is the voltage setting during the AC drive, v_D is the amplitude of the AC signal, α corresponds to the lever arm of the barrier gate, and $f_D = f_{\text{Q2}} - f_{\text{Q3}}$ is the drive frequency of the AC SWAP gate between Q2 and Q3.

The density matrix ρ after each gate is then given by composing $\rho_1 = U\rho_0 U^\dagger$ with the unitary matrix U chosen from the set above. The uncorrelated probabilistic phase error of each qubit is modelled via the Pauli-Z error channel

$$\Lambda(\rho) = (1 - p)\rho + p\sigma_z\rho\sigma_z \tag{5.6}$$

applied on each qubit independently with probability p. The logical error probability for the three-qubit phase flip code $\Gamma(p)$ is given by the probability to measure $|\Psi\rangle_{Q4} = |\downarrow\rangle$. The probability to measure $|\Psi\rangle_{Q4} = |\downarrow\rangle$ after the PSB measurement of readout system Q3Q4 is given by the positive valued operator (POVM) outcome

$$\Gamma(p) = \mathrm{tr}(\rho_{\mathrm{final}} F_{|\Psi\rangle_{Q4}=|\downarrow\rangle}) \tag{5.7}$$

with

$$F_{|\Psi\rangle_{Q4}=|\downarrow\rangle} = \mathbb{1}_2 \otimes \mathbb{1}_2 \otimes \begin{pmatrix} F_{\downarrow\downarrow} & 0 & 0 & 0 \\ 0 & F_{\downarrow\uparrow} & 0 & 0 \\ 0 & 0 & F_{\uparrow\downarrow} & 0 \\ 0 & 0 & 0 & F_{\uparrow\uparrow} \end{pmatrix} \tag{5.8}$$

with the same parameters and definitions as above. For an ideal measurement $\Gamma(p) = 1-3p^2+2p^3$ directly shows the insensitivity of the three-qubit phase code to phase errors by suppressing terms linear in p.

Coherent and incoherent unintentional phase errors will provide an additional reduced visibility and an offset of the measurement outcomes which we will account for by introducing the two fitting parameters a and b. The final formula to fit our data is then given by plugging in the numbers $F_{\downarrow\downarrow} = 0.95$, $F_{\uparrow\downarrow} = 0.085$, $F_{\downarrow\uparrow} = 0.02$, $F_{\uparrow\uparrow} = 0.24$ in Eq. (5.7)

$$\Gamma(p) = a\,(0.95 - 1.73\epsilon\, p - 2.79\, p^2 + 3.9\epsilon\, p^2 + 1.86 p^3 - 2.17\epsilon\, p^3) + b. \tag{5.9}$$

The strong suppression of phase errors for an ideal measurement is reduced for a erroneous SWAP-gate $\epsilon > 0$ by not suppressing all linear terms in Eq. (5.9).

Additionally, the symmetric behavior expected for a theoretical $\Gamma(p)$ under the reflection on the straight line $l(p)$ through points $(p, \Gamma(p)) = (0, a\,F_{\downarrow\downarrow})$ and $(p, \Gamma(p)) = (1, a\,F_{\downarrow\uparrow})$ is broken through the erroneous SWAP-gate [227]. Note, that $(F_{\downarrow\downarrow} - F_{\downarrow\uparrow})$ defines the visibility window of the measurement. This symmetry is given by the fact that the code itself cannot distinguishes between no error ($p = 0$) and an error on all qubits ($p = 1$). We want to note that in our case the imperfect SWAP-gate combined with a finite dark signal ($F_{\downarrow\uparrow} \neq 0$, $F_{\downarrow\uparrow} \neq 0$, $F_{\uparrow\uparrow} \neq 0$ or $F_{\uparrow\uparrow} \neq F_{\downarrow\downarrow}$) of the measurement signal can leave the impression that this symmetry is broken. In short, a single error is detected with a higher contrast $(F_{\downarrow\downarrow} - F_{\downarrow\uparrow})$ than two errors $(F_{\uparrow\uparrow} - F_{\uparrow\downarrow})$ giving rise to a skewing of the signal. As a final remark, there are other errors which give similar correlations than the erroneous SWAP gate. Since these errors cannot be distinguished in the measurement signal, the error probability ϵ considers all of them and for simplicity are attributed to the dominating SWAP error.

6

COHERENT SPIN QUBIT SHUTTLING THROUGH GERMANIUM QUANTUM DOTS

Quantum links can interconnect qubit registers and are therefore essential in networked quantum computing. Semiconductor quantum dot qubits have seen significant progress in the high-fidelity operation of small qubit registers but establishing a compelling quantum link remains a challenge. Here, we show that a spin qubit can be shuttled through multiple quantum dots while preserving its quantum information. Remarkably, we achieve these results using hole spin qubits in germanium, despite the presence of strong spin-orbit interaction. In a minimal quantum dot chain, we accomplish the shuttling of spin basis states over effective lengths beyond 300 μm and demonstrate the coherent shuttling of superposition states over effective lengths corresponding to 9 μm, which we can extend to 49 μm by incorporating dynamical decoupling. These findings indicate qubit shuttling as an effective approach to route qubits within registers and to establish quantum links between registers.

This chapter has been adapted from F. van Riggelen-Doelman, C.-A. Wang, S.L. de Snoo, W.I.L. Lawrie, N.W. Hendrickx, M. Rimbach-Russ, A. Sammak, G. Scappucci, C. Déprez, M. Veldhorst, in print with Nature Communications (2024) [242].

6.1. INTRODUCTION

The envisioned approach for semiconductor spin qubits towards fault-tolerant quantum computation centers on the concept of quantum networks, where qubit registers are interconnected via quantum links [167]. Significant progress has been made in controlling few-qubit registers [121, 126]. Recent efforts have led to demonstrations of high fidelity single- and two-qubit gates [117, 118, 120, 190], quantum logic above one Kelvin [116, 196, 243] and operation of a 16 quantum dot array [244]. However, scaling up to larger qubit numbers requires changes in the device architecture [87, 166, 245, 246].

Inclusion of short-range and mid-range quantum links could be particularly effective to establish scalability, addressability, and qubit connectivity. The coherent shuttling of electron or hole spins is an appealing concept for the integration of such quantum links in spin qubit devices. Short-range coupling, implemented by shuttling a spin qubit through quantum dots in an array, can provide flexible qubit routing and local addressability [168, 247]. Moreover, it allows to increase connectivity beyond nearest-neighbour coupling and decrease the number of gates needed to execute algorithms. Mid-range links, implemented by shuttling spins through a multitude of quantum dots, may entangle distant qubit registers for networked computing and allow for qubit operations at dedicated locations [168, 207, 248, 249]. Furthermore, such quantum buses could provide space for the integration of on-chip control electronics [167], depending on their footprint.

The potential of shuttling-based quantum buses has stimulated research on shuttling electron charge [250–252] and spin [113, 247, 253–259]. While nuclear spin noise prevents high-fidelity qubit operation in gallium arsenide, demonstrations of coherent transfer of individual electron spins through quantum dots are encouraging [113, 253–256]. In silicon, qubits can be operated with high-fidelity and this has been employed to displace a spin qubit in a double quantum dot [247, 257]. Networked quantum computers, however, will require integration of qubit control and shuttling through chains of quantum dots, incorporating quantum dots that have at least two neighbours.

Meanwhile, quantum dots defined in strained germanium (Ge/SiGe) heterostructures have emerged as a promising platform for hole spin qubits [124, 125]. The high quality of the platform allowed for rapid development of single spin qubits [140, 141], singlet-triplet qubits [151, 233, 260], a four qubit processor [126], and a 4×4 quantum dot array with shared gate control [244]. While the strong spin orbit interaction allows for fast and all-electrical control, the resulting anisotropic g-tensor [125, 127] complicates the spin dynamics and may challenge the feasibility of a quantum bus.

Here, we demonstrate that spin qubits can be shuttled through quantum dots. These experiments are performed with two hole spin qubits in a 2×2 germanium quantum dot array. Importantly, we operate in a regime where we can implement single qubit logic and coherently transfer spin qubits through an intermediate quantum dot. Furthermore, by performing experiments with precise voltage pulses and sub-nanosecond time resolution, we can mitigate finite qubit rotations induced by spin-orbit interactions. In these optimized sequences we find that the shuttling performance is limited by dephasing and can be extended through dynamical decoupling.

6.2. COHERENT SHUTTLING OF SINGLE HOLE SPIN QUBITS

Fig. 6.1.a shows a germanium 2×2 quantum dot array identical to the one used in the experiment [126]. The chemical potentials and the tunnel couplings of the quantum dots are controlled with virtual gates (vP_i, vB_{ij}), which consist of combinations of voltages on the plunger gates and the barrier gates. We operate the device with two spin qubits in quantum dots QD_1 and QD_2 and initialised the $|\downarrow\downarrow\rangle$ state (see Supplementary Information, Note 2). We use the qubit in QD_1 as an ancilla to readout the hole spin in QD_2, using latched Pauli spin blockade [126, 149, 236]. The other

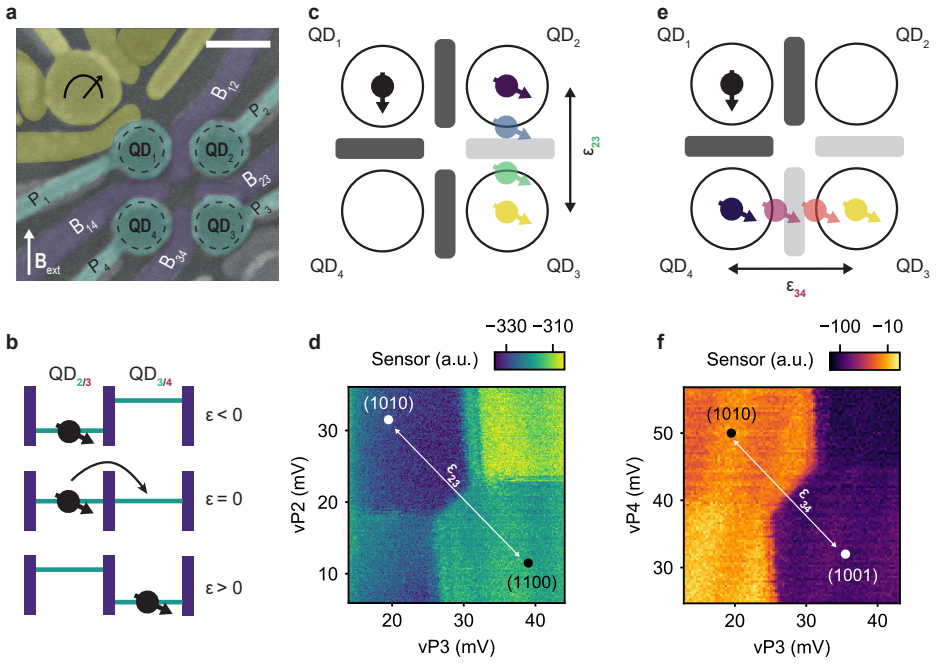

Figure 6.1: **Coherent shuttling of hole spin qubits in germanium double quantum dots - schematics and detuning axes. a**, False colored scanning electron microscope image of a representative quantum dot device. The quantum dots are formed under the plunger gates (light blue) and separated by barrier gates (dark blue) which control the tunnel couplings. A single hole transistor is defined by the yellow gates and is used as charge sensor. The scale bar corresponds to 100 nm. Unless specified otherwise, an external magnetic field of 0.25 T is applied in the direction indicated by the arrow. **b**, Schematic showing the principle of bucket brigade mode shuttling. The detuning energy $\epsilon_{23/34}$ between the two quantum dots is progressively changed such that it becomes energetically favorable for the hole to tunnel from one quantum dot to another. **c**, **e**, Schematic illustrating the shuttling of a spin qubit between QD_2 and QD_3 (e) and between QD_3 and QD_4 (i). **d**, **f**, Charge stability diagrams of QD_2-QD_3 (f) and QD_3-QD_4 (j). To shuttle the qubit from one site to another, the virtual plunger gate voltages are varied along the detuning axis (white arrow), which crosses the interdot charge transition line.

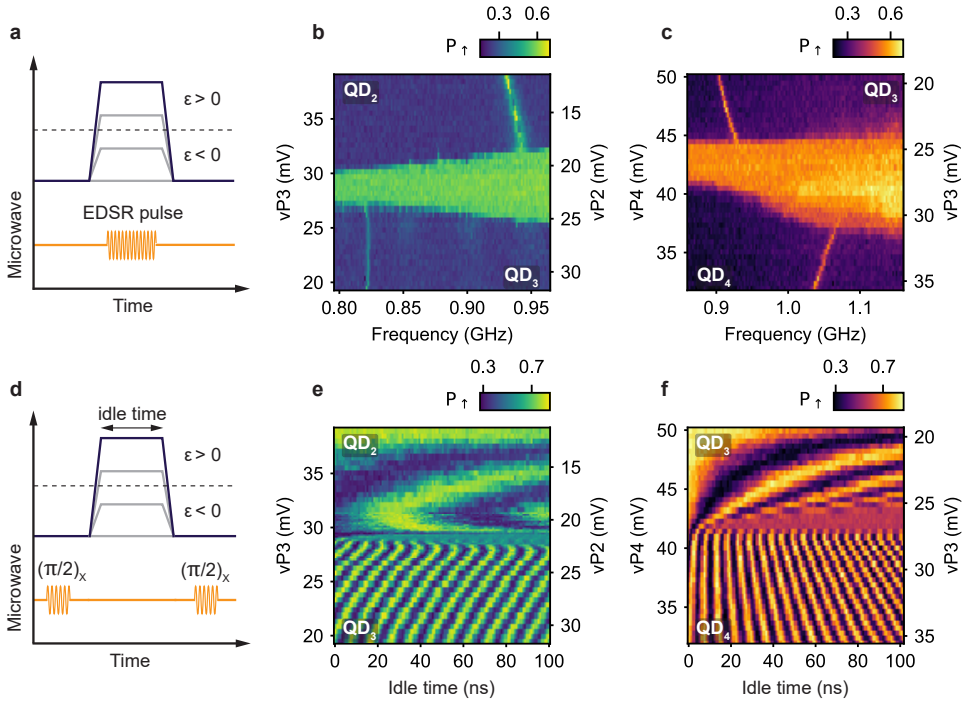

Figure 6.2: **Coherent shuttling of hole spin qubits in germanium double quantum dots - measurement results. a**, Schematic of the pulses used for the shuttling experiments shown in (b) and (c), where the resonance frequency of the qubit is probed after the application of a detuning pulse using a 4 μs EDSR pulse. **b, c** Probing of the resonance frequency along the detuning axis for the double quantum dot QD_2-QD_3 (b) and QD_3-QD_4 (c). The ramp time used to change the detuning is 40 ns for the measurement shown in (b) and 12 ns for the measurement shown in (c). Nearby the charge transition, the resonance frequency cannot be resolved due to a combination of effects discussed in Supplementary Information, Note 4. **d**, Schematic of the pulses used for coherent shuttling experiments of which the results are shown in (e) and (f). The qubit is prepared in a superposition state using a $\pi/2$ pulse and is transferred to the empty quantum dot with a detuning pulse of varying amplitude, and then brought back to its initial position after an idle time. After applying another $\pi/2$ pulse we readout the spin state. **e**, **f**, Coherent free evolution of a qubit during the shuttling between QD_2-QD_3 (e) and QD_3-QD_4 (f). Since the Larmor frequency varies along the detuning axes, the qubit initialized in a superposition state acquires a phase that varies with the idle time resulting in oscillations in the spin-up $P_\uparrow$ probabilities.

qubit starts in QD_2 and is shuttled to the other quantum dots by changing the detuning energies ($\epsilon_{23/34}$) between the quantum dots (Fig. 6.1.b, c and e). The detuning energies are varied by pulsing the plunger gate voltages as illustrated in Fig. 6.1.d and f. Additionally, we increase the tunnel couplings between QD_2-QD_3 and QD_3-QD_4 before shuttling to allow for adiabatic charge transfer. The hole carrying the spin remains in its orbital ground state and with increasing $|\epsilon|$, the charge becomes localized in the quantum dot with the lowest chemical potential as displayed in Fig. 6.1.b. In our experiments, we tune to have adiabatic evolution with respect to charge, and study adiabatic and diabatic shuttling with respect to spin.

The g-tensor of hole spin qubits in germanium is sensitive to the local electric field. Therefore, the Larmor frequency (f_L) is different in each quantum dot [140, 141, 233]. We exploit this effect to confirm the shuttling of a hole spin from one quantum dot to another. In Fig. 6.2.a. we show the experimental sequence used to measure the qubit resonance frequency, while changing the detuning to transfer the qubit. Fig 6.2.b (c) shows the experimental results for spin transfers from QD_2 to QD_3 (QD_3 to QD_4). Two regions can be clearly distinguished in between which f_L varies by 110 (130) MHz. This obvious change in f_L clearly shows that the hole is shuttled from QD_2 to QD_3 (QD_3 to QD_4) when applying a sufficiently large detuning pulse. To investigate whether such transfer is coherent, we probe the free evolution of qubits prepared in a superposition state after applying a detuning pulse (Fig. 6.2.d) [257]. The resulting coherent oscillations are shown in Fig. 6.2.e (f). They are visible over the full range of voltages spanned by the experiment and arise from a phase accumulation during the idle time. Their frequency f_{osc} is determined by the difference in resonance frequency between the starting and end point in detuning as shown in Fig. 6.9 in the Supplementary Information. The abrupt change in f_{osc} marks the point where the voltage pulse is sufficiently large to transfer the qubit from QD_2 to QD_3 (QD_3 to QD_4). These results clearly demonstrate that single hole spin qubits can be coherently transferred.

6.3. THE EFFECT OF STRONG SPIN-ORBIT INTERACTION ON SPIN SHUTTLING

The strong spin-orbit interaction in our system has a significant impact on the spin dynamics during the shuttling. It appears when shuttling a qubit in a $|\downarrow\rangle$ state between QD_2 and QD_3 using fast detuning pulses with voltage ramps of 4 ns. Doing this generates coherent oscillations shown in Fig. 6.3.b that appear only when the qubit is in QD_3. They result from the strong spin-orbit interaction and the use of an almost in-plane magnetic field [158]. In this configuration, the direction of the spin quantization axis depends strongly on the local electric field [127, 260–263] and can change significantly between neighbouring quantum dots. Therefore, rapid shuttling of a hole results in a change of angle between the spin state and the local spin quantization axis. In particular, a qubit in a basis state in QD_2 becomes a qubit in a superposition state in QD_3 when it is shuttled diabatically with respect to the change in quantization axis. Consequently, the spin precesses around the quantization axis of QD_3 until it is shuttled back (Fig. 6.3.a). This leads to qubit rotations and the aforementioned oscillations.

While these oscillations are clearly visible for voltage pulses with ramp times t_{ramp} of few nanoseconds, they fade as the ramp times are increased, as shown in Fig. 6.3.c, and vanish for $t_{ramp} > 30$ ns. The qubit is transferred adiabatically and can follow the change in quantization axis and therefore remains in the spin basis state in both quantum dots. From the visibility of the oscillations, we estimate that the quantization axis of QD_3 (QD_4) is tilted by at least 42° (33°) compared to the quantization axis of QD_2 (QD_3). These values are corroborated by independent estimations made by fitting the evolution of f_L along the detuning axes (see Supplementary Information, Note 5).

Fig. 6.3.d and Fig. 6.3.e display the magnetic field dependence of the oscillations generated

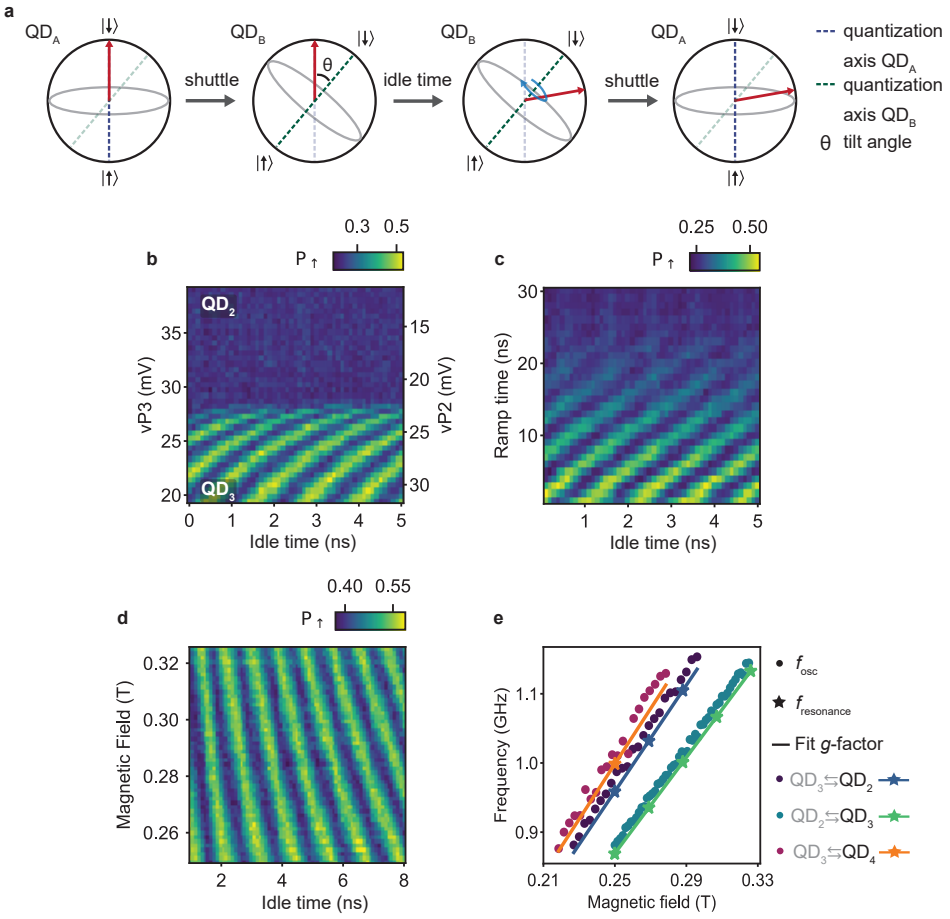

Figure 6.3: **Rotations induced while shuttling by the difference in quantization axes. a**, Schematic explaining the effect of the change in quantization axis direction that the qubit experiences during the shuttling process. The difference in quantization axis between quantum dots is caused by the strong spin-orbit interaction. **b**, Oscillations induced by the change in quantization axis while shuttling diabatically a qubit in a $|\downarrow\rangle$ state between QD_2 and QD_3. Ramp times of 4 ns are used for the detuning pulses. Note that the oscillations have a reduced visibility, meaning that the difference in quantization axes does not induce a full spin flip. The angle between the quantization axes of the two quantum dots can be estimated from the amplitude of the oscillations, see Supplementary Information, Note 5.**c**, Oscillations due to the change in quantization axis at a fixed point in detuning, as function of the voltage pulse ramp time used to shuttle the spin. When the ramp time is long enough, typically above 30 ns, the spin is shuttled adiabatically and the oscillations vanish. **d**, Magnetic-field dependence of the oscillations induced by the difference in quantization axis. **e**, Frequency of the oscillations f_{osc} induced by the change in quantization axis as a function of magnetic field for different shuttling processes. The oscillation frequency f_{osc} for QD_3 is extracted from measurements displayed in (d) (and similar experiments for the other quantum dot pairs) and is plotted with points. f_{osc} scales linearly with the magnetic field. Comparing f_{osc} with resonance frequencies measured using EDSR pulses (data points depicted with stars) reveals that f_{osc} is given by the Larmor frequency of the quantum dot towards which the qubit is shuttled (black label).

by diabatic shuttling. Their frequencies f_{osc} increase linearly with the field and match the Larmor frequencies f_L measured for a spin in the target quantum dot. This is consistent with the explanation that the oscillations are due to the spin precessing around the quantization axis of the second quantum dot.

6.4. SHUTTLING PERFORMANCE

To quantify the performance of shuttling a spin qubit, we implement the experiments depicted in Fig. 6.4.a, c and d [247, 257] and study how the state of a qubit evolves depending on the number of subsequent shuttling events. For hole spins in germanium, it is important to account for rotations induced by the spin-orbit interaction. This can be done by aiming to avoid unintended rotations, or by developing methods to correct them. An example of the first approach is transferring the spin qubits adiabatically. This implies using voltage pulses with ramps of tens of nanoseconds, which are significant with respect to the dephasing time. However, this strongly limits the shuttling performance (see Fig. 6.16 in the Supplementary Information). Instead, we can mitigate rotations by carefully tuning the duration of the voltage pulses, such that the qubit performs an integer number of 2π rotations around the quantization axis of the respective quantum dot. This approach is demanding, as it involves careful optimization of the idle times in each quantum dot as well as the ramp times, as depicted in Fig. 6.4.b. However, it allows for fast shuttling, with ramp times of typically 4 ns and idle times of 1 ns, significantly reducing the dephasing experienced by the qubit during the shuttling. We employ this strategy in the rest of our experiments.

We first characterize the shuttling of a spin qubit initialized in a basis state. We do this by preparing a qubit in a $|\uparrow\rangle$ or $|\downarrow\rangle$ state and transferring it multiple times between the quantum dots. Fig. 6.5.a and b display the spin-up fraction $P_\uparrow$ measured as a function of the number of shuttling steps n. The probability of ending up in the initial state shows a clear exponential dependence on n. No oscillations of $P_\uparrow$ with n are visible, confirming that the pulses have been successfully optimized to account for unwanted spin rotations. We extract the characteristic decay constants n^* by fitting the data for the shuttling of qubits prepared in $|\uparrow\rangle$ and $|\downarrow\rangle$ states separately as they originate from distinct sets of experiments. In all cases, we find a characteristic decay $n^* \simeq 3000$ shuttles between quantum dots, corresponding to a polarization transfer fidelities of $F = \exp(-1/n^*) \simeq 99.97$ % per shuttle within the sequence. This is similar to the fidelities reached in silicon devices [118, 257], despite the anisotropic g-tensors due to the strong spin-orbit interaction in our platform.

The exponential decay of the spin polarization to approximately 0.5 can emerge from different effects. At the charge anticrossing, the spin polarization life time is strongly reduced (see Fig. 6.10 in the Supplementary Information), due to high frequency charge noise and coupling to phonons [156]. Passing the charge anticrossing repeatedly thus leads to a randomization of the spin. Moreover, while the qubit starts in a basis state, it undergoes coherent rotations due to the diabatic spin shuttling and thus it is in a superposition state in the second quantum dot. The qubit, although initially in the spin basis state, then becomes sensitive to dephasing which can also lead to an exponential decay of $P_\uparrow$. The experimental decay observed probably results from a combination of these mechanisms.

We emphasize that the exact impact of dephasing on the performances of the shuttling of spin basis state depends on the difference in quantization axes of the quantum dots and on the pulse sequence used (see Supplementary Information, Note 11). In our experiment, the dephasing is probably mitigated by a decoupling effect induced by repeatedly waiting in the initial quantum dot (see explanation Supplementary Information, Note 11). While extrapolating this result to a long chain of quantum dots is not straightforward, similar noise-averaging effects may occur in the presence of spatially correlated noise in the chain [264]. In the absence of decoupling effects

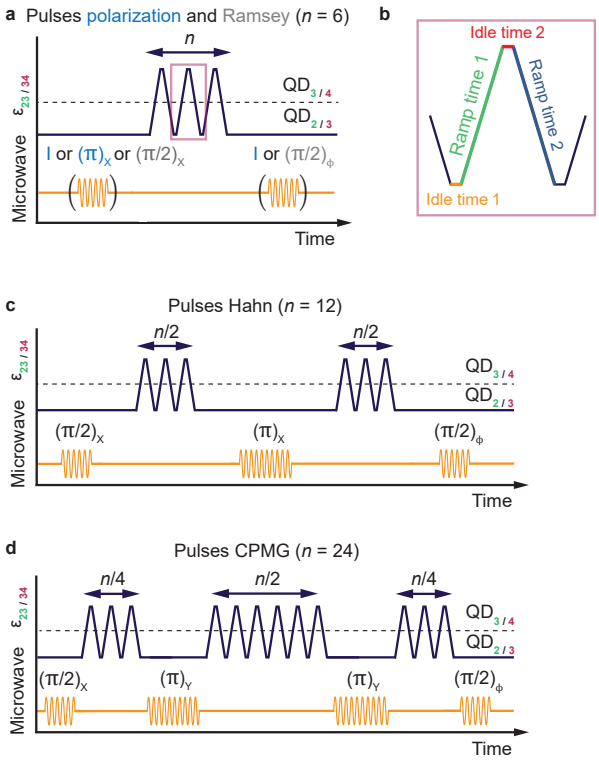

Figure 6.4: **Quantifying the performance for the shuttling of basis states in double quantum dots - pulse sequences. a**, Schematic of the pulse sequence used for quantifying the performance of shuttling basis states (blue) or a superposition state (grey). The spin qubit is prepared in the quantum dot where the shuttling experiment starts, by either applying an identity gate (shuttling a $|\downarrow\rangle$ state), a $(\pi)_X$ pulse (shuttling a $|\uparrow\rangle$ state) or $(\pi/2)_X$ pulse (shuttling a superposition state, also referred to as Ramsey shuttling experiments). Detuning pulses are applied to the plunger gates to shuttle the hole from one quantum dot to another, back and forth, and finally the appropriate pulses are applied to prepare for readout. Moving the qubit from one quantum dot to another is counted as one shuttling event $n = 1$. Since the hole always needs to be shuttled back for readout, n is always an even number. The schematic shows an example for $n = 6$. **b**, Zoom-in on the detuning pulses used for the shuttling. To make an integer number of 2π rotation(s) around the quantization axis of the second quantum dot, all ramp and idle times in the pulse need to be optimized. **c**, Pulse sequence used for implementing a Hahn echo shuttling experiment. In the middle of the shuttling experiment, an echo pulse $(\pi)_X$ is applied in the quantum dot where the spin qubit was initially prepared. Example for $n = 12$. **d**, Pulse sequence for a CPMG shuttling experiment. Two $(\pi)_Y$ pulses are inserted between the shuttling pulses. Example for $n = 24$.

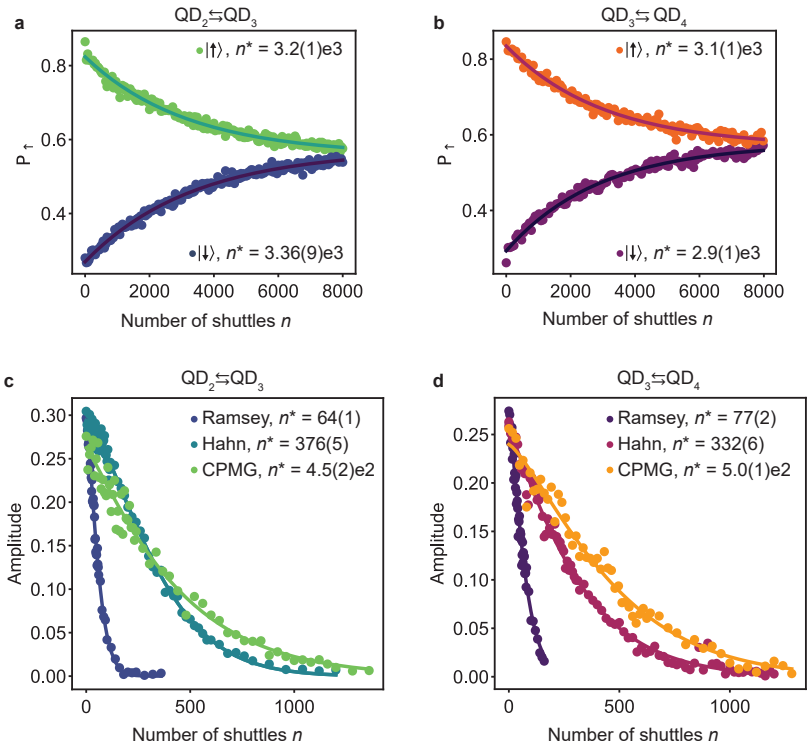

Figure 6.5: **Quantifying the performance for the shuttling coherent spin states in double quantum dots - results. a, b**, Spin-up probabilities $P_\uparrow$ measured after shuttling n times a qubit prepared in a spin basis state between QD_2 and QD_3 (c) and between QD_3 and QD_4 (d). The decay of $P_\uparrow$ as a function of n is fitted to an exponential function $P_\uparrow = P_0 \exp(-n/n^*) + P_{sat}$. **c, d**, Performance of the shuttling of superposition state between QD_2 and QD_3 (g) and QD_2 and QD_3 (h) for different shuttling sequences. The decay of the coherent amplitude A of the superposition state are fitted by $A_0 \exp(-(n/n^*)^\alpha)$ where α is a fitting parameter. The error bars indicate one standard deviation from the best fits.

and for the purpose of shuttling basis states, adiabatic shuttling still provides a good alternative as we find n^* to remain above 1000, corresponding to fidelities per shuttle within the sequence above 99.90 % (see Supplementary Information, Note 11).

We now focus on the performance of coherent shuttling. We prepare a superposition state via an EDSR $(\pi/2)_X$ pulse, shuttle the qubit, apply another $\pi/2$ pulse and measure the spin state. Importantly, one must account for $\hat{z}$-rotations experienced by the qubits during the experiments and the corresponding phase accumulation defined with respect to the qubit rotating frame in the initial quantum dots. The latter can be equivalently defined with respect to the lab frame. Therefore, we vary the phase of the EDSR pulse ϕ for the second $\pi/2$ pulse. For each n, we then extract the amplitude A of the $P_\uparrow$ oscillations that appear as function of ϕ [247, 257]. Fig. 6.5.c, d show the evolution of A as a function of n for shuttling between adjacent quantum dots. We fit the experimental results using $A_0 \exp(-(n/n^*)^\alpha)$ and find characteristic decay constants $n^*_{23} = 64 \pm 1$ and $n^*_{34} = 77 \pm 2$. Remarkably, these numbers compare favourably to $n^* \simeq 50$ measured in a SiMOS electron double quantum dot [257], where the spin-orbit coupling is weak.

The exponents, $\alpha_{23} = 1.36 \pm 0.05$ and $\alpha_{34} = 1.28 \pm 0.06$, characterize the spectrum of the noise experienced by the qubit while it is shuttled and suggest that the noise is neither purely quasi static nor white. The non-integer values of α contrast with observations in silicon [247, 257], and suggest that the shuttling of hole spins in germanium is limited by other mechanisms. Two types of errors can be distinguished. Errors may occur during the diabatic part of the spin dynamics. On the other hand, errors can also be induced by the dephasing experienced by the qubits during the finite time spent in each quantum dot, including the ramp times (see Supplementary Information, Note 11). To investigate the effect of dephasing, we modify the shuttling sequence and include a $(\pi)_X$ echoing pulse in the middle as displayed in Fig. 6.4.d. We note that the echoing pulses are defined with respect to the rotating frame of the qubit in the starting quantum dots. Fig. 6.5.c and d show the experimental results and it is clear that in germanium the coherent shuttling performance is improved significantly using an echo pulse: we can extend the shuttling by a factor of four to five, reaching a characteristic decay of more than 300 shuttles. Similarly, the use of CPMG sequences incorporating two decoupling $(\pi)_Y$ pulses (Fig. 6.4.d) allows further, though modest, improvements. These enhancements in the shuttling performance confirm that dephasing is limiting the shuttling performance, contrary to observations in SiMOS [257]. We speculate that the origin of the difference is two-fold. Firstly, due to the stronger spin-orbit interaction, the spin is more sensitive to charge noise, resulting in shorter dephasing times. Secondly, the excellent control over the potential landscape in germanium allows minimizing the errors which are due to the shuttling itself.

6.5. SHUTTLING THROUGH INTERMEDIATE QUANTUM DOTS

For distant qubit coupling, it is essential that a qubit can be coherently shuttled through chains of quantum dots. This is more challenging, as it requires control and optimization of a larger amount of parameters while more noise sources may couple to the system. Within a chain, a quantum dot will have at least two neighbours. To transport spin states from one site to another they have to pass through intermediates quantum dots. Therefore, an array of three quantum dots could be considered as the minimum size to explore the performance of shuttling in a chain.

We perform two types of experiments to probe the shuttling through chains of quantum dots, labelled corner shuttling and triangular shuttling. Fig. 6.6.b shows a schematic of the corner shuttling, which consists of transferring a qubit from QD_2 to QD_3 to QD_4 and back along the same route. The triangular shuttling, depicted in Fig. 6.6.c, consists of shuttling the qubit from QD_2 to QD_3 to QD_4, and then directly back to QD_2, without passing through QD_3 (for the charge stability diagram QD_4-QD_2 and a detailed description see Supplementary Information, Note 8).

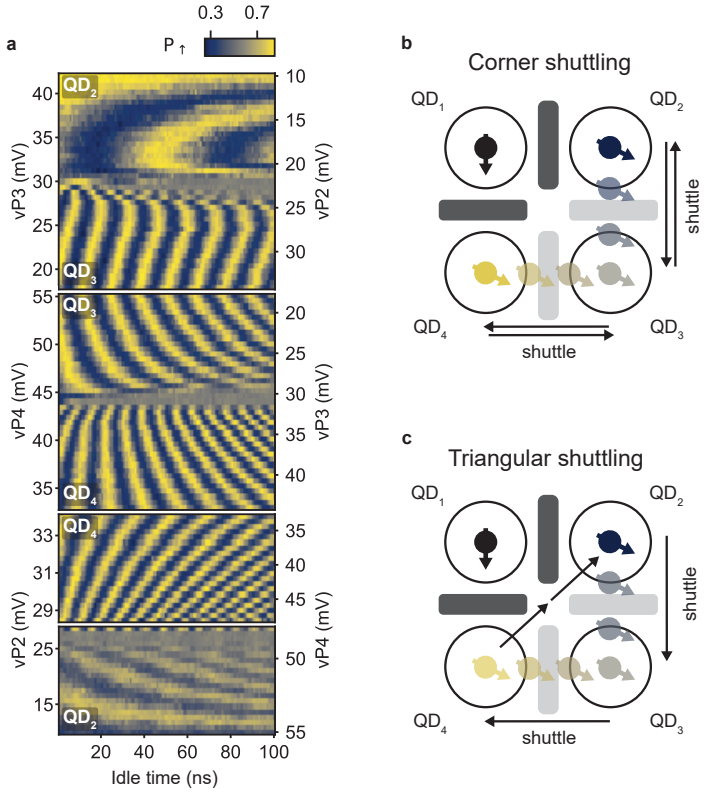

Figure 6.6: **Coherent shuttling through quantum dots - free evolution and schematics. a**, Results of free evolution experiments, similar to those displayed in Fig. 6.2.e and f for the corner and triangular shuttling processes. In these experiments, the amplitude of the detuning pulse is increased in steps, in order to shuttle a qubit from QD_2 to QD_3 and back (top panel), from QD_2 to QD_3 to QD_4 and back (second panel). The measurement in the third panel is identical to the measurement in the second panel, but the final point in the charge stability diagram is stepped towards the charge degeneracy point between QD_2 and QD_4. In the bottom panel the qubit is shuttled in a triangular fashion: from QD_2 to QD_3 to QD_4 to QD_2. The ramp times for this experiment are chosen in such a way that the shuttling is adiabatic with respect to the changes in quantization axis. **b**, **c**, Schematic illustrating the shuttling of a spin qubit around the corner: from QD_2 to QD_3 to QD_4 and back via QD_3 (b) and in a triangular fashion: from QD_2 to QD_3 to QD_4 and directly back to QD_2 (c). The double arrow from QD_4 to QD_2 indicates that this pulse is made in two steps, in order for the spin to shuttle via the charge degeneracy point of QD_4 - QD_2 and avoid crossing charge transition lines.

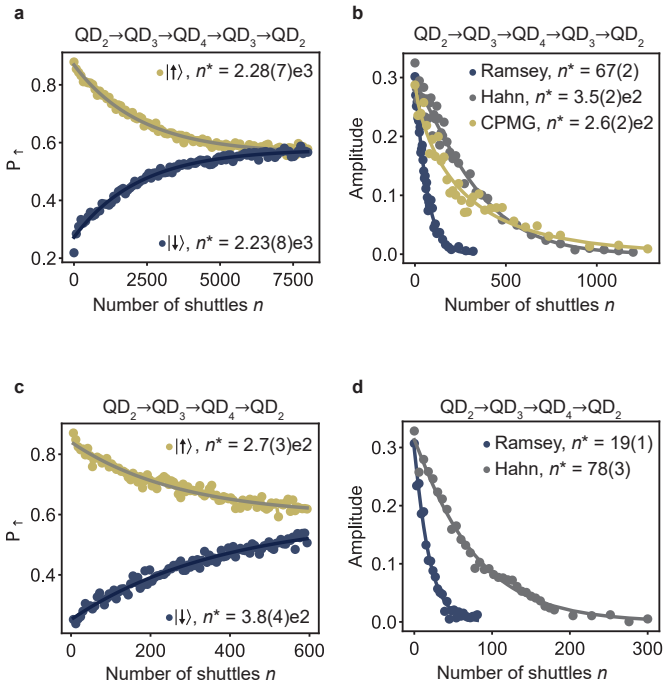

Figure 6.7: **Coherent shuttling through quantum dots. a**, **c**, Performance for the corner shuttling (a) and the triangular shuttling (c) of a qubit prepared in the basis states. **b**, **d**, Performance for shuttling a qubit prepared in a superposition state for the corner shuttling (b) and the triangular shuttling (d) and for different shuttling sequences. Shuttling performance for different processes are summarized in the Supplementary Information, Table 6.1. The error bars indicate one standard deviation from the best fits.

To probe the feasibility of shuttling through a quantum dot, we first measure the free evolution of a coherent state while varying the detuning between the respective quantum dots. The results are shown in Fig 6.6.a. We find a remarkably clear coherent evolution for hole spin transfer from QD_2 to QD_3 to QD_4 and to QD_2. We observe one sharp change in the oscillation frequency for each transfer to the next quantum dot. We also note that after completing one round of the triangular shuttling, the phase evolution becomes constant, in agreement with a qubit returning to its original position. We thereby conclude that we can shuttle through quantum dots as desired.

We now focus on quantifying the performance of shuttling through quantum dots by repeated shuttling experiments. To allow comparisons with previous experiments, we define n as the number of shuttling steps between two quantum dots. Meaning that one cycle in the corner shuttling experiments results in $n = 4$, while a loop in triangular shuttling takes $n = 3$ steps. The results for shuttling basis states are shown in Fig. 6.7.a and Fig. 6.7.c. We note that the spin polarization decays faster compared to the shuttling in double quantum dots, in particular for the triangular shuttling. The corresponding fidelities per shuttle within the sequence are $F \simeq 99.96$ % for the corner shuttling and $F \geq 99.63$ % for the triangular shuttling.

For the corner shuttling, the faster decay of the basis states suggests a slight increase of the systematic error per shuttling. This may originate from the use of a more elaborated pulse sequence, which makes pulse optimization more challenging. Nonetheless, the characteristic decay constant n^* remains above 2000 and corresponds to effective distances beyond 300 μm (taking a 140 nm quantum dot spacing). The fast decay for the triangular shuttling is likely originating from the diagonal shuttling step. The tunnel coupling between QD_2 and QD_4 is low and more challenging to control, due to the absence of a dedicated barrier gate. The low tunnel coupling demands slower ramp times ($t_{ramp} \simeq 36$ ns) for the hole transfer. This increases the dephasing experienced by the qubit during each shuttle and also the time spent close to the (1,1,0,0)-(1,0,0,1) charge degeneracy point, where fast spin randomization will likely occur.

Remarkably, we find that the performance achieved for coherent corner shuttling (as shown in Fig. 6.7.b) are comparable to those of coherent shuttling between neighbouring quantum dots. This stems from the performance being limited by dephasing. However, the performance for the CPMG sequence appears inferior when compared to the single echo-pulse sequence. Since the shuttling sequence becomes more complex, we speculate that it is harder to exactly compensate for the change in quantization axes. Imperfect compensation may introduce transversal noise, which is not fully decoupled using the CPMG sequence. Alternatively, simulations shown in Fig. 6.21 in the Supplementary Information suggest that the decoupling achieved using a CPMG sequence depends on the idle time in the initial quantum dots. For an idle time corresponding to a $(2k+1)\pi$ (with k an integer) phase accumulation, the decoupling achieved using either an ideal echo or a CPMG sequence is very similar. In such a scenario, the effect of imperfect decoupling pulses would become more apparent in a CMPG sequence and would lead to decreased performance.

The performance of the coherent triangular shuttling, displayed in Fig. 6.7.d, fall short compared to the corner shuttling. Yet, the number of shuttles reached remains limited by dephasing as shown by the large improvement of n^* obtained using dynamical decoupling. The weaker performance are thus predominantly a consequence of the use of longer voltage ramps. A larger number of coherent shuttling steps may be achieved by increasing the diagonal tunnel coupling, which could be obtained by incorporating dedicated barrier gates.

6.6. CONCLUSION

We have demonstrated coherent spin qubit shuttling through quantum dots. While holes in germanium provide challenges due to an anisotropic g-tensor, we find that spin basis states can be

shuttled $n^* = 2230$ times and coherent states up to $n^* = 67$ times and even up to $n^* = 350$ times when using echo pulses. The small effective mass and high uniformity of strained germanium allow for a comparatively large quantum dot spacing of 140 nm. This results in effective length scales for shuttling basis states of $l_{\mathrm{spin}} = 312$ µm and for coherent shuttling of $l_{\mathrm{coh}} = 9$ µm. By including echo pulses we can extend the effective length scale to $l_{\mathrm{coh}} = 49$ µm. These results compare favourably to effective lengths obtained in silicon [247, 257–259]. However, we note that, in general, extrapolating the performance of shuttling experiments over few sites to predict the performance of practical shuttling links requires caution. Quantum dot chains that would allow to couple spin qubits over appreciable length scales will put higher demands on tuning, uniformity, and the ability to tune all the couplings, making the optimization of the shuttling more challenging. Moreover, the spin dynamics and thus the coherent shuttling performance will depend on the noise in the quantum dot chain. For example, if the noise is local, echo pulses may prove less effective. However, in that case, motional narrowing [253, 255, 259, 264–266] may facilitate the shuttling.

Furthermore, operating at even lower magnetic fields will boost the coherence times [127, 158, 190] and thereby increase the shuttling performance. Moreover, at lower magnetic fields the Larmor frequency is lower, which eases the requirements for the precision of the timing of the shuttling pulses. At very low fields, charge noise might not be the limiting noise source anymore and even further improvements may be achieved exploiting purified germanium [127, 158, 190]. Finally, shuttling could help mitigate problems in qubit addressability which may arise at low magnetic field.

While we have focused on bucket-brigade-mode shuttling, our results also open the path to conveyor-mode shuttling in germanium, where qubits would be coherently displaced in propagating potential wells using shared gate electrodes. This complementary approach holds promise for making scalable mid-range quantum links and has recently been successfully investigated in silicon [259], though on limited length scales. For holes in germanium, the small effective mass and absence of valley degeneracy will be beneficial in conveyor-mode shuttling. Rotations induced by the spin-orbit interaction while shuttling in conveyor-mode could be compensated by applying an appropriate EDSR pulse after the qubit transfer. Such methods could also be used in bucket-brigade-mode shuttling, as suggested by preliminary experiments shown in Supplementary Information, Note 12. It may allow for even faster qubit transfers and thus shuttling over longer distances.

Importantly, quantum links based on shuttling and spin qubits are realized using the same manufacturing techniques. Their integration in quantum circuits may provide a path toward networked quantum computing.

6.7. SUPPLEMENTARY INFORMATION

NOTE 1: EXPERIMENTAL PROCEDURE

To perform the experiments presented, we follow a systematic procedure composed of several steps. We start by preparing the system in a (1,1,1,1) charge state with the hole spins in QD_1 and QD_2 initialized in a $|\downarrow\rangle$ state, while the other spins are randomly initialized. Subsequently, QD_3 and QD_4 are depleted to bring the system in a (1,1,0,0) charge configuration. After that, the virtual barrier gate voltage vB_{12} is increased to isolate the ancilla qubit in QD_1. The tunnel couplings between QD_2 and QD_3 and, depending on the experiment, between QD_3 and QD_4 are then increased by lowering the corresponding barrier gate voltages on vB_{23} and vB_{34}. This concludes the system initialization.

Thereafter, the shuttling experiments are performed. Note that to probe the shuttling between QD_3 and QD_4, the qubit is first transferred adiabatically (with respect to the change in quantization axis) from QD_2 to QD_3. To determine the final spin state after the shuttlings, the qubit is trans-

ferred back adiabatically to QD_2. Next, the system is brought back in the (1,1,1,1) charge state, the charge regime in which the readout is optimized. This is done by first increasing vB_{23} and vB_{34}, then decreasing vB_{12} and finally reloading one hole in both QD_3 and QD_4. We finally readout the spin state via latched Pauli spin blockade by transferring the qubit in QD_1 to QD_2 and integrating the signal from the charge sensor for 7 µs. Spin-up probabilities are determined by repeating each experiment a few thousand times. Details about the experimental setup can be found in section 2.3 of this thesis.

NOTE 2: SUB-NANOSECOND RESOLUTION ON VOLTAGE PULSES

For these experiments, we use voltage pulses applied to the electrostatic gates by the arbitrary wave form generators (AWGs). These pulses are compiled as a sequence of ramps, using control software. The ramps are defined by high precision floating points: time stamps and voltages. The maximum resolution in time is set by the maximum sample rate of the AWGs, which is 1 GSa/s and which translates to a resolution of 1 ns. Using this sample rate, the signal that is outputted by the AWGs has discrete steps, as depicted in Fig. 6.8.a. Simply moving this sampled pulse in time is only possible with a precision of 1 ns. However, it is possible to achieve sub-nanosecond resolution by slightly adjusting the voltages of the pulse instead. As illustrated in Fig. 6.8.a, in this way it is possible to delay a pulse with less than 1 ns. Quantitatively: to achieve a time delay of τ, the voltages forming the ramp are shifted by $-\tau \frac{\mathrm{d}V_{\mathrm{ramp}}(t)}{\mathrm{d}t}$. The output of the AWGs has a higher order low-pass filter with a cut-off frequency of approximately 400 MHz. This filter smoothens the output signal and effectively removes the effect of the time discretization, as is shown in Fig. 6.8.b. The time shift of the pulse is not affected by the filter, since it does not change the frequency spectrum of the pulse. To summarize, combining the high precision in the voltages of the pulse with the output filtering of the AWGs allows to output a smooth voltage ramp that is delayed by τ <1 ns, despite the limited sampling rate. Applying this technique to all voltage ramps results in sub-nanosecond resolution on the overall pulse sequence.

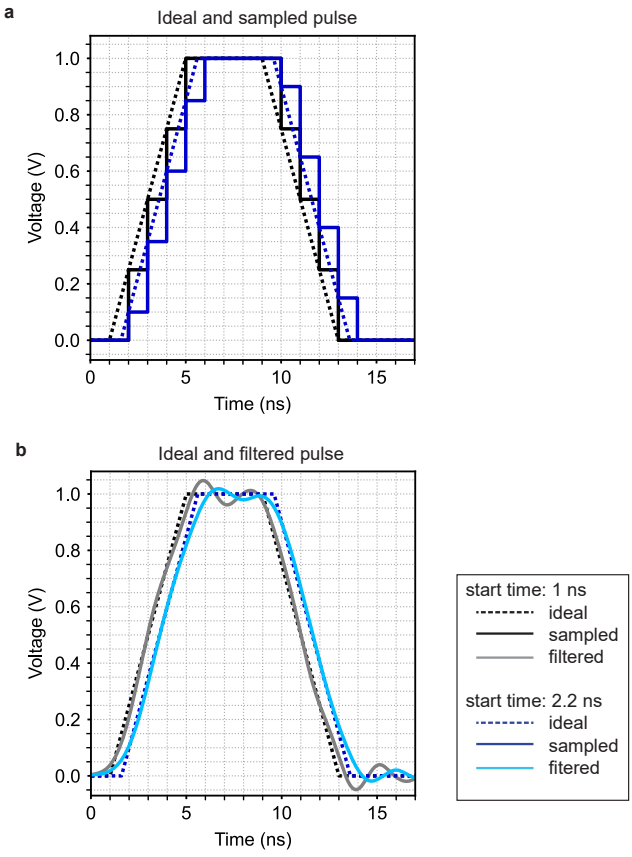

Figure 6.8: **AWG pulses with sub-nanosecond precision. a**, Ideal voltage pulse starting at 1 ns (dotted black) and ideal voltage pulse delayed by 0.6 ns with respect to the first one (dotted blue). For both pulses, the discretized sampling is plotted in solid lines. The delay between the two pulses combined with the sampling, leads to a shift of the voltage steps. **b**, Ideal pulses (starting at 1 ns and 1.6 ns) and pulses as outputted by the AWG after filtering without (light grey) and with the 0.6 ns delay (light blue). The filtering clearly smoothens the sampled pulses such that the outputted signals closely resemble the ideal pulses.

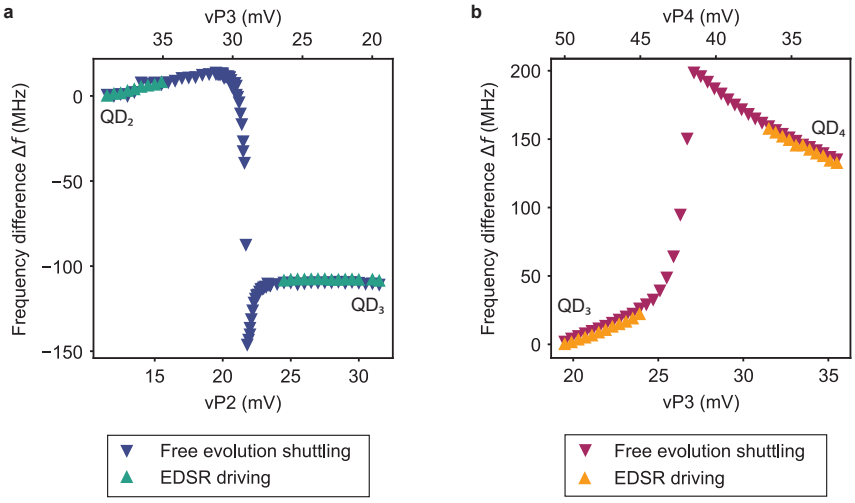

Figure 6.9: **Evolution of the Larmor frequency for shuttling in double quantum dots. a**, **b**, Larmor frequency differences $\Delta f = f_L(\text{vP2, vP3}) - f_L^{QD2}$ (a) and $\Delta f = f_L(\text{vP3, vP4}) - f_L^{QD3}$ (b) measured along the detuning axis of QD_2-QD_3 (a) and QD_3-QD_4 (b). The quantum dot where the shuttling experiment starts is taken as the reference point for the frequency. Δf is independently evaluated from measurements of the resonance frequency using an EDSR pulse (data displayed in Fig. 1.g and k) and from the frequency of the coherent oscillations that appear when a qubit is shuttled in a superposition state (data displayed in Fig. 1.h and l). Both sets of data points overlap in (a) and (b), confirming that the coherent oscillations arise due to a change in Larmor frequency along the detuning axis. For the free evolution experiments, the shuttling between QD_2 and QD_3 (shown in (a)) is completely adiabatic (ramp times of 40 ns) while the shuttling between QD_3 and QD_4 (shown in (b)) is only partially adiabatic (ramp times of 4 ns). In the latter case, the frequency difference measured is barely affected by the limited adiabaticity as the visibility M of the oscillations induced by the change in quantization axes ($M < 0.1$ from Fig.6.11) is sufficiently small compared to that of the oscillations arising from the phase evolution of the superposition state ($V \approx 0.5$ when the hole is in QD_4). Moreover, the Larmor frequency of spins in both QD_3 and QD_4 are close to 1 GHz. The free evolution experiments were performed with a time resolution of 1 ns, meaning that the oscillations due to the diabaticity of the shuttling only show up as an aliasing pattern and do not disturb the oscillations due to free evolution.

	n^*, $\|\downarrow\rangle$ transfer	n^*, $\|\uparrow\rangle$ transfer	n^*, $\frac{\|\downarrow\rangle - i\|\uparrow\rangle}{\sqrt{2}}$ transfer	α, $\frac{\|\downarrow\rangle - i\|\uparrow\rangle}{\sqrt{2}}$ transfer
$QD_2 \rightleftarrows QD_3$	$(3.36\pm0.09)\times10^3$	$(3.2\pm0.1)\times10^3$	Ramsey: 64 ± 1	1.36±0.05
			Hahn: 376 ± 5	1.44±0.04
			CPMG: $(4.5\pm2)\times10^2$	1.14±0.06
$QD_3 \rightleftarrows QD_4$	$(2.9\pm0.1)\times10^3$	$(3.1\pm0.1)\times10^3$	Ramsey: 77 ± 2	1.28±0.06
			Hahn: 332 ± 6	1.17±0.04
			CPMG: $(5.0\pm0.1)\times10^2$	1.3±0.07
Corner	$(2.23\pm0.08)\times10^3$	$(2.28\pm0.07)\times10^3$	Ramsey: 67 ± 2	1.11±0.06
			Hahn: $(3.5\pm0.2)\times10^2$	1.2±0.1
			CPMG: $(2.6\pm0.2)\times10^2$	0.76±0.07
Triangular	$(3.8\pm0.4)\times10^2$	$(2.7\pm0.3)\times10^2$	Ramsey: 19 ± 1	1.08±0.07
			Hahn: 78 ± 3	1.07±0.05

Table 6.1: **Summary of shuttling performance.** For the spin basis state shuttling experiments, the spin polarization decays are fitted by $P_0\exp(-(n/n^*))+P_{\text{sat}}$, with n the number of shuttles. For the coherent shuttling experiments, the coherence decays are fitted by $A_0\exp(-(n/n^*)^\alpha)$, where n^* represents the number of shuttles that can be achieved before the polarization or the coherence drops by $1/e$.

NOTE 3: SPIN RANDOMIZATION NEARBY THE INTERDOT CHARGE TRANSITION

In Fig. 6.2.b and c, we show the evolution of the qubit resonance frequency f_L along the detuning axis of the QD_2-QD_3 quantum dot pair and of the QD_3-QD_4 quantum dot pair. f_L is measured by shuttling the spin and applying a 4 µs long EDSR pulse on one plunger gate. While f_L can be clearly determined when the hole is well-localized in one quantum dot, it cannot be measured nearby the charge transition as the spin-up probability has a high value over the whole range of frequency spanned. We think that this is the result of a combination of different effects.

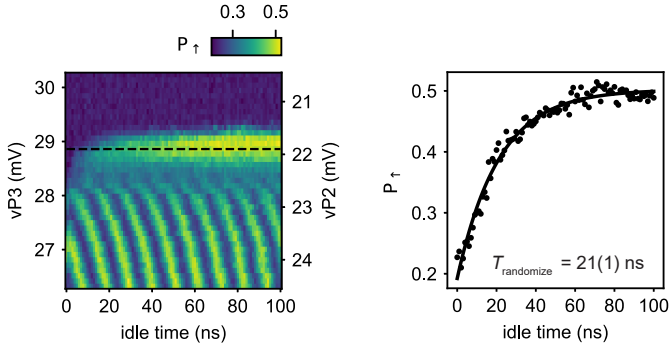

Figure 6.10: **Randomization of spin states around the QD_2 - QD_3 charge transition. a**, Shown is the result of the shuttling of a spin in the $|\downarrow\rangle$ state while changing the detuning and the idle time. Note that in contrast to the measurement shown in Fig. 6.3b of the main text, the time resolution on the x-axis is not large enough to distinguish the oscillations with gigahertz frequency, instead what is visible here is an aliasing pattern. **b**, The data plotted and fitted here correspond to a linecut of (a), taken at the dashed line. The typical time it takes for the spin to randomize (while starting in the $|\downarrow\rangle$ state) is 20 ± 1 ns and is extracted by fitting an exponential function. The error bar corresponds to one standard deviation from the best fit.

Since the two quantum dots have different quantization axes, the system effectively behaves as a flopping-mode qubit nearby the charge transition [261, 267–269] and the EDSR driving is thus expected to be more efficient. This appears, in Fig. 6.2.b, when the qubit is in QD_2: along the resonance line, we observe an alternation of high and low spin-up probabilities that witness rapid variations of the Rabi frequency. As a consequence, the power broadening increases significantly in the vicinity of the charge transition which prevents us from resolving the qubit resonance frequency. We have not observed such effects in the other quantum dots and speculate it is due to the driving efficiency and the depahsing. In this studied device, the four qubits can usually be efficiently driven with one particular plunger gate. This drivability is likely the origin why the effect disappears once the qubit is in in QD_3 in Fig. 6.2b.

The gradient of shear strains induced by the thermal contraction of the gate electrodes can lead to large increases of the Rabi frequency [145]. It is likely that this effect is enhanced in the vicinity of the charge transition, as the hole is delocalized between the two quantum dots and its wavefunction extends below the edges of several gates. Finally, nearby the charge transition, excitations to higher energy states induced by charge noise are more likely to occur [156], especially on the relatively long timescale of 4 µs. These transitions to higher energy states lead to a randomization of the spin states, which explains the large spin-up probabilities observed over the full frequency range.

This last argument is supported by the data shown in Fig. 6.10. This figure shows the result of

shuttling a qubit in a $|\downarrow\rangle$ state while changing the detuning and varying the idle time (similar to Fig. 6.3a of the main text). It becomes clear that once the spin approaches the charge anticrossing between QD_2 and QD_3 (indicated by the striped black line in Fig. 6.10a), the time it takes for the spin state to be randomized decreases very rapidly to about $T_{\text{randomize}} = 21 \pm 1$ ns (fit to an exponential decay shown in Fig. 6.10.b). The randomization of the spin close to the charge anticrossing could also be an explanation for the fact that the spin-up probability measured for shuttling basis states decays to the value of 0.5 instead of 0.

NOTE 4: QUANTIFYING THE QUANTIZATION AXIS TILT ANGLE

ESTIMATION BASED ON THE VISIBILITY OF THE OSCILLATIONS INDUCED BY THE CHANGE IN QUANTIZATION AXIS

The tilt angle θ between the quantization axis of two different quantum dots can be estimated based on the amplitude of the oscillations induced by diabatically shuttling a qubit in the $|\downarrow\rangle$ state. This approximation relies on a simple geometric construction in the Bloch sphere.

Fig. 6.11.a shows the Bloch sphere projected on the plane defined by the quantization axes of the two quantum dots (dark blue and dark green). At the beginning of the experiment, the qubit is initialized in the $|\downarrow\rangle$ state (red arrow). After shuttling to the neighboring quantum dot, the qubit state changes due to the difference between the quantization axes. In the Bloch sphere, this can be represented by rotations of the state vector around the second quantization axis. After half a period (orange arrow), the state projection on the quantization axis of the quantum dot where the experiment started differs maximally from that of the initial state. This sets the visibility M of the oscillations induced by the change of quantization axis.

In practise, this visibility is reduced due to imperfect initialization and readout. This can be taken into account by assuming that the state vectors have a norm $V < 1$ with V being the visibility of Rabi oscillations measured in the quantum dot where the shuttling experiment starts. We neglect relaxation which is irrelevant at the time scale of few nanoseconds [155] and thus assume that the norm of the vector state stays constant during the rotations. We find that:

$$\theta = \frac{1}{2} \arccos(1 - 2M/V) \text{ with } 0 \leq \theta \leq \pi. \tag{6.1}$$

We use this expression to evaluate θ_{23} (θ_{34}), the tilt angle between the quantization axes of QD_2 and QD_3 (QD_3 and QD_4). Fig. 6.11.b and c show the oscillations induced by the change in quantization axis as function of the pulse ramp time t_{ramp}. The amplitude $M/2$ of these oscillations is fitted and plotted in 6.11.d. As discussed in the main text, the amplitude of the oscillations drop rapidly to zero as t_{ramp} increases, because the shuttling becomes more adiabatic with respect to the difference in quantization axis. For the evaluation of θ we use the amplitude $M/2 = 0.14$ (0.07) of the oscillations at the shortest $t_{\text{ramp}} = 2$ ns. We remark that there is no clear saturation of M at the smallest ramp times, which suggests that the shuttling process is still not fully diabatic and that higher visibilities could be achieved by shuttling faster. Rabi oscillations for the driving of the qubit in QD_2 (QD_3) have a visibility of $V = 0.61$ (0.48) giving us $\theta_{23} \geq 42°$ ($\theta_{34} \geq 33°$). These large values for θ illustrate the strong influence of the local electric field on the direction of the quantization axis in germanium hole spin qubits operated with an in-plane external magnetic field.

ESTIMATIONS BASED ON FITS WITH A FOUR-LEVEL MODEL

To get an additional independent evaluation of the tilt angles, we can fit the evolution of the qubit resonance with a four-level model. To derive such a model, we consider a single hole in a germanium double quantum dot placed in an external magnetic field B. We assume that there is a finite tunnel coupling t_c between the two quantum dots QD_A and QD_B and their quantization

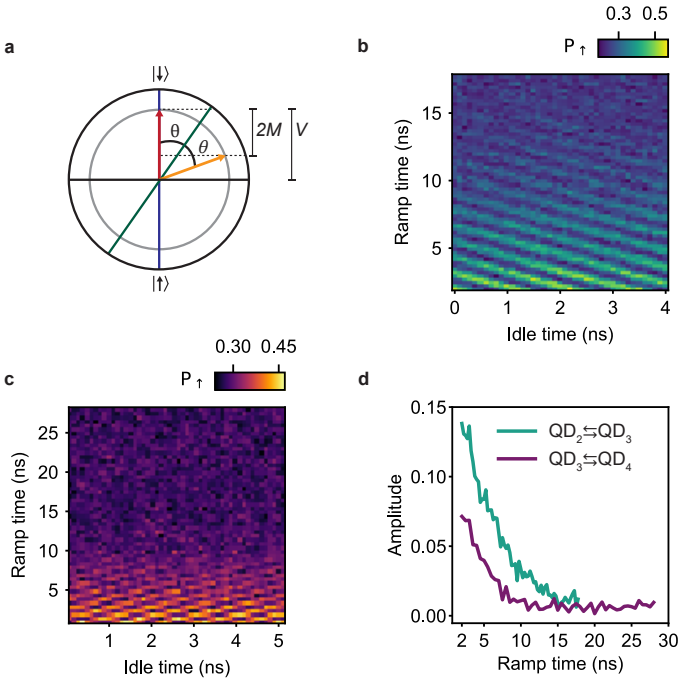

Figure 6.11: **Estimation of the tilt angle based on the amplitude of the oscillations induced by the difference in quantization axis. a,** Geometric construction in the Bloch sphere allowing to determine the tilt angle θ between the quantization axes of adjacent quantum dots (blue and green). θ is determined from the visibility M of the oscillations induced by the change in quantization axes and the visibility of the Rabi oscillations V. **b**, **c**, Oscillations induced while shuttling a qubit in a $|\downarrow\rangle$ state between QD_2 and QD_3 (b) and between QD_3 and QD_4 (c) for increasing ramp times. **d**, Amplitude of the oscillations as function of the ramp times.

axes are tilted with respect to each other by an angle θ. This last assumption is sufficient to take into account all effects of the spin-orbit interaction, providing a suitable basis transformation and a renormalization of the tunneling terms.

The system can be described in the basis $\{|A,\uparrow_A\rangle, |A,\downarrow_A\rangle, |B,\uparrow_A\rangle, |B,\downarrow_A\rangle\}$, where 'A' or 'B' indicates the position of the hole (in quantum dot QD_A or QD_B) and $\uparrow_A$ or $\downarrow_A$ specifies its spin states in the frame of quantum dot A. Its Hamiltonian is then given by:

$$H_{\text{model}} = H_{\text{charge}} + H_{\text{Zeeman}} =$$

$$\begin{pmatrix} \epsilon & 0 & t_c & 0 \\ 0 & \epsilon & 0 & t_c \\ t_c & 0 & -\epsilon & 0 \\ 0 & t_c & 0 & -\epsilon \end{pmatrix} + \frac{1}{2} B \mu_B \begin{pmatrix} g_A(\epsilon) & 0 & 0 & 0 \\ 0 & -g_A(\epsilon) & 0 & 0 \\ 0 & 0 & g_B(\epsilon)\cos(\theta) & g_B(\epsilon)\sin(\theta)e^{i\varphi} \\ 0 & 0 & g_B(\epsilon)\sin(\theta)e^{-i\varphi} & -g_B(\epsilon)\cos(\theta) \end{pmatrix}, \quad (6.2)$$

where ϵ is the detuning energy of the double quantum dot system (taken as zero at the charge transition), μ_B is the Bohr magneton and g_i are the g-factors in the different quantum dots, φ is the

azimuthal angle between the two quantization axes. Note that, with this convention, ϵ corresponds to half of the difference between the electrochemical potentials of the two quantum dots and a tunnel gap of $2t_c$ at the anticrossing. We remark that this model is similar to that of a flopping-mode qubit [267]. Diagonalizing the Hamiltonian, we obtain the qubit resonance frequency f_L given by:

$$f_L = \frac{\mu_B B}{h} \frac{\sqrt{(2\epsilon^2 + t_c^2)(g_A(\epsilon)^2 + g_B(\epsilon)^2) + 2\epsilon(g_B(\epsilon)^2 - g_A(\epsilon)^2)\sqrt{\epsilon^2 + t_c^2} + 2g_A(\epsilon)g_B(\epsilon)t_c^2\cos(\theta)}}{2\sqrt{\epsilon^2 + t_c^2}}, \tag{6.3}$$

The evolution of f_L along the detuning axes can then be fitted to extract the tilt angles and the tunnel couplings between neighbouring quantum dots. For this purpose, we first express the detuning energies in terms of gate voltages as $\epsilon_{23} = \frac{\eta_{23}}{2}(vP_3 - vP_3^0)$ and $\epsilon_{34} = \frac{\eta_{34}}{2}(vP_4 - vP_4^0)$ where $\eta_{23} = 0.166$ meV/mV and $\eta_{34} = 0.150$ meV/mV are the effective lever arms along the detuning axis. They are defined as $\eta_{23} = \beta_3 + \beta_2\gamma_{23}$ and $\eta_{34} = \beta_4^* + \beta_3^*\gamma_{34}$ where $\beta_2 = 0.084$ meV/mV, $\beta_3 = 0.080$ meV/mV ($\beta_3^{(*)} = 0.084$ meV/mV, $\beta_4^{(*)} = 0.075$ meV/mV) are the virtual gate lever arms measured nearby the QD_2-QD_3 (QD_3-QD_4) charge transition via photon-assisted tunnelling experiments [270] and where $\gamma_{23} = |\Delta vP_2/\Delta vP_3| = 1.026$ ($\gamma_{34} = |\Delta vP_3/\Delta vP_4| = 0.889$) are the slopes of the detuning axis. We extract the evolution of f_L as function of vP_3 (vP_4) from the data displayed in Fig. 6.12.a-b (Fig. 6.13.a-c) and fit it with eq.(Fig. 6.3).

Fig. 6.12.c-d display the evolution of f_L along the ϵ_{23} detuning axis which is fitted to the above model assuming a linear dependence of g with vP_3. We observe that the model reproduces well the measured evolution. This allows to estimate an interdot tunnel coupling t_c of 4.4 ± 0.2 GHz and a tilt angle θ_{23} of $51.8 \pm 0.7°$. The error bars correspond to one standard deviation from the best fit. This evaluation is consistent with the lower bound found using the previous method.

Fig. 6.13.d-e display the evolution of f_L along the ϵ_{34} detuning axis. In this case, fitting the data does not allow to extract the tilt angle, even if we assume a quadratic dependence of the g-factor with the gate voltage. Indeed, for $0° \leq \theta \lesssim 40°$, the shape of f_L curve is nearly solely determined by the tunnel coupling and the variation of the g-factor with vP_4. Consequently, the data can be equally well fitted by models where θ_{34} is fixed at 0°, 10°, 20°, 30°or 40°. This leads to such a large uncertainty on the value of θ_{34} that it prevents us from extracting it. Nevertheless, the tunnel coupling between QD_3 and QD_4 can still be estimated from these fits and, for θ_{34} fixed to 40°(30°), we find $t_c = 8 \pm 1$ ($t_c = 6.2 \pm 0.8$) GHz.

What does become clear, however, is that we cannot obtain proper fits of the data with model where θ_{34} is fixed to values larger than 40°. The underlying reason appears when plotting the expected evolution of f_L in such model: for $\theta_{34} \gtrsim 50°$, f_L should display a minimum that we do not observe experimentally. This suggests that θ_{34} is lower than 50°.

This analysis also allows us to estimate the degree of adiabaticity of the charge transfers between the neighbouring quantum dots i and j. For that, we use the Landau-Zener formula $P_{LZ}^{ij} = \exp(\frac{-2\pi t_c^2 t_{ramp}}{2\hbar\Delta\epsilon_{ij}})$ that gives us the probability of having a transition to the excited charge state while changing the detuning linearly by $\Delta\epsilon_{ij} = \frac{\eta_{ij}}{2}\Delta vP_{ij}$ in a time t_{ramp}. We emphasize that the factor 2 in front of $\Delta\epsilon_{ij}$ comes from our definition of ϵ_{ij}. Taking $\Delta vP_3 = 19.5$ mV for shuttling between QD_2 and QD_3, $\Delta vP_4 = 18$ mV for shuttling between QD_3 and QD_4 and $t_{ramp} = 4$ ns, we find $P_{LZ}^{23} \simeq 2 \times 10^{-2}$ and $P_{LZ}^{34} \simeq 2 \times 10^{-7}(9 \times 10^{-5})$. The values obtained for the shuttling between QD_3 and QD_4 suggest that the charge transfer between these two quantum dots is adiabatic. In contrast, there is non-negligible probability of exciting higher charge states while shuttling between QD_2 and QD_3 with these settings.

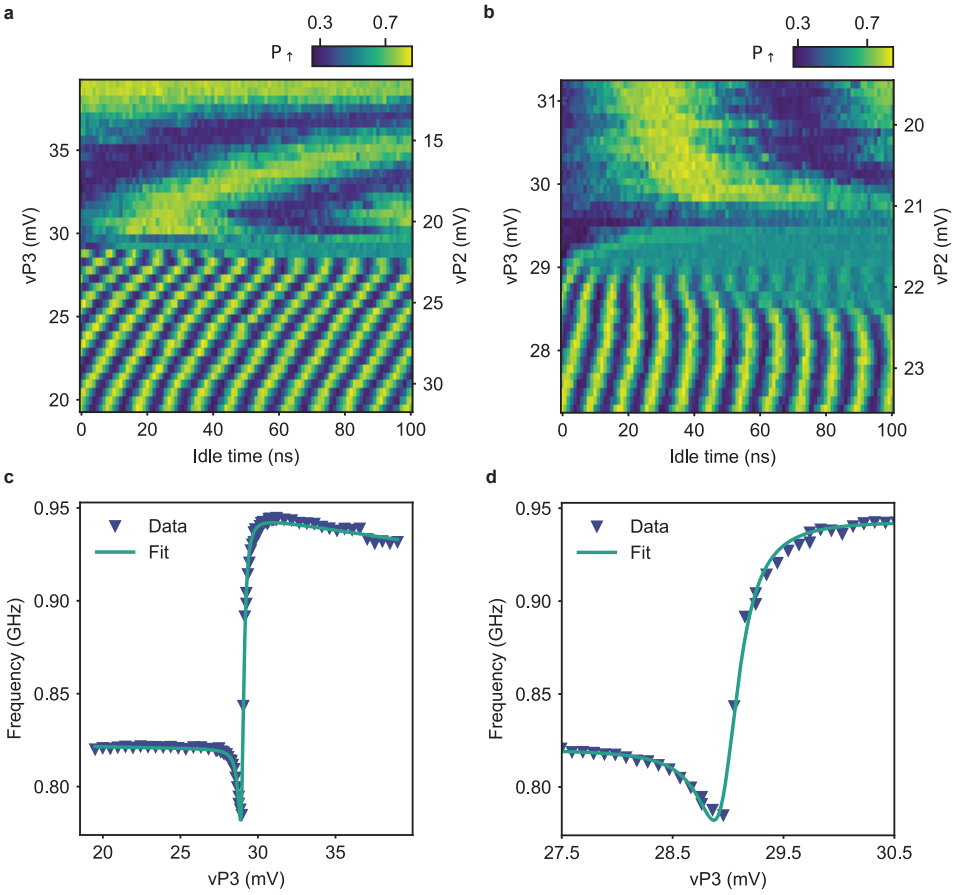

Figure 6.12: **Evaluation of the tilt angle between QD_2 and QD_3 quantization axes using a four-level model. a**, Free evolution experiments for shuttling a qubit in superposition state between QD_2 and QD_3 back-and-forth. The superposition state is prepared in QD_2. **b**, Zoom-in on the vicinity of the charge transition. The two data sets are identical to those displayed in Fig. 1.h. **c**, **d**, Resonance frequency extracted from the oscillations along the detuning axis in (a) and (b) and fit with the model of eq. (6.3).

To improve the fidelity of the shuttling process between QD_2 and QD_3, we increased the tunnel coupling by lowering the barrier gate voltage vB_{23} from -40 mV to -75 mV. Fig. 6.14 shows the results of similar analysis performed after lowering the barrier gate voltage. Fitting the evolution of the resonance frequency along the detuning axis, we find that $t_c = 16.1 \pm 0.6$ GHz and $\theta_{23} = 54.2 \pm 0.6°$. For these experiments, $\eta_{23} = 0.164$ and $\Delta vP_3 = 24$ mV, thus we find $P_{LZ}^{23} \simeq 2 \times 10^{-19}$. In this gate voltage configuration, the shuttling process is fully adiabatic with respect to the charge degree of freedom. Consequently, we used these barrier gate voltage settings to have better shuttling performance and, in particular, for the experiments presented in Fig. 6.5 and Fig. 6.7.

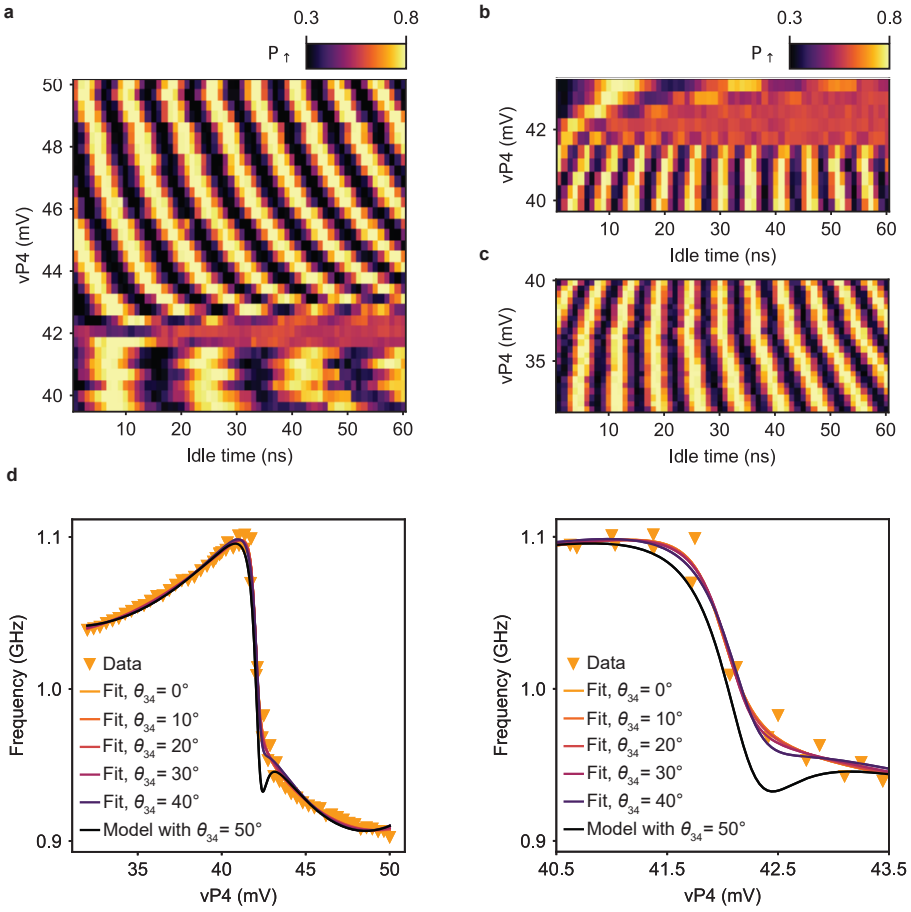

Figure 6.13: **Evaluation of the tilt angle between QD_3 and QD_4 quantization axes using a four-level model. a**, **b**, **c**, Free evolution experiments for the adiabatic shuttling of a qubit in a superposition state between QD_3 and QD_4 back-and-forth. In (a) the qubit is prepared in superposition in QD_4, while in (b) and (c) the superposition state is prepared in QD_3. **d**, **e**, Evolution of the resonance frequency along the detuning axis, extracted from the oscillations in (a), (b) and (c), and fits with models of eq. (6.3) where the tilt angle is fixed. The expected evolution for $\theta_{34} = 50°$ is computed using the parameters extracted from the fit with $\theta_{34} = 40°$.

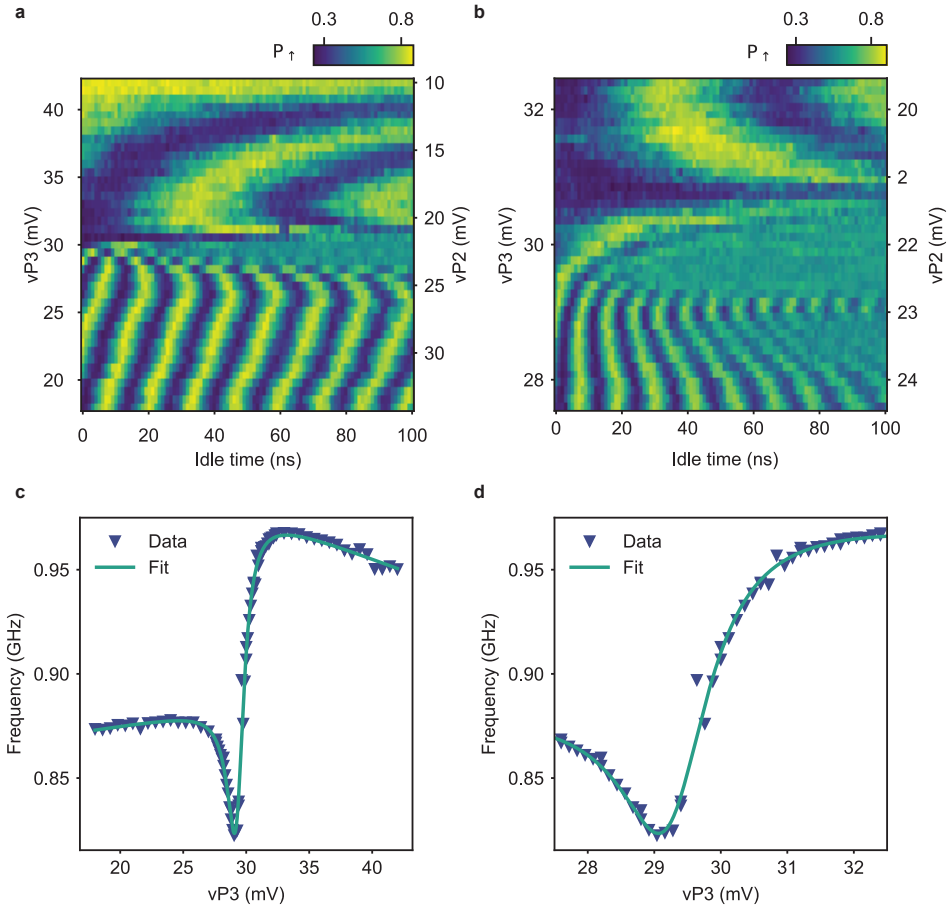

Figure 6.14: **Evaluation of the tilt angle between QD_2 and QD_3 quantization axes using a four-level model at a lower barrier gate voltage. a**, Free evolution experiments for shuttling a qubit in a superposition state between QD_2 and QD_3 back-and-forth. The superposition state is prepared in QD_2. **b**, Zoom-in on the vicinity of the charge transition. **c**, **d**, Resonance frequency extracted from the oscillations along the detuning axis extracted from (a) and (b) and fit with the model of eq. (6.3). Compared to Fig. 6.12, here the barrier gate voltage vB_{23} is lower (−75 mV instead of −40 mV) leading to a higher tunnel coupling. These settings correspond to the settings used to acquire the data displayed in Fig. 6.5 and Fig. 6.7.

	$QD_2 \rightleftarrows QD_3$	$QD_3 \rightleftarrows QD_4$	Corner	Triangular
T_2^* in QD_2 (ns)	$(2.8\pm0.1)\times10^2$	N. A	$(2.8\pm0.1)\times10^2$	$(2.8\pm0.1)\times10^2$
α in QD_2	1.8±0.2	N. A	1.8±0.2	1.8±0.2
T_2^* QD_3 (ns)	$(4.1\pm0.3)\times10^2$	$(5.0\pm0.3)\times10^2$	$(4.1\pm0.3)\times10^2$	$(4.1\pm0.3)\times10^2$
α QD_3	1.6±0.2	1.8±0.3	1.6±0.2	1.6±0.2
T_2^* (ns) in QD_4	N. A.	$(3.1\pm0.2)\times10^2$	$(3.1\pm0.3)\times10^2$	$(3.1\pm0.3)\times10^2$
α in QD_4	N. A.	1.8±0.2	1.4±0.3	1.4±0.3
t^* (ns) shuttling	339±5	408±9	$(3.5\pm0.1)\times10^2$	$(3.4\pm0.2)\times10^2$
α shuttling	1.41±0.05	1.30±0.07	1.13±0.07	1.11±0.08

Table 6.2: **Dephasing times and decay coefficients for static and shuttled qubits.** The dephasing times T_2^* for static qubits are measured with standard Ramsey experiments (data shown Fig. 6.15), performed at the starting and the end points of the shuttling pulses. The dephasing time t^* for shuttled qubits are extracted by fitting the amplitude as a function of the total time, as shown in Fig. 6.15. The error bars indicate one standard deviation from the best fits. The voltages applied on the barrier gates vary between experiments, which can lead to different T_2^* and α values for a static qubit in a given quantum dot.

NOTE 5: SHUTTLING AS A FUNCTION OF TIME AND DEPHASING TIMES

To get some insight on how the shuttling performance compare to the typical coherence times in the system, we plot in Fig. 6.15 the qubit dephasing times T_2^* along side the results of the shuttling experiments as function of time. We evaluate the T_2^* of a static qubit at the locations in the charge stability diagrams corresponding to the starting and the end points of the shuttling pulses. The T_2^* values are measured using a standard Ramsey protocol. The resulting oscillations are fitted by $A\cos(2\pi t f+\varphi_0)\exp(-(t/T_2^*)^\alpha)+A_0$ allowing to extract both T_2^* and the decay coefficients α. The corresponding data and fits are shown in Fig. 6.15.a-b.

Moreover, for all the shuttling processes, we calculate for each number of shuttling events n the total time between the two $\pi/2$ pulses of the Ramsey shuttling experiments. Fig. 6.15.c-f show the results of shuttling experiments used to quantify the performances. These data are identical to those shown in Fig. 6.5 and Fig. 6.7, but the amplitude decay is shown as a function of the time duration of the shuttling experiments.

An overview of the fit parameters is shown in Table 6.2. Since the total measurement time for the shuttling experiments (several thousands of seconds) is very different from that for the Ramsey experiments (several hundreds of seconds), and therefore the type and amount of noise integrated are different, some caution is required when comparing the decay parameters. However, it is clear that the dephasing times of static and moving qubits are of the same order of magnitude.

NOTE 6: ADIABATIC SHUTTLING

For completeness, we also investigate the performance of the shuttling processes when the shuttling pulses are adiabatic, i.e. when there is no spin rotation induced by the difference between the quantization axes of the quantum dots. Fig. 6.16 shows the results of such investigations for the shuttling of basis states and for the shuttling of superposition states. In both cases, we obtain significantly lower performance compared to those achieved with diabatic pulses (see Fig. 6.5). According to our findings, dephasing can largely explain this difference in performance for the coherent shuttling experiments. As the time required for each shuttling event is increased in the adiabatic experiments, the qubit experiences more dephasing during each shuttling step and the phase coherence is lost after a smaller number of shuttling steps n. The use of echoing pulses al-

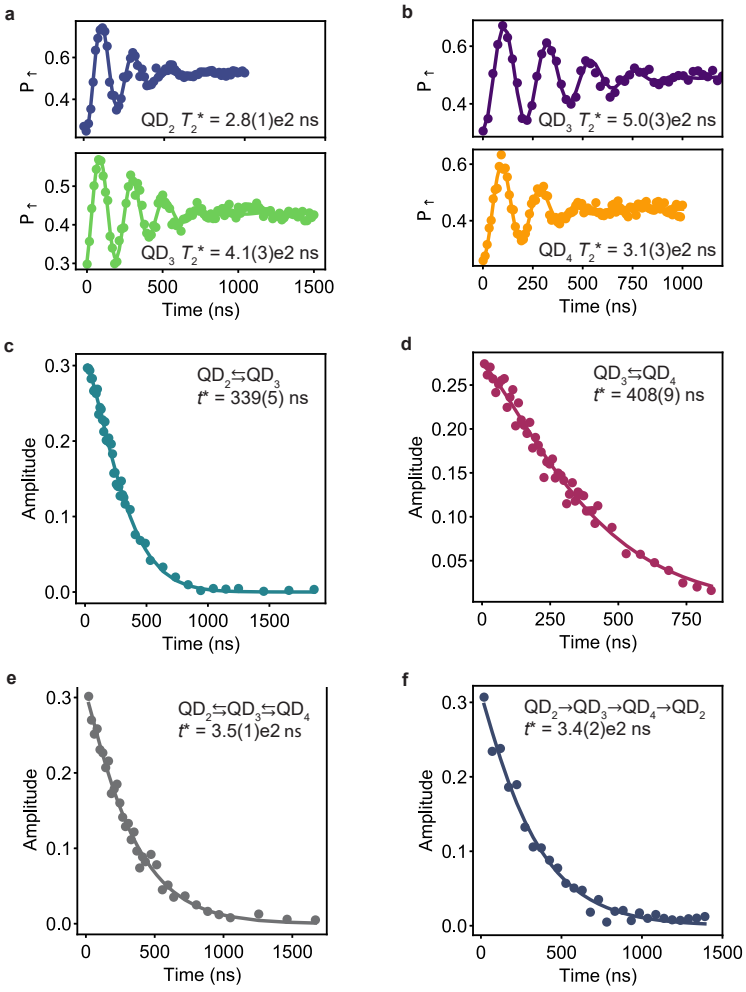

Figure 6.15: **Comparison of the dephasing times for static and shuttled qubits. a**, **b**, Results of Ramsey experiments for a spin in QD_2 and QD_3 (a) (QD_3 and QD_4 in (b)) at the same plunger and barrier gate voltages settings as the shuttling experiments between QD_2 and QD_3 (a) (QD_3 and QD_4 in (b)). **c**, **d**, The result of the shuttling experiment, to assess the shuttling performance with a superposition state (without echo pulse), between QD_2 and QD_3 (c) (QD_3 and QD_4 in (d)), same as in Fig. 3g (3h) of the main text. However, here the amplitude is plotted as a function of the total time between the two $\pi/2$-pulses. **e**, **f**, Similar to (a) and (b), but for the corner shuttling and the triangular shuttling. The gate voltage settings for these experiments are the same as for the Ramsey experiments shown in (a) for QD_2 and QD_3 and for QD_4 shown in (b). The error bars indicate one standard deviation from the best fits.

lows us to get an improvement of the coherent shuttling performance by a factor 6 to 8, larger than those obtained for diabatic shuttling.

For shuttling basis states, the lower performance suggests that the probability of having a spin-flip during a shuttle increases if the latter is performed adiabatically. This could originate from the

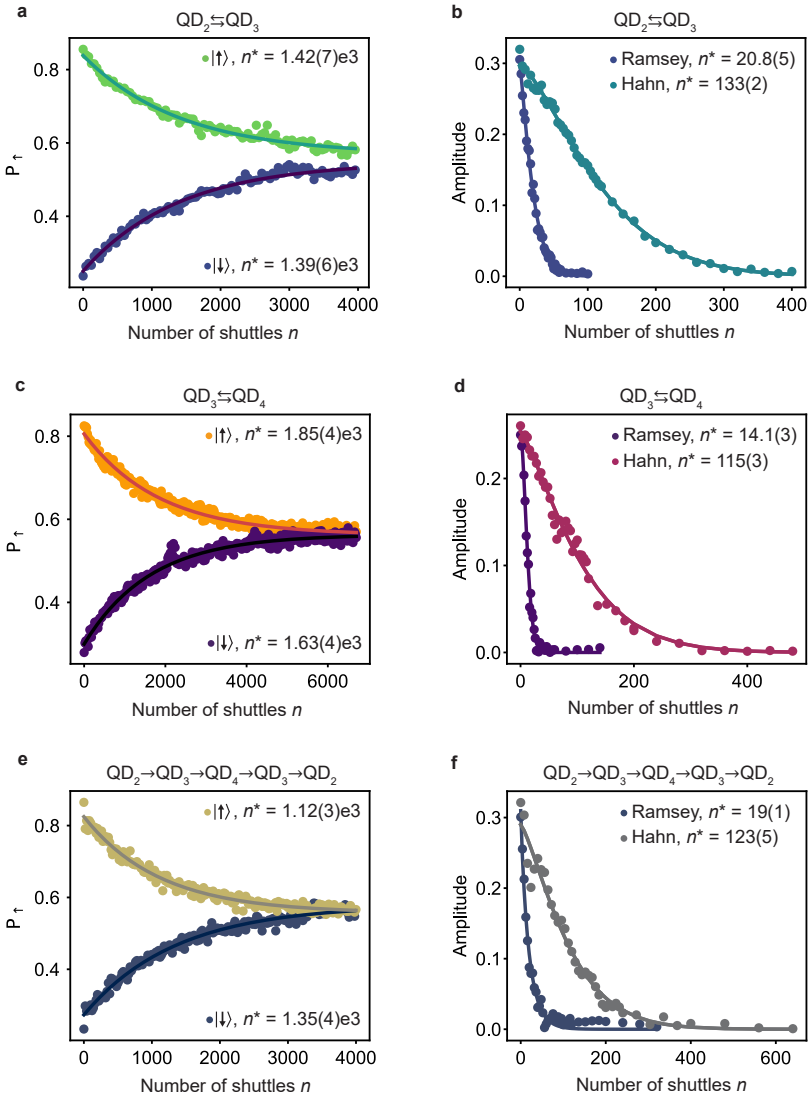

Figure 6.16: **Performance of adiabatic shuttling. a**, **b**, **c**, Spin polarization as a function of the number of shuttling steps n for a qubit initialized in the basis states. **d**, **e**, **f**, Amplitude as a function of the number of shuttling steps n for qubits initialized in a superposition state, without (Ramsey) and with echo pulse (Hahn).

longer time spent in the vicinity of the charge transition, where spin randomization induced by charge noise is enhanced [156]. Overall, the data in Fig. 6.16 clearly show that an approach based on diabatic spin shuttling is preferable for hole spin qubits in germanium.

NOTE 7: CHARGE STABILITY DIAGRAM OF PAIR QD_2-QD_4

The charge stability diagram of the quantum dot pair QD_2-QD_4, measured in a configuration identical to that of the triangular shuttling, is displayed in Fig. 6.17. No clear interdot charge anticrossing is visible, which suggests that the tunnel coupling between the two quantum dots is very low. This is expected, considering the device geometry, and it forces us to split the final pulse for the triangular shuttling in two parts. As depicted in Fig. 6.17, the voltages are first changed to bring the system close to the (1100)-(1001) degeneracy point before applying a second pulse that brings the system in the (1100) charge state. This reduces the probability that we excite the (1101) charge state, while transferring the qubit.

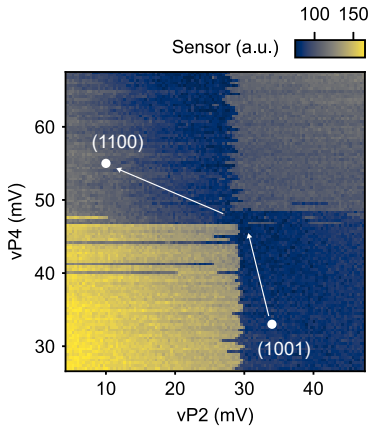

Figure 6.17: **Charge stability diagram of quantum dot pair QD_2-QD_4.** No clear interdot transition can be distinguished. The shuttling of a spin qubit from QD_2 to QD_4 is performed using two voltage pulses (white arrows). The labels $(N_1 N_2 N_3 N_4)$ represent the charge occupation in the quantum dots.

NOTE 8: OPTIMIZATION OF THE SHUTTLING PULSES TO MITIGATE THE EFFECTS OF SPIN-ORBIT INTERACTION

In this section, we illustrate and discuss the importance of careful pulse optimization. Fig. 6.18 shows the results of experiments where we probe the performance of the coherent shuttling between QD_2 and QD_3 using the Ramsey sequence depicted in Fig. 6.4.a. The detuning pulses used for all these experiments are identical, except for the idle time t_{idle} in QD_3 (idle time 2 in Fig. 6.4.b). This idle time in QD_3 was optimized to 0.95 ns for the experiments displayed in the main text.

We observe that the evolution of amplitudes extracted at the end of the shuttling sequence is strongly dependent on the idle time in QD_3. For $t_{\text{idle}} = 0.9$ and $t_{\text{idle}} = 1$ ns, which are close to the optimum, the amplitude shows a smooth and progressive decay. When t_{idle} is increased, oscillations of the amplitude as function of the number of shuttling steps n appear and their periodicity varies with t_{idle}. These oscillations witness the rotations induced by the change of quantization axes, which are imperfectly compensated for $t_{\text{idle}} \geq 1.1$ ns. They lead to coherent errors after each shuttling event, which add up, and significantly modify the state of the qubit. For example, for $t_{\text{idle}} = 1.6$ ns, the superposition state is virtually transformed to a spin basis state after a few shuttling rounds. This emphasizes the necessity of optimizing the voltage pulses to compensate for the effect of rotations induced by the spin-orbit interaction.

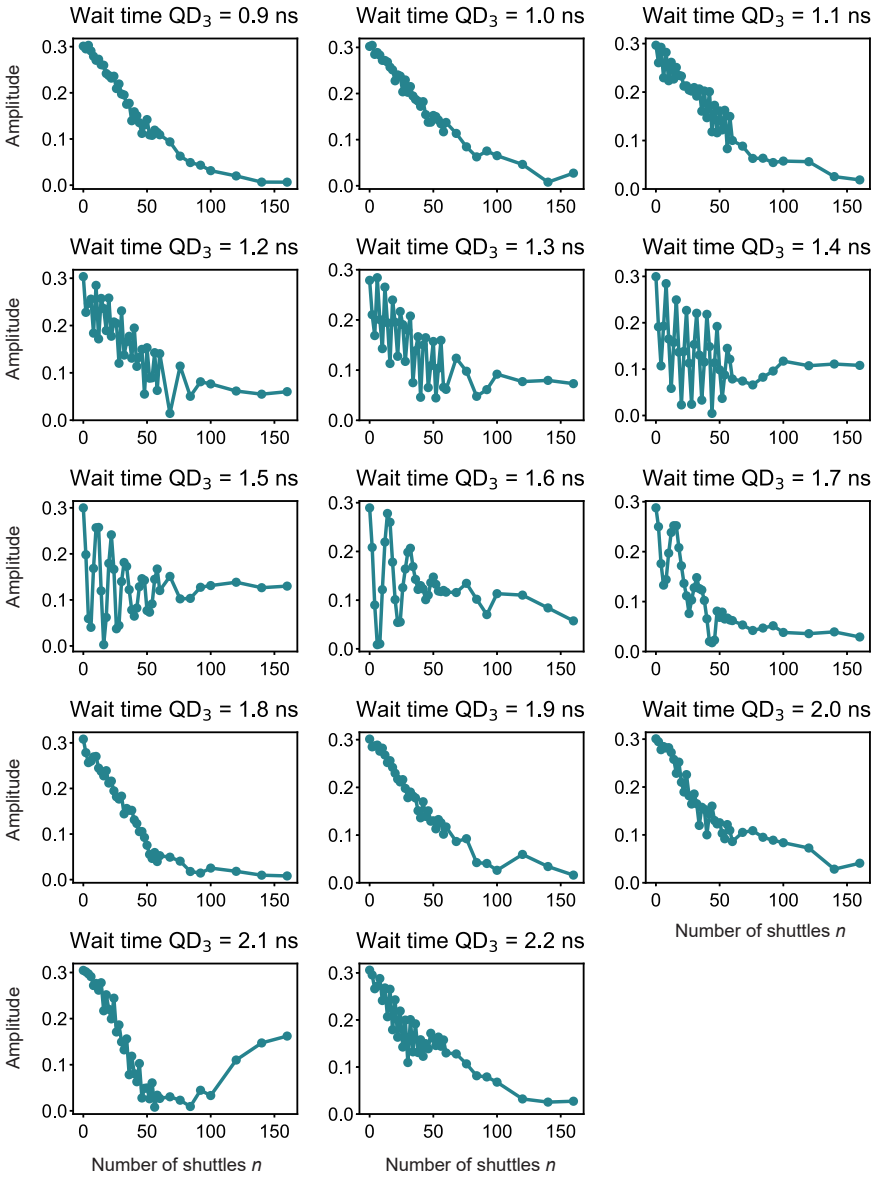

Figure 6.18: **Signatures of non-optimized idle times in Ramsey shuttling experiments.** Results of coherent shuttling experiments between QD_2 and QD_3 obtained using Ramsey sequences. The idle time spent in QD_3 is different for the results shown in the different subplots, as indicated by the titles. For non-optimized idle times, oscillations of the amplitude as function of the number of shuttles n appear and the amplitude can saturate to a non-zero value at large n.

The optimized idle times for each shuttling process can be found by performing measurements similar to those displayed in Fig. 6.18, and by looking for a regular decay of the amplitude as function of n. This optimization can also be done by studying the decay of the spin-up probabilities in spin basis state shuttling experiments.

NOTE 9: QUBIT DYNAMICS DURING COHERENT SHUTTLING EXPERIMENTS FOR NON-OPTIMIZED IDLE TIMES

In Fig. 6.18, we see that for non-optimized idle times, like $t_{\text{idle}} = 1.5$ ns, the amplitude can saturate to a finite value at large n. This is in contrast to what we observe for optimized idle times $t_{\text{idle}} = 0.9$ ns and $t_{\text{idle}} = 1$ ns, which decay to zero. To understand this feature, we carry out simulations of the dynamics of a qubit initialized in the $\frac{|\downarrow\rangle - i|\uparrow\rangle}{\sqrt{2}}$ superposition state which is shuttled between two neighboring quantum dots. Each shuttling step is modelled by a rotation. This rotation arises from the precession around the quantization axis of the quantum dot towards which the qubit is shuttled. We also calculate for every even n the expected measurement result, i.e. the amplitude of the $P_\uparrow$ oscillations that appear when the phase ϕ of the second $\pi/2$ pulse is varied. This is shown in Fig. 6.19.c, with two examples corresponding to a non-optimized idle time and an optimized idle time.

Fig. 6.19.a displays the trajectory in the Bloch sphere of the qubit for the first 14 shuttling steps, in the reference frame of the quantum dot where the shuttling experiment starts. The different states of the qubit map a circle which is tilted compared to the equator. The product of the two rotations generated by shuttling back-and-forth is equivalent to a single rotation around a fixed axis. Consequently, multiple shuttling cycles can be seen as successive rotations around this fixed axis which elucidates the trajectory observed in the Bloch sphere. This also explains the oscillations of the amplitude as function of n seen in Fig. 6.18, as the distance between origin and the projection of the state on xy-plane can vary significantly depending on the number of shuttles for an non-optimized idle time. In contrast, when the idle times are well-optimized, the qubit states are on the equator of the Bloch sphere and no oscillations of the amplitude with n can be observed.

Next, we include the effects of dephasing in the simulations, by assuming that the qubit frequencies fluctuate between repetitions of a given experiment with a fixed n. We observe that the state of the qubit is spread along a circle with a distribution that becomes more uniform as n increases, meaning when the qubit experiences more dephasing. An example is shown in Fig. 6.19.b for $n = 98$, corresponding to the data shown in Fig. 6.19.c. The center of the circle, which is equivalent to the statistical average of the qubit state when the qubit is completely dephased, is not on the equator on Bloch sphere. This explains the finite amplitude observed in the measurements at large n. Except for the revival of the amplitude observed for $t_{\text{idle}} = 2.1$ ns, these simulations capture most of the features observed in Fig. 6.18.

NOTE 10: MODELLING OF THE QUBIT DYNAMICS

MODEL USED AND UNDERLYING ASSUMPTIONS

In general, the quantum process of $2n$ shuttles, between QD_2 and QD_3 back-and-forth n times, is given by the sequential application of the individual processes:

$$\mathscr{U}_{2n \text{ shuttles}} = \langle \prod_{j=0}^{n} \mathscr{U}^{(j)}_{\text{QD2}} \mathscr{U}^{(j)}_{\text{r,QD2}} \mathscr{U}^{(j)}_{\text{QD3}} \mathscr{U}^{(j)}_{\text{r,QD3}} \rangle , \tag{6.4}$$

where $\mathscr{U}^{(j)}_{\text{QD2(QD3)}}$ is the j-th superoperator describing the dynamics in quantum dot $QD_2(QD_3)$, $\mathscr{U}^{(j)}_{\text{r,QD2(r,QD3)}}$ is the j-th superoperator describing the dynamics of ramping to quantum dot QD_2 (QD_3), and $\langle\cdot\rangle$ denotes averaging over different noise initializations. The dynamics

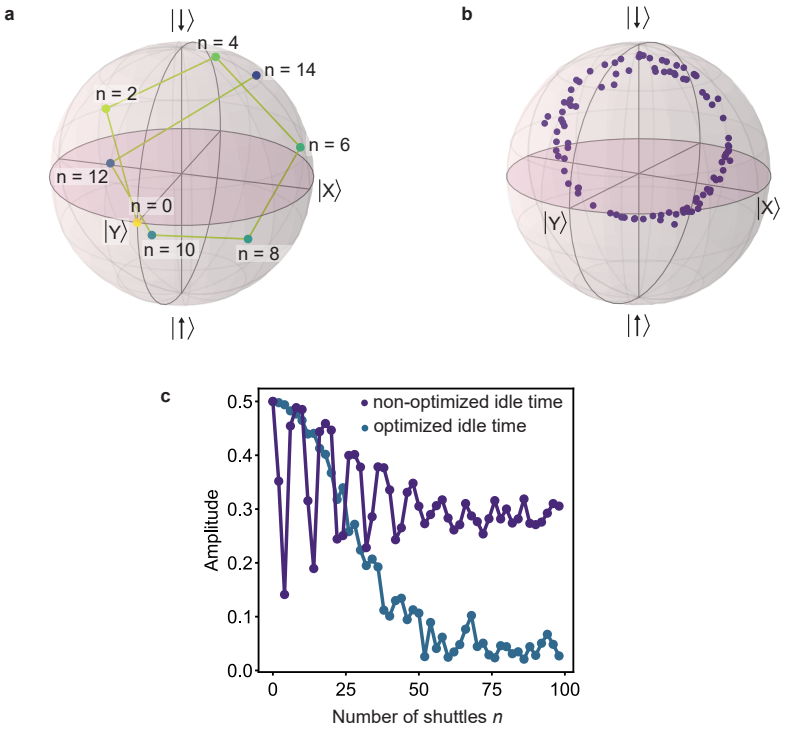

Figure 6.19: **Simulation of the effect of non-optimized idle times. a**, Distribution of the qubit states in the Bloch sphere after an even number of shuttles, for an non-optimized idle time. **b**, Spread of the qubit state after a large number of shuttles, when the qubit is dephased. **c**, Simulated measurement results, i.e. amplitude of the oscillations appearing while varying the phase of the second $\pi/2$ pulse, as a function of n, for a non-optimized idle time and an optimized idle time.

within the qubit subspace without decoherence is given by:

$$U_{\mathrm{QD2}} = \exp\left(-i\frac{\phi_{\mathrm{QD2}}}{2}\sigma_z\right) \tag{6.5}$$

$$U_{\mathrm{r,QD2}}U_{\mathrm{QD3}}U_{\mathrm{r,QD3}} = \exp\left(-i\frac{\phi_{\mathrm{QD3}}}{2}(\cos(\theta_{23})\sigma_z + \sin(\theta_{23})\sigma_x)\right), \tag{6.6}$$

where θ_{23} is the effective tilt angle between the quantization axes that also takes the ramping time into consideration, $\phi_{\mathrm{QD2(QD3)}}$ are the effective phases accumulated around the corresponding quantization axis and $\sigma_{x,y,z}$ are the Pauli matrices in QD_2. In the superoperator representation, the unitary dynamics can be conveniently expressed by:

$$\mathscr{U}_{\mathrm{QD2}} = U_{\mathrm{QD2}} \otimes U^*_{\mathrm{QD2}} \tag{6.7}$$

$$= e^{\mathscr{H}_{\mathrm{QD2}}}. \tag{6.8}$$

Here, $\mathscr{H}_{\mathrm{QD2}} = -i\phi_{\mathrm{QD2}}(\sigma_z \otimes \mathbf{1}_2 - \mathbf{1}_2 \otimes \sigma_z)/2$ and $\otimes$ denotes the Kronecker product. To describe the effect of decoherence we consider for each process low-frequency charge noise (modelled as

quasistatic fluctuations of accumulated phases $\phi_{\mathrm{QD2(QD3)}} \rightarrow \phi_{\mathrm{QD2(QD3)}} + \delta\phi_{\mathrm{QD2(QD3)}}$), and high-frequency charge noise which causes dephasing and relaxation at the charge anticrossing. The latter noise sources are modelled within a standard Lindblad equation (allowing us to drop the index j) and described by the following Lindblad operators in superoperator representation using row-stacking convention [271]:

$$\mathscr{L}_{\mathrm{QD2}} = \begin{pmatrix} -\gamma^{\mathrm{r}}_{\mathrm{QD2}} & 0 & 0 & \gamma^{\mathrm{r}}_{\mathrm{QD2}} \\ 0 & -\gamma^{\mathrm{r}}_{\mathrm{QD2}} - \gamma^{\varphi}_{\mathrm{QD2}} & \gamma^{\mathrm{r}}_{\mathrm{QD2}} & 0 \\ 0 & \gamma^{\mathrm{r}}_{\mathrm{QD2}} & -\gamma^{\mathrm{r}}_{\mathrm{QD2}} - \gamma^{\varphi}_{\mathrm{QD2}} & 0 \\ \gamma^{\mathrm{r}}_{\mathrm{QD2}} & 0 & 0 & -\gamma^{\mathrm{r}}_{\mathrm{QD2}} \end{pmatrix}, \tag{6.9}$$

$$\mathscr{L}_{\mathrm{r,QD2}} = \begin{pmatrix} -\gamma^{\mathrm{r}}_{\mathrm{r,QD2}} & 0 & 0 & \gamma^{\mathrm{r}}_{\mathrm{r,QD2}} \\ 0 & -\gamma^{\mathrm{r}}_{\mathrm{r,QD2}} - \gamma^{\varphi}_{\mathrm{r,QD2}} & \gamma^{\mathrm{r}}_{\mathrm{r,QD2}} & 0 \\ 0 & \gamma^{\mathrm{r}}_{\mathrm{r,QD2}} & -\gamma^{\mathrm{r}}_{\mathrm{r,QD2}} - \gamma^{\varphi}_{\mathrm{r,QD2}} & 0 \\ \gamma^{\mathrm{r}}_{\mathrm{r,QD2}} & 0 & 0 & -\gamma^{\mathrm{r}}_{\mathrm{r,QD2}} \end{pmatrix}, \tag{6.10}$$

$$\mathscr{L}_{\mathrm{QD3}} = \left(R(\theta_{23}) \otimes R(-\theta_{23})^T\right) \begin{pmatrix} -\gamma^{\mathrm{r}}_{\mathrm{QD3}} & 0 & 0 & \gamma^{\mathrm{r}}_{\mathrm{QD3}} \\ 0 & -\gamma^{\mathrm{r}}_{\mathrm{QD3}} - \gamma^{\varphi}_{\mathrm{QD3}} & \gamma^{\mathrm{r}}_{\mathrm{QD3}} & 0 \\ 0 & \gamma^{\mathrm{r}}_{\mathrm{QD3}} & -\gamma^{\mathrm{r}}_{\mathrm{QD3}} - \gamma^{\varphi}_{\mathrm{QD3}} & 0 \\ \gamma^{\mathrm{r}}_{\mathrm{QD3}} & 0 & 0 & -\gamma^{\mathrm{r}}_{\mathrm{QD3}} \end{pmatrix} \left(R(-\theta_{23}) \otimes R(\theta_{23})^T\right), \tag{6.11}$$

$$\mathscr{L}_{\mathrm{r,QD3}} = \left(R(\theta_{23}) \otimes R(-\theta_{23})^T\right) \begin{pmatrix} -\gamma^{\mathrm{r}}_{\mathrm{r,QD3}} & 0 & 0 & \gamma^{\mathrm{r}}_{\mathrm{r,QD3}} \\ 0 & -\gamma^{\mathrm{r}}_{\mathrm{r,QD3}} - \gamma^{\varphi}_{\mathrm{r,QD3}} & \gamma^{\mathrm{r}}_{\mathrm{r,QD3}} & 0 \\ 0 & \gamma^{\mathrm{r}}_{\mathrm{r,QD3}} & -\gamma^{\mathrm{r}}_{\mathrm{r,QD3}} - \gamma^{\varphi}_{\mathrm{r,QD3}} & 0 \\ \gamma^{\mathrm{r}}_{\mathrm{r,QD3}} & 0 & 0 & -\gamma^{\mathrm{r}}_{\mathrm{r,QD3}} \end{pmatrix} \left(R(-\theta_{23}) \otimes R(\theta_{23})^T\right), \tag{6.12}$$

where $R(\theta) = e^{-i\theta\sigma_y/2}$ rotates the quantization axis by θ in the xz-plane. Here, $\gamma^{\varphi}_{\mathrm{QD2(QD3)}}$ is the dephasing rate and $\gamma^{\mathrm{r}}_{\mathrm{QD2(QD3)}}$ the relaxation/excitation rate for idling in $\mathrm{QD_2(QD_3)}$ and $\gamma^{\varphi}_{\mathrm{r,QD2(QD3)}}$ is the dephasing rate and $\gamma^{r}_{\mathrm{r,\,QD2(QD3)}}$ the relaxation/excitation rate for shuttling from $\mathrm{QD_3}$ to $\mathrm{QD_2}$ ($\mathrm{QD_2}$ to $\mathrm{QD_3}$). To simplify the expressions, we further assumed that the qubit is coupled to a hot qubit bath at the anticrossing [156] giving rise to equal relaxation and excitation rates. This assumption is justified by the fast randomization of the spin state at the anticrossing observed in Fig. 6.10.

The basic repetition, a 2-shuttle process, can now be described as a Markov chain:

$$\mathscr{U}_{2\ \mathrm{shuttles}} = \langle e^{\mathscr{H}_{\mathrm{QD2}} + \mathscr{L}_{\mathrm{QD2}}} e^{\mathscr{L}_{\mathrm{r,QD2}}} e^{\mathscr{H}_{\mathrm{QD3}} + \mathscr{L}_{\mathrm{QD3}}} e^{\mathscr{L}_{\mathrm{r,QD3}}} \rangle . \tag{6.13}$$

Here, we make the following assumptions. Firstly, high-frequency noise, causing relaxation and dephasing processes and described by $\gamma^{\varphi}_{\mathrm{r,QD2(QD3)}}$ and $\gamma^{\mathrm{r}}_{\mathrm{r,QD2(QD3)}}$, is relevant only exactly at the anticrossing and is instantaneous. Secondly, we neglect high-frequency noise during the idling in

QD_2 and QD_3 since idling dynamics is dominated by low-frequency noise. This allows us to add the coherent part of the dynamics during the ramp before (after) reaching the anticrossing to the dynamics described by $\mathcal{H}_{QD2}$ ($\mathcal{H}_{QD3}$). We note that this is a good approximation if $\langle\phi_{QD3}\rangle$ is close to an integer multiple of 2π, i.e. the shuttling rounds are well calibrated. Using the Zassenhaus expansion formula, we can now further approximate the 2-shuttling process by a product of two matrices:

$$\mathcal{U}_{2\text{ shuttles}} = \langle e^{\mathscr{C}} e^{\mathscr{D}} \rangle . \tag{6.14}$$

Here, the $\mathscr{C}$-matrix only consists of the average phase accumulated $\langle\phi_{QD2}\rangle$ and describes a unitary process while all decoherence is included in the D-matrix. For n being an even integer, a $2n$-shuttle process can then be written as:

$$\mathcal{U}_{2n\text{ shuttles}} = \left\langle \prod_{i=1}^{n/2} e^{\mathscr{D}} \begin{pmatrix} 1 & 0 & 0 & 0 \\ 0 & e^{-i\langle\phi_{QD2}\rangle} & 0 & 0 \\ 0 & 0 & e^{i\langle\phi_{QD2}\rangle} & 0 \\ 0 & 0 & 0 & 1 \end{pmatrix} e^{\mathscr{D}} \right\rangle , \tag{6.15}$$

with the decoherence matrix:

$$\mathscr{D} \approx \mathscr{L}_{r,QD2} + \mathscr{L}_{r,QD3} + \mathcal{H}_{QD2} + \mathcal{H}_{QD3} - \langle \mathcal{H}_{QD2} \rangle . \tag{6.16}$$

SHUTTLING OF SPIN BASIS STATES

The return probability of the basis states, which are identical for both basis states as the excitation and relaxation rate are assumed to be equal close to the charge anticrossing, can be computed from the superoperator $\langle\widetilde{\uparrow}|\mathcal{U}_{2n\text{ shuttle}}|\widetilde{\uparrow}\rangle$, where $|\widetilde{\uparrow}\rangle$ is the vectorized density matrix of the $|\uparrow\rangle$ basis state. We now consider two extreme cases, $\langle\phi_{QD2}\rangle = m$ with even or odd m multiple of π. If m is an even multiple of π, we can simplify the expression to $\mathcal{U}_{2n\text{ shuttles}} = \langle e^{n\mathscr{D}} \rangle$, while for m being an odd multiple of π, the sequence corresponds to a Hahn echo experiment with a phase-flip operation instead of a bit-flip operation. In Fig. 6.20, we have simulated the basis state decay for varying m considering (a) uncorrelated and (b) correlated charge noise. While most cases shows only a single, and slow exponential decay, the special case of $m = 2\pi k$ (with k an integer) shows a fast initial Gaussian followed by a slow exponential decay. Regardless of the chosen value of m, the decay converges to $\langle\widetilde{\uparrow}|\mathcal{U}_{n\to\infty}|\widetilde{\uparrow}\rangle = \frac{1}{2}$. We find that for most m, the initial rapid decay is absent due to decoupling over potentially many shuttle rounds. Thus, the (partial) noise-decoupling effect occurs for most choices of the waiting times in the initial quantum dot. We find that the fast decay of the basis states can only be observed for $\langle\phi_{QD2}\rangle = m \pm \delta$ with m being multiples of 2π and $\delta \leq 0.02\pi$. Since our experimental results do not show a fast Gaussian decay of the basis states, we believe that our timing is chosen such that the fast initial Gaussian dephasing is echoed out [264]. Consequently, we can fit the decay for the shuttling of spin basis states to an exponential decaying function $\exp(-n/n^*)$. We note that the final slow decay can either originate from spin randomization or from dephasing.

RAMSEY, HAHN-ECHO, AND CPMG DYNAMICAL DECOUPLING

The decay of the superposition states can be computed from the same superoperator via the amplitude

$$A = \frac{1}{2} \max_{\varphi} \left[\langle\widetilde{\varphi}_+|\mathcal{U}_{2n\text{ shuttle}}|\widetilde{\phi}_+\rangle - \langle\widetilde{\varphi}_-|\mathcal{U}_{2n\text{ shuttle}}|\widetilde{\phi}_+\rangle \right] , \tag{6.17}$$

where $|\widetilde{\xi}_\pm\rangle$ is the vectorized density matrix of the state $|\xi_\pm\rangle = \frac{1}{2}(|\uparrow\rangle \pm e^{i\xi}|\downarrow\rangle)$ with $\xi = \varphi, \phi$. The initial phase of the superposition state is in general unknown due to the unsynchronized clock between

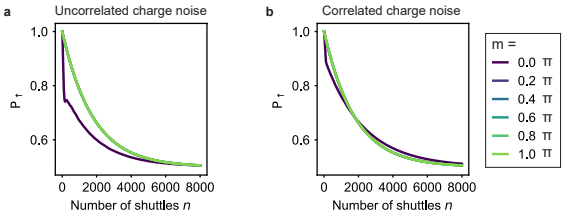

Figure 6.20: **Simulation of the basis state decay.** Evolution of the spin-up probability $P_\uparrow$ as a function of the number of shuttling events simulated using Eq. (6.4) for **a**, uncorrelated and **b**, correlated quasistatic fluctuations for various $\langle\phi_{QD2}\rangle = m$. For both correlated and uncorrelated noise, the fast initial decay vanishes, except when m is close to (a multiple of) 2π. In the simulation the following parameters were chosen: quantization axis difference $\theta_{23} = 52°$, high-frequency dephasing rate $\gamma^{\varphi}_{r,QD2} = \gamma^{\varphi}_{r,QD3} = 0.00125$, relaxation rate $\gamma^{r}_{r,QD2} = \gamma^{r}_{r,QD3} = 0.000125$, standard deviation of the quasistatic fluctuations $\sigma_{\phi_{QD2}} = \sigma_{\phi_{QD3}} = 0.004$. For uncorrelated fluctuations $\sigma_{\phi_{QD2}} \to \sqrt{2}\sigma_{\phi_{QD2}}$ to get identical free induction decays. These parameters lead to a pure dephasing after $n^* = 63$ shuttles in absence of decoupling.

the AWG and the vector source (see section below) and may vary for each single shot measurement of the experiment. However, the phase difference between initial and final state is fixed for each shot. We have numerically confirmed that the dynamics is only slightly affected by an additional averaging over the initial phase of the initial superposition state for $\langle\phi_{QD2}\rangle = m$ with m being close to multiples of 2π (same regime in which the fast initial decay can be observed for the basis state). For other choices, the initial phase has a negligible impact and is averaged out after a few shuttling rounds.

The quantum process of a dynamical decoupled $2n$ shuttles, shuttling between QD_2 and QD_3 back-and-forth n times, is given by the sequential application of the individual processes:

$$\mathcal{U}^{\text{Echo}}_{2n\text{ shuttles}} = \langle \prod_{j=0}^{n/2} \mathcal{U}^{(j)}_{QD2}\mathcal{U}^{(j)}_{r,QD2}\mathcal{U}^{(j)}_{QD3}\mathcal{U}^{(j)}_{r,QD3}\,\mathcal{U}_{x,\pi/2} \prod_{j=n/2}^{n} \mathcal{U}^{(j)}_{QD2}\mathcal{U}^{(j)}_{r,QD2}\mathcal{U}^{(j)}_{QD3}\mathcal{U}^{(j)}_{r,QD3}\rangle, \tag{6.18}$$

$$\mathcal{U}^{\text{CPMG}}_{2n\text{ shuttles}} = \langle \prod_{j=0}^{n/4} \mathcal{U}^{(j)}_{QD2}\mathcal{U}^{(j)}_{r,QD2}\mathcal{U}^{(j)}_{QD3}\mathcal{U}^{(j)}_{r,QD3}\,\mathcal{U}_{y,\pi/2} \prod_{j=n/4}^{3n/4} \mathcal{U}^{(j)}_{QD2}\mathcal{U}^{(j)}_{r,QD2}\mathcal{U}^{(j)}_{QD3}\mathcal{U}^{(j)}_{r,QD3}\,\mathcal{U}_{y,\pi/2} \prod_{j=3n/4}^{n} \mathcal{U}^{(j)}_{QD2}\mathcal{U}^{(j)}_{r,QD2}\mathcal{U}^{(j)}_{QD3}\mathcal{U}^{(j)}_{r,QD3}\rangle, \tag{6.19}$$

where $\mathcal{U}_{x,y,\pi/2}$ are superoperator representation of the spin-flips around the x and y axis. For corner shuttling, shuttling between QD_2 to QD_3 to QD_4 and back n times, one needs to make the substitution:

$$\mathcal{U}^{(j)}_{r,QD2}\mathcal{U}^{(j)}_{QD3}\mathcal{U}^{(j)}_{r,QD3} \to \mathcal{U}^{(j)}_{r,QD2}\mathcal{U}^{(j)}_{QD3}\mathcal{U}^{(j)}_{r,QD3}\mathcal{U}^{(j)}_{QD4}\mathcal{U}^{(j)}_{r,QD4}\mathcal{U}^{(j)}_{QD3}\mathcal{U}^{(j)}_{r,QD3}, \tag{6.20}$$

where $\mathcal{U}^{(j)}_{QD4}$ is the j-th superoperator describing the dynamics in dot QD_4, $\mathcal{U}^{(j)}_{r,QD4}$ is the j-th superoperator describing the dynamics of ramping to quantum dot QD_4. The dynamics within

the qubit subspace without decoherence is analogously given by:

$$U_{\mathrm{r,QD2}}U_{\mathrm{QD3}}U_{\mathrm{r,QD3}}U_{\mathrm{QD4}}U_{\mathrm{r,QD4}}U_{\mathrm{QD3}}U_{\mathrm{r,QD3}} = \exp\left(-i\frac{\phi_{\mathrm{QD3}}}{2}(\cos(\theta_{23})\sigma_z + \sin(\theta_{23})\sigma_x)\right) \times \exp\left(-i\frac{\phi_{\mathrm{QD4}}}{2}(\cos(\theta_{34}+\theta_{23})\sigma_z + \sin(\theta_{34}+\theta_{23})\sigma_x)\right) \times \exp\left(-i\frac{\phi_{\mathrm{QD3}}}{2}(\cos(\theta_{23})\sigma_z + \sin(\theta_{23})\sigma_x)\right),$$

where θ_{34} is the effective tilt angle between the quantization axes of QD_3 and QD_4 that also takes the ramping time into consideration, $\phi_{\mathrm{QD3,a(b)}}$ is the effective phases accumulated in QD_3 before (after) shuttling to QD_4, and ϕ_{QD4} is the effective phases accumulated in QD_4.

Note that in general the quantization axes of QD_2, QD_3 and QD_4 do not need to lay in the same plane. To account for the misalignment we use the Euler-angle decomposition, i.e. by adding a rotation around the quantization axis of QD_3 before the shuttling to QD_4 and adding the inverse rotation after the shuttling back to QD_3. The additional phase commutes (by design) with the idling dynamics in QD_3. Consequently, the additional rotation can be added/subtracted from the rotation accumulated during idling in QD_3 (care has to be taken with the relaxation decay dynamics). Since we do not know the phase of the rotation in our experiment, we assume in our simulations that all three quantization axes are in the xz-plane. We have numerically confirmed that the dynamics is only mildly affected by this choice and only close to $\langle\phi_{\mathrm{QD2}}\rangle = m$ with m being a multiple of 2π.

In Fig. 6.21, we have simulated for the corner shuttling the evolution of the coherence, i.e. the amplitude (see Eq. (6.17)) of the superposition state, for a (a) Ramsey, (b) Hahn-echo, and (c) CPMG dynamical decoupling sequence for various m using uncorrelated quasistatic charge noise. When m is a multiple of 2π, the dynamical decoupling for the CPMG sequence shows a significant improvement compared to the Hahn-echo. In contrast, when m is a multiple of π, a Hahn-echo sequence achieves a similar decoupling effect as the CPMG sequence because of the interplay between the phase and spin flips in QD_2. This could possibly explain the reduced effect of CPMG measured in corner shuttling. We note that simulations considering time-correlated phase fluctuations, instead of quasistatic phase fluctuations, show qualitatively similar results for the improvement of decoupling using CPMG sequences compared to Hahn-echo sequences.

NOTE 11: DRIVING A SPIN QUBIT AFTER SHUTTLING TO COMPENSATE UNINTENDED ROTATIONS

Since the rotations induced by diabatic shuttling are coherent, it should be possible to compensate these rotations by applying a microwave pulse. This requires the synchronisation of the internal clocks of the arbitrary waveform generators (AWGs) and the microwave source. Fig. 6.22.a shows the pulse sequence used to investigate this strategy. A spin prepared in the $|\downarrow\rangle$ state is shuttled back-and-forth once between QD_2 and QD_3. The idle time in QD_3 is purposely chosen such that the spin does not experience a $2\pi m$ rotation around the tilted quantization axis. As a result, after the shuttling, the spin is not in the $|\downarrow\rangle$ state anymore. Back in QD_2, an EDSR pulse is applied of which the phase ϕ and duration t_{MW} are varied. Finally, the spin is readout.

Fig. 6.22.b and c show the result of this experiment, without and with synchronisation of internal clocks of the AWG and microwave source. From Fig. 6.22.b it is clear that, if the internal clocks are not synchronized, the measured spin-up probability does not depend on the phase of the microwave pulse. Due to the lack of synchronization, the phase of the EDSR pulse (with phase ϕ and duration t_{MW}) varies between the single shot measurements of a single experiment, viewed in the lab frame. Therefore, the information about the phase of the spin after shuttling is lost and

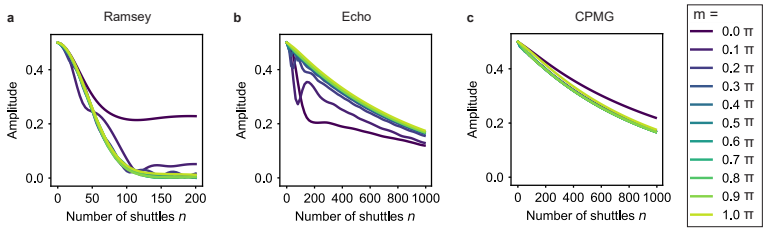

Figure 6.21: **Simulation of the dynamics for the Ramsey, Hahn-echo and CPMG sequences for corner shuttling.** Evolution of the superposition state for corner shuttling as a function of the number of shuttling events using eq. (6.17) for uncorrelated quasistatic fluctuations for varying phases $\langle\phi_{\mathrm{QD2}}\rangle = m$ and assuming perfect single-qubit gates $\mathscr{U}_{x,y,\pi/2}$. The gain of implementing a CPMG dynamical decoupling sequence compared to an echo is negligible. In the simulation the following parameters were chosen: quantization axis differences $\theta_{23} = 52°$ and $\theta_{34} = 40°$, high-frequency dephasing rate $\gamma^{\varphi}_{\mathrm{QD2}} = \gamma^{\varphi}_{r,\mathrm{QD3}} = \gamma^{\varphi}_{r,\mathrm{QD4}} = 0.00125$, relaxation rate $\gamma^{\mathrm{r}}_{r,\mathrm{QD2}} = \gamma^{\mathrm{r}}_{r,\mathrm{QD3}} = \gamma^{\mathrm{r}}_{r,\mathrm{QD4}} = 0.000125$, standard deviation of the quasistatic fluctuations $\sigma_{\phi_{\mathrm{QD2}}} = \sigma_{\phi_{\mathrm{QD3}}} = \sigma_{\phi_{\mathrm{QD4}}} = 0.009$. These parameters lead to a pure dephasing after $n^* = 63$ shuttles in absence of decoupling. We note that the decay in these simulations are underestimated as they include only quasistatic noise.

it is not possible to coherently drive the spin. In Fig. 6.22.c, we recover an oscillation in spin-up probability as a function of the phase of the microwave source, which indicates that the state of the spin is well-defined after the shuttling. It is therefore possible to coherently drive the spin after shuttling. The results in Fig. 6.22.b and c illustrate the importance of the synchronization of AWGs and microwave source clocks in the prospect of using a final EDSR pulse to compensate rotations induced by shuttling. The experiments presented in the main text of the manuscript were performed without synchronisation between the microwave source and the AWGs.

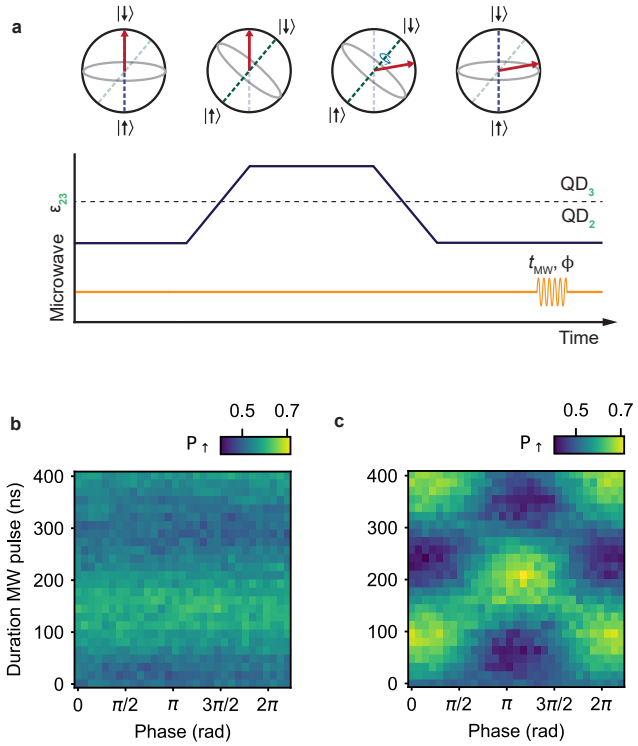

Figure 6.22: **Compensating shuttling-induced oscillations with a final EDSR pulse. a**, Schematic of the pulse sequence used for testing the effect of an EDSR pulse after shuttling a spin qubit. A spin qubit is initialized in the $|\downarrow\rangle$ state and shuttled back-and-forth between QD_2 an QD_3. Finally, a microwave pulse of duration t_{MW} and phase ϕ is applied. **b**, Results of the measurement sequence depicted in (a), in the case where the clock of the AWGs and the microwave source are not synchronized. **c**, Results in the case where the clocks of the AWGs and the microwave source are synchronized. The reduced visibility of the oscillations in the spin-up probability, compared to the data presented in the main text, is due to a different tuning of the device.

7

Discussion and Outlook

She told me
"A bit of madness is key
To give us new colors to see
Who knows where it will lead us?
And that's why they need us"[272]

7.1. CRITERIA FOR GOOD QUBITS, STATUS UPDATE

In the beginning of this thesis (see section 2.1) five criteria that define a good qubit [102] are discussed. In short, (1) qubits should be scalable and well characterized, (2) it should be possible to initialize them, (3) they should have long coherence times, and (4) a universal gate set, and (5) it should be possible to measure them. Significant progress has been made towards meeting those criteria using hole spin qubits defined in quantum dots in germanium. Some of this progress has been achieved both before and parallel to the work presented in this thesis. For instance (in random order), in the development of the heterostructure [124, 129, 131], forming quantum dots which can host the spin qubit [122, 128, 130], demonstrating a well defined qubit [123, 140], initialization and readout [140], implementing of single- and two-qubit gates [141, 202, 203] and in measuring and improving coherence time [127, 155, 158]. The work in this thesis builds on those results. Chapter 3 continues this work by increasing the number and the quality of the quantum dots that could be used to host qubits. Properties of quantum dots that are important to facilitate qubits, such as good control over the charge filling and the tunnel coupling between the quantum dots, are demonstrated. Moreover, it is shown that four quantum dots can indeed be controlled simultaneously. The work in chapter 4 presents a leap forward, defining four qubits and implementing single qubit gates. Two qubit gates are implemented in a different way, a controlled-Z rotation instead of a CROT. Additionally, a three- and a four-qubit gate are demonstrated. Chapter 5 contributes by introducing yet another way of performing a two-qubit gate: the resonant SWAP gate, and by implementing a three-qubit gate by compiling it with single- and two- qubit gates. Interestingly enough, the results presented in chapter 6 relate more to criteria 6 and 7 from the DiVincenzo criteria than any of the first five. Criteria 6 and 7 come down to the following: the ability to convert a stationary qubit into a flying qubit and bring this moving qubit to a specific destination. To call shuttling flying is a stretch, but a stationary qubit is transformed into a moving qubit and coherently transported to a certain location (two quantum dots over) and back.

7.2. ADDITIONAL CRITERIA FOR SCALABILITY

The criteria described by DiVincenzo have been composed in 2000 and the research field of quantum computing has been transformed since then. Presently, one of the most important challenges has become the scalability of a qubit platform. Although this was mentioned in the DiVincenzo criteria, it was not a criterion in itself. In the first place, scalability means increasing the number of qubits. The execution of practical quantum algorithms will require many more qubits compared to the current capacity available on any platform. How many qubits are needed depends on the envisioned application and on how the algorithm can be implemented. However, just increasing the qubit count will not be sufficient [273]. It is very likely that decoherence and the error rates in qubit operations will limit the implementation of algorithms severely, especially when the number of qubits increases.

Although there are ideas for noisy intermediate-scale quantum applications [274] using approximately 50-100 qubits, to reach the full potential of quantum computing, it will be necessary to implement quantum error correction. How many physical qubits are required per logical qubit depends on the specific error correction code, but also on the fidelity of the qubit operations (qubit gates, initialization and readout). Moreover, scaling is not just a matter of the numbers, because the full potential of the qubits is only accessible if the qubits are well connected to each other, i.e. a two-qubit gate is possible between them. Furthermore, being able to implement qubit gates in parallel instead of sequential can make a significant difference for how efficient an algorithm can be implemented. Therefore, the criterion ‘scalable’, and consequently the necessity to implement an error correction code, points to (at least) three additional criteria: high fidelity, high connectivity and high parallelism.

Consider the results presented in this thesis with those three scalability criteria in mind. In chapter 4 the fidelity of the single qubit gates is evaluated, resulting in 99.9% fidelity for three out of four qubits. This is regarded as an important milestone, because 99.9% fidelity is often quoted in relation to the surface error correction code [221]. This experiment also shows that connectivity, especially when the connection cannot be turned off completely, can compete with the high fidelity. One of the qubits does not reach a single-qubit gate fidelity of 99.9%, which can be related to finite exchange and cross talk to the neighbouring qubits. These effects also played a significant role in the experiments presented in chapter 5. Moreover, the results in chapter 5 show that calibrating single qubit gates to have a high fidelity, in an experiment designed to qualify this fidelity, is one thing. In the phase flip code, single-qubit gates are implemented parallel to each other. The purpose is to make the implementation of the algorithm more compact, and therefore be less effected by the dephasing of the qubits. However, because there is finite connectivity between the qubits, applying single qubit gates in parallel, makes maintaining high fidelity more challenging.

Where the fidelity of the single-qubit gate is quantified and a high value is found, the same can not be said for the initialization, readout and two-qubit gates used for the experiments in this thesis. Moreover, the results presented in chapter 6 (and other recent work [127]) about the influence of strong spin-orbit interaction on hole spin qubits suggest that there is more physics to explore. The quantization axis of the qubit strongly depends on the electrostatic environment in which the hole is confined. This is related to the first DiVincenzo criterion, about the well defined qubit. The ability to manipulate the direction of the quantization axis for all spin qubits in a device requires understanding of the underlying physics, which presents an intriguing challenge. Additionally, understanding and controlling the quantization axis will also be instrumental in optimizing the initialization and readout using Pauli spin blockade.

When it comes to fidelity, connectivity and parallelism, the results in this thesis do not only highlights aspects still to be improve, but also provides suggestions on how to tackle these challenges. The shuttling experiments presented in chapter 6 shows that it is possible to increase the connectivity between hole spin qubits beyond nearest neighbours. Furthermore, it is demonstrated that the shuttling can be fast and the performances are decent. There are ample opportunities identified to improve the shuttling fidelity even further and follow-up experiments show that it is possible to shuttle hole spin qubits with a fidelity of 99.992% [275].

High fidelity shuttling is an important step towards making hole spin qubits a scalable qubit platform. A proposal, much cited throughout the spin-qubit community, is to have small dense two-dimensional spin qubit arrays connected on chip via long-range qubit couplers [167]. This would leave space on the chip to integrate classical control electronics and in this way minimize the number of control lines that need to interface with the outside. Shuttling would be suitable to facilitate such long-range couplers. Although, one could argue that conveyor-mode shuttling would be more suitable to bridge the distance (in the order of tens of micrometers) required to integrate control electronic on chip, in contrast to the bucket-brigade method used in chapter 6.

There are more advantages to extending the connectivity between spin qubits. The surface code is an error correction code which is often proposed as a code that can be made applicable for spin qubits, because it requires the integration of spin qubits in a two-dimensional array with nearest neighbour connectivity and it has a relatively high error threshold [162, 221, 276]. However, increasing the connectivity opens up possibilities for implementing other types of error correction codes, such as the one recently proposed by IBM [277]. Error correction codes which make use of higher connectivity between the qubits can operate with fewer physical qubits per logical qubit and can suppress errors more efficiently.

The results in chapter 6 also demonstrate that when a hole spin qubit is shuttled diabatically between two quantum dots with a difference in quantization axis coherent spin rotations will be the result. This mechanism can be utilized to implement single qubit gates. Moreover, since it is

possible using this method to operate the qubits at a very low magnetic field (in the order of few tens of mT), the coherence time of the qubits increases to microseconds, while the time it takes to implement a single-qubit gate stays in the order of a few tens of nanoseconds. Consequently, in recent work we demonstrate high fidelity single qubit gates in this way [275]. With this mode of operation, the power required for single-qubit gates is much lower than with EDSR driving. In this same work, a two-qubit gate with a fidelity of 99.3% was demonstrated. An important milestone, which was missing until recently. This high fidelity two-qubit gate is possible due to increased coherence times at lower magnetic field and the fact that, despite the low magnetic field, the difference in Zeeman splitting between the qubits was still significant, due to the different g-tensors of the spins. Furthermore, shuttling opens up possibilities for implementing a two-qubit gate in a slightly different way. Where now the barrier gate between adjacent qubits is used to tune the exchange interaction, it is also possible the use the distance between the two qubits to tune the exchange [247]. These different ways of implementing single- and two-qubit gates show that it is beneficial to keep an open mind and not only try to optimize the already existing strategies.

In order to make use of the advantages of increased connectivity between spin qubits, it is necessary to choose an architecture which facilitates this connectivity. What could be a possibility is to arrange the hole spin qubits in a sparse quantum dot array [168, 248]. In a sparse quantum dot array, only part of the quantum dots are used to host spin qubits, while the other quantum dots are not occupied with charge carriers. This type of architecture would provide several advantages. Firstly, empty rows of quantum dots would function as shuttling lanes facilitating high connectivity. Secondly, an empty quantum dot next to a spin qubit can be used to implemented the single-qubit gate by shuttling. Thirdly, the empty quantum dots between the qubits would spatially isolate them from each other, combined with the lower power required for the implementation of single qubit gates, this could reduce residual exchange and cross talk and hopefully facilitate high-fidelity parallel gates. Also in this architecture, control over the g-tensors of the qubits would be beneficial. Although much more thought and consideration is needed to come up with an actual design for a hole-spin qubit chip, it seems that a sparse qubit array can combine connectivity and parallelism, while maintaining high fidelity operations.

7.3. TOWARDS A USEFUL QUANTUM COMPUTER

Now that many proof-of-principle concepts have been demonstrated, a key challenge is to develop a compelling architecture to scale spin qubits to large numbers. The construction of a large qubit array is far from sufficient to build a quantum computer, and many advances are needed to integrated the qubit chip in a full stack system, which will consist of various different layers of hardware and software. The image shown in Fig. 7.1 gives an impression. To build such a system requires many people with different backgrounds and expertise. To name a few: physicists specialized in materials to optimize the semiconductor platform, physicists and engineers to optimize the qubits, software engineers to optimize and automate calibration, electrical engineers to design the control electronics, computer scientist to design the programming language and invent the quantum algorithms to be im-

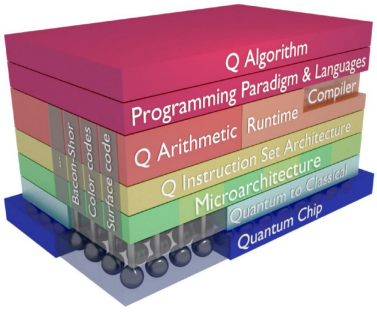

Figure 7.1: **The quantum computing stack.** Source image see Ref. [278].

plemented, etc.

In other words, building a full stack quantum computer requires a diverse and interdisciplinary group of people. People who are experts in their field, but know enough about the other layers of the full stack and the other expertise involved to be able to effectively communicate with their colleagues with a different background. Moreover, it requires people who have an open mind and can appreciate the work and ideas of others. It would be beneficial if the talent pool from which these people are chosen would be as large as possible and therefore include all different genders and nationalities.

Having a diverse group of people working on the development of the quantum computer is also important for another reason. Although, as discussed in the introduction, there are already quite some ideas for the applications of quantum computers [85], it is probable that we at the moment can only foresee a fraction of the tasks the quantum computer will be used for. This is in some sense comparable to the invention of the laser. When in 1960 the first working laser was demonstrated, people thought of it as 'a solution looking for a problem' [75]. However, the laser was immediately used in scientific research, to gain better understanding of the working of lasers themselves and soon it turned out to be a useful tool in other fields of science as well. Presently, lasers are omnipresent in industry and in our daily lives, with applications ranging from scanning a bar code in the supermarket to optical-fiber communication and from eye surgery to a laser pointer for presentations. Since the possible applications of a quantum computer are still so uncertain and unpredictable, there are still also many possibilities. Initially, quantum computers might also be used for scientific research, to better understand quantum computers themselves and other quantum systems. However, it is possible that in the more distant future, the range of applications for the quantum computer will be as wide as they currently are for the laser. Therefore, including many people with a diverse background in the development of the quantum computer and in working towards useful applications, will help to ensure that a quantum computer will be used to tackle a wide range of problems, benefiting as many people as possible.

ACKNOWLEDGEMENTS

The work presented in this thesis would not have been possible without the effort, support and help of many people. Moreover, many people, both inside and outside QuTech, contributed to making my PhD a great experience. On these few pages, I would like to say thank you to all of you.

First of all, Menno, thank you for giving me the opportunity to be part of your research group. You gave me the support I needed, whether it was for hands-on tips for measurements or for something like getting extra time for an exam. I really appreciate your enthusiasm, optimism and creativity. It works contagiously and that was exactly what I needed when I was facing challenges during my PhD. The research of the group has been very successful, which is thanks to your vision as a group leader. Being part of your group is something to be proud of and I could not have wished for a better promoter.

Lieven, thank you for being my co-promoter and for welcoming me into your group when I was a TNO employee. This experience inspired me to pursue a PhD. I admire your calm and fair way of leading your group and QuTech as a whole. Giordano, there would be no germanium without you; you and your group provided the foundation on which the research in this thesis is build. I appreciate how you contribute to the positive atmosphere in the spin qubit groups, for example by inviting us all to your birthday party. I would like to express my appreciation for all my committee members, Sander Otte, Barbara Terhal, Gloria Platero, Natiala Ares and Anasua Chatterjee. Thank you for taking the time to review my thesis and be part of the defense ceremony. Barbara, I really appreciate your thorough and kind feedback, for my thesis as well as the phase flip paper.

The two people who honor me by being my paranymphs are an inspiration to me, both as individuals and as scientists. Anne-Marije, in a group formed mostly of men, I could not have wished for a better friend and ally. It was easy to be myself with you. I took courage from doing 'scary' things together with you, like attending conferences, presenting results and being proud of our achievements. I admire your intelligence, hard work and ambition. During your PhD, you were not always lucky with samples and set-ups, but your persistence paid off. The amazing results that you achieved in the end are impressive. I am glad that you stuck around after your PhD and that you are now also working on germanium ;).

Margriet, people sometimes asked me how it is for me that you made some similar choices as I did, if I either pushed you to do so or found it annoying to share 'my space' with you. I could always answer honestly that you make your own decisions and that I am very happy to have you around. I am so proud that you are pursuing a PhD and that you have found your place at QuTech. Thank you for helping me start writing my thesis again everyday by meeting me for coffee in the morning. I admire your energy, joyfulness, enthusiasm and intelligence and I hope and expect that your scientific career will far surpass mine ♡.

I would like to thank all of the former and current members of the Veldhorst research group. To Gertjan, Luca, Nico and Will, thank you for welcoming me in the group and turning the 'Veldhorstjongens' into the 'Veldhorst genderneutrals'.

Will, we have worked on so many projects together, figuring out how spin-qubit measurements work and searching for the best approach to a research project in general. I am proud and happy with the results that we achieved together. Thank you for fabricating the famous 2-by-2 germanium sample, which at time of writing is still cold! I really appreciate you for being the multitalented person that you are, just as skilled at playing the piano as you are at science. Thank you

for all the nice conversations, for coffees in the city center of Delft during corona and for making music together. All the best to you and Kaja. Corentin, it was a true pleasure to work with you. Your hard work, patience, organizational talents and eye for detail make you a very good scientist. Together we made the shuttling project the work that I am the most proud of, thank you very much. I trust you will take the shuttling project many steps further. Nico, all the research in this thesis was either led by you, in collaboration with you, or building upon your work. Thank you for the huge head start that this gave me in my PhD! I wish you good luck in making germanium a commercial success with Groove. Max, your contribution elevated the projects on which we worked together to a higher level. You always patiently answered my questions, more than once when necessary. You gave me good and kind advice at the right times. Thank you! Chien-An, I really appreciate your quiet and kind presence in the group. When you make a remark in a discussion, it usually is very clever and deliberate. Thank you for contributing to the group in that way! Hanifa, thank you for the energy that you bring to our group. I admire you taking on the challenging bilayer project and it was nice the share an office with you! Valentin, thank you for letting me join the measurements of the bichromatic driving project when I was so fed up with writing and for eating my weird fish dish at the plane from Seoul to Tokyo! Francesco, thank you for the collaboration on the crossbar project and the 3-4-3 project. Thank you for contributing to the group in your steadfast way. Matthijs and me really enjoyed the dinners with you and Grazia, thank you! Sander, your contribution to our research by developing software can hardly be overstated. Thank you for answering all my questions, fixing bugs and helping me with installing a new python environment (again). Most importantly, working with QConstruct for the shuttling experiment made our life in the lab so much better, thank you! Marcel, thank you for contributing to a nice atmosphere in the group, throughout our time in the Veldhorst group. We mostly worked parallel to each other, but it was great to help each other in the practical aspects of finalizing our PhD. Cécile, I enjoyed your presence in the group, thank you! Good luck with the conveyor belt shuttling (please remember the sushi for presentations). Sasha, I appreciate your bold optimism. I hope you make the 6-by-6 work!

To all of you, not in the least also Stefan, Damian, Dario, Michael, Dennis and Job, thank you for the useful feedback during the group meetings, the nice conversations during lunch and coffee breaks, the great group Uitjes and our informal group dinners.

The spin qubit groups at QuTech form a very nice and inspiring working environment, both inside and outside the lab. In the last years many people joined those groups, and I would like to thank each and everyone of you. Specifically, Tobias, I really appreciate you for your enthusiasm, kindness and humor. Thank you for the nice borrels, especially after my go-nogo, for the good team we made as paranymphs for Anne-Marije, for giving me a guided tour through Zürich and for the dinners that we had together with Christina and Matthijs! Irene, for your efforts to make QuTech more diverse and inclusive. Pablo, for all the friendly chats that we had about music and work. Lucas, Maia and Davide, it was a pleasure to share an office with you.

One of the great aspects of QuTech is that if I had a problem, I could always find someone with the right knowledge and skills who is willing to help me. Thank you to all the technicians, among others, Olaf, Reymond, Reymond, Jason, Siebe, Roy and Jelle. Our set-ups would not be running without you. Thank you to all the support staff, among others, Marja and Jenny. QuTech would not be running without you. Thank you Grazia, for your efforts as diversity officer and for our frequent coffee breaks together.

For most of my time as a PhD-candidate, I had the honor of being an OdC member. I would like to thank the Board of Directors, all the OdC members and especially Csilla for the interesting and fruitful discussion we had, striving to make QuTech an even better place to work.

One of the best parts of my time at QuTech was being part of the QuTech band Q2. Rehearsals gave me new energy after a day in the lab and performing with you for QuTech at the Chrismas

Parties, Uitjes and Summer BBQs was one of the most thrilling things I have ever done. Thank you once again for performing at my wedding. It was an honor to play along side such talented musicians. Thank you to all the members of Q2: (among others) Gustavo, Loek, Joe, Hans, Sander, Matteo, Matteo, Leo, Jelle, Will, Bart, Tim, Sayr, Christian, Ruud, Conor, Julia, Nicolas, Christopher, Timo, Marina, Davide, Tzula, Anne-Marije, Maia, Pablo and Hanifa.

Ook wil ik hierbij mijn vrienden bedanken voor alle gezelligheid en goede gesprekken in de afgelopen jaren. Dank jullie wel, Nora, Lucinda, Karlien, Christina, Grazia, Monique, Sara en Adinda.

Roos, Margriet, Jasmijn en Bas, jullie maken Delft mijn thuis. Koffie en lunch op zondag is een van de hoogtepunten van mijn week. Roos, het is inspirerend hoe jij kiest voor je passie en er werk van maakt. Jouw taarten zijn ongeëvenaard, daar heeft QuTech ook van mogen genieten de laatste jaren. Jasmijn, ik ben zo trots op jou. Ik bewonder je musicaliteit, je intelligentie en hoe je helemaal jezelf bent. Ik hoop dat je nog heel lang ons huis beschouwt als jouw tweede thuis. Dankjewel Kato, jij maakt mijn wereld vrolijker! Papa en mama, dat ik voor natuurkunde heb gekozen is omdat jullie mij stimuleerde om een 'echt vak' te leren. Tegelijkertijd heb ik altijd geweten dat jullie trots op mij zijn en van mij houden ongeacht wat ik presteer. Pap, jij hebt me geleerd om groot(er) te denken. Mam, een aantal van jouw gevleugelde uitspraken hebben mij door mijn PhD geholpen: 'Waar een wil is, is een weg', 'Doorgaan met ademhalen' en 'Morgen is er weer een dag'. Lieve Riggels, dank jullie wel voor alles!

Familie Doelman, dank julllie wel dat jullie mij hebben opgenomen in de familie. Ik ben er trots op dat ook de naam 'Doelman' op mijn scriptie prijkt!

Matthijs, het hoogtepunt voor mij van de afgelopen vijf jaar was zonder enige twijfel en met afstand onze trouwdag. Dankjewel voor al je liefde, steun, aanmoediging en feedback. Zonder jou was ik niet begonnen aan een PhD en zonder jou had het zeker niet tot zo'n goed einde kunnen brengen. *All's well that ends well to end up with you* ♡ [279].

BIBLIOGRAPHY

1. Swift, T. *Marjorie* from the album Evermore.
2. Adichie, C. N. *The danger of a single story* https://www.youtube.com/watch?v=D9Ihs241zeg.
3. Born, M. Über Quantenmechanik. *Zeitschrift für Physik* **26,** 379–395 (1924).
4. Mensing, L. Die Rotations-Schwingungsbanden nach der Quantenmechanik. *Zeitschrift für Physik* **36,** 814–823 (1926).
5. Mensing, L. & Pauli, W. Über die Dielektrizitätskonstante von Dipolgasen nach der Quantenmechanik. *Physikalische Zeitschrift,* 814–823 (1926).
6. Mensing, L. Zur Theorie des Zusammenstoßes von Atomen mit langsamen Elektronen. *Zeitschrift für Physik* **45,** 603–609 (1927).
7. Münster, G. (K)eine klassische Karriere? *Physik Journal* (2020).
8. Roloff, D. D. *Picture Lucy Mensing* 1928. https://blog.muenchner-stadtbibliothek.de/lucy-mensing-vergessene-mathematikerin-femaleheritage/.
9. Born, M. & Jordan, P. Zur Quantenmechanik. *Zeitschrift für Physik* **34,** 858–888 (1925).
10. Born, M., Heisenberg, W. & Jordan, P. Zur Quantenmechanik. II. *Zeitschrift für Physik* **35,** 557–615 (1926).
11. Wikipedia page Matrix Mechanics, accessed at 2024-01-18. https://en.wikipedia.org/w/index.php?title=Matrix_mechanics&oldid=1187389722.
12. Jordan, P. Die Anfangsjahre der Quanten-mechanik — Erinnerungen. *Physikalische Blätter* **31,** 97–103 (1975).
13. Göppert-Mayer, M. Über Elementarakte mit zwei Quantensprüngen. *Annalen der Physik* **401,** 273–294 (1931).
14. Kaiser, W. & Garrett, C. G. B. Two-Photon Excitation in CaF_2:Eu^{2+}. *Physical Review Letters* **7,** 229–231 (1961).
15. Gamow, G. & Rutherford, E. Mass defect curve and nuclear constitution. *Proceedings of the Royal Society of London. Series A, Containing Papers of a Mathematical and Physical Character* **126,** 632–644 (1997).
16. Weizsäcker, C. F. v. Zur Theorie der Kernmassen. *Zeitschrift für Physik* **96,** 431–458 (1935).
17. Goeppert-Mayer, M. & Sklar, A. L. Calculations of the Lower Excited Levels of Benzene. *The Journal of Chemical Physics* **6,** 645–652 (2004).

18. Goeppert-Mayer, M. Double Beta-Disintegration. *Physical Review* **48,** 512–516 (1935).
19. Mayer, M. G. On Closed Shells in Nuclei. *Physical Review* **74,** 235–239 (1948).
20. Mayer, M. G. Nuclear Configurations in the Spin-Orbit Coupling Model. I. Empirical Evidence. *Physical Review* **78,** 16–21 (1950).
21. Mayer, M. G. Nuclear Configurations in the Spin-Orbit Coupling Model. II. Theoretical Considerations. *Physical Review* **78,** 22–23 (1950).
22. Mayer, M. G. Rare-Earth and Transuranic Elements. *Physical Review* **60,** 184–187 (1941).
23. *The Nobel Prize in Physics 1963,* Accessed at 2024-01-16. https://www.nobelprize.org/prizes/physics/1963/mayer/facts/.
24. Sachs, R. G. Maria Goeppert Mayer, a biographical memoir. *National Academy of Sciences Washington D.C.* (1979).
25. Wikipedia page Maria Goeppert Mayer, accessed at 2023-09-12. https://en.wikipedia.org/w/index.php?title=Maria_Goeppert_Mayer&oldid=1174935722.
26. University of Chicago Photographic Archive Hanna Holborn Gray Special Collections Research Center, U. o. C. L. *Picture Maria Göppert* https://bliqphotonics.com/honouring-maria-goeppert-mayer/.
27. Meitner, L. & Frisch, O. R. Disintegration of Uranium by Neutrons: a New Type of Nuclear Reaction. *Nature* **143,** 239–240 (1939).
28. Frisch, O. R. *What little I remember* ISBN: 978-0-521-22297-6 (Cambridge University Press, 1979).
29. Pauli, W. Über den Zusammenhang des Abschlusses der Elektronengruppen im Atom mit der Komplexstruktur der Spektren. *Zeitschrift für Physik* **31,** 765–783 (1925).
30. Meitner, L. Fission and Nuclear Shell Model. *Nature* **165,** 561–561 (1950).
31. Meitner, L. Die Muttersubstanz des Actiniums, Ein Neues Radioaktives Element von Langer Lebensdauer. *Zeitschrift für Elektrochemie und angewandte physikalische Chemie* **24,** 169–173 (1918).
32. Meitner, L., Hahn, O. & Strassmann, F. Über die Umwandlungsreihen des Urans, die durch Neutronenbestrahlung erzeugt werden. *Zeitschrift für Physik* **106,** 249–270 (1937).
33. Meitner, L. Über den Zusammenhang zwischen beta- und gamma-Strahlen. *Zeitschrift für Physik* **9,** 145–152 (1922).
34. Matsakis, D., Coster, A., Laster, B. & Sime, R. A renaming proposal: "The Auger–Meitner effect". *Physics Today* **72,** 10–11 (2019).
35. Sime, R. L. Lise Meitner's escape from Germany. *American Journal of Physics* **58,** 262–267 (1990).

36. Sime, R. L. *Lise Meitner : a life in physics* ISBN: 978-0-520-08906-8 (Berkeley : University of California Press, 1996).
37. Wikipedia page Lise Meitner, accessed at 2024-01-25. https://en.wikipedia.org/w/index.php?title=Lise_Meitner&oldid=1194487548.
38. Bettmann, v. G. I. *Picture Lise Meitner* https://www.nytimes.com/2023/10/02/science/lise-meitner-fission-nobel.html.
39. Einstein, A., Podolsky, B. & Rosen, N. Can Quantum-Mechanical Description of Physical Reality Be Considered Complete? *Physical Review* **47,** 777–780 (1935).
40. Hermann, G. Die naturphilosophischen Grundlagen der Quantenmechanik. *Naturwissenschaften* **23,** 718–721 (1935).
41. Henry-Hermann, G. Die Überwindung des Zufalls. Kritische Betrachtungen Zu Leonard Nelsons Begründung der Ethik Als Wissenschaft. *Journal for General Philosophy of Science / Zeitschrift für Allgemeine Wissenschaftstheorie* **17,** 384–386 (1953).
42. Crull, E. M. & Bacciagaluppi, G. *Grete hermann - between physics and philosophy* English. ISBN: 978-94-024-0968-0 (Dordrecht, The Netherlands : Springer, 2016).
43. Herzenberg, C. L. Grete Hermann: An early contributor to quantum theory. http://arxiv.org/abs/0812.3986 (2008).
44. De Boer, D. Grete Hermann 1935. *Nederlands Tijdschrift voor Natuurkunde,* 30–33 (2023).
45. Otto Lohrisch-Achilles, U. B. *Picture Grete Hermann* https://www.uni-bremen.de/unispitzen/professorinnen-im-portrait.
46. Hermann, G. in *Grete Henry-Hermann: Philosophie – Mathematik – Quantenmechanik : Texte zur Naturphilosophie und Erkenntnistheorie, mathematisch-physikalische Beiträge sowie ausgewählte Korrespondenz aus den Jahren 1925 bis 1982* 185–203 (Springer Fachmedien, 2019). ISBN: 978-3-658-16241-2.
47. Crull, E. M. in *The Oxford handbook of the history of quantum interpretations* (Oxford University Press, Oxford, 2022). ISBN: 978-0-19-884449-5.
48. Bohr, N. & Rosenfeld, L. *Complementarity: Bedrock of the Quantal Description* ISBN: 978-0-444-89892-0 (Elsevier, 1996).
49. Douwel, P. P. *Grete Hermann, vrouwelijke quantumheld naast Bohr en Heisenberg, komt eindelijk in de geschiedenisboeken* (2021). https://www.volkskrant.nl/wetenschap/grete-hermann-vrouwelijke-quantumheld-naast-bohr-en-heisenberg-komt-eindelijk-in-de-geschiedenisboeken~bb47362d/.
50. Schrödinger, E. Die gegenwärtige Situation in der Quantenmechanik. *Naturwissenschaften* **23,** 807–812 (1935).
51. VonNeumann, J. Mathematische Grundlagen der Quantenmechanik. (Springer, 1932).
52. BELL, J. S. On the Problem of Hidden Variables in Quantum Mechanics. *Reviews of Modern Physics* **38,** 447–452 (1966).

53. Kaiser, D. History: Shut up and calculate! *Nature* **505,** 153–155 (2014).
54. Levine, A. G. *MIT Radiation Laboratory* (2009). http://www.aps.org/programs/honors/history/historicsites/mit.cfm.
55. David Mermin, N. What's Wrong with this Pillow? *Physics Today* **42,** 9–11 (1989).
56. Kaiser, D. *How the hippies saved physics: science, counterculture, and the quantum revival* ISBN: 978-0-393-07636-3 (W.W. Norton & Company, Inc., New, 2011).
57. Wu, C.-S. The Continuous X-Rays Excited by the Beta-Particles of $_{15}P^{32}$. *Physical Review* **59,** 481–488 (1941).
58. Wu, C.-S. & Segrè, E. Radioactive Xenons. *Physical Review* **67,** 142–149 (1945).
59. Wu, C. S., Ambler, E., Hayward, R. W., Hoppes, D. D. & Hudson, R. P. Experimental Test of Parity Conservation in Beta Decay. *Physical Review* **105,** 1413–1415 (1957).
60. Lidofsky, L. Chien-Shiung Wu, 29 May 1912. 16 February 1997. *Proceedings of the American Philosophical Society* **145,** 116–126 (2001).
61. Frank, M. *The Little-Known Origin Story behind the 2022 Nobel Prize in Physics* (2023). https://www.scientificamerican.com/article/the-little-known-origin-story-behind-the-2022-nobel-prize-in-physics/.
62. Wikipedia page Chien-Shiung Wu, accessed at 2023-08-22. https://en.wikipedia.org/w/index.php?title=Chien-Shiung_Wu&oldid=1171390811.
63. Gilbert, L. *Picture Chien-Shiung Wu* National Portrait Gallery Smithsonian Institution. Acquired through the generosity of friends of Linda Thrift in recognition of her many years of service to the National Portrait Gallery. (1978). https://npg.si.edu/object/npg_NPG.2015.12.
64. Duarte, F. J. The origin of quantum entanglement experiments based on polarization measurements. *The European Physical Journal H* **37,** 311–318 (2012).
65. Silva, I. in *The Oxford Handbook of the History of Quantum Interpretations* (Oxford University Press, Oxford, 2022). ISBN: 978-0-19-884449-5.
66. Wheeler, J. A. Polyelectrons. *Annals of the New York Academy of Sciences* **48,** 219–238 (1946).
67. Pryce, M. H. L. & Ward, J. C. Angular Correlation Effects with Annihilation Radiation. *Nature* **160,** 435–435 (1947).
68. Wu, C. S. & Shaknov, I. The Angular Correlation of Scattered Annihilation Radiation. *Physical Review* **77,** 136–136 (1950).
69. Bohm, D. & Aharonov, Y. Discussion of Experimental Proof for the Paradox of Einstein, Rosen, and Podolsky. *Physical Review* **108,** 1070–1076 (1957).
70. Bohm, D. & Aharonov, Y. Further discussion of possible experimental tests for the paradox of Einstein, Podolsky and Rosen. *Il Nuovo Cimento (1955-1965)* **17,** 964–976 (1960).

71. Kasday, L. R., Ullman, J. D. & Wu, C. S. Angular correlation of compton-scattered annihilation photons and hidden variables. *Nuovo Cimento B Serie* **25,** 633–661 (1975).

72. Clauser, J. F. & Horne, M. A. Experimental consequences of objective local theories. *Physical Review D* **10,** 526–535 (1974).

73. Aspect, A., Grangier, P. & Roger, G. Experimental Realization of Einstein-Podolsky-Rosen-Bohm Gedankenexperiment: A New Violation of Bell's Inequalities. *Physical Review Letters* **49.** Publisher: American Physical Society, 91–94 (1982).

74. Maiman, T. H. Stimulated Optical Radiation in Ruby. *Nature* **187,** 493–494 (1960).

75. Townes, C. H. in *A Century of Nature: Twenty-One Discoveries that Changed Science and the World* (University of Chicago Press, 2003).

76. MacFarlane, A. G. J., Dowling, J. P. & Milburn, G. J. Quantum technology: the second quantum revolution. *Philosophical Transactions of the Royal Society of London. Series A: Mathematical, Physical and Engineering Sciences* **361,** 1655–1674 (2003).

77. Dieks, D. Communication by EPR devices. *Physics Letters A* **92,** 271–272 (1982).

78. Wootters, W. K. & Zurek, W. H. A single quantum cannot be cloned. *Nature* **299,** 802–803 (1982).

79. Feynman, R. P. Simulating physics with computers. *International Journal of Theoretical Physics* **21,** 467–488 (1982).

80. Feynman, R. P. Quantum mechanical computers. *Foundations of Physics* **16,** 507–531 (1986).

81. Manin, Y. I. *The computable and the non-computable* (Sovetskoe Radio, Moskva, 1980).

82. Lloyd, S. Universal Quantum Simulators. *Science* **273,** 1073–1078 (1996).

83. Shor, P. W. Scheme for reducing decoherence in quantum computer memory. *Physical Review A* **52,** R2493–R2496 (1995).

84. Aharonov, D. & Ben-Or, M. Fault-Tolerant Quantum Computation with Constant Error Rate. *SIAM Journal on Computing* **38,** 1207–1282 (2008).

85. Fedorov, A. K., Gisin, N., Beloussov, S. M. & Lvovsky, A. I. Quantum computing at the quantum advantage threshold: a down-to-business review. http://arxiv.org/abs/2203.17181 (2022).

86. Alexeev, Y. *et al.* Quantum Computer Systems for Scientific Discovery. *PRX Quantum* **2,** 017001 (2021).

87. Reiher, M., Wiebe, N., Svore, K. M., Wecker, D. & Troyer, M. Elucidating reaction mechanisms on quantum computers. *Proceedings of the National Academy of Sciences* **114,** 7555–7560 (2017).

88. Shor, P. W. Polynomial-Time Algorithms for Prime Factorization and Discrete Logarithms on a Quantum Computer. *SIAM Review* **41,** 303–332 (1999).

89. Grover, L. K. *A fast quantum mechanical algorithm for database search* in *Proceedings of the twenty-eighth annual ACM symposium on Theory of Computing* (Association for Computing Machinery, New York, NY, USA, July 1996), 212–219. ISBN: 978-0-89791-785-8.

90. Greiner, M., Mandel, O., Esslinger, T., Hänsch, T. W. & Bloch, I. Quantum phase transition from a superfluid to a Mott insulator in a gas of ultracold atoms. *Nature* **415,** 39–44 (2002).

91. Kaufman, A. M. & Ni, K.-K. Quantum science with optical tweezer arrays of ultracold atoms and molecules. *Nature Physics* **17,** 1324–1333 (2021).

92. Cirac, J. I. & Zoller, P. Quantum Computations with Cold Trapped Ions. *Physical Review Letters* **74,** 4091–4094 (1995).

93. Blatt, R. & Wineland, D. Entangled states of trapped atomic ions. *Nature* **453,** 1008–1015 (2008).

94. Knill, E., Laflamme, R. & Milburn, G. J. A scheme for efficient quantum computation with linear optics. *Nature* **409,** 46–52 (2001).

95. Politi, A., Matthews, J. C. F. & O'Brien, J. L. Shor's Quantum Factoring Algorithm on a Photonic Chip. *Science* **325,** 1221–1221 (2009).

96. Pelucchi, E. *et al.* The potential and global outlook of integrated photonics for quantum technologies. *Nature Reviews Physics* **4,** 194–208 (2021).

97. Petersson, K. D., Petta, J. R., Lu, H. & Gossard, A. C. Quantum Coherence in a One-Electron Semiconductor Charge Qubit. *Physical Review Letters* **105,** 246804 (2010).

98. Loss, D. & DiVincenzo, D. P. Quantum computation with quantum dots. *Physical Review A* **57,** 120–126 (1998).

99. Arute, F. *et al.* Quantum supremacy using a programmable superconducting processor. *Nature* **574,** 505–510 (2019).

100. Nakamura, Y., Pashkin, Y. A. & Tsai, J. S. Coherent control of macroscopic quantum states in a single-Cooper-pair box. *Nature* **398,** 786–788 (1999).

101. DiVincenzo, D. P. *Looking back at the DiVincenzo criteria* (2018). https://blog.qutech.nl/2018/02/22/looking-back-at-the-divincenzo-criteria/.

102. DiVincenzo, D. P. The Physical Implementation of Quantum Computation. *Fortschritte der Physik* **48,** 771–783 (2000).

103. Hanson, R., Kouwenhoven, L. P., Petta, J. R., Tarucha, S. & Vandersypen, L. M. K. Spins in few-electron quantum dots. *Reviews of modern physics, 79 (4)* (2007).

104. Van der Wiel, W. G. *et al.* Electron transport through double quantum dots. *Reviews of Modern Physics* **75,** 1–22 (2002).

105. Kouwenhoven, L. P. *et al.* in *Mesoscopic Electron Transport* 105–214 (Springer Netherlands, Dordrecht, 1997). ISBN: 978-94-015-8839-3.

106. Elzerman, J. *et al.* Single-shot read-out of an individual electron spin in a quantum dot. *Nature: international weekly journal of science* **430,** 431–435 (2004).

107. Ciorga, M. *et al.* Addition spectrum of a lateral dot from Coulomb and spin-blockade spectroscopy. *Physical Review B* **61,** R16315–R16318 (2000).

108. Koppens, F. H. L. *et al.* Driven coherent oscillations of a single electron spin in a quantum dot. *Nature* **442,** 766–771 (2006).

109. Foletti, S., Bluhm, H., Mahalu, D., Umansky, V. & Yacoby, A. Universal quantum control of two-electron spin quantum bits using dynamic nuclear polarization. *Nature Physics* **5,** 903–908 (2009).

110. Petta, J. R. *et al.* Coherent Manipulation of Coupled Electron Spins in Semiconductor Quantum Dots. *Science* **309,** 2180–2184 (2005).

111. Shulman, M. D. *et al.* Demonstration of Entanglement of Electrostatically Coupled Singlet-Triplet Qubits. *Science* **336,** 202–205 (2012).

112. Volk, C. *et al.* Loading a quantum-dot based "Qubyte" register. *npj Quantum Information* **5,** 1–8 (2019).

113. Mortemousque, P.-A. *et al.* Coherent control of individual electron spins in a two-dimensional quantum dot array. *Nature Nanotechnology* **16,** 296–301 (2021).

114. Veldhorst, M. *et al.* An addressable quantum dot qubit with fault-tolerant control-fidelity. *Nature Nanotechnology* **9,** 981–985 (2014).

115. Yoneda, J. *et al.* A quantum-dot spin qubit with coherence limited by charge noise and fidelity higher than 99.9%. *Nature Nanotechnology* **13,** 102–106 (2018).

116. Yang, C. H. *et al.* Silicon qubit fidelities approaching incoherent noise limits via pulse engineering. *Nature Electronics* **2,** 151–158 (2019).

117. Xue, X. *et al.* Quantum logic with spin qubits crossing the surface code threshold. *Nature* **601,** 343–347 (2022).

118. Noiri, A. *et al.* Fast universal quantum gate above the fault-tolerance threshold in silicon. *Nature* **601,** 338–342 (2022).

119. Mądzik, M. T. *et al.* Precision tomography of a three-qubit donor quantum processor in silicon. *Nature* **601,** 348–353 (2022).

120. Mills, A. R. *et al.* Two-qubit silicon quantum processor with operation fidelity exceeding 99%. *Science Advances* **8,** eabn5130 (2022).

121. Philips, S. G. J. *et al.* Universal control of a six-qubit quantum processor in silicon. *Nature* **609,** 919–924 (2022).

122. Hendrickx, N. W. *et al.* Gate-controlled quantum dots and superconductivity in planar germanium. *Nature Communications* **9,** 2835 (2018).

123. Watzinger, H. *et al.* A germanium hole spin qubit. *Nature Communications* **9,** 3902 (2018).

124. Sammak, A. *et al.* Shallow and Undoped Germanium Quantum Wells: A Playground for Spin and Hybrid Quantum Technology. *Advanced Functional Materials* **29,** 1807613 (2019).

125. Scappucci, G. *et al.* The germanium quantum information route. *Nature Reviews Materials* **6,** 926–943 (2021).

126. Hendrickx, N. W. *et al.* A four-qubit germanium quantum processor. *Nature* **591,** 580–585 (2021).

127. Hendrickx, N. W. *et al.* Sweet-spot operation of a germanium hole spin qubit with highly anisotropic noise sensitivity. http://arxiv.org/abs/2305.13150 (2023).

128. Froning, F. N. M. *et al.* Single, double, and triple quantum dots in Ge/Si nanowires. *Applied Physics Letters* **113,** 073102 (2018).

129. Lodari, M. *et al.* Low percolation density and charge noise with holes in germanium. *Materials for Quantum Technology* **1,** 011002 (2021).

130. Lawrie, W. I. L. *et al.* Quantum dot arrays in silicon and germanium. *Applied Physics Letters* **116,** 080501 (2020).

131. Lodari, M. *et al.* Light effective hole mass in undoped Ge/SiGe quantum wells. *Physical Review B* **100,** 041304 (2019).

132. Dimoulas, A., Tsipas, P., Sotiropoulos, A. & Evangelou, E. K. Fermi-level pinning and charge neutrality level in germanium. *Applied Physics Letters* **89,** 252110 (2006).

133. Hendrickx, N. W. *Qubit arrays in germanium* PhD thesis (Technische Universiteit Delft, 2021).

134. Philips, S. G. J. *Scaling a spin qubit quantum processor from two to six qubits* PhD thesis (Technische Universiteit Delft, 2023).

135. *Pulse-lib* https://github.com/stephanlphilips/pulse_lib.

136. *QConstruct* https://gitlab.tudelft.nl/qutech-qdlabs/qconstruct.

137. Griffiths, D. J. & Schroeter, D. F. *Introduction to Quantum Mechanics* Third Edition (2018).

138. Terrazos, L. A. *et al.* Theory of hole-spin qubits in strained germanium quantum dots. *Physical Review B* **103,** 125201 (2021).

139. Jen, W. K. *Rabi oscillation and rotating frame* (2023). https://bernwo.github.io/posts/rabi-oscillation-and-rotating-frame/.

140. Hendrickx, N. W. *et al.* A single-hole spin qubit. *Nature Communications* **11,** 3478 (2020).

141. Hendrickx, N. W., Franke, D. P., Sammak, A., Scappucci, G. & Veldhorst, M. Fast two-qubit logic with holes in germanium. *Nature* **577,** 487–491 (2020).

142. Kato, Y. *et al.* Gigahertz Electron Spin Manipulation Using Voltage-Controlled g-Tensor Modulation. *Science* **299,** 1201–1204 (2003).

143. Crippa, A. *et al.* Electrical Spin Driving by g-Matrix Modulation in Spin-Orbit Qubits. *Physical Review Letters* **120,** 137702 (2018).

144. Martinez, B., Abadillo-Uriel, J. C., Rodríguez-Mena, E. A. & Niquet, Y.-M. Hole spin manipulation in inhomogeneous and nonseparable electric fields. *Physical Review B* **106,** 235426 (2022).

145. Abadillo-Uriel, J. C., Rodríguez-Mena, E. A., Martinez, B. & Niquet, Y.-M. Hole-Spin Driving by Strain-Induced Spin-Orbit Interactions. *Physical Review Letters* **131,** 097002 (2023).

146. Meunier, T., Calado, V. E. & Vandersypen, L. M. K. Efficient controlled-phase gate for single-spin qubits in quantum dots. *Physical Review B* **83,** 121403 (2011).

147. Danon, J. & Nazarov, Y. V. Pauli spin blockade in the presence of strong spin-orbit coupling. *Physical Review B* **80,** 041301 (2009).

148. Seedhouse, A. E. *et al.* Pauli Blockade in Silicon Quantum Dots with Spin-Orbit Control. *PRX Quantum* **2,** 010303 (2021).

149. Harvey-Collard, P. *et al.* High-Fidelity Single-Shot Readout for a Spin Qubit via an Enhanced Latching Mechanism. *Physical Review X* **8,** 021046 (2018).

150. Yang, C. H. *et al.* Charge state hysteresis in semiconductor quantum dots. *Applied Physics Letters* **105,** 183505 (2014).

151. Wang, C.-A. *et al.* Probing resonating valence bonds on a programmable germanium quantum simulator. *npj Quantum Information* **9,** 1–8 (2023).

152. Sigillito, A. J., Gullans, M. J., Edge, L. F., Borselli, M. & Petta, J. R. Coherent transfer of quantum information in a silicon double quantum dot using resonant SWAP gates. *npj Quantum Information* **5,** 110 (2019).

153. Geyer, S. *et al.* Anisotropic exchange interaction of two hole-spin qubits. *Nature Physics,* 1–6 (2024).

154. Wang, Z. *et al.* Optimal operation points for ultrafast, highly coherent Ge hole spin-orbit qubits. *npj Quantum Information* **7,** 1–8 (2021).

155. Lawrie, W. *et al.* Spin Relaxation Benchmarks and Individual Qubit Addressability for Holes in Quantum Dots. *Nano letters* (2020).

156. Krzywda, J. A. & Cywiński, Ł. Interplay of charge noise and coupling to phonons in adiabatic electron transfer between quantum dots. *Physical Review B* **104,** 075439 (2021).

157. Philippopoulos, P. *Hyperfine and spin-orbit interactions in semiconductor nanostructures* PhD thesis (McGill University, 2020).

158. Lawrie, W. I. L. *Spin Qubits in Silicon and Germanium* PhD thesis (Technische Universiteit Delft, 2022).

159. Itoh, K. *et al.* High purity isotopically enriched 70Ge and 74Ge single crystals: Isotope separation, growth, and properties. *Journal of Materials Research* **8,** 1341–1347 (1993).

160. Itoh, K. M. & Watanabe, H. Isotope engineering of silicon and diamond for quantum computing and sensing applications. *MRS Communications* **4,** 143–157 (2014).

161. Nielsen, M. A. & Chuang, I. L. *Quantum computation and quantum information* ISBN: 978-1-107-00217-3 (Cambridge University Press, Cambridge ; New York, 2000).

162. Hetényi, B. & Wootton, J. R. Tailoring quantum error correction to spin qubits. *Physical Review A* **109,** 032433 (2024).

163. Takeda, K., Noiri, A., Nakajima, T., Kobayashi, T. & Tarucha, S. Quantum error correction with silicon spin qubits, 23.

164. Van Riggelen, F. *et al.* A two-dimensional array of single-hole quantum dots. *Applied Physics Letters* **118,** 044002 (2021).

165. Terhal, B. M. Quantum error correction for quantum memories. *Reviews of Modern Physics* **87,** 307–346 (2015).

166. Franke, D. P., Clarke, J. S., Vandersypen, L. M. K. & Veldhorst, M. Rent's rule and extensibility in quantum computing. *Microprocessors and Microsystems* **67,** 1–7 (2019).

167. Vandersypen, L. M. K. *et al.* Interfacing spin qubits in quantum dots and donors—hot, dense, and coherent. *npj Quantum Information* **3,** 1–10 (2017).

168. Li, R. *et al.* A crossbar network for silicon quantum dot qubits. *Science advances* **4,** eaar3960 (2018).

169. Helsen, J., Steudtner, M., Veldhorst, M. & Wehner, S. Quantum error correction in crossbar architectures. *Quantum Science and Technology* **3,** 035005 (2018).

170. Kandel, Y. P. *et al.* Coherent spin-state transfer via Heisenberg exchange. *Nature* **573,** 553–557 (2019).

171. Mukhopadhyay, U., Dehollain, J. P., Reichl, C., Wegscheider, W. & Vandersypen, L. M. K. A 2 × 2 quantum dot array with controllable inter-dot tunnel couplings. *Applied Physics Letters* **112,** 183505 (2018).

172. Muhonen, J. T. *et al.* Storing quantum information for 30 seconds in a nanoelectronic device. *Nature Nanotechnology* **9,** 986–991 (2014).

173. Zajac, D. M., Hazard, T. M., Mi, X., Nielsen, E. & Petta, J. R. Scalable Gate Architecture for a One-Dimensional Array of Semiconductor Spin Qubits. *Physical Review Applied* **6,** 054013 (2016).

174. Zwanenburg, F. A. *et al.* Silicon quantum electronics. *Reviews of Modern Physics* **85,** 961–1019 (2013).

175. Maurand, R. *et al.* A CMOS silicon spin qubit. *Nature Communications* **7,** 13575 (2016).

176. Pillarisetty, R. Academic and industry research progress in germanium nanodevices. *Nature* **479,** 324–328 (2011).

177. Ansaloni, F. *et al.* Single-electron operations in a foundry-fabricated array of quantum dots. *Nature Communications* **11,** 6399 (2020).

178. Chanrion, E. *et al.* Charge Detection in an Array of CMOS Quantum Dots. *Physical Review Applied* **14,** 024066 (2020).

179. Gilbert, W. *et al.* Single-Electron Operation of a Silicon-CMOS 2 × 2 Quantum Dot Array with Integrated Charge Sensing. *Nano Letters* **20,** 7882–7888 (2020).

180. Duan, J. *et al.* Remote Capacitive Sensing in Two-Dimensional Quantum-Dot Arrays. *Nano Letters* **20,** 7123–7128 (2020).

181. Bulaev, D. V. & Loss, D. Spin Relaxation and Decoherence of Holes in Quantum Dots. *Physical Review Letters* **95,** 076805 (2005).

182. Bulaev, D. V. & Loss, D. Electric Dipole Spin Resonance for Heavy Holes in Quantum Dots. *Physical Review Letters* **98,** 097202 (2007).

183. DiCarlo, L. *et al.* Differential Charge Sensing and Charge Delocalization in a Tunable Double Quantum Dot. *Physical Review Letters* **92,** 226801 (2004).

184. Tarucha, S., Austing, D. G., Honda, T., van der Hage, R. J. & Kouwenhoven, L. P. Shell Filling and Spin Effects in a Few Electron Quantum Dot. *Physical Review Letters* **77,** 3613–3616 (1996).

185. Liles, S. D. *et al.* Spin and orbital structure of the first six holes in a silicon metal-oxide-semiconductor quantum dot. *Nature Communications* **9,** 3255 (2018).

186. Lim, W. H., Yang, C. H., Zwanenburg, F. A. & Dzurak, A. S. Spin filling of valley–orbit states in a silicon quantum dot. *Nanotechnology* **22,** 335704 (2011).

187. Reimann, S. M. & Manninen, M. Electronic structure of quantum dots. *Reviews of Modern Physics* **74,** 1283–1342 (2002).

188. Van Diepen, C. J. *et al.* Automated tuning of inter-dot tunnel coupling in double quantum dots. *Applied Physics Letters* **113** (2018).

189. Zajac, D. M. *et al.* Resonantly driven CNOT gate for electron spins. *Science* **359,** 439–442 (2018).

190. Lawrie, W. I. L. *et al.* Simultaneous single-qubit driving of semiconductor spin qubits at the fault-tolerant threshold. *Nature Communications* **14,** 3617 (2023).

191. Veldhorst, M. *et al.* A two-qubit logic gate in silicon. *Nature* **526,** 410–414 (2015).

192. Watson, T. F. *et al.* A programmable two-qubit quantum processor in silicon. *Nature* **555,** 633–637 (2018).

193. Huang, W. *et al.* Fidelity benchmarks for two-qubit gates in silicon. *Nature* **569,** 532–536 (2019).

194. He, Y. *et al.* A two-qubit gate between phosphorus donor electrons in silicon. *Nature* **571,** 371–375 (2019).

195. Mądzik, M. T. *et al.* Conditional quantum operation of two exchange-coupled single-donor spin qubits in a MOS-compatible silicon device. *Nature Communications* **12,** 181 (2021).

196. Petit, L. *et al.* Universal quantum logic in hot silicon qubits. *Nature* **580,** 355–359 (2020).

197. Pioro-Ladrière, M. *et al.* Electrically driven single-electron spin resonance in a slanting Zeeman field. *Nature Physics* **4,** 776–779 (2008).

198. Tokura, Y., van der Wiel, W. G., Obata, T. & Tarucha, S. Coherent Single Electron Spin Control in a Slanting Zeeman Field. *Physical Review Letters* **96,** 047202 (2006).

199. Knill, E. *et al.* Randomized benchmarking of quantum gates. *Physical Review A* **77,** 012307 (2008).

200. Cerfontaine, P. *et al.* Closed-loop control of a GaAs-based singlet-triplet spin qubit with 99.5% gate fidelity and low leakage. *Nature Communications* **11,** 4144 (2020).

201. Xue, X. *et al.* Benchmarking Gate Fidelities in a Si/SiGe Two-Qubit Device. *Physical Review X* **9,** 021011 (2019).

202. Wang, K. *et al.* Ultrafast coherent control of a hole spin qubit in a germanium quantum dot. *Nature Communications* **13,** 206 (2022).

203. Froning, F. N. M. *et al.* Ultrafast hole spin qubit with gate-tunable spin–orbit switch functionality. *Nature Nanotechnology* **16,** 308–312 (2021).

204. Scarlino, P. *et al.* Second-Harmonic Coherent Driving of a Spin Qubit in a Si/SiGe Quantum Dot. *Physical Review Letters* **115,** 106802 (2015).

205. Gullans, M. J. & Petta, J. R. Protocol for a resonantly driven three-qubit Toffoli gate with silicon spin qubits. *Physical Review B* **100,** 085419 (2019).

206. Hetényi, B., Kloeffel, C. & Loss, D. Exchange interaction of hole-spin qubits in double quantum dots in highly anisotropic semiconductors. *Physical Review Research* **2,** 033036 (2020).

207. Taylor, J. M. *et al.* Fault-tolerant architecture for quantum computation using electrically controlled semiconductor spins. *Nature Physics* **1,** 177–183 (2005).

208. Veldhorst, M., Eenink, H. G. J., Yang, C. H. & Dzurak, A. S. Silicon CMOS architecture for a spin-based quantum computer. *Nature Communications* **8,** 1766 (2017).

209. Hensgens, T. *et al.* Quantum simulation of a Fermi–Hubbard model using a semiconductor quantum dot array. *Nature* **548,** 70–73 (2017).

210. Andrews, R. W. *et al.* Quantifying error and leakage in an encoded Si/SiGe triple-dot qubit. *Nature Nanotechnology* **14,** 747–750 (2019).

211. Russ, M. *et al.* High-fidelity quantum gates in Si/SiGe double quantum dots. *Physical Review B* **97,** 085421 (2018).

212. Chan, K. W. *et al.* Assessment of a Silicon Quantum Dot Spin Qubit Environment via Noise Spectroscopy. *Physical Review Applied* **10,** 044017 (2018).

213. Barnes, E., Kestner, J. P., Nguyen, N. T. T. & Das Sarma, S. Screening of charged impurities with multielectron singlet-triplet spin qubits in quantum dots. *Physical Review B* **84,** 235309 (2011).

214. Van Riggelen, F. *et al.* Phase flip code with semiconductor spin qubits. *npj Quantum Information* **8,** 1–7 (2022).

215. Preskill, J. Reliable quantum computers. *Proceedings of the Royal Society of London. Series A: Mathematical, Physical and Engineering Sciences* **454,** 385–410 (1998).

216. Cory, D. G. *et al.* Experimental Quantum Error Correction. *Physical Review Letters* **81,** 2152–2155 (1998).

217. Moussa, O. Demonstration of Sufficient Control for Two Rounds of Quantum Error Correction in a Solid State Ensemble Quantum Information Processor. *Physical Review Letters* **107** (2011).

218. Schindler, P. *et al.* Experimental Repetitive Quantum Error Correction. *Science* **332,** 1059–1061 (2011).

219. Reed, M. D. *et al.* Realization of three-qubit quantum error correction with superconducting circuits. *Nature* **482,** 382–385 (2012).

220. Taminiau, T. H., Cramer, J., van der Sar, T., Dobrovitski, V. V. & Hanson, R. Universal control and error correction in multi-qubit spin registers in diamond. *Nature Nanotechnology* **9,** 171–176 (2014).

221. Fowler, A. G., Mariantoni, M., Martinis, J. M. & Cleland, A. N. Surface codes: Towards practical large-scale quantum computation. *Physical Review A* **86,** 032324 (2012).

222. Rosenblum, S. *et al.* Fault-tolerant detection of a quantum error. *Science* **361,** 266–270 (2018).

223. Campagne-Ibarcq, P. *et al.* Quantum error correction of a qubit encoded in grid states of an oscillator. *Nature* **584,** 368–372 (2020).

224. Andersen, C. K. *et al.* Repeated quantum error detection in a surface code. *Nature Physics* **16,** 875–880 (2020).

225. Marques, J. F. *et al.* Logical-qubit operations in an error-detecting surface code. *Nature Physics* **18,** 80–86 (2022).

226. Waldherr, G. *et al.* Quantum error correction in a solid-state hybrid spin register. *Nature* **506,** 204–207 (2014).

227. Cramer, J. *et al.* Repeated quantum error correction on a continuously encoded qubit by real-time feedback. *Nature Communications* **7,** 11526 (2016).

228. Abobeih, M. H. *et al.* Fault-tolerant operation of a logical qubit in a diamond quantum processor. *Nature* **606,** 884–889 (2022).

229. Nigg, D. *et al.* Quantum computations on a topologically encoded qubit. *Science* **345,** 302–305 (2014).

230. Egan, L. *et al.* Fault-tolerant control of an error-corrected qubit. *Nature* **598,** 281–286 (2021).

231. Rispler, M., Cerfontaine, P., Langrock, V. & Terhal, B. M. Towards a realistic GaAs-spin qubit device for a classical error-corrected quantum memory. *Physical Review A* **102,** 022416 (2020).

232. Zheng, G. *et al.* Rapid gate-based spin read-out in silicon using an on-chip resonator. *Nature Nanotechnology* **14,** 742–746 (2019).

233. Jirovec, D. *et al.* A singlet-triplet hole spin qubit in planar Ge. *Nature Materials* **20,** 1106–1112 (2021).

234. Paquelet Wuetz, B. *et al.* Atomic fluctuations lifting the energy degeneracy in Si/SiGe quantum dots. *Nature Communications,* 7730 (2022).

235. Ercan, H. E. *et al.* Measurement-free implementations of small-scale surface codes for quantum-dot qubits. *Physical Review A* **97,** 012318 (2018).

236. Studenikin, S. A. *et al.* Enhanced charge detection of spin qubit readout via an intermediate state. *Applied Physics Letters* **101,** 233101 (2012).

237. Barenco, A. *et al.* Elementary gates for quantum computation. *Physical Review A* **52,** 3457–3467 (1995).

238. Smolin, J. A. & Divincenzo, D. P. Five Two-Bit Quantum Gates are Sufficient to Implement the Quantum Fredkin Gate. *Physical Review A* **53,** 2855–2856 (1995).

239. Heinz, I. & Burkard, G. Crosstalk analysis for simultaneously driven two-qubit gates in spin qubit arrays. *Physical Review B* **105,** 085414 (2022).

240. Piot, N. *et al.* A single hole spin with enhanced coherence in natural silicon. *Nature Nanotechnology* **17,** 1072–1077 (2022).

241. Harris, F. On the use of windows for harmonic analysis with the discrete Fourier transform. *Proceedings of the IEEE* **66,** 51–83 (1978).

242. Van Riggelen-Doelman, F. *et al.* Coherent spin qubit shuttling through germanium quantum dots. https://arxiv.org/abs/2308.02406v1 (2023).

243. Camenzind, L. C. *et al.* A hole spin qubit in a fin field-effect transistor above 4 kelvin. *Nature Electronics* **5,** 178–183 (2022).

244. Borsoi, F. *et al.* Shared control of a 16 semiconductor quantum dot crossbar array. *Nature Nanotechnology,* 1–7 (2023).

245. Van Meter, R. & Horsman, D. A blueprint for building a quantum computer. *Communications of the ACM* **56,** 84–93 (2013).

246. Wecker, D., Bauer, B., Clark, B. K., Hastings, M. B. & Troyer, M. Gate-count estimates for performing quantum chemistry on small quantum computers. *Physical Review A* **90,** 022305 (2014).

247. Noiri, A. *et al.* A shuttling-based two-qubit logic gate for linking distant silicon quantum processors. *Nature Communications* **13,** 5740 (2022).

248. Boter, J. M. *et al.* Spiderweb Array: A Sparse Spin-Qubit Array. *Physical Review Applied* **18,** 024053 (2022).

249. Künne, M. *et al.* The SpinBus Architecture: Scaling Spin Qubits with Electron Shuttling. http://arxiv.org/abs/2306.16348 (2023).

250. Mills, A. R. *et al.* Shuttling a single charge across a one-dimensional array of silicon quantum dots. *Nature Communications* **10,** 1063 (2019).

251. Seidler, I. *et al.* Conveyor-mode single-electron shuttling in Si/SiGe for a scalable quantum computing architecture. *npj Quantum Information* **8,** 1–7 (2022).

252. Xue, R. *et al.* Si/SiGe QuBus for single electron information-processing devices with memory and micron-scale connectivity function. *Nature Communications* **15,** 2296 (2024).

253. Flentje, H. *et al.* Coherent long-distance displacement of individual electron spins. *Nature Communications* **8,** 501 (2017).

254. Fujita, T., Baart, T. A., Reichl, C., Wegscheider, W. & Vandersypen, L. M. K. Coherent shuttle of electron-spin states. *npj Quantum Information* **3,** 1–6 (2017).

255. Mortemousque, P.-A. *et al.* Enhanced Spin Coherence while Displacing Electron in a Two-Dimensional Array of Quantum Dots. *PRX Quantum* **2,** 030331 (2021).

256. Jadot, B. *et al.* Distant spin entanglement via fast and coherent electron shuttling. *Nature Nanotechnology* **16,** 570–575 (2021).

257. Yoneda, J. *et al.* Coherent spin qubit transport in silicon. *Nature Communications* **12,** 4114 (2021).

258. Zwerver, A. *et al.* Shuttling an Electron Spin through a Silicon Quantum Dot Array. *PRX Quantum* **4,** 030303 (2023).

259. Struck, T. *et al.* Spin-EPR-pair separation by conveyor-mode single electron shuttling in Si/SiGe. *Nature Communications* **15,** 1325 (2024).

260. Jirovec, D. *et al.* Dynamics of Hole Singlet-Triplet Qubits with Large g-Factor Differences. *Physical Review Letters* **128,** 126803 (2022).

261. Mutter, P. M. & Burkard, G. All-electrical control of hole singlet-triplet spin qubits at low-leakage points. *Physical Review B* **104,** 195421 (2021).

262. Bosco, S., Benito, M., Adelsberger, C. & Loss, D. Squeezed hole spin qubits in Ge quantum dots with ultrafast gates at low power. *Physical Review B* **104,** 115425 (2021).

263. Wang, C.-A., Scappucci, G., Veldhorst, M. & Russ, M. Modelling of planar germanium hole qubits in electric and magnetic fields. http://arxiv.org/abs/2208.04795 (2022).

264. Bosco, S., Zou, J. & Loss, D. High-fidelity spin qubit shuttling via large spin-orbit interaction. http://arxiv.org/abs/2311.15970 (2023).

265. Huang, P. & Hu, X. Spin qubit relaxation in a moving quantum dot. *Physical Review B* **88,** 075301 (2013).

266. Langrock, V. *et al.* Blueprint of a Scalable Spin Qubit Shuttle Device for Coherent Mid-Range Qubit Transfer in Disordered Si/SiGe/SiO_2. *PRX Quantum* **4,** 020305 (2023).

267. Benito, M. & Burkard, G. Hybrid superconductor-semiconductor systems for quantum technology. *Applied Physics Letters* **116,** 190502 (2020).

268. Croot, X. *et al.* Flopping-mode electric dipole spin resonance. *Physical Review Research* **2,** 012006 (2020).

269. Hu, R.-Z. *et al.* Flopping-mode spin qubit in a Si-MOS quantum dot. *Applied Physics Letters* **122,** 134002 (2023).

270. Oosterkamp, T. H. *et al.* Microwave spectroscopy of a quantum-dot molecule. *Nature* **395,** 873–876 (1998).

271. Blume-Kohout, R. *et al.* A Taxonomy of Small Markovian Errors. *PRX Quantum* **3,** 020335 (2022).

272. Pasek, B., Hurwitx, J. & Noble Paul, J. *Audition (The Fools Who Dream)* from the movie Lalaland, sang by Emma Stone.

273. Devoret, M. H. & Schoelkopf, R. J. Superconducting Circuits for Quantum Information: An Outlook. *Science* **339,** 1169–1174 (2013).

274. Preskill, J. Quantum Computing in the NISQ era and beyond. *Quantum* **2,** 79 (2018).

275. Wang, C.-A. *et al.* Operating semiconductor quantum processors with hopping spins. http://arxiv.org/abs/2402.18382 (2024).

276. Wang, D. S., Fowler, A. G. & Hollenberg, L. C. L. Surface code quantum computing with error rates over 1%. *Physical Review A* **83,** 020302 (2011).

277. Bravyi, S. *et al.* High-threshold and low-overhead fault-tolerant quantum memory. *Nature* **627,** 778–782 (2024).

278. *Image full stack quantum computer* https://qutech.nl/research-engineering/quantum-computing/.

279. Shakespeare, W. & Swift, T. *Lover* from the album Lover.

Curriculum Vitæ

Floor van Riggelen-Doelman

August 27, 1990	Born in Amersfoort, the Netherlands.

Education

2002–2008	Secondary School - Atheneum Corderius College, Amersfoort (2002–2003) CSG Reggesteyn, Rijssen and Nijverdal (2003–2008)
2008–2012	Bachelor of Science in Astronomy & Physics University of Utrecht
2008–2012	Bachelor of Science in Liberal Arts & Sciences University of Utrecht
2013–2015	Master of Physics University of Amsterdam *MSc Thesis:* Characterization of a lasing plasmonic particle array *Supervisors:* dr. H. Schokker and dr. prof. A.F. Koenderink
2019–2023	Ph.D. in Experimental Physics Delft University of Technology *Thesis:* Distributing quantum information with holes in germanium *Promotor:* dr. M. Veldhorst

Professional Experience

2015–2017	Trainee Netherlands Organization for Applied Scientific Research (TNO)
2017–2019	Junior Scientist at Quantum Technology Department Netherlands Organization for Applied Scientific Research (TNO)

List of Publications

11. *Operating semiconductor quantum processors with hopping spins*
C.-A. Wang, V. John, H. Tidjani, C.X. Yu, A. Ivlev, C. Déprez, **F. van Riggelen-Doelman**, B.D. Woods, N.W. Hendrickx, W.I.L. Lawrie, L.E.A. Stehouwer, S. Oosterhout, A. Sammak, M. Friesen, G. Scappucci, S.L. de Snoo, M. Rimbach-Russ, F. Borsoi, M. Veldhorst, in print with Science (2024).
10. *Coherent spin qubit shuttling through germanium quantum dots*
F. van Riggelen-Doelman, C.-A. Wang, S.L. de Snoo, W.I.L. Lawrie, N.W. Hendrickx, M. Rimbach-Russ, A. Sammak, G. Scappucci, C. Déprez, M. Veldhorst, in print with Nature Communications (2024).
9. *Bichromatic Rabi control of semiconductor qubits*
V. John, F. Borsoi, Z. György, C.-A. Wang, G. Széchenyi, **F. van Riggelen-Doelman**, W.I.L. Lawrie, N.W. Hendrickx, A. Sammak, G. Scappucci, A. Pályi, M. Veldhorst, Physical review letters **132** (6), 067001.
8. *Shared control of a 16 semiconductor quantum dot crossbar array*
F. Borsoi, N.W. Hendrickx, V. John, M. Meyer, S. Motz, **F. van Riggelen-Doelman**, A. Sammak, S.L. de Snoo, G. Scappucci, M. Veldhorst, Nature Nanotechnology **19** (1), 21-27 (2024).
7. *Simultaneous single-qubit driving of semiconductor spin qubits at the fault-tolerant threshold*
W.I.L. Lawrie, M. Rimbach-Russ, **F. van Riggelen**, N.W. Hendrickx, , S.L. de Snoo, A. Sammak, G. Scappucci, J. Helsen, M. Veldhorst, Nature Communications **14** (1), 3617 (2023).
6. *Phase flip code with semiconductor spin qubits*
F. van Riggelen, W.I.L. Lawrie, M. Russ, N.W. Hendrickx, A. Sammak, M. Rispler, B.M. Terhal, G. Scappucci, M. Veldhorst, npj Quantum Information **8** (1), 124 (2022).
5. *A four-qubit germanium quantum processor*
N.W. Hendrickx, W.I.L. Lawrie, M. Russ, **F. van Riggelen**, S.L. de Snoo, R.N. Schouten A. Sammak, G. Scappucci, M. Veldhorst, Nature **591** (7851), 580-585 (2021).
4. *A two-dimensional array of single-hole quantum dots*
F. van Riggelen, N.W. Hendrickx, W.I.L. Lawrie, M. Russ, A. Sammak, G. Scappucci, M. Veldhorst, Applied Physics Letters **118** (4) (2021).
3. *Spin relaxation benchmarks and individual qubit addressability for holes in quantum dots*
W.I.L. Lawrie, N.W. Hendrickx, **F. van Riggelen**, M. Russ, L. Petit, A. Sammak, G. Scappucci, M. Veldhorst, Nano letters **20** (10), 7237-7242 (2020).
2. *Quantum dot arrays in silicon and germanium*
W.I.L. Lawrie, H.G.J. Eenink, N.W. Hendrickx, J.M. Boter, L. Petit, S.V. Amitonov, M. Lodari, B. Paquelet Wuetz, C. Volk, S.G.J. Philips, G. Droulers, N. Kalhor, **F. van Riggelen**, D. Brousse, A. Sammak, L.M.K. Vandersypen, G. Scappucci, M. Veldhorst, Applied Physics Letters **116** (8) (2020).
1. *Systematic study of the hybrid plasmonic-photonic band structure underlying lasing action of diffractive plasmon particle lattices*
A.H. Schokker, **F. van Riggelen**, Y. Hadad, A. Alù, A.F. Koenderink, Physical Review B **95** (8), 085409 (2017).